

UNCLASSIFIED

AD NUMBER

AD487431

LIMITATION CHANGES

TO:

Approved for public release; distribution is unlimited.

FROM:

Distribution authorized to U.S. Gov't. agencies and their contractors;  
Administrative/Operational Use; JUN 1966. Other requests shall be referred to Air Force Rocket Propulsion Lab., Edwards AFB., CA.

AUTHORITY

AFRPL ltr 20 Dec 1971

THIS PAGE IS UNCLASSIFIED

UNCLASSIFIED

AFRPL-TR-66-95

21

1  
6  
4  
2  
8  
4

FREE STANDING PYROLYTIC GRAPHITE  
THRUST CHAMBERS FOR  
SPACE OPERATION AND ATTITUDE CONTROL

PHASE I: ANALYSIS AND PRELIMINARY DESIGN

J.G. Campbell  
M.L. Haas  
C.D. Coulbert

THE MARQUARDT CORPORATION  
Van Nuys, California

June 1966

This document is subject to special export controls  
and each transmittal to foreign governments or  
foreign nationals may be made only with prior approval  
of AFRPL (RPPR-STINFO), Edwards, California 93523.

AIR FORCE ROCKET PROPULSION LABORATORY  
Research and Technology Division  
Air Force Systems Command  
United States Air Force  
Edwards Air Force Base, California

UNCLASSIFIED

When U.S. Government drawings, specifications, or other data are used for any purpose other than a definitely related Government procurement operation, the Government thereby incurs no responsibility nor any obligation whatsoever, and the fact that the Government may have formulated, furnished, or in any way supplied the said drawings, specifications, or other data, is not to be regarded by implication or otherwise, or in any manner licensing the holder or any other person or corporation, or conveying any rights or permission to manufacture, use or sell any patented invention that may in any way be related thereto.

**UNCLASSIFIED**

**AFRPL-TR-66-95**

**21**

**FREE STANDING PYROLYTIC GRAPHITE  
THRUST CHAMBERS FOR  
SPACE OPERATION AND ATTITUDE CONTROL**

**PHASE I: ANALYSIS AND PRELIMINARY DESIGN**

**J.G. Campbell  
M.L. Haas  
C.D. Coulbert**

**THE MARQUARDT CORPORATION  
Van Nuys, California**

**June 1966**

**This document is subject to special export controls  
and each transmittal to foreign governments or  
foreign nationals may be made only with prior approval  
of AFRPL (RPPR-STINFO), Edwards, California 93523.**

**UNCLASSIFIED**



# UNCLASSIFIED

AFRPL-TR-66-95

Report 6106

## FOREWORD

This report covers work performed by The Marquardt Corporation under Phase I, Analysis and Preliminary Design, of Contract No. AF 04(611)-10790, during the period 15 June 1965 to 31 December 1965. The work was sponsored by the Air Force Rocket Propulsion Laboratory, Research and Technology Division, Edwards Air Force Base, California, Air Force Systems Command, United States Air Force, as Air Force Systems Command Project No. 3058, Air Force Program Element Code 6.24.05.18.4. The AFRPL Project Engineer was Mr. Gary Goodrich, RPRRC.

The Project Manager, Mr. C. D. Coulbert, was responsible for the overall program supervision. The Project Engineer, Mr. J. G. Campbell, was responsible for technical supervision.

The report number assigned to this document by The Marquardt Corporation is 6106.

This technical report has been reviewed and is approved.

UNCLASSIFIED

# UNCLASSIFIED

AFRPL-TR-66-95

Report 6106

## ABSTRACT

Free standing pyrolytic graphite (PG) thrust chambers have been evaluated for application to high energy upper stage and attitude control liquid rocket engines. This Phase I Analysis Report presents the results of stress analyses, heat transfer analyses, and a vendor product survey and evaluation. The results of PG thrust chamber firings with  $F_2/H_2$ ,  $F_2/BA1014$ , and  $N_2O_4/0.5 N_2H_4 - 0.5$  UDMH propellants at thrust levels of 100, 1000, and 5000 pounds will be reported in a subsequent technical report.

The analytical stress calculations which included the effects of PG anisotropy, creep, and growth showed the structural feasibility of fabricating and firing free standing PG thrust chambers up to 5000 pounds thrust. Operation at chamber pressures up to 300 psia appears feasible. However, the effects of growth and creep at high operating temperatures may be critical and experimental data are required to establish valid design criteria.

The heat transfer studies investigated the transient and steady state temperature distributions within the PG chambers for each of the propellants considered. The high inside surface temperatures encountered in the full scale thrust chamber using fluorine propellants create a problem of heat soak back in the injector after the run which must be resolved in future designs.

Five pyrolytic graphite vendors supplied samples of their pyrolytic graphite products in the form of free standing, thin walled tubes 2 inches in diameter and 4 inches long. A total of 78 tubes was purchased. These were evaluated by burst testing in order to evaluate their structural capability for free standing pyrolytic graphite rocket thrust chambers. The pyrolytic graphite fabrication parameters which were evaluated included mandrel material, mandrel surface finish, substrate nucleated and regenerative microstructures, controlled delaminations, boron alloying, and fiber reinforcement.

The critical effect of nodule size on maximum tube strength was confirmed. Maximum tube strengths were achieved with boron alloying and with regenerative microstructure. A burst pressure of 1000 psig appears to be a reasonable target for currently available pyrolytic graphite at room temperature.

The results of continuing manufacturing studies by the vendors and the evaluation of test firings to be made during the experimental phase of this program will provide a better definition of the full potential of pyrolytic materials as a thrust chamber material.

UNCLASSIFIED

**UNCLASSIFIED**

**AFRPL-TR-66-95**

**Report 6106**

**This page intentionally left blank**

**UNCLASSIFIED**

CONTENTS

<u>Section</u>		<u>Page</u>
--	Abstract. . . . .	111
I	INTRODUCTION. . . . .	1
	A. Background. . . . .	1
	B. Structural Problems . . . . .	2
	C. Heat Transfer Problems. . . . .	5
	D. Chemical Erosion. . . . .	6
	E. Analysis and Preliminary Design . . . . .	6
II	PRELIMINARY DESIGN STUDIES. . . . .	7
	A. Scope of Studies. . . . .	7
	B. Propellant Performance. . . . .	7
	C. Thrust Chamber Dimensions . . . . .	7
III	PROPERTIES OF PYROLYTIC GRAPHITE. . . . .	9
IV	HEAT TRANSFER STUDIES . . . . .	11
	A. Wall Temperature Gradients. . . . .	11
	B. Postrun Injector Temperatures . . . . .	14
V	STRESS ANALYSES . . . . .	19
	A. Method of Analysis. . . . .	19
	B. Experimental Residual Stress Data . . . . .	34
	C. Proof Stresses. . . . .	36
	D. 100-pound Thrust Configuration, N <sub>2</sub> O <sub>4</sub> /0.5 N <sub>2</sub> H <sub>4</sub> -0.5 UDMH. . . . .	36
	E. 100-pound Thrust Configuration, F <sub>2</sub> /BA1014 . . . . .	36
	F. 100-pound Thrust Configuration, Comparison of Propellant Combinations . . . . .	38
	G. 1000-pound Thrust Configuration, N <sub>2</sub> O <sub>4</sub> /0.5 N <sub>2</sub> H <sub>4</sub> -0.5 UDMH . . . . .	38
	H. 5000-pound Thrust Configuration, F <sub>2</sub> /BA1014. . . . .	39
	I. Controlled Temperature Chamber. . . . .	40
	J. Expansion Nozzle. . . . .	40
	K. Shear Stresses. . . . .	41
	L. Vibration Stress Analysis . . . . .	41
	M. Tensile Strength. . . . .	43
VI	PYROLYTIC GRAPHITE PRODUCT EVALUATION . . . . .	45
	A. Vendor Survey . . . . .	45
	B. Evaluation of Pyrolytic Graphite Tubes. . . . .	45
	C. Conclusions . . . . .	52
--	REFERENCES. . . . .	53
--	DISTRIBUTION. . . . .	185

**UNCLASSIFIED**

AFRPL-TR-66-95

Report 6106

This page intentionally left blank

**UNCLASSIFIED**

## ILLUSTRATIONS

<u>Figure</u>		<u>Page</u>
1.	Coordinates of Free Standing Pyrolytic Graphite Thrust Chamber. . . . .	76
2.	Propellant Performance, $N_2O_4/0.5 N_2H_4-0.5 UDMH$ . . . . .	77
3.	Propellant Performance, $F_2/BA1014$ . . . . .	78
4.	Propellant Performance, $F_2/H_2$ . . . . .	79
5.	Combustion Temperature vs. C* Efficiency, Shifting Equilibrium. . . . .	80
6.	100-pound Thrust Configuration. . . . .	81
7.	Chamber Dimension Nomenclature. . . . .	82
8.	Modulus of Elasticity of Pyrolytic Graphite, Analysis Standard . . . . .	83
9.	Coefficient of Thermal Expansion in the a-Direction for Pyrolytic Graphite, Analysis Standard . . . . .	84
10.	Coefficient of Thermal Expansion in the c-Direction for Pyrolytic Graphite, Analysis Standard . . . . .	85
11.	Thermal Conductivity in the a-Direction for Pyrolytic Graphite, Analysis Standard . . . . .	86
12.	Thermal Conductivity in the c-Direction for Pyrolytic Graphite, Analysis Standard . . . . .	87
13.	Specific Heat for Pyrolytic Graphite, Analysis Standard . . . . .	88
14.	Modulus of Elasticity in the a-Direction for Pyrolytic Graphite. . . . .	89
15.	Thermal Conductivity in the c-Direction for Pyrolytic Graphite. . . . .	90
16.	Growth and Creep in the a-Direction for Pyrolytic Graphite, Analysis Standard . . . . .	91
17.	Throat Wall Temperature vs. Time, 100-lb Thrust Configuration, $N_2O_4/0.5 N_2H_4-0.5 UDMH$ , $P_c = 50$ psia . . . . .	92
18.	Throat Wall Temperature vs. Time, 100-lb Thrust Configuration, $N_2O_4/0.5 N_2H_4-0.5 UDMH$ , $P_c = 100$ psia. . . . .	93
19.	Throat Wall Temperature vs. Time, 100-lb Thrust Configuration, $N_2O_4/0.5 N_2H_4-0.5 UDMH$ , $P_c = 300$ psia. . . . .	94

## ILLUSTRATIONS (Continued)

<u>Figure</u>		<u>Page</u>
20.	Combustion Chamber Wall Temperature vs. Time, 100-lb Thrust Configuration, $N_2O_4/0.5 N_2H_4-0.5 UDMH$ , $P_c = 50$ psia. . . . .	95
21.	Combustion Chamber Wall Temperature vs. Time, 100-lb Thrust Configuration $N_2O_4/0.5 N_2H_4-0.5 UDMH$ , $P_c = 100$ psia. . . . .	96
22.	Combustion Chamber Wall Temperature vs. Time, 100-lb Thrust Configuration, $N_2O_4/0.5 N_2H_4-0.5 UDMH$ , $P_c = 300$ psia . . . . .	97
23.	Combustion Chamber Wall Temperature Distribution, 100-lb Thrust Configuration, $N_2O_4/0.5 N_2H_4-0.5 UDMH$ , $P_c = 100$ psia. .	98
24.	Combustion Chamber Inside Wall Temperature vs. C* Efficiency, 100-lb Thrust Configuration, $N_2O_4/0.5 N_2H_4-0.5 UDMH$ . . . . .	99
25.	Combustion Chamber Inside Wall Temperature vs. Oxidizer-Fuel Ratio, 100-lb Thrust Configuration, $N_2O_4/0.5 N_2H_4-0.5 UDMH$ . .	100
26.	Throat Wall Temperature vs. Time, 100-lb Thrust Configuration, $F_2/BA1014$ , $P_c = 50$ psia. . . . .	101
27.	Throat Wall Temperature vs. Time, 100-lb Thrust Configuration, $F_2/BA1014$ , $P_c = 100$ psia . . . . .	102
28.	Throat Wall Temperature vs. Time, 100-lb Thrust Configuration, $F_2/BA1014$ , $P_c = 300$ psia . . . . .	103
29.	Combustion Chamber Wall Temperature vs. Time, 100-lb Thrust Configuration, $F_2/BA1014$ , $P_c = 50$ psia . . . . .	104
30.	Combustion Chamber Wall Temperature vs. Time, 100-lb Thrust Configuration, $F_2/BA1014$ , $P_c = 100$ psia. . . . .	105
31.	Combustion Chamber Wall Temperature vs. Time, 100-lb Thrust Configuration, $F_2/BA1014$ , $P_c = 300$ psia . . . . .	106
32.	Combustion Chamber Wall Temperature Distribution, 100-lb Thrust Configuration, $F_2/BA1014$ , $P_c = 100$ psia . . . . .	107
33.	Combustion Chamber Inside Wall Temperature vs. C* Efficiency, 100-lb Thrust Configuration, $F_2/BA1014$ . . . . .	108
34.	Combustion Chamber Inside Wall Temperature vs. Oxidizer-Fuel Ratio, 100-lb Thrust Configuration, $F_2/BA1014$ . . . . .	109
35.	Throat Wall Temperature Comparison, 100-lb Thrust Configuration, $F_2/BA1014$ and $F_2/H_2$ . . . . .	110

UNCLASSIFIED

-viii-



## ILLUSTRATIONS (Continued)

<u>Figure</u>		<u>Page</u>
36.	Combustion Chamber Wall Temperature Comparison, 100-lb Thrust Configuration, $F_2/BA1014$ and $F_2/H_2$ . . . . .	111
37.	Combustion Chamber and Throat Inside Wall Temperatures vs. Oxidizer-Fuel Ratio, 100-lb Thrust Configuration, $F_2/H_2$ . . . . .	112
38.	Variation of Radial Thermal Conductivity with Throat Wall Temperature and Time, 100-lb Thrust Configuration, $N_2O_4/0.5 N_2H_4-0.5 UDMH$ . . . . .	113
39.	Variation of Radial Thermal Conductivity with Throat Wall Temperature and Time, 100-lb Thrust Configuration, $F_2/BA1014$ . . . . .	114
40.	Combustion Chamber Wall Temperature vs. Time, 1000-lb Thrust Configuration, $N_2O_4/0.5 N_2H_4-0.5 UDMH$ , $P_c = 50$ psia. . . . .	115
41.	Combustion Chamber Wall Temperature vs. Time, 1000-lb Thrust Configuration $N_2O_4/0.5 N_2H_4-0.5 UDMH$ , $P_c = 100$ psia. . . . .	116
42.	Combustion Chamber Wall Temperature vs. Time, 1000-lb Thrust Configuration $N_2O_4/0.5 N_2H_4-0.5 UDMH$ , $P_c = 300$ psia. . . . .	117
43.	Throat Wall Temperature vs. Time, 1000-lb Thrust Configuration, $N_2O_4/0.5 N_2H_4-0.5 UDMH$ , $P_c = 100$ psia. . . . .	118
44.	Combustion Chamber Wall Temperature vs. Time, 5000-lb Thrust Configuration, $F_2/BA1014$ , $P_c = 50$ psia. . . . .	119
45.	Combustion Chamber Wall Temperature vs. Time, 5000-lb Thrust Configuration, $F_2/BA1014$ , $P_c = 100$ psia . . . . .	120
46.	Combustion Chamber Wall Temperature vs. Time, 5000-lb Thrust Configuration, $F_2/BA1014$ , $P_c = 300$ psia . . . . .	121
47.	Throat Wall Temperature vs. Time, 5000-lb Thrust Configuration, $F_2/BA1014$ , $P_c = 100$ psia . . . . .	122
48.	Outside Wall Temperature vs. Wall Thickness, Controlled Wall Temperature Chamber, Inside Wall Temperature = $4500^\circ F$ . . . . .	123
49.	Dimensions of Thermal Model Chambers Used for Preliminary Heat Soak Back Analysis. . . . .	124
50.	Injector Soak Back Temperature, 100-lb Thrust Thermal Model Chamber, No Thermal Resistance Between Chamber and Igniter, $F_2/BA1014$ . . . . .	125
51.	Injector Soak Back Temperature, 100-lb Thrust Thermal Model Chamber, Infinite Thermal Resistance Between Chamber and Injector, $F_2/BA1014$ . . . . .	126

UNCLASSIFIED



## ILLUSTRATIONS (Continued)

<u>Figure</u>		<u>Page</u>
52.	Injector Soak Back Temperature vs. Injector Emissivity, 5000-lb Thrust Configuration . . . . .	127
53.	Combustion Chamber Inside Wall Cooldown vs. Time After Shutdown, 5000-lb Thrust Configuration, $F_2/BA1014$ . . . . .	128
54.	Injector Soak Back Temperature vs. Contraction Ratio, 5000-lb Thrust Configuration . . . . .	129
55.	Injector Soak Back Temperature vs. Combustion Chamber Inside Wall Temperature at Shutdown, 5000-lb Thrust Configuration . .	130
56.	Residual Stresses on the Surfaces of As-deposited PG Cylinders and Cones. . . . .	131
57.	Model for Axial Stress Analysis at Throat. . . . .	132
58.	PG Thrust Chamber Configuration Used for Residual Stress Measurements . . . . .	133
59.	Circumferential Proof Stress on Inside Surface of Combustion Chamber for As-deposited Material . . . . .	134
60.	Circumferential Proof Stress on Outside Surface of Combustion Chamber for As-deposited Material . . . . .	135
61.	Chamber Operating Stresses vs. $t/r$ , 100-lb Thrust Configuration, $N_2O_4/0.5 N_2H_4-0.5 UDMH$ . . . . .	136
62.	Throat Operating Stresses vs. $t/r$ , 100-lb Thrust Configuration, $N_2O_4/0.5 N_2H_4-0.5 UDMH$ . . . . .	137
63.	Throat Operating Stresses vs. Chamber Pressure, 100-lb Thrust Configuration, $N_2O_4/0.5 N_2H_4-0.5 UDMH$ . . . . .	138
64.	Chamber Operating Stresses vs. $C^*$ Efficiency, 100-lb Thrust Configuration, $F_2/BA1014$ . . . . .	139
65.	Chamber Operating Stresses vs. Oxidizer-Fuel Ratio, 100-lb Thrust Configuration, $F_2/BA1014$ . . . . .	140
66.	Chamber Operating Stresses vs. $t/r$ , 100-lb Thrust Configuration, $F_2/BA1014$ . . . . .	141
67.	Chamber Transient Stresses, Circumferential Stress on Inside Surface vs. Time, 100-lb Thrust Configuration, $F_2/BA1014$ . . .	142
68.	Chamber Transient Stresses, Circumferential Stress on Outside Surface vs. Time, 100-lb Thrust Configuration, $F_2/BA1014$ . . .	143

UNCLASSIFIED

-x-

## ILLUSTRATIONS (Continued)

<u>Figure</u>		<u>Page</u>
69.	Chamber Transient Stresses, Axial Stress on Inside Surface vs. Time, 100-lb Thrust Configuration, $F_2/BA1014$ . . . . .	144
70.	Chamber Transient Stresses, Axial Stresses on Outside Surface vs. Time, 100-lb Thrust Configuration, $F_2/BA1014$ . . .	145
71.	Throat Operating Stresses at 600 seconds vs. t/r, 100-lb Thrust Configuration, $F_2/BA1014$ . . . . .	146
72.	Chamber Total and Incremental Circumferential Stresses vs. t/r, 100-lb Thrust Configuration, $F_2/BA1014$ . . . . .	147
73.	Chamber Total and Incremental Axial Stresses vs. t/r, 100-lb Thrust Configuration, $F_2/BA1014$ . . . . .	148
74.	Throat Total and Incremental Circumferential Stresses at 600 seconds vs. t/r, 100-lb Thrust Configuration, $F_2/BA1014$ . . . .	149
75.	Throat Circumferential Operating Stresses vs. Firing Time, 100-lb Thrust Configuration, $F_2/BA1014$ , t/r = 0.08 . . . . .	150
76.	Throat Circumferential Operating Stresses vs. Firing Time, 100-lb Thrust Configuration, $F_2/BA1014$ , t/r = 0.12 . . . . .	151
77.	Throat Circumferential Operating Stresses vs. Firing Time, 100-lb Thrust Configuration, $F_2/BA1014$ , t/r = 0.16 . . . . .	152
78.	Throat Circumferential Postrun Stresses vs. Firing Time, 100-lb Thrust Configuration, $F_2/BA1014$ , t/r = 0.08 . . . . .	153
79.	Throat Circumferential Postrun Stresses vs. Firing Time, 100-lb Thrust Configuration, $F_2/BA1014$ , t/r = 0.12 . . . . .	154
80.	Throat Circumferential Postrun Stresses vs. Firing Time, 100-lb Thrust Configuration, $F_2/BA1014$ , t/r = 0.16 . . . . .	155
81.	Comparison of Propellants, Chamber Operating Stresses on Outside Surface vs. t/r, 100-lb Thrust Configuration . . . . .	156
82.	Chamber Circumferential Operating Stresses on Inside Surface vs. t/r, 1000-lb Thrust Configuration, $N_2O_4/0.5 N_2H_4-0.5 UDMH$ . . . . .	157
83.	Chamber Circumferential Operating Stresses on Outside Surface vs. t/r, 1000-lb Thrust Configuration, $N_2O_4/0.5 N_2H_4-0.5 UDMH$ . . . . .	158
84.	Chamber Axial Operating Stresses vs. t/r, 1000-lb Thrust Configuration, $N_2O_4/0.5 N_2H_4-0.5 UDMH$ . . . . .	159

UNCLASSIFIED

## ILLUSTRATIONS (Continued)

<u>Figure</u>		<u>Page</u>
85.	Chamber Operating Stresses at 600 seconds vs. t/r, 5000-lb Thrust Configuration, F <sub>2</sub> /BA1014. . . . .	160
86.	Chamber Circumferential Operating Stresses vs. Firing Time, 5000-lb Thrust Configuration, F <sub>2</sub> /BA1014. . . . .	161
87.	Chamber Circumferential Postrun Stresses vs. Firing Time, 5000-lb Thrust Configuration, F <sub>2</sub> /BA1014. . . . .	162
88.	Operating Stresses, Controlled Wall Temperature Chamber vs. t/r, 100-lb Thrust Configuration . . . . .	163
89.	Operating Stresses, Controlled Wall Temperature Chamber vs. t/r, 5000-lb Thrust Configuration. . . . .	164
90.	Tensile Strength of Pyrolytic Graphite in the a-Direction. . .	165
91.	Setup for Rupture Test of Pyrolytic Graphite Tubes . . . . .	166
92.	Typical Pyrolytic Graphite Tube After Rupture Test Failure . .	167
93.	Microstructure of PG Tube S-103, Rupture Pressure = 370 psig, National CS Graphite Mandrel . . . . .	168
94.	Microstructure of PG Tube S-102, Rupture Pressure = 380 psig, National ATJ Graphite Mandrel. . . . .	169
95.	Microstructure of PG Tube S-101, Rupture Pressure = 680 psig, Speer 3499S Graphite Mandrel . . . . .	170
96.	Microstructure of PG Tube S-104, Rupture Pressure = 900 psig, Poco EP192C Graphite Mandrel . . . . .	171
97.	Microstructure of PG Tube G102, Rupture Pressure = 940 psig, ATJ Graphite Mandrel . . . . .	172
98.	Microstructure of PG Tube G202, Rupture Pressure = 690 psig, ATJ Graphite Mandrel . . . . .	173
99.	Microstructure of PG Tube G203, Rupture Pressure = 2100 psig, ATJ Graphite Mandrel . . . . .	174
100.	Microstructure of PG Tube P401, Rupture Pressure = 100 psig, ATJ Graphite Mandrel . . . . .	175
101.	Strain on Outside Surface (from Strain Gages) vs. Internal Pressure, Tube H101 (Controlled Delaminations) . . . . .	176

UNCLASSIFIED  
-xii-

## ILLUSTRATIONS (Continued)

<u>Figure</u>		<u>Page</u>
102.	Strain on Outside Surface (from Strain Gages) vs. Internal Pressure, Tube H102 (Controlled Delaminations) . . . . .	177
103.	Indicated Hoop Stress on Outside Surface vs. Theoretical Hoop Stress, Tube H101 (Controlled Delaminations). . . . .	178
104.	Indicated Hoop Stress on Outside Surface vs. Theoretical Hoop Stress, Tube H102 (Controlled Delaminations). . . . .	179
105.	HTM Fiber Reinforced Pyrolytic Graphite Tube . . . . .	180
106.	Microstructure of PG Tube H202, Rupture Pressure = 600 psig. .	181
107.	Microstructure of PG Tubes R101, R502, and R1001 (50X) . . . .	182

UNCLASSIFIED

## TABLES

<u>Table</u>		<u>Page</u>
I	Performance of Three Propellant Combinations. . . . .	55
II	Thrust for 100-pound Thrust Configuration . . . . .	56
III	Wall Thicknesses of 100-pound Thrust Configuration. . . . .	57
IV	Dimensions of 1000- and 5000-pound Thrust Configurations. . . . .	58
V	Wall Thicknesses of 1000-pound Thrust Configuration . . . . .	59
VI	Wall Thicknesses of 5000-pound Thrust Configuration . . . . .	60
VII	Thermal Model Heat Soak Back Summary. . . . .	61
VIII	Parameters for the 5000-pound Thrust Chamber Soak Back Analysis. . . . .	62
IX	Comparison of Measured and Predicted Residual Stresses in Pyrolytic Graphite Thrust Chambers . . . . .	63
X	Summary of Pyrolytic Graphite Vendor Survey . . . . .	64
XI	Description of Pyrolytic Graphite Tubes . . . . .	71
XII	Description of Super Temp Pyrolytic Graphite Tubes. . . . .	72
XIII	Description of General Electric Co. Pyrolytic Graphite Tubes. .	74
XIV	Description of Raytheon Co. Pyrolytic Graphite Tubes. . . . .	75

## NOMENCLATURE

Symbol	Description	Units
c	Elastic stiffness	$\frac{\text{lb/in.}^2}{\text{in./in.}}$
C*	Characteristic velocity	ft/sec
D <sub>c</sub>	Chamber diameter	in.
D <sub>e</sub>	Exit diameter	in.
D <sub>t</sub>	Throat diameter	in.
E <sub>1</sub>	Modulus of elasticity in the a-direction	psi
E <sub>3</sub>	Modulus of elasticity in the c-direction	psi
F <sub>zz</sub>	Axial load	lbs
N	Number of cylindrical elements	none
O/F	Oxidizer-fuel ratio	none
P <sub>c</sub>	Chamber pressure	psia
r	Radius	in.
r <sub>i</sub>	Inside radius	in.
R <sub>t</sub>	Throat radius	in.
s	Elastic compliance	$\frac{\text{in./in.}}{\text{lb/in.}^2}$
t	Wall thickness	in.
t/r	Ratio of wall thickness to radius of curvature	none
T	Actual temperature	°F
T <sub>F</sub>	Combustion temperature	°F
T <sub>D</sub>	Datum temperature	°F
u	Radial displacement	in.
α <sub>a</sub>	Coefficient of thermal expansion in the a-direction	in./in.°F
α <sub>c</sub>	Coefficient of thermal expansion in the c- direction	in./in.°F
ε	Strain	in./in.
ε <sub>c</sub>	Contraction ratio	none
θ	Circumferential coordinate direction	none
ν	Poisson's ratio	none
σ	Stress	lb/in. <sup>2</sup>

**UNCLASSIFIED**

**AFRPL-TR-66-95**

**Report 6106**

**This page intentionally left blank**

**UNCLASSIFIED**



## I. INTRODUCTION

### A. Background

Future missions in space using high energy propulsion systems will require versatile, reliable rocket engines. These requirements pose the challenge of developing thrust chamber materials that can cope with the higher temperatures and higher heat fluxes of the high energy propellants. Also, space maneuvers calling for throttling and multiple starts make it desirable to develop lightweight thrust chamber designs which are insensitive to duty cycle.

One of the most unusual structural materials to become available for possible application to such lightweight thrust chambers is free standing pyrolytic graphite (PG). This unique form of carbon, resulting from the pyrolysis of a hydrocarbon gas in a high temperature vacuum furnace, is formed by deposition on a suitable substrate or mandrel as an impervious layer of pure graphite which approaches theoretical density and possesses unusual anisotropic physical and mechanical properties.

By using suitable starting materials in the deposition process, alloys and composites with the pyrolytic graphite may also be formed with a wide range of properties. The main limitation on the use of pure PG with the storable hypergolic liquid propellants has been excessive oxidation. However, new pyrolytic graphite alloys currently being developed possess improved oxidation resistance as well as increased strength. It appears that pure PG is the most chemically resistant material available for the fluorine propellant environment.

A free standing PG thrust chamber is formed by pyrolysis of hydrocarbon gas, with subsequent deposition of the carbon on the inside surface of a female mandrel. The carbon deposit is later separated from the mandrel, resulting in a free standing shell. The deposition, or a-b plane (as shown in Figure 1), is parallel to the mandrel surface and is a plane in which high tensile strength and thermal conductivity exist in all directions. The shear strength in the a-b plane is very low. All directions within the a-b plane are usually referred to as the a-direction. In the c-direction, normal to the deposition plane, the tensile strength and thermal conductivity are very low. The elastic properties also vary greatly in different directions. For example, the coefficient of thermal expansion is about fifteen times as large in the c-direction as it is in the a-direction. As a consequence of the highly anisotropic nature of PG, the thermal stresses in a free standing PG chamber are much more complex than those encountered with more conventional materials which are usually isotropic.

The structural stresses in a free standing PG chamber are fortunately of greatest magnitude in the same direction as the high a-direction tensile strength, whereas lower tensile stresses exist in the weaker c-direction. However, the anisotropy which is responsible for the unusual properties of PG also creates some special structural and heat transfer problems which are discussed below.



## B. Structural Problems

A free standing PG thrust chamber is a thin walled axisymmetric shell with regions of complex curvature near the throat and perhaps also near the injector-chamber joint.

The effects of complex curvature have not been included in the present work, except for some approximations of residual stresses near the throat. Instead, the stress analysis has been made for a cylindrical shell, which is a good approximation for most portions of the thrust chamber. It is expected that the cylindrical shell approximation is also good for circumferential stresses at the throat, but not for axial stresses at the throat, which are highly sensitive to the actual shape of the throat region.

The structural features of free standing PG thrust chambers are discussed below.

### 1. Residual Stress

If the temperature of an isotropic cylinder is changed from one uniform temperature to another uniform temperature, the stresses in the cylinder do not change, if the material is perfectly elastic. However, an anisotropic cylinder experiences changes in its stress distribution when it is taken from one uniform temperature to another. The stresses existing in the PG after it is cooled from the deposition temperature to room temperature are termed residual stresses.

The change of circumferential stress on the inside and outside surfaces of a thin walled cylindrical shell of free standing PG during a uniform temperature change can be calculated from the following equation:

$$\sigma = \frac{E_a (\alpha_c - \alpha_a) T}{(1 - \nu_{12}^2)} \cdot \frac{t}{r_1} \quad (1)$$

Where

$T$  = Temperature change

$E_a$  = Modulus of elasticity in the a-direction

$\alpha_c$  = Coefficient of thermal expansion in the c-direction

$\alpha_a$  = Coefficient of thermal expansion in the a-direction

$t$  = Wall thickness

$r_1$  = Inside radius

$\nu_{12}$  = Poisson's ratio in the deposition plane

$\sigma$  = Circumferential (hoop) stress

A theoretical estimate of circumferential residual stresses can be calculated from Equation (1) by assuming that the pyrolytic graphite is stress-free at the deposition temperature, say 4000°F. If room temperature is assumed to be 0°F, the residual stresses will then equal the change in stress for a 4000°F temperature change as calculated by Equation (1). The theoretical circumferential residual stresses will have their maximum tensile value at the inside surface of the pyrolytic graphite and will have their maximum compressive value at the outside surface. Residual stresses also arise in the radial and axial directions.

Probably the most important characteristic of residual stresses in free standing pyrolytic graphite is in the fact, as seen from Equation (1), that the magnitude of the residual hoop stresses increases in direct proportion to  $t/r$ , the ratio of wall thickness to radius. Radial stresses are also proportional to  $t/r$ . As a result, the value of the thickness to radius ratio is a critical factor in design optimization and fabrication. It has been found that parts with residual hoop stresses much less than the  $a$ -direction strength have been impossible to produce, due to many factors such as interaction between the mandrel and the pyrolytic graphite before separation.

A general rule of thumb is that free standing PG parts cannot be fabricated without cracks or delaminations if the ratio of wall thickness to radius ( $t/r$ ) exceeds 1/10. On the other hand, the residual stresses do not theoretically restrict the size of free standing parts which can be made. Axisymmetric shapes with diameters as large as 34 inches can be produced in existing furnaces.

## 2. Limited Chamber Wall Thickness

The limitation on the maximum  $t/r$  value leads to the important conclusion that the maximum feasible wall thickness increases with the size of the thrust chamber. For example, a chamber with a 1-inch throat diameter is limited to a wall thickness at the throat of about 0.050 inch, whereas a chamber with a throat diameter of 10 inches can use a wall thickness at the throat of about 1/2 inch.

## 3. As-deposited Residual Stresses

Several techniques have been developed for measuring residual stresses in free standing PG. It has been found that the measured residual stresses are considerably different than the theoretical stresses predicted from Equation (1) using a stress-free temperature of 4000°F. In fact, there is no stress-free temperature which would lead to theoretical residual stresses consistent with the measured stresses. The term "as-deposited" refers to the residual stresses and the type of pyrolytic graphite actually produced by the deposition process.

Several theoretical studies of as-deposited residual stresses in PG are reported in References 1 and 2. These analyses are complex, and their validity has not been conclusively proven. A second approach to consideration of as-deposited residual stresses is to rely on experimental data. Unfortunately, such data are available over a limited range of  $t/r$  values. However, the present study has used extrapolations of these data, as discussed in Section V.

#### 4. Proof Stresses

At motor ignition, chamber pressure will apply pressurization stresses suddenly to the free standing PG structure. The stresses resulting from superposition of the as-deposited residual stresses with the pressurization stresses, while the PG is still at room temperature, are defined as "proof stresses".

#### 5. Growth

When pyrolytic graphite is exposed to elevated temperatures, in the absence of applied stress, it experiences a permanent change in dimensions with elongation in the a-direction and contraction in the c-direction. This phenomenon in PG is usually referred to as "growth", and is due to changes in the crystal lattice dimensions. The rate and total amount of growth increase with temperature, and growth is quite rapid at temperatures near 6000°F (Reference 3).

Growth of PG in self-restrained shapes such as cylinders or thrust chambers has an effect on the stress distribution which is somewhat analogous to the effect of anisotropic thermal stresses. Strains are induced in the PG, with resultant changes in the stress distribution. This phenomenon might increase or decrease the maximum stresses in the PG, depending on the temperatures, firing time, and duty cycle.

Growth is a permanent deformation, and therefore may have important effects on the strength of PG either during a firing cycle, or even after cooldown, at which time the residual stresses will be changed from the original as-deposited values. An analysis of growth stresses is given in Reference 4.

The effect of growth on the strength of PG is unknown. In fact, the strength of as-deposited PG shapes is still under continuous reevaluation. Therefore, it is necessary to compare the stresses after growth with the strength of as-deposited PG.

#### 6. Creep

Creep describes the tendency of materials to permanently deform during exposure to stress and temperature. Although the distinction between creep and plastic deformation is hard to define in practice, the deformation attributable to creep is ideally that related to the duration of exposure to stress and temperature, while plastic deformation can be idealized as instantaneous permanent deformation. Similarly, the distinction between creep and growth, in the case of PG, is difficult to define in practice, but can be attributed to the presence or absence of applied stress.

There are better data for growth of PG than there are for creep, although deformation under creep would be expected to exceed that of growth. In any case, creep of PG might cause important strains (and resultant stresses) in free standing chambers, especially at high temperatures.

UNCLASSIFIED

## 7. Operating Stresses

During motor firing, the inside surface of a free standing pyrolytic graphite thrust chamber will rise to within a few hundred degrees of the combustion temperature in areas of high heating rates such as the throat, while a large temperature gradient will exist across the wall, due to the low thermal conductivity in the c-direction. The operating stresses in the thrust chamber will consist of the total of four components: (1) pressurization stresses, (2) residual stresses, (3) thermal stresses, and (4) creep and growth stresses. A complete structural analysis of the PG chamber requires analysis of the operating stresses for the complete history of the chamber. Thermal gradients will change rapidly immediately after ignition, will reach steady state values, and then will change again following shutdown. Stresses may change even during steady state (temperature) conditions if the wall temperature is high enough to cause creep and growth. The stresses during a multiple firing will depend on the temperature history of the chamber and the length of elapsed time during previous firings.

## 8. Postrun Stresses

If permanent deformation of the PG occurs due to growth, plastic behavior, or creep, the stresses in the chamber will differ from the as-deposited residual stresses. The residual stresses at room temperature, after one or more motor firing cycles, are defined as postrun stresses.

## C. Heat Transfer Problems

Most of the important heat transfer problems in a free standing PG thrust chamber are caused by the very low thermal conductivity of the PG in the radial or c-direction. As a consequence, the heat sink effectiveness of the PG wall is small, and, if radiation cooling is the only cooling process in effect, the inner surface temperature will rise rapidly in regions of high heating rates such as the nozzle throat. Steady state temperatures at the inner surface will be reached within a few seconds, depending on combustion chamber conditions, and will be close to the combustion gas temperature.

Another heat transfer problem is the heating of the injector during and after motor operation. The high a-direction thermal conductivity will speed the conduction of heat along the chamber wall to the injector joint and to the exit nozzle. At the same time, the inside surface will act almost as a black body radiating to the injector face. During motor operation, the injector face will also be heated by convection and radiation from the combustion gas. This heat can be absorbed during firing by propellant cooling. After shutdown, the hot chamber walls will continue to radiate heat to the injector face. The inner wall temperature, (and hence the radiation flux) will decrease with time as the stored heat is conducted and radiated away.

The principal problem caused by overheating the injector is that of propellant vaporization, causing ignition delay or pressure transients on restart. Injector heating after shutdown may also cause thermal stresses and structural problems in the injector, or may even cause melting of low temperature components or brazed joints in the injector.

UNCLASSIFIED



#### D. Chemical Erosion

The combustion temperatures of the  $F_2/H_2$  and  $F_2/N_2H_4$  blend will range between 5500° and 7500°F, depending on mixture ratio, combustion efficiency, and chamber pressure. The inside surface of the PG chamber may approach the combustion temperature for long duration runs, raising the question of the rate of chemical erosion of the PG by the combustion gases. High erosion rates, coupled with the limitations on wall thickness, might severely restrict the run times that free standing PG chambers could endure without weakening the wall to the point of failure. An important point here is the fact that the rate of chemical erosion would be about the same for different size motors at the same chamber pressure. Larger chambers can use thicker walls, hence the allowable run times would be greater. The major combustion product of  $F_2/H_2$  and  $F_2$ /Hydrazine blend is hydrogen fluoride. Based on thermodynamic equilibrium calculations, it is predicted that HF will begin to react with graphite at temperatures above 4500°F. Other combustion products, such as hydrogen, nitrogen, and fluorine, will also react with graphite. However, the rate of chemical erosion is impossible to predict without experimental kinetic data, which are presently lacking. No analysis of the chemical erosion problem has been done in the current analysis and preliminary design phase.

#### E. Analysis and Preliminary Design

This Phase I report presents the results of a six-month analytical and design study which has been conducted to investigate the structural and heat transfer characteristics of free standing PG chambers. The analyses were performed for chamber pressures up to 300 psia. The following combinations of propellants and thrust levels were considered:

1. 100-lb Thrust Level
  - a.  $N_2O_4/0.5N_2H_4$  - 0.5 UDMH
  - b.  $F_2/BA1014^*$
  - c.  $F_2/H_2$
2. 1000-lb Thrust Level
  - a.  $N_2O_4/0.5N_2H_4$  - 0.5 UDMH
3. 5000-lb Thrust Level
  - a.  $F_2/BA1014^*$

A pyrolytic graphite product evaluation was also made, consisting of a vendor survey of current production techniques, together with laboratory testing of 2-inch diameter PG tubes.

- - - - -  
\* Hydrazine blend: 67%  $N_2H_4$  + 24% MMH + 9%  $H_2O$

UNCLASSIFIED

## II. PRELIMINARY DESIGN STUDIES

### A. Scope of Studies

Preliminary design studies were made to establish the size and shape of PG chambers for stress and heat transfer analyses. These design studies were made for those combinations of thrust and propellants which were to be used later in thrust chamber test firings, as follows:

#### 1. 100-pound Thrust (Sea Level)

$\text{N}_2\text{O}_4/0.5 \text{ N}_2\text{H}_4 - 0.5 \text{ UDMH}$

$\text{F}_2/\text{BA1014}$

$\text{F}_2/\text{GH}_2$

#### 2. 1000-pound Thrust (Space)

$\text{N}_2\text{O}_4/0.5 \text{ N}_2\text{H}_4 - 0.5 \text{ UDMH}$

#### 3. 5000-pound Thrust (Space)

$\text{F}_2/\text{BA1014}$

### B. Propellant Performance

The performance of the three propellant combinations which were studied is given in Table I. The design mixture ratios used for most of the analytical parameter studies were chosen as 2.0 for  $\text{N}_2\text{O}_4/0.5 \text{ N}_2\text{H}_4 - 0.5 \text{ UDMH}$  and  $\text{F}_2/\text{BA1014}$ , and 12.0 for  $\text{F}_2/\text{H}_2$ . Most of the heat transfer and stress studies were done for thrust chamber sizes based on a  $C^*$  efficiency of 95%, using shifting equilibrium.

The variations in combustion temperature and specific impulse with changes in mixture ratio are given for  $\text{N}_2\text{O}_4/0.5 \text{ N}_2\text{H}_4 - 0.5 \text{ UDMH}$  in Figure 2, for  $\text{F}_2/\text{BA1014}$  in Figure 3, and for  $\text{F}_2/\text{H}_2$  in Figure 4.

The variation in combustion temperature with changes in  $C^*$  efficiency is given for the three propellant combinations in Figure 5.

### C. Thrust Chamber Dimensions

#### 1. 100-pound Thrust Configuration

Analytical parameter studies for the 100-pound thrust level were to be made for three different propellant combinations and for chamber

UNCLASSIFIED

pressures of from 50 to 300 psia. Due to the large number of conditions to be studied, it was decided to choose a standard 100-pound thrust configuration and to study the effects of various propellant combinations and combustion conditions on that configuration. The parameters to be varied included the wall thickness-to-radius ratio ( $t/r$ ), which is a particularly significant parameter for pyrolytic graphite chambers, since both pressure stresses and residual stresses are related to  $t/r$ . Thus, much of the optimization of chamber dimensions is reflected in the effect of  $t/r$ .

The 100-pound thrust configuration is shown in Figure 6. This configuration had been previously manufactured and tested by several agencies and PG chambers were immediately available for further testing if desired.

A comparison of the thrusts for the three propellant combinations using the 100-pound thrust configuration is shown in Table II. It is interesting to note that the thrust would be almost identical at a given chamber pressure for all three propellant combinations.

Wall thicknesses in the throat and combustion chamber of the 100-pound thrust configuration are shown in Table III for various values of  $t/r$ .

## 2. 1000-and 5000-pound Thrust Configurations

The dimensions for the 1000-pound space thrust configuration using  $N_2O_4/0.5 N_2H_4 - 0.5$  UDMH and for the 5000-pound space thrust configuration using  $F_2/BA1014$  are given in Table IV, using the nomenclature for dimensions given in Figure 7. The dimensions of the 1000-and 5000-pound thrust chambers were varied with chamber pressure to keep the thrust constant.

The chambers were sized using a radius of curvature ( $R_N$ ) at the throat of twice the throat diameter ( $D_t$ ) and a radius of curvature ( $R$ ) at the transition of the nozzle convergent section which was equal to the combustion chamber radius. The chamber lengths listed in Table IV are for a chamber  $L^*$  of 40 inches. The nozzle lengths are for a 15 degree half-angle exit cone.

The wall thicknesses for the 1000-pound and 5000-pound thrust configurations are shown in Tables V and VI, respectively.

UNCLASSIFIED

### III. PROPERTIES OF PYROLYTIC GRAPHITE

A search of the literature was made to determine the most applicable thermal and mechanical properties of pyrolytic graphite in the temperature range of 0° to 7000°F. The properties of PG which were chosen to be used in the heat transfer and stress studies are called the "analysis standard" properties. In no case were any data found for temperatures above 5000°F, but the analysis standard properties to be used for the parametric stress analyses are all extrapolated to 7500°F to facilitate computer operation during iterative calculations.

PG will experience sublimation at temperatures near 6600°F. The flame temperature of  $F_2/H_2$  can be as high as 7500°F, but for the mixture ratios and C\* efficiencies of practical importance, the wall temperature will not exceed 6500°F, and will be even lower if injector film cooling is used. Furthermore, the endothermic or exothermic effects of chemical reactions between the PG and combustion gases will influence the actual temperature of the inner surface of the thrust chamber. However, these effects cannot be calculated at this time since the kinetics of these reactions are not known.

The analysis standard curves were established in two steps. First, all available data on a particular property was plotted on one graph. Then, a "best" single curve was determined from this collection, taking into account when the data were measured. That is, more credence was given to recent data. No attempt was made to identify the differences in material properties from one vendor to another for several reasons. First, the material properties are undoubtedly dependent on microstructure. Second, a wide variety of microstructures have been and are being made by each of the vendors so it is misleading to attempt to label some particular type of PG as being representative of one vendor. Finally, much of the past testing has indiscriminately mixed the results from different types of microstructure, and the effort required to review all of the old data in detail was beyond the scope of this program. All that was attempted in drafting the analysis standard properties was to choose properties that probably were representative of much of the material currently being produced.

Other than room temperature values, no data were available for the modulus of elasticity in the c-direction nor for the Poisson's ratios. Therefore, constant values of 0.95 for  $\nu_{13}$  and -0.17 for  $\nu_{12}$  were used. Poisson's ratios were assumed constant for all temperatures, the modulus in the c-direction was assumed to vary in the same proportion as the modulus in the a-direction, using the ratio of the room temperature values  $(E_c/E_a)_{RT}$  as a scaling factor. Although this arbitrary estimate of c-direction modulus seems to be highly questionable, it can be justified by the fact that the value of c-direction modulus does not heavily influence the stresses in free standing PG. Since only limited data were found for the compressive modulus, these data were included with the tensile data to give one modulus curve. Thermal expansion coefficients were determined as mean values from 0°F to the temperature of interest. The elastic constants at elevated temperatures were checked against certain restrictions derived from the strain energy and compressibility criteria given in Reference 5. These restrictions were not violated in any of the stress analyses.

UNCLASSIFIED



The total normal emissivity in the c-direction was taken to be constant at a value of 0.8. This was based on personal communication with R. J. Champetier, Aerospace Corporation.

An extensive search was made for experimental data on the creep of PG in the a-direction. Several types of data were found (References 6 to 10). Only Kotlensky's data (References 6 and 10) could be used for stress analysis, and these data were limited to creep at one stress level. The other references (References 7, 8, and 9) present either flexural creep data, which are not usable, or present exploratory data with temperatures varying during loading so that creep under constant loading and temperature could not be evaluated. A DDC literature search and contact with those organizations which have tested PG in the past showed that no other creep data were available. The results of the stress analyses showed that creep will have a large effect on the structural capability of free standing PG chambers for the high temperature propellants such as F<sub>2</sub>/BA1014. Therefore, more creep and growth data are needed.

The analysis standard curves are presented in Figures 8 through 13. The data scatter for two important properties, a-direction modulus and c-direction thermal conductivity, are shown in Figures 14 and 15. The data for Figures 14 and 15 were obtained from References 8 and 11 to 15. Again, it should be emphasized that the properties from each reference typically represent materials from many sources. For example, the PG properties from Lockheed (Reference 8) were actually measured by Aerojet General Corporation and Jet Propulsion Laboratory (JPL). Furthermore, the PG used in the tests was made by General Electric Co. (Schenectady), High Temperature Materials, Inc., General Electric Co. (Detroit), and Raytheon. One interesting comparison of the effect of microstructure is shown in Figure 14, which shows modulus of elasticity in the a-direction for substrate nucleated PG made by General Electric Co. (Detroit) and for continuously nucleated PG made by Raytheon Co.

The data scatter for c-direction thermal conductivity (Figure 15) is greater than for any other property of PG. The principal cause is probably due to the effects of delaminations and microcracks in the PG, as discussed in Reference 13. The trend is toward lower c-direction conductivity in PG which is free of microcracks and delaminations.

The growth and creep data used in the stress analysis are plotted in Figure 16. The creep curve is taken from Reference 6 and it represents the uniaxial tensile creep of PG in the a-direction. The applied stress was 12,000 psi and the temperature was 4712°F. The creep curve shown in Figure 16 was one of several curves presented in Reference 6, all between 4200°F and 5000°F. These curves showed a somewhat mixed trend for the 400 minutes duration of the tests, and they are also difficult to interpret at short times. The creep-versus-time curve lies above the growth-versus-time curve at 4712°F, as expected.

UNCLASSIFIED

#### IV. HEAT TRANSFER STUDIES

Heat transfer calculations were made to determine the temperature gradients in free standing PG thrust chamber walls (required for thermal stress analysis) and the temperature rise of the injector after shutdown.

##### A. Wall Temperature Gradients

Transient heating calculations were made with an IBM 7040 computer program to evaluate the radial temperature gradients in the wall of free standing PG thrust chambers. The chambers were considered to be radiating to space from the outside surface, using an emissivity of 0.8 for the PG.

The analysis standard thermal properties (See Section III) were used in all heat transfer calculations except where otherwise noted. The convective heating rates of the inside wall by the combustion gas were calculated from the Bartz equation as modified in Reference 16 to use the reference enthalpy method. Heating of the wall by radiation from the combustion gases was not considered. Two reasons justifying this simplification were as follows: (1) Radiation heating is usually much less than convective heating unless the chamber dimensions are very large and (2) The inner PG wall will in many cases approach the combustion temperature, so that little change in steady state wall temperatures will result from an increased heating rate. The transient heating rates would be somewhat underestimated by neglecting radiation, but in any case the convective heating rates cannot be predicted with any high degree of accuracy. Only radial heat conduction was assumed.

All heat transfer and stress analyses presented in this report are for a C\* efficiency of 95% and the design mixture ratio (See Table II) unless otherwise specified.

##### 1. 100-pound Thrust, $N_2O_4/0.5 N_2H_4-0.5$ UDMH

The transient temperature rise of the inside and outside surfaces of the throat of the 100-pound thrust chamber with  $N_2O_4/0.5 N_2H_4-0.5$  UDMH are shown in Figures 17, 18, and 19 for chamber pressures of 50, 100, and 300 psia, respectively. Corresponding curves for the combustion chamber are shown in Figures 20, 21, and 22. The dimensions of the 100-pound thrust configuration are shown in Figure 6. The throat diameter is 0.75 in. and the chamber diameter is 2.0 ins. Various values of wall thickness (See Table III) were studied, since  $t/r$  (the thickness-to-radius ratio) is a significant parameter both for residual and pressurization stresses. It can be seen that the inner wall temperature is within a few hundred degrees of the combustion gas temperature, except for the thinnest walls and the lowest chamber pressure, where radiation cooling reduces the wall temperature somewhat.

Typical transient temperature gradients in the chamber wall can be obtained from the heating curves (Figure 23) for the combustion chamber at 100 psia and a wall thickness of 0.045 in.

a. Effect of C\* Efficiency

The effect of varying C\* efficiency on the steady state inner combustion chamber wall temperature is shown in Figure 24 for a chamber pressure of 100 psia, an O/F ratio of 2.0, and a wall thickness of 0.045 in.

b. Effect of Mixture Ratio

The effect of varying the mixture ratio on the steady state inner combustion chamber wall temperature is shown in Figure 25.

2. 100-pound Thrust,  $F_2/BA1014$

The transient temperature rise of the inner and outer wall surfaces of the throat and the chamber wall for the 100-pound thrust chamber are shown in Figures 26 through 31. All of these calculations were for  $F_2/BA1014$  at an O/F ratio of 2.0 and a C\* efficiency of 95%.

Typical temperature gradients in the combustion chamber wall with  $F_2/BA1014$  at 100 psia are shown in Figure 32.

a. Effect of C\* Efficiency

The effect of varying the C\* efficiency from 85% to 100% on the steady state inner combustion chamber wall temperatures is shown in Figure 33.

b. Effect of Mixture Ratio

The effect of varying the mixture ratio on the steady state combustion chamber temperature is shown in Figure 34.

3. 100-pound Thrust,  $F_2/H_2$

A comparison of the temperature rise of the throat of the 100-pound chamber using  $F_2/H_2$  at an O/F ratio of 12 and  $F_2/BA1014$  at an O/F ratio of 2.0 is shown in Figure 35. A similar comparison for the combustion chamber is shown in Figure 36. It is seen that the difference between the wall temperatures for the two propellant combinations is very small. Therefore, all heat transfer and stress analyses for  $F_2/BA1014$  are also applicable to  $F_2/H_2$ .

a. Effect of Mixture Ratio

The effect of varying the mixture ratio of  $F_2/H_2$  from 10 to 14 is shown in Figure 37. The wall temperatures vary by 250°F at most over this range.

4. Thermal Conductivity Effects in 100-pound Thrust Chambers

The effectiveness of increased radial thermal conductivity in reducing the inner wall temperatures was studied by comparing the following materials:

1. Pyrolytic Graphite

Thermal conductivity (c-direction)  $\approx 0.75$  Btu/hr ft<sup>2</sup>F  
Specific gravity = 2.2

2. Carb-i-tex 100

Thermal conductivity (Against grain) = 3.0 Btu/hr ft<sup>2</sup>F  
Specific gravity = 1.38

3. Carbon Fibre Composite

Thermal conductivity (Against grain) = 10.0 Btu/hr ft<sup>2</sup>F  
Specific gravity = 1.38

It was assumed that the Carb-i-tex and composite chambers were formed so that the radial direction was against the grain. The temperature variation of the thermal conductivity for pyrolytic graphite was included, but the conductivities for Carb-i-tex and the composite material were assumed to be constant. The specific heat for graphite (See Figure 10) was used for all three materials.

The comparison was made for the throat of the 100-pound thrust configuration at 100 psia with a t/r of 0.12. The results for N<sub>2</sub>O<sub>4</sub>/0.5 N<sub>2</sub>H<sub>4</sub>-0.5 UDMH (Figure 38) and for F<sub>2</sub>/BA1014 (Figure 39) show that a four-fold increase in the radial thermal conductivity (from 0.75 to 3.0 Btu/hr ft<sup>2</sup>F) would reduce the steady state inner wall temperature by only 300°F at most. There is a crossover in the transient heating curves because of the changing importance of density and radial thermal conductivity as the wall temperature rises.

5. 1000-pound Thrust, N<sub>2</sub>O<sub>4</sub>/50-50

In contrast to the 100-pound thrust chamber analysis, which studied the same size chamber at different values of wall thickness and chamber pressure, the analyses of the 1000- and 5000-pound thrust configurations was done by changing the chamber size at various chamber pressures so as to keep the same thrust. The relationships of wall thickness and t/r for the 1000-pound thrust configurations is shown in Table V.

The temperature rise of the 1000-pound thrust combustion chamber wall is shown in Figures 40, 41, and 42 for chamber pressures of 50, 100, and 300 psia, respectively. The temperature rise of the throat at 100 psia is shown in Figure 43. Heat transfer and stress analyses for the throat were made only at 100 psia, since additional analysis at 50 or 300 psia was not considered warranted in view of the uncertainty in throat residual stresses. All of these curves are for N<sub>2</sub>O<sub>4</sub>/0.5 N<sub>2</sub>H<sub>4</sub>-0.5 UDMH at an O/F ratio of 2.0 and a C\* efficiency of 95%.



## 6. 5000-pound Thrust, $F_2/BA1014$

The temperature rise of the 5000-pound thrust combustion chamber wall is shown in Figures 44, 45, and 46 for chamber pressures of 50, 100, and 300 psia, respectively. The temperature rise of the throat at 100 psia is shown in Figure 47.

The heating rates for the 5000-pound thrust chamber were based on using  $F_2/BA1014$  at a mixture ratio of 2.0 and a C\* efficiency of 95%. The relationships of wall thickness and t/r for the 5000-pound thrust chambers are shown in Table VI.

## 7. Controlled Wall Temperature Chamber

Pyrolytic graphite chambers with a 4500°F temperature at the inner surface were of interest because thermochemical calculations show that 4500°F is the threshold for chemical erosion of pyrolytic graphite by HF, one of the principal combustion products of  $F_2/BA1014$  or  $F_2/H_2$ , and because growth is negligible below 4500°F, according to the data in Figure 16. Therefore, some stress and heat transfer analyses were made for such a chamber, referred to as the controlled wall temperature chamber.

The steady state outside wall temperatures of this chamber for various wall thicknesses are shown in Figure 48. An average c-direction thermal conductivity of 0.75 Btu/hr ft°F was used. The outer wall was radiation cooled with an emissivity of 0.8.

### B. Postrun Injector Temperatures

Free standing PG chambers have a low thermal conductivity across the wall, and as a result the inner wall temperature is quite hot and cools down slowly, compared to most other types of thrust chambers. This raises the problem of possible overheating of the injector by radiation and conduction from the PG walls after motor shutdown. This postrun injector heating is sometimes referred to as "soak back".

#### 1. Preliminary Soak Back Analysis

A preliminary analysis of the postrun injector temperature rise (soak back) was made by studying the following simplified thermal models of free standing PG chambers:

1. 100-pound thrust,  $F_2/BA1014$ ,  $P_c = 100$  psia
2. 1000-pound thrust,  $N_2O_4/0.5 N_2H_4-0.5 UDMH$ ,  $P_c = 100$  psia
3. 5000-pound thrust,  $F_2/BA1014$ ,  $P_c = 100$  psia

A sketch of the dimensions of these thermal models is shown in Figure 49. The injectors were assumed to be 1/2-inch thick monel with an emissivity of 0.25. A check of these model injector weights with the actual weight of two Marquardt injectors (a 100-pound and a 1000-pound injector)

showed an adequate correlation, so that the model injector weights are considered representative.

The preliminary soak back calculations were made by assuming that the PG walls at the time of motor shutdown were at the combustion chamber steady state temperatures. Two cases were studied for each model: (1) no thermal resistance between chamber walls and injector and (2) infinite thermal resistance between chamber walls and injector. No heat loss from the nozzle throat or from the injector was considered in these preliminary analyses.

The maximum injector temperatures reached during soak back are shown in Table VII. The temperatures of the chamber and injector after shutdown are shown for the 100-pound thrust chamber in Figure 50 for the case of no thermal resistance between the chamber and the injector.

Similar data for the case of infinite thermal resistance between the 100-pound thrust chamber and the injector are shown in Figure 51. For the 100-pound thrust chamber, infinite (i.e., very large) resistance can reduce the injector temperature to an acceptable value of about 230°F. However, as shown in Table VII, the soak back problem becomes more severe as the chamber size and wall thickness are increased. Therefore, a more detailed thermal analysis was made for the 5000-pound thrust chamber, as described below.

## 2. Final Soak Back Analysis of 5000-pound Thrust Chambers

The chamber contours for the final analysis of the soak back problem for the 5000-pound thrust chamber were more representative of an actual thrust chamber than the thermal model used in the preliminary soak back analysis. The chamber dimensions were those listed in Table VI, using the nomenclature of Figure 7. A summary of the analysis parameters is given in Table VIII.

The analysis included radiant reflections within the chamber and radiation losses through the throat and it was performed with the IBM 7040 Thermal Analyzer Computer Program, using the radiosity method (Reference 17). The emissivity of the inside surface of the PG chamber was taken as 0.80. Infinite resistance to conduction between the chamber walls and injector was assumed, since radiation from the inside wall surface to the injector is the principal mode of heat soak back for the 5000-pound thrust chamber.

Heat soak back can be alleviated by increasing the injector weight, but it was desired that the effects of PG thrust chamber parameters (such as thickness) be studied separately. Therefore, the injector weight for the final 5000-pound thrust chamber soak back analysis was kept constant at 17.05 pounds. The initial PG wall temperature throughout the chamber and throat region was taken as the steady state temperature of the combustion chamber. The wall thickness throughout the chamber and throat region was taken as the wall thickness in the combustion chamber for the chosen contraction ratio and a combustion chamber  $t/r$  ratio of 0.045.

Several assumptions were made for the initial PG wall temperature to account for the possible effects of film cooling.

a. Injector Emissivity Effects

The injector soak back temperature could be reduced by lowering the emissivity of the injector, since radiation from the PG walls to the injector is a large part of the total heat soak back. The following values of injector emissivity were studied:

1. Emissivity = 0.05 (Silver plated injector)
2. Emissivity = 0.25 (Monel injector)
3. Emissivity = 0.8

The injector soak back temperatures for these values of injector emissivity are shown in Figure 52 for an initial inside PG wall temperature of 4500°F, which would require film cooling of the wall. Soak back temperatures for an emissivity of 0.05 and an initial inside wall temperature of 5600°F are also shown in Figure 52. Decreasing the injector emissivity from 0.25 to 0.05 by silver coating or polishing would reduce the injector temperature from about 700° to about 200°F. Available data indicate that silver does not react with fluorine up to about 700°F, and therefore it is possible that a silver coated injector might maintain a low emissivity even in combustion chamber conditions. However, examination of Monel injectors after test firings has shown them to be covered with deposits. The source and composition of these deposits, or whether they would occur in space operation, are not known. Any deposits on the injector would increase its emissivity (perhaps to 0.8). With a high injector emissivity, the injector temperature would approach the inside wall temperature in a relatively short time, as shown in Figure 52. Therefore, rapid cool down of the chamber wall is desirable.

b. Wall Thickness Effects

The rate of cool down of the chamber wall can be increased by decreasing the chamber wall thickness. A thinner wall cools down faster because of its lower heat capacity and reduced conduction resistance across the wall, as shown in Figure 53.

c. Contraction Ratio Effect

If the wall thickness is reduced, while keeping a constant chamber diameter, the t/r ratio of the wall will decrease, with possible loss of structural strength. However, if the chamber diameter (i.e., contraction ratio) is decreased in proportion to the decrease of wall thickness, the structural strength, as a first approximation, may be about the same, and the thinner wall should reduce the injector soak back temperature. In addition, the injector for smaller contraction ratios will have a smaller injector face area exposed to the radiation from the PG.

Injector soak back temperatures for the 5000-pound thrust chamber, for a constant  $t/r$  ratio of 0.045, are shown for contraction ratios of 2, 4, and 6 in Figure 54. The injector soak back temperature could be reduced from about 700°F to about 350°F by decreasing the contraction ratio from 4 to 2. The corresponding reduction in wall thickness would be from 0.264 to 0.186 inch.

#### d. Film Cooling Effects

A lower inside wall temperature at shutdown would result in a lower injector soak back temperature. Therefore, the following cases of film cooling of the PG wall were analyzed for a 5000-pound thrust chamber, with a contraction ratio of 4.0, and injector emissivity of 0.25, and a combustion chamber  $t/r$  ratio of 0.045:

1. Inside wall temperature at shutdown of 5600°F (No film cooling)
2. Inside wall temperature at shutdown of 4500°F
3. Inside wall temperature at shutdown of 2500°F within 5 inches of the injector and 4500°F elsewhere.

The effect of film cooling on injector soak back temperature is shown in Figure 55, which shows a reduction from 1000°F, without film cooling, to 550°F for the case of a film cooled temperature of 2500°F to 4500°F.

#### e. Injector Cover

Another method studied for reducing the injector soak back temperature utilized a pyrolytic graphite cover plate for the injector face, with appropriate openings for the injector holes. For the case of a 0.5-inch thick cover, a chamber  $t/r$  ratio of 0.045, an injector emissivity of 0.25, and an inner PG wall temperature at shutdown of 5600°F, the injector soak back temperature was 1100°F. In this case, the front face of the injector cover was assumed to be at a temperature of 5600°F at shutdown. The injector and the back face of the cases were assumed to be at ambient temperature at shutdown. The resulting high temperature of the injector was partly due to the amount of heat stored within the cover plate at shutdown.

#### f. Conclusions

It appears that a combination of smaller contraction ratios (or thinner PG walls), low injector emissivity, and film cooled PG walls will be required to limit the 5000-pound thrust injector soak back temperatures to acceptable values.



This page intentionally left blank

## V. STRESS ANALYSES

Stress analyses of pyrolytic graphite thrust chambers were made to investigate the capability of the free standing PG structure to withstand the thermal and pressurization stresses during steady state and cyclic operation. Most of the stress analysis was done using an IBM 7040 computer program which was written for analysis of a cylindrical shell of pyrolytic graphite. The shape effects of the nozzle throat region were not included in the IBM program. The variation of elastic properties with temperature was included in the analysis. Permanent deformation, or growth, of PG was also included. Plastic deformation and creep were not included in the analyses, except in a very approximate manner. The outside pressure was assumed to be zero, corresponding to operation in space. The method of analysis is described below:

### A. Method of Analysis

#### 1. Anisotropic Cylinder Analysis

A program for the IBM 7040 computer was written for the general solution of the stresses in the center of an infinitely long cylindrical shell, using cylindrical coordinates  $r$ ,  $\theta$ , and  $z$ . As shown in Figure 1, the crystallographic c-direction of the pyrolytic graphite is parallel to the radial coordinate ( $r$ ), and the crystallographic a-b plane of the pyrolytic graphite corresponds to a cylindrical shell containing the axial direction ( $z$ ) and the circumferential direction ( $\theta$ ). Internal pressure, temperature, and axial loads were assumed to be axisymmetric, resulting in plane axial strain whereby all principal shear stresses and principal shear strains vanish.

One of the main features of the program is its ability to handle temperature-dependent elastic and thermal properties.

The technique used is to subdivide the cylinder into  $N$  concentric cylindrical elements, where the value of  $N$  may be adjusted to suit the variability of the material properties (both elastic and thermal), the radial temperature gradients, and any other relevant conditions. Each of the  $N$  elements is then assumed to have homogeneous elastic and thermal properties, determined by the temperature in the center of the element, although the elastic properties may vary from layer to layer. An expression for the stresses and displacements can be found for each layer and when the conditions of continuity at the internal boundaries as well as the axial load and conditions at the external boundaries are taken into account, the stresses and displacements can be found throughout the cylinder.

Pyrolytic graphite is a transversely isotropic material with the axis of symmetry in the c-direction. Therefore, the generalized Hooke's Law can be written as follows:

$$\epsilon_{\theta\theta} = s_{11} \sigma_{\theta\theta} + s_{12} \sigma_{zz} + s_{13} \sigma_{rr} + \alpha_{\theta} (T - T_D) + \gamma_{\theta} \quad (2)$$

$$\epsilon_{zz} = s_{12} \sigma_{\theta\theta} + s_{11} \sigma_{zz} + s_{13} \sigma_{rr} + \alpha_{\theta} (T - T_D) + \gamma_{\theta} \quad (3)$$

$$\epsilon_{rr} = s_{13} \sigma_{\theta\theta} + s_{13} \sigma_{zz} + s_{33} \sigma_{rr} + \alpha_r (T - T_D) + \gamma_r \quad (4)$$

$$\sigma_{\theta\theta} = c_{11} \epsilon_{\theta\theta} + c_{12} \epsilon_{zz} + c_{13} \epsilon_{rr} - \lambda_{\theta} (T - T_D) - \tau_{\theta} \quad (5)$$

$$\sigma_{zz} = c_{12} \epsilon_{\theta\theta} + c_{11} \epsilon_{zz} + c_{13} \epsilon_{rr} - \lambda_{\theta} (T - T_D) - \tau_{\theta} \quad (6)$$

$$\sigma_{rr} = c_{13} \epsilon_{\theta\theta} + c_{13} \epsilon_{zz} + c_{33} \epsilon_{rr} - \lambda_r (T - T_D) - \tau_r \quad (7)$$

Where

$\sigma_{ij}$  = Stresses

$\epsilon_{ij}$  = Strains

$s_{ij}$  = Elastic compliances

$c_{ij}$  = Elastic stiffnesses

$\alpha_i$  = Coefficients of mean thermal expansion

$\lambda_i$  = Thermal stress coefficients

$\gamma_i$  = Growth strains

$\tau_i$  = Growth stress factors

$T$  = Actual temperature

$T_D$  = Datum temperature

The system of symbols and subscripts is similar to that explained in Reference 18.

The pyrolytic graphite is assumed to be stress free at the datum temperature, which was assumed in the current study to be 0°F (room temperature, approximately).

The stiffnesses can be written in terms of the compliances as follows:

$$c_{11} + c_{12} = s_{33}/X_1 \quad (8)$$

$$c_{11} - c_{12} = \frac{1}{s_{11} - s_{12}} \quad (9)$$

$$c_{13} = -s_{13}/X_1 \quad (10)$$

$$c_{33} = \frac{s_{11} + s_{12}}{X_1} \quad (11)$$

$$X_1 = s_{33} (s_{11} + s_{12}) - 2s_{13}^2 \quad (12)$$

The compliances can be defined in terms of the conventional elastic constants as follows:

$$s_{11} = 1/E_1 \quad (13)$$

$$s_{33} = 1/E_3 \quad (14)$$

$$s_{12} = -\nu_{12}/E_1 \quad (15)$$

$$s_{13} = -\nu_{13}/E_1 \quad (16)$$

Where

$E_1$  = Modulus of elasticity in the a-direction

$E_3$  = Modulus of elasticity in the c-direction

$\nu_{12}$  = Poisson's ratio between contraction in the b-direction and elongation in the loaded a-direction

$\nu_{13}$  = Poisson's ratio between contraction in the c-direction and elongation in the loaded a-direction

The thermal stress coefficients ( $\lambda_1$ ) are related to the coefficients of thermal expansion as follows:

$$\lambda_\theta = (c_{11} + c_{12}) \alpha_\theta + c_{13} \alpha_r \quad (17)$$

$$\lambda_r = 2 c_{13} \alpha_\theta + c_{33} \alpha_r \quad (18)$$

In addition, a relationship exists between the growth strains and growth stress factors:

$$\tau_\theta = (c_{11} + c_{12}) \gamma_\theta + c_{13} \gamma_r \quad (19)$$

$$\tau_r = 2 c_{13} \gamma_\theta + c_{33} \gamma_r \quad (20)$$

For this problem, the only equilibrium equation not identically equal to zero is the following:

$$\frac{\partial \sigma_{rr}}{\partial r} + \frac{\sigma_{rr} - \sigma_{\theta\theta}}{r} = 0 \quad (21)$$

The strain-displacement equations are as follows, where  $u$  = Radial displacement:

$$\epsilon_{rr} = \frac{\partial u}{\partial r} \quad (22)$$

$$\epsilon_{\theta\theta} = \frac{u}{r} \quad (23)$$

$$\epsilon_{zz} = C_3 \text{ (constant)} \quad (24)$$

By substituting these strain-displacement equations into the stress-strain equations and thence into the equilibrium equation, we obtain the following differential equation for the radial displacement ( $u$ ):

$$\frac{d^2 u}{dr^2} + \frac{1}{r} \frac{du}{dr} - \frac{c_{11}}{c_{33}} \frac{u}{r^2} = \frac{(\lambda_r - \lambda_\theta) (T - T_D) - (c_{13} - c_{12}) C_3 + (\tau_r - \tau_\theta)}{c_{33} r} + \frac{\lambda_r}{c_{33}} \frac{dT}{dr} \quad (25)$$

In the above equation, all elastic constants ( $c_{11}$ ,  $c_{12}$ ,  $c_{13}$ ,  $c_{33}$ ,  $\lambda_1$ ,  $\tau_1$ ) have been assumed to be independent of radius. That is, for the particular element we are concerned with, all material properties are assumed constant and equal to the values of these properties evaluated from conditions at the mid-point of the element.

If we define  $A$  as follows:

$$A = \sqrt{c_{11}/c_{33}} \quad (26)$$

and define  $\phi$  as follows:

$$\phi = \frac{(\lambda_r - \lambda_\theta) (T - T_D) + (c_{12} - c_{13}) C_3 + (\tau_r - \tau_\theta)}{c_{33} r} + \frac{\lambda_r}{c_{33}} \frac{dT}{dr} \quad (27)$$

the solution to Equation (25) can be written as follows:

$$u = (C_1 + V_1) r^A + (C_2 + V_2) r^{-A} \quad (28)$$

where  $C_1$  and  $C_2$  are constants of integration and

$$V_1 = \frac{1}{2A} \int r^{-A+1} \phi \, dr \quad (29)$$

$$V_2 = -\frac{1}{2A} \int r^{A+1} \phi \, dr \quad (30)$$

This solution is not correct, however, if  $A = 1.0$  or  $A = 2.0$ . It means that the solution, instead of containing  $r$  to various powers, has an exponential term in it. If, in the analysis, this constant should be equal to 1.0 or 2.0 for a particular element, an error message will be printed out giving the element containing the violation and for the sake of computation a value of  $A$  of 1.001 or 2.001 will be assigned for that particular element.

A linear temperature distribution of the form

$$T - T_D = a_0 + a_1 r \quad (31)$$

is fitted for each element and Equation (28) for  $u(r)$  now becomes

$$u = C_1 r^A + C_2 r^{-A} + \frac{Ba_0 + DC_3 + E}{1 - A^2} r + \frac{(B + C) a_1 r^2}{4 - A^2} \quad (32)$$



Where

$$B = \frac{(\lambda_r - \lambda_\theta)}{c_{33}} \quad (33)$$

$$C = \frac{(c_{12} - c_{13})}{c_{33}} \quad (34)$$

$$D = \frac{\lambda_r}{c_{33}} \quad (35)$$

$$E = \frac{(\tau_r - \tau_\theta)}{c_{33}} \quad (36)$$

The equations for the stresses can now easily be found as follows:

$$\left. \begin{aligned} \sigma_{rr} = & (c_{13} + Ac_{33}) C_1 r^{A-1} + (c_{13} - Ac_{33}) C_2 r^{-A-1} \\ & + \frac{(c_{13} + 2c_{33})(B+C)a_1 r}{4-A^2} + \frac{(c_{13} + c_{33})(Ba_0 + E)}{(1-A^2)} \\ & + \left[ \frac{(c_{13} + c_{33})D}{1-A^2} + c_{13} \right] C_3 - \lambda_r (T - T_D) - \tau_r \end{aligned} \right\} \quad (37)$$

$$\left. \begin{aligned} \sigma_{zz} &= (c_{12} + Ac_{13}) C_1 r^A -1 + (c_{12} - Ac_{13}) C_2 r^{-A} -1 \\ &+ \frac{(c_{12} + c_{13}) (Ba_0 + E)}{1 - A^2} + \left[ \frac{(c_{12} + c_{13}) D}{1 - A^2} + c_{11} \right] C_3 \\ &+ \frac{(c_{12} + 2c_{13}) (B + C) a_1 r}{4 - A^2} - \lambda_\theta (T - T_D) - \tau_\theta \end{aligned} \right\} \quad (38)$$

$$\left. \begin{aligned} \sigma_{\theta\theta} &= (c_{11} + Ac_{13}) C_1 r^A -1 + (c_{11} - Ac_{13}) C_2 r^{-A} -1 \\ &+ \frac{(c_{11} + c_{13}) (Ba_0 + E)}{1 - A^2} + \left[ \frac{(c_{11} + c_{13}) D}{1 - A^2} + c_{12} \right] C_3 \\ &+ \frac{(c_{11} + 2c_{13}) (B + C) a_1 r}{4 - A^2} - \lambda_\theta (T - T_D) - \tau_\theta \end{aligned} \right\} \quad (39)$$

The constant  $C_3$  depends on the axial restraint. If the ends of the cylinder are assumed fixed,  $C_3 = 0$ . For a finite axial strain,  $C_3$  will not be zero and must be determined from the boundary condition

$$\int_{r_1}^{r_0} \sigma_{zz} r dr = \frac{F_{zz}}{2\pi} \quad (40)$$

Where:

$F_{zz}$  = Axial load

$r_1$  = Inside radius of cylinder

$r_0$  = Outside radius of cylinder

# UNCLASSIFIED

AFRPL-TR-66-95

Report 610

Since the expression for  $\sigma_{zz}$  will contain different numerical coefficients for each element, this integration must be broken into N parts, as follows:

$$\int_{r_1}^{r_o} \sigma_{zz} r dr = \sum_{n=1}^N \int_{r_{1,n}}^{r_{o,n}} \sigma_{zz,n} r dr \quad (41)$$

Therefore, from Equations (38), (40), and (41),

$$\begin{aligned} \frac{F_{zz}}{2\pi} = & \sum_{n=1}^N \left[ \int_{r_{1,n}}^{r_{o,n}} \left\{ (c_{12,n} + A_n c_{13,n}) C_{1,n} r^{A_n} \right. \right. \\ & + (c_{12,n} - A_n c_{13,n}) C_{2,n} r^{-A_n} + \frac{(c_{12,n} + c_{13,n})(B_n a_{o,n} + E_n)r}{1 - A_n^2} \\ & + \left[ \frac{(c_{12,n} + c_{13,n})D_n}{1 - A_n^2} + c_{11,n} \right] C_3 r + \frac{(c_{12,n} + 2c_{13,n})(B_n + C_n)a_{1,n}r^2}{4 - A_n^2} \\ & \left. \left. - \lambda_{\theta,n}(a_{o,n}r + a_{1,n}r^2) - \tau_{\theta,n}r \right\} dr \right] \quad (42) \end{aligned}$$

Simplifying, we get

$$\begin{aligned}
 \frac{F_{22}}{2\pi} = \sum_{n=1}^N & \left[ \frac{(c_{12,n} + A_n c_{13,n})}{1 + A_n} c_{1,n} r^{A_n + 1} \right. \\
 & + \frac{(c_{12,n} - A_n c_{13,n})}{1 - A_n} c_{2,n} r^{-A_n + 1} + \frac{(c_{12,n} + c_{13,n}) (B_n a_{0,n} + E_n) r^2}{2 (1 - A_n^2)} \\
 & + \left[ \frac{(c_{12,n} + c_{13,n}) D_n}{1 - A_n^2} + c_{11,n} \right] c_3 \frac{r^2}{2} + \frac{(c_{12,n} + 2c_{13,n}) (B_n + C_n) a_{1,n} r^3}{3 (4 - A_n^2)} \\
 & \left. - \lambda_{\theta,n} \left( a_{0,n} \frac{r^2}{2} + a_{1,n} \frac{r^3}{3} \right) - \tau_{\theta,n} \frac{r^2}{2} \right] \Bigg|_{r_{1,n}}^{r_{0,n}} \quad (43)
 \end{aligned}$$

Letting

$$H_{1,n} = \frac{(c_{12,n} + A_n c_{13,n})}{(1 + A_n)} \quad (44)$$

$$H_{2,n} = \frac{(c_{12,n} - A_n c_{13,n})}{(1 - A_n)} \quad (45)$$

$$H_{3,n} = \frac{(c_{12,n} + 2c_{13,n}) (B_n + C_n) a_{1,n} - \lambda_{\theta,n} a_{1,n} (4 - A_n^2)}{3 (4 - A_n^2)} \quad (46)$$

$$H_{4,n} = \frac{(c_{12,n} + c_{13,n}) (B_n a_{0,n} + E_n) - \lambda_{\theta,n} a_{0,n} (1 - A_n^2) - \tau_{\theta,n} (1 - A_n^2)}{2 (1 - A_n^2)} \quad (47)$$

$$H_{5,n} = \left[ \frac{c_{11,n} (1 - A_n^2) + (c_{12,n} + c_{13,n}) D_n}{2 (1 - A_n^2)} \right] \quad (48)$$

we get

$$\frac{F_{zz}}{2\pi} = \sum_{n=1}^N \left[ H_{1,n} C_{1,n} r^{A_n+1} + H_{2,n} C_{2,n} r^{-A_n+1} + H_{3,n} r^3 + H_{4,n} r^2 + H_{5,n} C_3 r^2 \right] \Bigg|_{r_{1,n}}^{r_{0,n}} \quad (49)$$

and

$$\frac{F_{zz}}{2\pi} = \sum_{n=1}^N \left[ H_{1,n} C_{1,n} (r_{0,n}^{A_n+1} - r_{1,n}^{A_n+1}) + H_{2,n} C_{2,n} (r_{0,n}^{-A_n+1} - r_{1,n}^{-A_n+1}) + H_{3,n} (r_{0,n}^3 - r_{1,n}^3) + H_{4,n} (r_{0,n}^2 - r_{1,n}^2) + H_{5,n} C_3 (r_{0,n}^2 - r_{1,n}^2) \right] \quad (50)$$

Since there are two unknown constants for each of the  $N$  elements ( $C_{1,n}$  and  $C_{2,n}$ ) plus the unknown axial constant  $C_3$ , we need a total of  $(2N + 1)$  equations to solve for these  $(2N + 1)$  unknowns. Two equations can be obtained for each boundary between any two elements, expressing the fact that the radial stress and radial displacement are continuous functions, as follows:

$$\sigma_{rr,n} \Big|_{r_{0,n}} = \sigma_{rr,n+1} \Big|_{r_{1,n+1}} \quad n = 1, \dots, N-1 \quad (51)$$

$$u_n \Big|_{r_{0,n}} = u_{n+1} \Big|_{r_{1,n+1}} \quad n = 1, \dots, N-1 \quad (52)$$

This gives  $2(N-1)$  equations, since there are  $(N-1)$  common boundaries. In addition, at the inner boundary  $\sigma_{rr} = -P_0$ , that is

$$\sigma_{rr,1} \Big|_{r_{1,1}} = -P_0 \quad (\text{Internal pressure}) \quad (53)$$

and at the outer boundary  $\sigma_{rr} = 0$ , that is

$$\sigma_{rr,N} \Big|_{r_{0,N}} = 0 \quad (\text{For operation in space}) \quad (54)$$

These two equations and the axial load equation, Equation (50), when added to the previous  $2(N-1)$  equations give a total of  $2N + 1$  equations. The computer program solves for the  $(2N+1)$  unknowns and then substitutes them into Equations (37), (38), (39), and (32) to give the complete stress and radial displacement distribution. The stresses calculated in this manner have a saw-tooth distribution across the wall, which can be smoothed out by increasing the number of cylindrical elements. A maximum of thirty elements are accommodated in the current computer program.

Room temperature is a convenient datum temperature because thermal expansion data are usually expressed as a mean coefficient, from room temperature to the actual temperature. If the datum temperature is not  $0^\circ\text{F}$ , a mean coefficient of thermal expansion must be used which is calculated as follows:

$$\alpha_1 = \frac{\alpha_{T_R} T - \alpha_{T_D} T_D}{T - T_D}$$

Where

$\alpha_{T_R}$  = Mean coefficient of thermal expansion from room temperature  $T_R$  to actual temperature  $T$

$\alpha_{T_D}$  = Mean coefficient of thermal expansion from room temperature  $T_R$  to datum temperature  $T_D$

If  $T_D = T_R$ , this equation reduces to  $\alpha_{T_R}$

Room temperature is also a convenient datum temperature because all experimentally determined residual stress data are collected at room temperature, so that subsequent superposition of the residual stress effects is simplified.

## 2. Superposition of Residual Stress Effects

The theory of elasticity, as used in this analysis, is based on the assumption that the material is stress-free in the initial state, before the application of temperature changes or mechanical loads. If the material actually contains initial stresses, the stress distribution after application of mechanical loads and temperature changes can be obtained, in the case of perfectly elastic materials, by superposition of the initial stresses on the incremental stresses (defined as the stresses caused by loading and temperature changes). In fact, initial stresses generally do occur in pyrolytic graphite, and are referred to as residual stresses.

If, as in the present analysis, the variation of elastic modulus with temperature is considered, the method of superposition cannot be used to get the total stresses, since the residual stresses are related to a room temperature value of elastic modulus, whereas the incremental stresses typically are related to such elevated temperatures that the elastic modulus has changed.

The procedure used for including the effects of residual stresses in this study was to superimpose, on the incremental stresses calculated by the theory of elasticity, a residual stress contribution calculated from the initial (residual) strains and the elevated temperature elastic properties at the point in question.

Since the residual stresses as found experimentally in as-deposited PG cannot be predicted with any success by theoretical means, it was necessary to use experimental residual stress data. Unfortunately, even the experimental residual stress data are not available in sufficient quantity to permit accurate extrapolation to other thickness and shapes of PG than those from which the residual stress data are collected. This problem will be discussed in more detail in Section V-B.

For superposition of the residual stress contribution, it was assumed that only the residual strains are constant and that the residual stress contribution would vary as the material properties varied. This is only an approximation since it does not consider the redistribution of residual strains for the case of nonuniform elastic properties associated with radial thermal gradients. A further assumption was made that the radial residual stress is zero, which is justifiable since the magnitude of the radial residual stresses within the wall is found experimentally to be low. In general, the data to be used were in the form of residual axial and circumferential stresses on the inside and outside surfaces of cylinders where the radial stresses are in fact zero. A linear distribution of circumferential and axial residual stresses across the wall was assumed. The residual strains were then calculated from the following stress-strain equations:



$$\epsilon_{\theta\theta} = s_{11} \sigma_{\theta\theta} + s_{12} \sigma_{zz} \quad (55)$$

$$\epsilon_{zz} = s_{12} \sigma_{\theta\theta} + s_{11} \sigma_{zz} \quad (56)$$

$$\epsilon_{rr} = s_{13} \sigma_{\theta\theta} + s_{13} \sigma_{zz} \quad (57)$$

$$\sigma_{\theta\theta} = c_{11} \epsilon_{\theta\theta} + c_{12} \epsilon_{zz} + c_{13} \epsilon_{rr} \quad (58)$$

$$\sigma_{zz} = c_{12} \epsilon_{\theta\theta} + c_{11} \epsilon_{zz} + c_{13} \epsilon_{rr} \quad (59)$$

By writing  $\epsilon_{rr}$  in terms of  $\epsilon_{\theta\theta}$  and  $\epsilon_{zz}$ , and substituting into Equations (58) and (59), the following equations can be derived:

$$\sigma_{\theta\theta} = \left( c_{11} - \frac{c_{13}^2}{c_{33}} \right) \epsilon_{\theta\theta} + \left( c_{12} - \frac{c_{13}^2}{c_{33}} \right) \epsilon_{zz} \quad (60)$$

$$\sigma_{zz} = \left( c_{12} - \frac{c_{13}^2}{c_{33}} \right) \epsilon_{\theta\theta} + \left( c_{11} - \frac{c_{13}^2}{c_{33}} \right) \epsilon_{zz} \quad (61)$$

Values of the residual strains  $\epsilon_{\theta\theta}$  and  $\epsilon_{zz}$  at the inner and outer surfaces were calculated from experimental residual stress data and input to the computer. Linear distributions of these residual strains across the wall were assumed, and at any point in the wall the stress component caused by the residual stresses was calculated from Equations (60) and (61), using the temperature-dependent elastic properties at the point in question. These residual stresses were then superimposed on the incremental stresses to get the total stresses.

### 3. Growth Analysis

The effect of growth of PG was included in the computer stress analysis by using values of circumferential growth strain ( $\lambda_\theta$ ) which were estimated for each element from the data of Reference 3, based on the temperature and elapsed time. The effects of temperature variations within each cylindrical element were approximated in a manner analogous to strain hardening laws.

The c-direction growth was assumed to be twice the magnitude, and opposite in sign, to the a-direction growth shown in Figure 16. The growth strains in both the axial and circumferential directions were the same.

#### 4. Creep Analysis

Creep effects were included in the computer analysis by using a value of growth strain ( $\lambda_0$ ) which included a contribution caused by creep. The amount of creep was estimated from the probable level of stress in each element. Many simplifications were necessary. For example, creep was assumed to be directly proportional to stress level, using linear interpolation of the data in Figure 16, between the zero stress curve (growth) and the 12,000 psi curve. In actuality, the creep of most materials is roughly described by the following equation:

$$\dot{\epsilon}_c = A \sigma^n \quad (62)$$

Where

$\dot{\epsilon}_c$  = Creep rate

$\sigma$  = Stress

A = Constant

n = Constant (Almost always greater than 1)

The values of n for pyrolytic graphite cannot be estimated from available data. It was also assumed that creep rates under compression in the a-direction were of the same magnitude, but opposite in sign, as the creep rates for tension.

The creep at temperatures above 4700°F was estimated using scaling factors obtained from Figure 16. The computer program, designed only for growth analysis, could not distinguish between axial and circumferential creep due to the different stress levels in these two directions. Therefore, the estimated circumferential creep was also used for axial creep.

A computer program which makes a more accurate analysis of creep is feasible, but was not undertaken because of the scarcity of creep data.

#### 5. Plastic Deformation

The current analysis can consider the temperature dependency of the elastic modulus, but it cannot consider plastic deformation. The effects of plastic deformation will not be important until the stress level and temperature are quite high. For example, at 4500°F, the plastic a-direction strain at a stress of 20,000 psi will be only 0.1%, compared to an elastic strain of 0.8%. Plastic strain will be more important at higher temperatures, but adequate data were not available for analysis.

## B. Experimental Residual Stress Data

Experimental residual stress data were collected in an attempt to permit prediction of residual stresses in PG thrust chambers of various sizes and wall thicknesses. Most of the data available were for axial and circumferential residual stresses at the inside and outside surfaces of cones and cylinders. More detailed data, including radial stresses and residual stresses within the wall, are reported for a few cases in References 1, 2, 4, and 19. The results of these studies show that residual stresses in PG are a function of many parameters such as the deposition conditions and thickness. At the present time, although some interesting hypotheses have been suggested for explanation of as-deposited residual stresses, the subject still remains largely undefined.

In the course of this work, the residual stresses on cylinders and thrust chambers were measured. The limited scope of this work was sufficient to show only that the extrapolation of cylindrical residual stress data to other thicknesses or shapes is not possible at the present time.

### 1. Cylinders and Cones

Experimental values of axial and circumferential residual stresses on the inside and outside of free standing PG cylinders and cones are shown in Figure 56. The open symbols are old data and the closed symbols are new data obtained during this program. The analysis standard curves for residual stresses to be used in the stress analysis are also shown in Figure 56.

Of necessity, the analysis standard curves were used for thrust chamber sizes and wall thickness/radius ratios far beyond the range of available data. Some of the new data obtained in this program were corrected by the ratio of the modulus of elasticity of the materials (boron-doped and continuously nucleated) and that of average PG (assumed to be  $4.5 \times 10^6$  psi). The as-deposited extrapolations are in fairly good agreement with the linear extrapolations up to a  $t/r$  ratio of about 0.085. No experimental data are available from tubes at  $t/r$  ratios above 0.085.

### 2. Residual Stresses in Thrust Chambers

The residual stresses in a cylindrical or conical combustion chamber would be expected to be similar to the residual stresses measured in cones and cylinders. However, the residual stresses in the vicinity of the throat of a free standing PG thrust chamber are complicated by the fact that two curvatures, the throat radius and the radius of curvature, have an influence on the residual stresses. The axial stresses are particularly affected by this double curvature. The curvature at the beginning of the contraction region will also cause additional axial stresses. The method of analysis used in calculating these stresses was that reported in Reference 20, wherein good correlation was obtained between one data point of experimental axial residual stress and an analysis model. This model for axial stresses at the throat consisted of superposition of the following:

1. As-deposited axial stresses, based on the analysis standard curves for tubes (Figure 56) and the cross sectional dimensions at the thrust chamber section of interest.
2. Circumferential residual stresses in a hypothetical cylinder with a radius equal to the radius of axial curvature at the thrust chamber section of interest. In the throat region, this hypothetical cylinder, assumed to be stress-free at 4000°F, would have an inside surface coinciding with the outside surface of the thrust chamber, as shown in Figure 57. At the transition (Section A) to the convergent section, the hypothetical cylinder would have an inside surface coinciding with the inside surface of the thrust chamber.

The above model was tested by measuring the residual stresses in two PG chambers of the configuration shown in Figure 58.

A comparison of the measured residual stresses in the PG chambers and the predicted residual stresses is shown in Table IX. The residual stresses were measured by strain gage isolation. Predictions were made both by use of the analytical model described above for consideration of the nozzle shape, and also on the basis of the analysis standard extrapolations for cylinders. Examination of Table IX leads to several conclusions, as follows:

1. The circumferential residual stresses in the throat were only about 40% as great as those predicted by the analysis standard curves for cylinders.
2. The axial residual stresses on the outside of the throat were the highest stresses measured, and they were far greater than those predicted by either the cylindrical or the nozzle shape models.
3. The residual stresses in Section A were more closely predicted by the cylindrical model (ignoring the effects of axial curvature) than by the analysis model for axial curvature. This is probably due to the fact that the amount of curvature at Section A was actually rather small.

The results of this comparison led to the conclusion that the reliability of axial residual stress predictions at the throat of PG thrust chambers is so low that analysis of these stresses was not warranted. Therefore, no operating or postrun axial stresses at the throat are presented in this report. A second conclusion was that the analysis of stresses in chambers with large  $t/r$  ratios (say 0.14) is not very accurate, using the analysis standards for as-deposited residual stresses. It is therefore obvious that much more data are required to permit evaluation of the effects of residual stress on the total stress in free standing pyrolytic graphite thrust chambers.

### C. Proof Stresses

Proof stress is defined as the pressurization stress superimposed on the residual stress. Room temperature is assumed. The circumferential proof stress in a cylinder (which is assumed to represent any cross section of the thrust chamber) is shown, for the inside surface, in Figure 59. It is shown that the optimum t/r ratio, to minimize the proof stress, is at very low t/r values (about 0.02) for an internal pressure of 100 psia, while shifting to higher values for higher pressures.

The circumferential proof stress on the outside surface is shown in Figure 60, which shows steadily decreasing stress with increasing t/r ratio values. The stresses at the inside and outside surfaces are used in most of the stress analysis since the stresses are almost always maximum at these surfaces.

It should be noted that the residual stresses and proof stresses discussed above will apply, in view of our assumptions, to all sizes of thrust chambers, since both the pressurization stresses and the as-deposited residual stresses are functions of the t/r ratio. The analysis of 100-pound thrust chambers was done using the basic C100-1 dimensions, that is, a  $D_t$  of 0.75 inch and a chamber diameter of 2.0 inches. Various wall thicknesses were used. The analyses of the 1000-pound and 5000-pound thrust chambers were made for various size chambers, keeping thrust constant at chamber pressures of 50, 100, and 300 psia. Unless otherwise specified, all analyses were for a  $C^*$  efficiency of 95%, the design mixture ratio (Table I), and a chamber pressure of 100 psia.

### D. 100-pound Thrust Configuration, $N_2O_4/0.5N_2H_4-0.5$ UDMH

Steady state operating stresses in the combustion chamber of the 100-lb configuration using  $N_2O_4/0.5N_2H_4-0.5$  UDMH are shown in Figure 61 as a function of t/r ratio. A similar curve for the throat is shown in Figure 62. The wall temperatures of the 100-pound thrust chamber with  $N_2O_4/0.5N_2H_4-0.5$  UDMH were not quite hot enough to cause growth, which, according to Reference 3, is zero for 10 minutes at 4700°F.

Steady state operating stresses at the throat of the 100-pound thrust chamber with  $N_2O_4/0.5N_2H_4-0.5$  UDMH are plotted versus chamber pressure in Figure 63.

Comparison of the proof stresses (Figures 59 and 60) with the operating stresses (Figures 61, 62, and 63) shows that the proof stresses are always higher than the operating stresses. In either case, the maximum stress is about 8000 psi tension, which is well within the capabilities of PG.

### E. 100-pound Thrust Configuration, $F_2/BA1014$

#### 1. $C^*$ Efficiency Effect

The variation of steady state operating stresses in the



combustion chamber with variations in  $C^*$  efficiency was calculated for the 100-pound thrust chamber for  $F_2/BA1014$ , using a wall thickness/radius ratio of 0.045. The axial and circumferential stresses at the inner and outer surfaces are plotted versus  $C^*$  efficiency in Figure 64 and it is shown that the effect is rather small, for  $C^*$  efficiencies between 90 and 100%. Most of the stress analysis was done using a  $C^*$  efficiency of 95%. The maximum wall temperature for this comparison was  $4520^\circ\text{F}$  for a  $C^*$  efficiency of 100%. Therefore, creep and growth were not included.

## 2. O/F Ratio Effect

The variation of steady state operating stresses in the  $F_2/BA1014$  combustion chamber with variations in O/F ratio were calculated for a 100-pound thrust chamber with a t/r ratio of 0.045. The effect of O/F ratio on combustion chamber stresses is very small, as shown in Figure 65. Most of the stress analysis was done using an O/F ratio of 2.0. The maximum wall temperature for this comparison was  $4310^\circ\text{F}$  for an O/F ratio of 2.5. Therefore, growth and creep were not included.

## 3. Operating Stresses

The steady state operating stresses in the combustion chamber of the 100-pound thrust  $F_2/BA1014$  chamber were calculated for wall thickness/radius ratios of 0.03, 0.045, 0.06, 0.08, and 0.10. The steady state operating stresses in the combustion chamber are plotted versus t/r ratio in Figure 66. The maximum tensile stresses on the outside surface, (both axial and circumferential) decrease with increasing wall thickness, and did not exceed 8500 psi at any t/r ratio.

The maximum temperature of the combustion chamber at 100 psia does not exceed  $4600^\circ\text{F}$ , so that growth will not affect the stresses. Somewhat higher temperatures will occur at the throat and growth must then be considered.

Transient stresses were calculated in the wall of the combustion chamber with a t/r ratio of 0.045 and a pressure of 100 psia, and they are shown in Figures 67 through 70, which show the axial and circumferential stresses at both the inside and outside surfaces. The stresses at the surfaces are nearly always greater than those within the wall. Examination of these curves shows that the stresses soon after motor ignition, when the radial temperature gradients are highest, are less severe than either the proof stresses or the steady state operating stresses. Creep and growth were not included in these calculations, since the wall temperature did not exceed  $4300^\circ\text{F}$ .

Steady state operating stresses at the throat of the 100-pound thrust chamber with  $F_2/BA1014$  were calculated assuming that growth had occurred over a firing time of 600 seconds. The stresses at the end of this time are shown in Figure 71 as a function of t/r ratio.

The importance of residual stresses in calculating operating stresses is illustrated in Figures 72, 73, 74, and 75, in which the steady state operating stresses for the 100-pound thrust chamber with  $F_2/BA1014$

are compared with the incremental stresses. The incremental stresses are those stresses due to pressure and temperature and they represent the operating stresses for a thrust chamber which is stress-free at room temperature, i.e., no residual stress. As discussed before, the total stresses are obtained by superimposing the incremental stresses with the residual stresses corrected to actual wall temperatures. This superposition procedure is an approximation and, in effect, superposes strains rather than stresses, which is preferable if the material is not perfectly elastic. It can be seen from Figures 72 through 75 that the residual stress contribution to the total stress is very important.

An analysis of the effect of growth during 10 minutes of firing was made in the throat section of the 100-pound thrust chamber for  $F_2/BA1014$ . Creep was not considered. Plots of circumferential stress versus firing time for  $t/r$  ratios of 0.08, 0.12, and 0.16 are shown in Figures 75, 76, and 77. The maximum tensile stress occurring anywhere within the wall is shown, and it usually is the surface stress. The operating stresses are generally within the range of 10,000 psi tension to 12,000 psi compression for firing times up to 600 seconds. The stress levels were outside the above limits for short times (less than 1 second) for thick walls with  $t/r$  ratios of 0.12 and 0.16. This was due to the analysis standard residual stresses being so high at these large values of  $t/r$ , thereby being the dominant stress at such short times. After steady state temperatures are reached, the changes in operating stresses are due to growth.

#### 4. Postrun Stresses

Circumferential postrun stresses in the throat of the 100-pound thrust  $F_2/BA1014$  chamber for  $t/r$  ratios of 0.08, 0.12, and 0.16 are presented in Figures 78, 79, and 80. Growth was included in this analysis, but creep was not. Therefore, these plots of postrun stresses can be compared with the operating stresses in Figures 75, 76, and 77.

In general, growth of the throat of the 100-pound thrust  $F_2/BA1014$  chamber does not cause operating or postrun stresses much greater than the original residual stresses, for firing times up to 10 minutes. However, it must be remembered that creep was not included in the above analysis.

#### F. 100-pound Thrust Configuration - Comparison of Propellant Combinations

The steady state operating stresses for the 100-pound chamber were compared for the two different propellant combinations and are shown in Figure 81. Only the outside surface stresses are shown, since these are the maximum stresses. It can be seen that the stresses resulting from using the  $N_2O_4/0.5N_2H_4 - 0.5$  UDMH propellants are consistently lower than the stresses resulting from using  $F_2/BA1014$ . This is also true for the inside surface stresses and is due to the lower temperatures reached with  $N_2O_4/0.5N_2H_4 - 0.5$  UDMH.

#### G. 1000-pound Thrust Configuration, $N_2O_4/0.5N_2H_4 - 0.5$ UDMH

The steady state operating stresses in the combustion chamber of the 1000-pound thrust chamber are shown in Figures 82, 83, and 84 for chamber



# UNCLASSIFIED

AFRPL-TR-66-95

Report 6106

pressures of 50, 100, and 300 psia. The propellants were  $N_2O_4/0.5N_2H_4-0.5$  UDMH at a C\* efficiency of 95% and a mixture ratio of 2.0. The stresses decrease for increasing t/r ratio in a similar manner to those shown for the 100-pound thrust chamber in Figure 61. The magnitude of the operating stresses is generally slightly higher than the 100-pound thrust chamber operating stresses, but they are still well within the stress limits of PG.

## H. 5000-pound Thrust Configuration, $F_2/BA1014$

### 1. Operating Stresses

Operating stresses in the combustion chamber of the 5000-pound thrust chamber after 600 seconds of firing are shown in Figure 85 for a chamber pressure of 100 psia. The propellants were  $F_2/BA1014$  at a C\* efficiency of 95% and a mixture ratio of 2.0. The stresses are fairly constant over the short t/r ratio range considered. Growth was considered for this t/r parameter curve but creep was not.

An analysis was made of the effect of creep of PG on the operating and postrun stresses of the 5000-pound thrust chamber at a chamber pressure of 100 psia and a t/r ratio of 0.045.

The steady state inside surface temperature of the combustion chamber, using  $F_2/BA1014$ , at an O/F of 2.0 and 95% C\* efficiency, was 5611°F.

The inclusion of creep effects had a similar effect on both the circumferential and axial stresses, and, therefore, only the circumferential stresses will be discussed. Figure 86 shows the circumferential operating stresses versus firing time.

The solid curve presents the stress analysis results without any creep considered. The dashed curve gives the results with creep included. Growth of PG was included in both analyses. By comparing the solid and dashed curves in Figure 86, it can be seen that creep changes the operating stresses by a very large amount. The stress on the outside surface was reduced by creep from 14,500 psi to 7500 psi after 600 seconds. The stress on the outside surface was changed by creep from - 12,000 psi to + 7,000 psi after 600 seconds.

Figure 86 also shows the maximum tensile stress (circumferential) occurring within the PG wall. As can be seen, this always occurs at the outside surface in the absence of creep, but sometimes occurs within the wall if creep is considered.

### 2. Postrun Stresses

The postrun stresses in the 5000-pound combustion chamber after various lengths of firing time are shown in Figure 87. The postrun stresses are calculated assuming that the chamber has cooled down to room temperature. The internal stresses are now different in magnitude from the original residual stresses because permanent deformation of the PG has occurred due to growth and creep.

UNCLASSIFIED

# UNCLASSIFIED

AFRPL-TR-66-95

Report 6106

The maximum postrun stresses on the inside surface are increased by the action of creep from - 32,000 psi (without creep) to + 40,000 psi (with creep) after 600 seconds.

The radial temperature drop across the 5000-pound thrust chamber wall was such that all creep and growth occurred within 0.100 inch of the inner surface.

It is concluded that creep of PG has a very large effect on the stresses of chambers if the wall temperature is at least 4700°F.

It appears that creep may improve the durability of a chamber for a single continuous firing, but would be damaging to the strength of the chamber for cyclic operation. The critical condition for cyclic operation would be motor ignition after cool down from a previous firing. It is also possible that a chamber might fail during cool down, due just to the internal postrun stresses exceeding the tensile strength of the PG. In any case, more creep data are required before precise conclusions can be drawn about stresses in free standing PG chambers.

## I. Controlled Temperature Chamber

Stress analysis was made of free standing PG chambers which were assumed to have an inner surface temperature of 4500°F. A linear temperature gradient across the wall was assumed, with outer wall temperatures (for radiation cooling) as presented in Figure 48.

The operating stresses on the inner and outer surfaces are presented in Figure 88 for a 100-pound thrust chamber at 100 psia, and in Figure 89 for a 5000-pound thrust chamber, also at 100 psia. The trend for both sizes of chambers is to lower operating stresses at large values of t/r ratio. For example, at a t/r ratio of 0.10, all operating stresses would be less than 8000 psi, which is well within the strength capabilities of PG.

Therefore, if the inner surface could be kept below 4500°F by film cooling, the PG chambers should be structurally sound.

However, the calculated operating stresses depend heavily on the as-deposited residual stresses. In general, because of the anisotropic nature of PG, high residual stresses are reversed into low operating stresses as the chamber temperature rises. Unfortunately, the available data on residual stresses at t/r ratios greater than 0.08 are not sufficient to give a firm foundation for stress analysis of thick walled chambers. This problem is especially acute in the case of 5000-pound thrust chambers which will probably have thicker walls than ever before produced in cylindrical shapes.

## J. Expansion Nozzle

Some analyses were made on the expansion nozzle of the 100-pound thrust altitude chamber at sections corresponding to expansion ratios of 20:1 and 40:1. The operating stresses are due almost entirely to thermal and residual stresses. At the 20:1 section, the circumferential stress due

UNCLASSIFIED

# UNCLASSIFIED

AFRPL-TR-66-95

Report 6106

to pressure is only 21 psi and the axial stress due to axial load is merely 7 psi. At the 40:1 section, there is no axial load and the circumferential stress due to pressure is only 13 psi. The total operating stresses for both sections are similar, because, while the thermal stresses are lower at the exit, the residual stresses are higher. At the inside surface, the circumferential stress is about 4300 psi compression, and the axial stress is about 5900 psi compression. On the outer surface of the nozzle, the circumferential stress is about 3900 psi tension and the axial stress is about 6400 psi tension. It appears that the expansion nozzle of a free standing PG chamber will not be a problem area.

## K. Shear Stress

The maximum shear stress ( $\tau$ ) acting on the a-c plane in the a-direction was calculated from the principal stresses ( $\sigma_\theta$  and  $\sigma_z$ ) using the formula

$$\tau = \frac{\sigma_\theta - \sigma_z}{2}$$

No data were found regarding the shear strength on this plane. In all of the parameter studies, the operating shear stress never exceeded 3000 psi except for several cases of postrun stress. Sometimes PG tubes fail during production in a spiral failure, which might indicate shear failure.

## L. Vibration Stress Analysis

A stress analysis was made of the 100-pound thrust chamber when exposed to vibration. The assumed power spectral density for the vibration loading is as follows:

10 to 90 cps	0.055 $g^2$ /cps at 10 cps, increases at 3 decibels (db) per octave to 0.5 $g^2$ /cps at 90 cps
90 to 250 cps	Constant at 0.5 $g^2$ /cps
250 to 2000 cps	0.5 $g^2$ /cps at 250 cps decreases at 3 db/octave to 0.06 $g^2$ /cps at 2000 cps

A preliminary analysis was made to determine the order of magnitude of the stresses to be expected in the 100-pound thrust altitude chamber. The configuration analyzed was a 100-pound thrust chamber, except that a 40:1 expansion nozzle was added. The critical mode of vibration was determined to be the transverse mode, which causes maximum stresses due to bending moments from the transverse loading.

UNCLASSIFIED

# UNCLASSIFIED

AFRPL-TR-66-95

Report 6106

To determine the maximum g level expected, the natural frequency and amplification factor of the chamber setup were estimated. The choice of natural frequency is unimportant because of the shape of the power spectral density distribution, and the amplification factor was taken to be 10, a typical value for many materials. The exact value of the amplification factor is not too important because it is raised to the 1/2 power in the equation for the g level, as follows:

$$g = \sqrt{\frac{\pi}{2} \left(\frac{g^2}{\text{cps}}\right)_{f_n} f_n (A F)} \quad (63)$$

Where

$\left(\frac{g^2}{\text{cps}}\right)_{f_n}$  = Power spectral density distribution value at  $f_n$

$f_n$  = Natural frequency

A F = Amplification factor

The 1 sigma g level is 44.3 g and the 3 sigma level is 133 g. This 3 sigma level is the usual maximum level used in calculations, since only 1.2 percent of all cycles are at or above this level.

The vibration stresses in the PG chamber at the throat section and the injector flange were analyzed. The maximum vibration stresses (at the 3 sigma level) are as follows:

Location	Shear (psi)	Bending (psi)
Injector flange	150	2,100
Throat	273	5,000

The vibration stresses are greater at the throat than at the injector flange, since the section properties of the throat are less, although the transverse bending moment is less. Although the bending stress of 5,000 psi is appreciable, it is within the strength capabilities of good quality PG. The axial residual stresses at the throat would have to be added to the bending stress due to vibration to get the total stress.

# UNCLASSIFIED

### M. Tensile Strength

Up until now, nothing has been said about the tensile strength of PG. Stress levels have been discussed without regard to possible failure of the chamber due to exceeding the tensile strength values. Curves of tensile strength of PG in the a-direction versus temperature are shown in Figure 90. It is seen that up to about 3000°F the strength is fairly constant and above 3000°F the tensile strength increases very rapidly. This variation must be taken into account when checking operating stress levels for failure. A stress level which will cause failure at room temperature may be well within the upper limit of tensile strength if the stress is reached when the chamber is hot. Considerations of biaxial loading or the effects of creep on the strength of PG cannot be evaluated at the present time.

Work is being done to increase the room temperature tensile strength of PG. It is assumed that the same general behavior of increasing tensile strength above 3000°F will be maintained.

In all cases examined in the parameter studies, the operating stresses were at no time above the average tensile strength corresponding to the temperature of the section where the stress is observed.

For the postrun stresses, the allowable tensile strength was exceeded in several cases. For high t/r ratios (greater than 0.12), the residual stress exceeded the average tensile strength. If these predictions of residual stress were correct, as well as the tensile strength data, it would mean that tubes with t/r ratios greater than 0.12 cannot even be fabricated. This has been confirmed in production of tubes. However, thrust chamber throats have been fabricated with t/r ratios as high as 0.16, for reasons not yet understood.

For practically all cases where growth and creep were considered, the postrun stresses for firing times in excess of a few minutes exceeded the stress limits. For those cases considering growth only, the stresses near and on the inside surface of the chamber were highly compressive. However, when creep was included in the analysis, these same stresses were highly tensile, again illustrating the need for good creep data.

**UNCLASSIFIED**

AFRPL-TR-66-95

Report 6106

This page intentionally left blank

**UNCLASSIFIED**  
-44-



## VI. PYROLYTIC GRAPHITE PRODUCT EVALUATION

The quality of pyrolytic graphite which can be produced at the current stage of development was evaluated by a vendor survey and by laboratory testing of free standing PG tubes made by a variety of techniques. Those aspects of PG quality of greatest interest for free standing PG thrust chambers are reproducibility and high internal pressurization strength.

A. Vendor Survey

The quality of PG depends on many factors such as furnace temperature and pressure, gas flow rate, mandrel material, and gas dilution by secondary gases such as argon or hydrogen. A survey was made of the deposition techniques presently being used by the manufacturers of PG. Those vendors interviewed were as follows:

1. Super Temp Corporation  
Santa Fe Springs, California
2. General Electric Company  
Metallurgical Products Dept.  
Detroit, Michigan
3. Pyrogenics, Incorporated  
Woodside, New York
4. High Temperature Materials, Incorporated  
Lowell, Massachusetts
5. Raytheon Company  
Research Division  
Waltham, Massachusetts

Some of the techniques used by the manufacturers are considered by them to be proprietary and are not described in this report. A summary of the results of the survey is given in Table X. Much of the development of PG has been for applications which have different requirements than those of free standing PG rocket thrust chambers. In particular, the requirement of high internal pressurization strength does not appear to have been a requirement for other applications, and hence the effect of the many deposition conditions on the rupture pressure of free standing PG had not been evaluated. The large number of possible combinations of the various deposition parameters precluded a complete evaluation of all of the possibilities. However, for this program, the vendor's judgment of those techniques which might most likely achieve high rupture pressure was solicited during the procurement of PG tubes for laboratory testing. Following the vendor survey, it was possible to evaluate the potential advantages of the deposition techniques suggested by the vendors, thereby selecting those techniques which appeared to have the greatest probability of success.

B. Evaluation of Pyrolytic Graphite Tubes

Two-inch diameter tubes of free standing pyrolytic graphite were

purchased from five vendors as part of a program to study the effects of various deposition techniques on rupture pressure. Since the primary goal was to maximize the rupture pressure, no limitations were placed on wall thickness. The vendors were asked to suggest any new or unusual deposition techniques which they thought might increase the rupture pressure. In addition, PG tubes made by a variety of proven techniques were obtained. All tubes were 4 inches long, and they had a nominal inside diameter of 2 inches and a nominal wall thickness of 0.060 inch, although a number of tubes of wall thickness greater than 0.060 inch were produced.

Since the object of the tube study was to investigate the rupture pressure of PG made by a variety of techniques, PG tubes produced by conventional techniques were not ordered from each of the vendors. Therefore, the strength of the tubes which were procured did not necessarily provide any comparison of the different vendors' overall capabilities.

The tubes were pressurized to rupture with the test setup shown in Figure 91. The appearance of a typical tube after rupture is shown in Figure 92. The pressurizing medium was soluble oil and water. No axial load was applied to the tube during the rupture test. A number of tubes were instrumented with circumferential strain gages on the outside surface to measure the modulus of elasticity during pressurization and the residual stress after rupture and strain gage isolation.

After rupture, 10X photographs of the surfaces and 50X photomicrographs of the c-plane edge were taken. The boron content of the boron-doped tubes were measured by the vendors.

A description of the tubes which were purchased is given in Table XI. A discussion of the tubes provided by each vendor follows.

#### 1. Super Temp Corporation

Four furnace runs were made by the Super Temp Corporation with eight mandrels loaded per run. The furnace conditions were kept uniform at a temperature of 4000°F and a pressure of 8.5 mm Hg. The variables studied were mandrel materials and mandrel machining. Only female mandrels were used, and the inside surface was machined with various lathe speeds and depths of final cut, as given in Table XII. All of the PG tubes produced by Super Temp were substrate nucleated.

##### a. Effect of Mandrel Material

It was found that the grain size of PG is related to the grain size of the graphite mandrel material. This is shown by comparing Figures 93 through 96. Each of these figures show 10X photographs of the inside and outside surfaces and a 50X photomicrograph of a PG tube sample made on different mandrel materials.

Tube S-103, shown in Figure 93, was deposited on a CS graphite mandrel (Maximum particle size = 0.030 inch). The grain size of Tube S-103 was about 0.020 inch. However, superimposed on the grain matrix were a very

# UNCLASSIFIED

AFRPL-TR-66-95

Report 6106

large number of nodules (anomalously large grains) up to 0.040 inch in diameter on the inside surface. Tube S-103 ruptured at 370 psig.

Tube S-102, shown in Figure 94, was deposited on an ATJ graphite mandrel (Maximum particle size = 0.006 inch). The grain size of Tube S-102 was about 0.015 inch. There were also a large number of nodules up to 0.060 inch. This tube ruptured at 380 psig, with a crack adjacent to an 0.060 inch nodule.

Tube S-101, shown in Figure 95, was deposited on a Speer 3499S graphite mandrel (Maximum particle size = 0.003 inch). The grain size of the PG was about 0.015 inch.

Tube S-104, shown in Figure 96, was deposited on a Poco EP 192C graphite mandrel (Maximum particle size = 0.001 inch). The grain size of the PG was about 0.008 inch.

The yield (percentage of uncracked tubes) and the rupture pressures of tubes deposited on CS and HLM mandrels were lower than for tubes deposited on ATJ, Speer, or Poco mandrels. One out of two tubes deposited were cracked when using CS and HLM mandrels, and the rupture pressures of the uncracked tubes were under 400 psig.

Tubes deposited on ATJ mandrels were of intermediate strength (485 psig average rupture pressure) and the yield was four tubes out of four mandrels loaded.

The average rupture pressure of tubes deposited on Speer 3499S graphite mandrels was 525 psig. For tubes deposited on Poco EP192C graphite mandrels, the average rupture pressure was about 590 psig, with 100 percent yield in both cases.

The results of these tests show that the attainment of high rupture pressure for thrust chambers which are too large for ATJ graphite mandrels may be difficult. A later furnace run was made by Super Temp with infiltrated CS and HLM graphite mandrels. No improvement in production yield or tube rupture pressure was obtained.

## b. Effect of Nodule Size

Earlier rupture tests of PG tubes, reported in Reference 22, had shown a correlation between small nodule size and high rupture pressure. A weak correlation of the same type can be found in the rupture test results of the Super Temp tubes. One reason for this weak correlation may be that the nodules in these tubes usually occurred in clusters or strings, and the measurement of the nodule effect in terms of the maximum nodule diameter is probably not very accurate.

It was hoped that the finer particle size and higher purity of Poco graphite mandrels might reduce the occurrence or the size of the nodules. This was not achieved during the four furnace runs by Super Temp.

# UNCLASSIFIED

# UNCLASSIFIED

WRPL-TR-66-95

Report 6106

However, visual inspection of the tubes deposited on Poco mandrels showed that the matrix of the PG tubes was fine grained and contained only small nodules. It still seems likely that improved PG strength should be obtained by using Poco mandrels. On the other hand, Poco graphite is not currently available in large enough sizes except for small thrust chambers. Several samples of PG with large nodules were polished on the c-plane edge to show the nodules and the point of their origination in cross section. By successive trials of polishing and examination under a microscope, it was concluded that probably all of the nodules in PG deposited on Poco graphite were originated at the graphite substrate. The cause of these nodules is still unknown. However, it is believed that the cause is probably small particles of some sort which are on the surface of the mandrel and act as a nucleating source for the nodule. Strict mandrel cleaning procedures did not eliminate this problem, and it is probable that the dirt particles accumulate on the mandrel surface while the mandrels are being loaded into the furnace. The carbon black insulation used in the furnace is one possible source of the impurity.

## 2. General Electric Company

Two furnace runs were made by the General Electric Company with eight mandrels per run. The first furnace run was made at 3800°F to produce boron-doped PG with a boron content of about 0.5 percent. Six good tubes were delivered from this run. The second furnace run was made with deposition conditions (3300°F) which were expected to produce continuously nucleated PG. Five good tubes were delivered. All mandrels were ATJ graphite, polished with 600 grit paper. All deposition conditions except temperature are considered proprietary by General Electric Company. Data describing the General Electric tubes are given in Table XIII.

The average rupture pressure of the boron doped tubes was 850 psig, and the average for the continuously nucleated tubes was 1140 psig, including one tube (G203) which ruptured at 2100 psig, the highest rupture pressure so far achieved with a PG or PG alloy tube.

### a. Boron-Doped Pyrolytic Graphite

Five tubes containing about 0.5 percent boron ruptured at an average rupture pressure of 850 psig. The grain size of these tubes was about 0.015 inch. The maximum nodule diameter in the uncracked tubes was 0.03 inch to 0.04 inch, while in the two cracked tubes it was 0.05 and 0.10 inch. The high rupture pressure of these tubes was partly due to the thicker walls (about 0.080 inch) compared with the 0.060-inch wall thickness of most other tubes studied in this program. A correlation of maximum nodule size with rupture pressure could not be established for the boron-doped tubes because four out of five tubes cracked near the same pressure, 900 psig.

The modulus of elasticity (about  $6 \times 10^6$  psi) was higher than for most pyrolytic graphite. The residual stresses on the outside surface of six boron-doped tubes are given in Table XIII. The circumferential residual stresses on the outside surface ranged from -6330 to -8640 psi (compression). However, the measured circumferential residual stress on

UNCLASSIFIED



# UNCLASSIFIED

AFRPL-TR-66-95

Report 6106

the inside surface of one tube (G104) was only +4220 psi(tension), which is rather low, considering the wall thickness and the modulus of elasticity.

The microstructure of Tube G102 shown in Figure 97 is typical of the boron alloy tubes.

## b. Continuously Nucleated Pyrolytic Graphite

Five tubes of continuously nucleated PG were ruptured at pressures ranging from 690 to 2100 psig. The grain size of these tubes was about 0.010 inch, less than the grain size of the boron-doped PG tubes, although ATJ mandrels were used for both types of tubes. The grains also appeared to be harder, with more sharply defined grain boundaries, than the boron-doped PG. This can be seen by comparing the inside surfaces of Tubes G202 and G203 (shown in Figures 98 and 99) with the inside surface of boron PG Tube G102 shown in Figure 97. Photomicrographs of both ends of Tubes G202 and G203 are shown to illustrate the change in microstructure over a 4-inch distance. One of the possible problems with continuously nucleated microstructure is the difficulty in maintaining the same microstructure over any length, since careful control of the local deposition conditions is required. It can be seen that there was a significant change in microstructure from the top to bottom of Tubes G202 and G203, and in part, these tubes appeared to be substrate nucleated rather than continuously nucleated.

The maximum nodule size in the continuously nucleated PG was 0.03 inch to 0.04 inch, and the absence of large nodules sometimes found in the boron PG tubes suggests the possibility that the growth of nodules is limited by the growth of new cones within the continuously nucleated PG.

The modulus of elasticity in the a-direction was somewhat higher (about  $5.0 \times 10^6$  to  $6.4 \times 10^6$  psi) for the continuously nucleated PG than for substrate nucleated PG (about  $4.5 \times 10^6$ ). There was some scatter in the data, as shown in Table XIII. Whether or not the properties of continuously nucleated PG are more susceptible to inconsistency than substrate nucleated PG is not known, although the scatter in the strengths of the 4-inch long tubes seemed to indicate this.

## 3. Pyrogenics, Incorporated

Three furnace runs were made by Pyrogenics, Incorporated. One tube was deposited in the first furnace run on a female mandrel, and contained controlled delaminations in a 0.160 inch thick wall. This tube, designated P101, contained many large nodules, up to 0.10 inch in diameter, and the delaminations were quite nonsymmetrical. This tube was not ruptured because the ID was too large for the rupture test fixture.

Tube P301 was a thicker wall (0.225 inch) tube deposited on a female mandrel in the second furnace run. There were many large nodules, up to 0.150 inch in diameter. The delaminations were nonsymmetrical and the ID was too small for the pressure test fixture.

UNCLASSIFIED

Tubes P401 and P402 were deposited on a male mandrel. The wall of Tube P401 was about 0.30-inch thick and contained about six non-symmetrical delaminations. The maximum nodule diameter was 0.140 inch, on the outside surface. The inner layer of this tube ruptured at 100 psig, causing leakage of the pressurizing liquid through the ends of the tubes. The microstructure and outside surface of Tube P401 are shown in Figure 100. The wall of Tube P402 was 0.120-inch thick and it contained two fairly uniform delaminations. The maximum nodule diameter on the outer surface was 0.060 inch. The inner layer of this tube ruptured at 40 psig.

#### 4. High Temperature Materials, Incorporated

##### a. Controlled Delaminations

Two furnace runs were made by High Temperature Materials, Incorporated, (HTM). In the first furnace run, three tubes with controlled delaminations were produced. The wall thickness was 1/8 inch and the wall was divided into three approximately equal thickness cylinders by the two delaminations. The tubes were pressurized to rupture in the test setup (Figure 91) which applied hoop stress but no axial stress. Tube H101 ruptured at 850 psig, and Tube H102 ruptured at 1100 psig. Tube H103 was not ruptured because the ID was too small for the test fixture.

The variation in strain on the outside surface with changes in internal pressure is shown in Figure 101 for Tube H101 and in Figure 102 for Tube H102. It is shown that the outer shell does not start to carry much hoop tension until about 500 psig internal pressure has been applied. This is further illustrated in Figures 103 and 104, which show the variation of indicated hoop stress ( $E \epsilon_{\sigma\sigma}$ ) on the outer surface (from strain gage measurements) with theoretical hoop stress ( $P r/t$ ) for a solid, thin walled cylinder.

At rupture, Tube H101 was carrying only 700 psi tensile stress on the outer shell, as contrasted to an average theoretical hoop stress for the entire tube of 6400 psi.

The outer shell of Tube H102 carried a stress of 2200 psi at rupture, compared to an average theoretical hoop stress at rupture of 8500 psi. It is interesting to note that the curve of indicated hoop stress versus internal pressure is almost duplicated for both tubes, although one of the tubes (H101) ruptured at a lower pressure than the other.

It appears that the controlled delamination concept is useful for extending the pressurization strength of PG chambers. Further improvement is possible by making thicker walls (with more delaminations) and perhaps by achieving a tighter fit between the lamina. However, some problems may arise when chamber shapes are deposited. The concept requires further evaluation and testing.

##### b. Fibre-Reinforced Pyrolytic Graphite

In the second furnace run, three PG tubes were deposited by HTM on a carbon fabric mandrel. The wall thicknesses were about 1/8

inch. The rupture pressures were 600 psig for Tube H202 and 580 psig for Tube H203. The third tube was not ruptured because the ID was too small for the test fixture.

A photograph of Tube H202 is shown in Figure 105 and the microstructure and outside surface are shown in Figure 106. The surface was quite uneven, compared to conventional PG tubes. Although the rupture strength was fairly good, the fibre-reinforced PG concept would require additional development.

#### 5. Raytheon Company

A number of furnace runs were made by the Raytheon Company to produce PG tubes of several different types. Two tubes were made in each run. A description of the Raytheon tubes is given in Table XIV.

Two tubes were deposited in the first furnace run at a deposition rate of 17.2 mils/hr. Both tubes (R101 and R102) ruptured near 400 psig. The wall thickness was about 0.060 inch. The microstructure of Tube R101 is shown in Figure 107.

Six tubes were deposited in a series of furnace runs at 20 mils/hr. None of the six tubes had very high rupture pressure, ranging from 60 to 460 psig.

Two tubes were deposited at 15 mils/hr to a wall thickness of about 0.090 inch. Tube R301 ruptured at 460 psig and Tube R302 ruptured at 540 psig.

Two tubes (R401 and R402), which were deposited at 30 mils/hr to a wall thickness of 0.090 inch, were ruptured at 230 and 380 psig, respectively.

Four tubes containing about 1.5% boron were produced. Two tubes were cracked, and two others ruptured at 320 and 380 psig. The microstructure of Tube R502, which ruptured at 380 psig, is shown in Figure 107.

Two tubes were deposited under conditions which were expected to produce high boron content (5% to 10%). However, the actual boron content achieved was only 1 to 2%. These tubes (R901 and R1001) were cracked and no rupture tests could be performed. The microstructure of Tube R1001 is shown in Figure 107.

Finally, two tubes with a 1/8-inch thick wall and containing one delamination were produced. The maximum nodule diameter in these tubes was 0.030 inch.

Tube R1101 ruptured at 1260 psig. The stress on the outer surface at rupture was indicated by a strain gage to be 6500 psi, compared to an average hoop stress, based on the entire thickness, of 11,100 psi.

Tube R1102 ruptured at 1000 psig, at which time the stress carried by the outer surface was 5800 psi, compared to an average hoop stress,



based on the entire thickness, of 8500 psi.

The delaminated tubes produced by Raytheon were similar in strength to those produced by HTM, although they contained only one delamination instead of two.

The rupture strength of most of the Raytheon tubes was low, with the exception of the two delaminated tubes. This is attributed to the unfavorable number and size of nodules. Raytheon is of the opinion that this may be due to a batch of ATJ graphite which was quite porous. In any case, no advantage could be established for any of the deposition parameters being evaluated.

### C. Conclusions

1. The highest rupture pressures of any PG tubes tested were attained using a continuously nucleated microstructure. The application of this type of PG to thrust chamber fabrication will require additional process development to provide the carefully controlled microstructure throughout the chamber length and thickness.
2. Pyrolytic graphite tubes containing carefully controlled delaminations can currently be produced to carry about 1000 psig internal pressure at room temperature. This type of structure may encounter other problems, however, when tested in rocket firings.
3. Boron alloys of PG as produced by the General Electric Company have shown higher tube rupture pressures than most substrate nucleated pyrolytic graphites.

# UNCLASSIFIED

AFRPL-TR-66-95

Report 6106

## VII. REFERENCES

1. General Electric Co. Document No. 63SD882, "(U) Study of Combined Cool-Down and Growth Stresses in Thin-Walled Pyrolytic Graphite Shells", 15 October 1963, AD345228. CONFIDENTIAL REPORT.
2. General Electric Co. Document No. 63SD883, "(U) Measurement of Residual Stresses in Boron-Pyrolytic Graphite Conical Structures", 15 October 1963, AD345077. CONFIDENTIAL REPORT.
3. SSD-TDR-63-340, "(U) Structural Changes in Pyrolytic Graphite at Elevated Temperatures", Aerospace Corp., 1 December 1963. UNCLASSIFIED REPORT.
4. Raytheon Co. Report S-682, "(U) Pyrographalloy Research and Development, Final Report Contract NOW63-0059-C (FBM), 16 July 1962 to 31 May 1964". CONFIDENTIAL REPORT.
5. Marquardt Report 5907, "(U) Final Report, Pyrolytic Graphite Thrust Chamber Development", 31 July 1962. UNCLASSIFIED REPORT.
6. Kotlensky, W. V. and H. E. Martens, "Mechanical Properties of PG to 2800°C", Presented at Fifth Carbon Conference, Penn State University, Vol. II of Proceedings 1963, pp 625-638.
7. Meers, J. T., National Carbon Co., "Some Effects of Annealing PG", Presented at Fifth Carbon Conference, Penn State University, Vol. II of Proceedings 1963, p 464.
8. Lockheed Missile System Division Report 801376, "PG Final Report", June 1962, pp 4-27, 4-28, and 4-29. CONFIDENTIAL REPORT.
9. WADD-TR-61-72, "R & D on Advanced Graphite Material, Vol. 37: Studies of Graphite Deposited by Pyrolytic Processes", National Carbon Co. May 1964. UNCLASSIFIED REPORT.
10. Jet Propulsion Laboratory, "Space Programs Summary No. 37-30. Volume IV: Analysis of High Temperature Creep in PG", W. V. Kotlensky, p 71-72. UNCLASSIFIED REPORT.
11. Gebhardt, J. J. and J. M. Berry, General Electric Co., "Mechanical Properties of Pyrolytic Graphite", AIAA Journal, Vol. 3, No. 2, February 1965, pp 302-307.
12. Donadio, R. N. and J. Pappis, "The Mechanical Properties of Pyrolytic Graphite", Raytheon Co. Publication T-574, Presented at the First Pyrolytic Graphite Symposium, ASTM, Palm Springs, California, 30-31 March 1964.

UNCLASSIFIED

# UNCLASSIFIED

AFRPL-TR-66-95

Report 6106

13. Pappis, J., "A Note on the Thermal Conductivity of Pyrolytic Graphite", Presented at the First Pyrolytic Graphite Symposium, ASTM, Palm Springs, California, 30-31 March 1964.
14. ASD-TDR-63-195, "Pyrolytic Graphite, Its High Temperature Properties", W. Bradshaw and J. R. Armstrong, Lockheed Aircraft Corporation, March 1963. UNCLASSIFIED REPORT.
15. General Electric Company, Specialty Alloys Section Publication, "Pyrolytic Graphite Engineering Handbook", May 1964.
16. Jet Propulsion Laboratory Report TR 32-43, "A Comparison of Analytical and Experimental Local Heat Fluxes in Liquid Propellant Rocket Thrust Chambers", W. E. Welsh and A. B. Witte, 1 February 1961. UNCLASSIFIED REPORT.
17. ASD-TR-61-119, "Radiation Heat Transfer Analysis for Space Vehicles, Part I", J. A. Stevenson and J. C. Grafton, North American Aviation, Inc., Space and Information Systems Division, December 1961. UNCLASSIFIED REPORT.
18. Hearmon, R.F.S. "An Introduction to Applied Anisotropic Elasticity", Oxford University Press, Amen House, London E. C. 4, 1961.
19. Lockheed Aircraft Corporation LMSC Report 801376, "(U) Pyrolytic Graphite Final Report. Vols. I and II", 1 June 1962, AD 329784 and AD 329785. CONFIDENTIAL REPORT.
20. Marquardt Report 5992, "(U) Final Report, Pyrolytic Refractory Thrust Chamber Development", 15 August 1963. UNCLASSIFIED REPORT.
21. Marquardt Report 6086, "(U) Refractory Thrust Chambers for Spacecraft Engines, Final Report", 22 March 1965. UNCLASSIFIED REPORT.

UNCLASSIFIED

UNCLASSIFIED

TABLE I  
PERFORMANCE OF THREE PROPELLANT COMBINATIONS  
Shifting Equilibrium  
C\* Efficiency = 95%

Propellant Combination	Chamber Pressure $P_c$ (psia)	Design Mixture Ratio O/F	Combustion Temperature $T_c$ (°F)	Characteristic Velocity $C^*$ (ft/sec)	Total Propellant Flow Rate per Unit Throat Area $\dot{w}_t/A_t$ (lb/ft <sup>2</sup> sec)	Vacuum Specific Impulse $c_e = 40$ $I_{sp}$ (sec)
$N_2O_4/0.5 N_2H_4$ -0.5 UDMH	50	2.0	4696	5296	43.7	313
	100	2.0	4808	5335	86.8	315
	300	2.0	4988	5395	257.0	317
$F_2/BAL014$	50	2.0	6343	6583	35.2	382
	100	2.0	6539	6645	69.7	383
	300	2.0	6869	6745	206.0	386
$F_2/H_2$	50	12.0	6233	7481	31.0	440
	100	12.0	6447	7556	61.3	442
	300	12.0	6804	7678	181.0	445

UNCLASSIFIED

TABLE II

## THRUST FOR 100-POUND THRUST CONFIGURATION

$$D_t = 0.75 \text{ in.}$$

$$C^* \text{ Efficiency} = 95\%$$

Shifting Equilibrium

Propellant Combination	Chamber Pressure $P_c$ (psia)	Design Mixture Ratio O/F	Sea Level Thrust $\epsilon_e = 2$ (lbs)	Space Thrust $\epsilon_e = 40$ (lbs)
$N_2O_4/0.5 N_2H_4 -0.5 UDMH$	50	2.0	19.5	42.1
	100	2.0	51.9	84.0
	300	2.0	181.0	251.0
$F_2/BA1014$	50	2.0	20.9	41.2
	100	2.0	52.2	82.1
	300	2.0	182.8	244.0
$F_2/H_2$	50	12.0	21.0	41.8
	100	12.0	52.6	83.2
	300	12.0	181.0	247.0

TABLE III

## WALL THICKNESSES OF 100-POUND THRUST CONFIGURATION

Contraction Ratio = 7.14

Thrust (lbs)	Chamber Pressure (psia)	Throat Diameter (in.)	Chamber Radius (in.)	Chamber		Throat	
				t/r	t (in.)	t/r	t (in.)
100	A11	0.75	1.00	0.03	0.03	0.03	0.0225
				0.045	0.045	0.045	0.0337
				0.06	0.06	0.06	0.045
				0.08	0.08	0.08	0.06
				0.10	0.10	0.10	0.075
				0.12	0.12	0.12	0.09
				0.16	0.16	0.16	0.12

UNCLASSIFIED

TABLE IV

## DIMENSIONS OF 1000- AND 5000-POUND CONFIGURATIONS

## Shifting Equilibrium

Expansion Area Ratio = 40

95% C\* Efficiency

 $R_N/R_t = 2$  $R/R_c = 1$  $L^* = 40$ 

Thrust (lbs)	Propellant Combination	Chamber Pressure (psia)	Throat Diameter (in.)	Contraction Ratio $\epsilon_c$	Chamber Radius $R_c$ (in.)	Combustion Chamber Length $L$ (in.)	Length of Cylindrical Chamber $L_c$ (in.)	Exit Diameter $D_e$ (in.)	Nozzle Length (15° Cone) $L_N$ (in.)
1000	$N_2O_4/0.5$ $N_2H_4-0.5$ UDMH	50	3.66	2	2.58	21.19	17.4	23.1	37.21
		50	3.66	4	3.6	13.01	7.05	23.1	37.21
		50	3.66	6	4.5	10.23	2.74	23.1	37.21
		100	2.6	2	1.84	20.73	18.01	16.4	26.46
		100	2.6	4	2.6	11.94	7.62	16.4	26.46
		100	2.6	6	3.2	9.09	3.76	16.4	26.46
		300	1.50	2	1.06	20.51	18.95	9.5	15.62
		300	1.50	4	1.5	11.10	8.59	9.5	15.62
		300	1.50	6	1.84	8.17	5.10	9.5	15.62
5000	$F_2/BA1014$	50	8.25	2	5.84	22.60	14.0	52.2	84.1
		50	8.25	4	8.25	16.14	2.44	52.2	84.1
		50	8.25	6	10.11	14.98	-1.84	52.2	84.1
		100	5.85	2	4.14	21.73	15.6	37.0	59.64
		100	5.85	4	5.85	14.39	4.63	37.0	59.64
		100	5.85	6	7.16	12.53	.478	37.0	59.64
		300	3.40	2	2.40	21.08	17.55	21.5	24.92
		300	3.40	4	3.40	11.29	5.64	21.5	24.92
		300	3.40	6	4.16	10.10	3.16	21.5	24.92

UNCLASSIFIED



# UNCLASSIFIED

AFRPL-TR-66-95

Report 6106

TABLE V

WALL THICKNESSES OF 1000-POUND THRUST CONFIGURATION

Contraction Ratio = 4

Thrust (lbs)	Chamber Pressure (psia)	Throat Diameter (ins.)	Chamber Radius (ins.)	Chamber		Throat	
				t/r	t (in.)	t/r	t (in.)
1000	50	3.66	3.6	0.03	0.108	0.03	0.055
				0.045	0.162	0.045	0.082
				0.06	0.216	0.06	0.101
				0.08	0.288	0.08	0.146
				0.10	0.360	0.10	0.183
				0.12	0.432	0.12	0.220
				0.16	0.576	0.16	0.293
1000	100	2.6	2.6	0.03	0.078	0.03	0.039
				0.045	0.117	0.045	0.058
				0.06	0.156	0.06	0.078
				0.08	0.208	0.08	0.104
				0.10	0.260	0.10	0.13
				0.12	0.312	0.12	0.156
				0.16	0.416	0.16	0.208
1000	300	1.50	1.50	0.03	0.045	0.03	0.022
				0.045	0.067	0.045	0.035
				0.06	0.090	0.06	0.045
				0.08	0.120	0.08	0.060
				0.10	0.150	0.10	0.075
				0.12	0.180	0.12	0.090
				0.16	0.240	0.16	0.120

UNCLASSIFIED

UNCLASSIFIED

TABLE VI

## WALL THICKNESSES OF 5000-POUND THRUST CONFIGURATION

Contraction Ratio = 4

Thrust (lbs)	Chamber Pressure (psia)	Throat Diameter (ins.)	Chamber Radius (ins.)	Chamber		Throat	
				t/r	t (in.)	t/r	t (in.)
5000	50	8.25	8.25	0.03	0.247	0.03	0.124
				0.045	0.371	0.045	0.186
				0.06	0.495	0.06	0.248
				0.08	0.660	0.08	0.330
				0.10	0.825	0.10	0.412
				0.12	0.990	0.12	0.495
				0.16	1.32	0.16	0.660
5000	100	5.85	5.85	0.03	0.176	0.03	0.08
				0.045	0.263	0.045	0.132
				0.06	0.351	0.06	0.176
				0.08	0.468	0.08	0.234
				0.10	0.585	0.10	0.293
				0.12	0.702	0.12	0.351
				0.16	0.936	0.16	0.468
5000	300	3.40	3.40	0.03	0.102	0.03	0.051
				0.045	0.153	0.045	0.076
				0.06	0.204	0.06	0.102
				0.08	0.272	0.08	0.136
				0.10	0.340	0.10	0.170
				0.12	0.408	0.12	0.204
				0.16	0.544	0.16	0.272

UNCLASSIFIED

TABLE VII  
THERMAL MODEL HEAT SOAK BACK SUMMARY

$P_c = 100 \text{ psia}$

Thrust (lbs)	Propellants	Combustion Chamber Diameter (ins.)	Wall Thickness (in.)	Injector Weight (lbs)	Maximum Injector Temperature After Soak Back	
					Perfect Insulation Chamber to Injector (°F)	No Insulation Chamber to Injector (°F)
100	F <sub>2</sub> /BA1014	2.0	0.045	.5	230	860
1000	N <sub>2</sub> O <sub>4</sub> /50-50	5.4	0.117	3.38	410	1160
5000	F <sub>2</sub> /BA1014	12.2	0.264	17.05	970	2180

TABLE VIII

## PARAMETERS FOR THE 5000-POUND THRUST CHAMBER SOAK BACK ANALYSIS

$$P_c = 100 \text{ psia}$$

$$L^* = 40$$

$$\text{Throat Diameter} = 5.850 \text{ in.}$$

Injector Emissivity	Emissivity Notes	Chamber Wall Temperature Near Injector (°F)	Chamber Temperature Near Throat (°F)	Film Cooling Notes	Contraction Ratio	Plotted in Figure
0.25	A	5600	5600	F	4	55
0.25	A	4500	4500	D	4	55
0.25	A	2500	4500	E	4	55
0.80	C	4500	4500	D	4	52
0.25	A	4500	4500	D	4	52
0.05	B	4500	4500	D	4	52
0.25	A	4500	4500	D	6	54
0.25	A	4500	4500	D	4	54
0.25	A	4500	4500	D	2	54

Notes:

- A. Emissivity of monel used in previous analysis
- B. Emissivity of polished pure silver = 0.02 to 0.03  
(Marks Mechanical Engineers Handbook  
McGraw Hill, New York 1958)
- C. Emissivity of injector covered with deposit
- D. Film cooling to inner wall temperature of 4500°F throughout chamber
- E. Film cooling to inner wall temperature of 2500°F for 5 inches from injector, and 4500°F elsewhere
- F. No film cooling

UNCLASSIFIED

TABLE IX  
COMPARISON OF MEASURED AND PREDICTED RESIDUAL STRESSES  
IN PYROLYTIC GRAPHITE THRUST CHAMBERS

Configuration shown in Figure 58  
Wall thickness = 0.060 inch

Location	Chamber Parameters	Location	Chamber No.	Residual Stress (psi)		
				Measured	Predicted (Nozzle Shape)	Predicted (Cylinder)
Throat	$\frac{R_N}{D_t} = 2.0$	Outside, Axial	C100-2-10	8980	1500	-1300
		Outside, Axial	C100-2-11	8369	1500	-1300
		Outside, Axial	C100-2-11	7732	1500	-1300
	$\frac{t}{R_t} = 0.14$	Inside, Axial	C100-2-10	-5647	-4000	0
		Inside, Axial	C100-2-10	-3099	-4000	0
		Inside, Axial	C100-2-11	-3831	-4000	0
		Outside, Circum.	C100-2-10	-6297	--	-12,600
		Outside, Circum.	C100-2-11	-3794	--	-12,600
		Outside, Circum.	C100-2-11	-4113	--	-12,600
Section A	$\frac{R}{R_c} = 1.0$	Inside, Circum.	C100-2-10	6753	--	15,600
		Inside, Circum.	C100-2-11	5379	--	15,600
		Outside, Axial	C100-2-10	-1139	-5300	3200
	$\frac{t}{R_c} = 0.075$	Outside, Axial	C100-2-11	884	-5300	3200
		Outside, Axial	C100-2-11	1724	-5300	3200
		Outside, Axial	C100-2-11	1591	-5300	3200
		Inside, Axial	C100-2-11	-3807	5000	-3400
		Inside, Axial	C100-2-11	-1532	5000	-3400
		Outside, Circum.	C100-2-10	-1618	--	-4600
		Inside, Circum.	C100-2-10	5923	--	5700
		Inside, Circum.	C100-2-11	4784	--	5700

UNCLASSIFIED

UNCLASSIFIED

TABLE X

## SUMMARY OF PYROLYTIC GRAPHITE VENDOR SURVEY

Vendors Included in Survey: Super Temp Corp., General Electric Co., Pyrogenics, Inc., Raytheon Co., High Temperature Materials, Inc.

Parameter	Summary of Survey
Mandrel Materials	<ol style="list-style-type: none"> <li>1. ATJ graphite used by most vendors for parts up to the available size of ATJ billets. (Available sizes = 9 x 20 x 24 in. and 16 1/2 in. diameter x 14 in.)</li> <li>2. For larger parts, HIM, CS, and AUC are used.</li> <li>3. Other grades of graphite considered and used in limited quantities include Speer 3499S, ZTA, POCO, RVA. These are newer grades and several are size limited.</li> </ol>
Desirable characteristics of mandrel materials	<ol style="list-style-type: none"> <li>1. Fine grain, uniformity within billet and from billet to billet plus purity (low ash).</li> <li>2. Also graphite should be isotropic, have uniform expansion coefficients, be machinable to good finish and close tolerances, free of outgassing, and should be available in larger sizes when required.</li> </ol>
Mandrel design criteria 1. Thickness 2. Terminal configuration 3. Graphite grain orientation	<ol style="list-style-type: none"> <li>1. 0.10 to 0.25 inch. Exact value is a proprietary function of design. It is normally designed to break sometime in the fabrication process.</li> <li>2. Amount and configuration of mandrel termination is critical and proprietary. Design determines success in removing part and method of trimming to final length.</li> <li>3. ATJ and other graphites are not isotropic. Graphite grain is oriented to prevent out-of-round mandrel expansion during deposition.</li> </ol>

UNCLASSIFIED



UNCLASSIFIED

TABLE X (Continued)

Parameter	Summary of Survey
Mandrel machining technique	<p>Generally, mandrels are machined with standard steel tools. Final finishing with steel wool, emery, or rouge paper is often used. Techniques are readily tailored to customer requirements. Possible variables include use of carbide tools, tool radius, tool feed, and type of microcut paper used.</p>
Mandrel cleaning procedures	<p>Mandrels are carefully cleaned by various techniques prior to installation in furnace. Common method is to wash with acetone and wipe with lint free paper (Kimwipe). Parts are either put directly in furnace or may be wrapped in paper or plastic for storage.</p> <p>Other cleaning techniques evaluated include vapor degreasing and vacuum cleaning.</p>
Mandrel inspection	<p>Primarily visual inspection for surface flaws in addition to dimensional check. Any pits or surface flaws are cause for rejection of mandrel. This rejection rate may vary between 5 and 25 percent of the mandrels.</p>
Mandrel predeposition treatments	<p>Exact prerun mandrel treatments are variable and proprietary. Type of treatment affects quality of part, cost, and rejection rate. Hence, a trade-off consideration is required. Prerun mandrel treatment affects both the surface finish of the PG and mandrel separation.</p> <p>Types of prerun treatments used or evaluated by several of the vendors include: flash coating, coating with colloidal graphite, high temperature mandrel soaking to eliminate outgassing, chlorine gas purification and others not specified.</p>

UNCLASSIFIED

TABLE X (Continued)

Parameter	Summary of Survey
Vendor recommendations for improved mandrels	<ol style="list-style-type: none"> <li>1. Tighter or narrower property specifications on mandrel graphite billets</li> <li>2. Larger sizes of fine grain graphite, i.e., larger ATJ billets</li> <li>3. Truly isotropic graphite in large sizes</li> <li>4. Gas purified graphite billets</li> </ol>
Size of furnaces available and production capability	<p>At least three of the vendors can make PG parts 36 inches in diameter and greater than 5 feet long. Each of the vendors has several production type furnaces as well as smaller furnaces devoted to R&amp;D work.</p> <p>Furnaces available in the industry cover a range of finished part sizes including diameters of 42, 36, 24, 12, 6, 4 inches and smaller.</p> <p>Most of the larger furnaces are induction heated. The smaller furnaces are resistance heated.</p> <p>In production runs, the larger furnaces are set up to make a number of parts by manifolding several setups in parallel. For symmetrical parts, they may also be produced in series.</p>
Deposition parameter control	<ol style="list-style-type: none"> <li>1. Heat up time</li> <li>2. Heat up parameters</li> </ol>

1. As fast as possible without causing excessive outgassing of the insulation. Varies with furnace size, power available and insulation. Typical times are 3 to 18 hours.

2. Start up parameter control is critical to prevent initiation of nodules. Exact procedures are proprietary but include such considerations as (1) leak checking (2) prevention of soot falling on mandrel surface (3) kind and rate of gas flow during heat up (4) furnace pressure.

UNCLASSIFIED

TABLE X (Continued)

Parameter	Summary of Survey
Deposition parameter control (Continued from previous page)	
3. Deposition gas	<p>3. Three vendors use natural gas commercially piped to plant. Composition is about 96 percent methane plus other hydrocarbons, CO<sub>2</sub>, and traces of sulphur. One vendor uses pure methane.</p> <p>Other gases have been evaluated but have not been shown to be more practical nor to produce better pyrolytic graphite. Higher carbon gases may have some advantage but this has not been demonstrated.</p> <p>4. Gas composition (which may be varied by using dilution or higher carbon content gas) affects deposition rate and axial thickness profile. Deposition rate may affect residual stress.</p>
4. Effect of gas composition	<p>5. These are the primary control parameters varied for each size and configuration to achieve the desired microstructure and wall thickness. Values used by each vendor vary considerably and there does not seem to be general correlation of these parameters with material strength.</p> <p>Continuously nucleated material has shown superior strength in sample testing. However, process conditions must be controlled over a narrower range to achieve continuously nucleated microstructure compared to substrate nucleated material. This range of conditions is so narrow, in fact, that it is difficult to maintain these conditions during a given run along the whole length of the same part (such as a thrust chamber).</p> <p>Interrelated parameters include vacuum pump capacity and available power.</p>
5. Temperature, pressure, and gas flow rate	

UNCLASSIFIED

UNCLASSIFIED

TABLE X (Continued)

Parameter	Summary of Survey
Deposition parameter control (Continued from previous page)	
6. Temperature control	<p>6. The temperature controlled may be the mandrel, the pyrolytic graphite part or a target in the center of the hot zone.</p> <p>The temperatures may be monitored continuously and checked periodically with an optical pyrometer. The prime consideration is prevention of fluctuations. Actual temperature control is within 25° to 50°F.</p> <p>Studies of deposition temperature effects have ranged from 1000° to 2600°C or wider.</p>
7. Pressure control	<p>7. Deposition pressure is usually measured at the furnace wall and may be recorded continuously or logged manually at regular intervals.</p> <p>Pressures tend to vary due to PG buildup in the stack causing increased pressure drops.</p> <p>Studies of deposition pressure effects have ranged from 0.1 mm Hg to 1/2 atmosphere or wider.</p>
8. Gas inlet design	<p>8. Gas inlet designs are proprietary. Inlet nozzles may be graphite or water cooled. Location and configuration of inlet nozzle determines axial deposition profile and circumferential uniformity.</p>
9. Deposition efficiency	<p>9. The stripping efficiency, (i.e., depletion of available carbon in the deposition gas) is a controlled variable interrelated with deposition profile and deposition rate. Practical values range from 20 to 75 percent.</p>

UNCLASSIFIED

TABLE X (Continued)

Parameter	Summary of Survey
Furnace cool down	<p>Postrun soaking at deposition temperature is not practiced. At the end of a deposition run, normal practice is to turn the power off and let the furnace cool as rapidly as possible. Attempts to force cool by purging with inert gas have not proven economical.</p> <p>Time to cool varies with furnace size, insulation, etc. Typical cooling times run to 15 and 36 hours for the larger furnaces.</p> <p>For economy, on production runs, the furnace is unloaded as hot as practical. Parts may be at temperatures well above 150°F when removed from the furnace.</p>
Handling and final trim	<p>Procedures developed to remove the finished part from the furnace stack and trim to final length are critical in avoiding residual stress failures. Recent work (AFML Contract AF 33(615)-3136) has shown advantage of new termination techniques.</p> <p>Most common failures on finished part are tensile cracks or delaminations. Some degree of control is possible over whether tensile cracks or delaminations are the most likely type of failure.</p> <p>Apparently, excess nodules and scaling are more controllable.</p>
Tolerance on run time	Within 0.2 percent of run time - i.e., 2 or 3 minutes out of 10 or 20 hours.
Tolerance on wall thickness for same run time	Within 10 percent easily or 1 to 5 percent if required.

UNCLASSIFIED

TABLE X (Continued)

Parameter	Summary of Survey
Axial and circumferential tolerances on given part	Within 5 percent or customer specifications.
Nodule size and distribution criteria	Specifications provided in catalogs by Super Temp., General Electric, and Pyrogenics, etc.
Inspection techniques	<p>1. Normally available: visual, dimensional, photomicrographs, dye check, density.</p> <p>2. Special techniques available by one or more vendors: <math>C_o</math> (lattice spacing), X-Ray (delaminations), I/Im (anisotropy), spectrochemical analysis, hardness.</p>
Mechanical measurements by vendors	<p>1. Normally available: Tensile strength RT (Room temperature) to 1000°F or higher (to 3000°C)</p> <p>Elastic moduli RT</p> <p>Residual stress RT</p> <p>Poisson's ratio RT</p> <p>Tube burst pressure RT</p> <p>2. Available from one or more vendors:</p> <p>Thermal conductivity to 1800°C</p> <p>Thermal expansion to 2800°C</p> <p>Emissivity to 2300°C</p> <p>Growth to 3000°C</p>

UNCLASSIFIED



TABLE XI

## DESCRIPTION OF PYROLYTIC GRAPHITE TUBES

Vendor	No. of Tubes	Description
Super Temp Corp.	32	Eight per furnace run. Different mandrel materials and mandrel finishing procedures. Uniform furnace conditions.
General Electric Co.	8	1 furnace run of boron-doped PG
	8	1 furnace run of continuously nucleated PG
Pyrogenics, Inc.	1	Controlled delaminations, female mandrel, 0.160-inch wall
	1	Controlled delaminations, female mandrel, 0.225-inch wall
	2	Controlled delaminations, male mandrel
High Temperature Materials, Inc.	3	Controlled delaminations, 0.125-inch wall
	3	Fabric reinforced, 0.125-inch wall
Raytheon Co.	2	17 mils/hr deposition rate, 0.06-inch thick
	6	20 mils/hr deposition rate, 0.06-inch thick
	2	15 mils/hr deposition rate, 0.09-inch thick
	2	30 mils/hr deposition rate, 0.09-inch thick
	4	1.5% boron
	2	High boron content
	2	Controlled delamination

Total:

78

UNCLASSIFIED

TABLE XII

DESCRIPTION OF SUPER TEMP PYROLYTIC GRAPHITE TUBES

Tube No.	Run No.	Mandrel Material	Mandrel Machining			Maximum Nodule Diameter (in.)	Wall Thickness Min-Max (in.)	Pressurization Hoop Stress at Rupture (psi)	Rupture Pressure (psig)
			Lathe Speed (rpm)	Lathe Travel (in./rev)	Depth of Final Cut (in.)				
S-101	1	Speer 3499S	400	0.0035	0.005	0.03	0.054 to 0.065	12,590	680
S-102	1	NAT. ATJ	400	0.0035	0.005	0.07	0.060 to 0.066	6,330	380
S-103	1	NAT. CS	400	0.0035	0.005	0.03	0.059 to 0.068	6,270	370
S-104	1	POCO EP192C	400	0.0035	0.005	0.03	0.056 to 0.065	16,070	900
S-105	1	NAT. ATJ	400	0.0035	0.005	0.03	0.054 to 0.066	12,960	700
S-106	1	NAT. CS	400	0.0035	0.005	0.06	0.047 to 0.065	-	Cracked
S-107	1	Speer 3499S	400	0.0035	0.005	0.05	0.055 to 0.065	6,360	350
S-108	1	POCO EP192C	400	0.0035	0.005	0.07	0.056 to 0.064	7,320	410
S-201	2	Speer 3499S	400	0.0035	0.005	0.02	0.055 to 0.076	5,270	290
S-202	2	NAT. ATJ	400	0.0035	0.005	0.05	0.069 to 0.080	5,220	360
S-203	2	HLM	400	0.0035	0.005	0.05	0.060 to 0.079	5,330	320
S-204	2	POCO EP192C	400	0.0035	0.005	0.02	0.057 to 0.068	21,750	1240
S-205	2	NAT. ATJ	400	0.0035	0.005	0.04	0.038 to 0.057	13,160	500
S-206	2	HLM	400	0.0035	0.005	0.04	0.034 to 0.051	-	Cracked
S-207	2	Speer 3499S	400	0.0035	0.005	0.02	0.041 to 0.057	11,950	490
S-208	2	POCO EP192C	400	0.0035	0.005	0.04	0.054 to 0.064	5,560	300
S-301	3	Speer 3499S	400	0.0035	0.005	0.03	0.050 to 0.060	9,200	460
S-302	3	Speer 3499S	400	0.0035	0.005	0.04	0.056 to 0.070	12,320	690
S-303	3	POCO EP192C	400	0.0035	0.005	0.04	0.060 to 0.069	7,500	450
S-304	3	POCO EP192C	400	0.0035	0.005	0.04	0.062 to 0.070	8,710	540
S-305	3	POCO EP192C	400	0.001	0.005	0.03	0.052 to 0.069	10,580	550
S-306	3	POCO EP192C	400	0.001	0.005	0.03	0.045 to 0.068	14,440	650
S-307	3	POCO EP192C	400	0.010	0.005	0.03	0.050 to 0.070	10,200	510
S-308	3	POCO EP192C	400	0.010	0.005	0.03	0.050 to 0.070	10,000	500

UNCLASSIFIED

UNCLASSIFIED

TABLE XII (Continued)

Tube No.	Run No.	Mandrel Material	Mandrel Machining			Maximum Nodule Diameter (in.)	Wall Thickness Min-Max (in.)	Pressurization Hoop Stress at Rupture (psi)	Rupture Pressure (psig)
			Lathe Speed (rpm)	Lathe Travel (in./rev)	Depth of Final Cut				
S-401	4	POCO EP192C	400	0.010	0.002	0.04	0.052 to 0.067	12,690	660
S-402	4	POCO EP192C	400	0.010	0.002	0.04	0.059 to 0.070	14,920	880
S-403	4	POCO EP192C	400	0.0035	0.002	0.05	0.059 to 0.071	6,440	380
S-404	4	POCO EP192C	400	0.0035	0.002	0.04	0.062 to 0.069	8,550	530
S-405	4	POCO EP192C	400	0.001	0.002	0.05	0.049 to 0.068	5,310	260
S-406	4	POCO EP192C	400	0.001	0.002	0.04	0.055 to 0.067	11,450	630
S-407	4	Speer 3499S	400	0.0035	0.002	0.04	0.056 to 0.067	8,040	450
S-408	4	Speer 3499S	400	0.0035	0.002	0.04	0.054 to 0.067	14,810	800

UNCLASSIFIED

UNCLASSIFIED

TABLE XIII  
DESCRIPTION OF GENERAL ELECTRIC CO. PYROLYTIC GRAPHITE TUBES

Tube No.	Type	Run No.	Boron Content (%)				Maximum Nodule Diameter (in.)	Modulus of Elasticity a-direction (psi)	Residual Stress Outside Surface		Wall Thickness Min-Max (in.)	Pressurization Hoop Stress at Rupture (psi)	Rupture Pressure (psig)
			Top		Bottom				Hoop (psi)	Axial (psi)			
			Inside	Outside	Inside	Outside							
G101	Boron doped	1	0.33	0.70	0.35	0.51	0.04	$5.44 \times 10^6$	-7610	3260	0.077 to 0.088	13,380	1050
G102	Boron doped		0.37	0.50	0.38	0.70	0.03	$5.61 \times 10^6$	-6760	2090	0.068 to 0.079	13,600	940
G103	Boron doped		0.42	0.73	0.28	0.38	0.04	$5.63 \times 10^6$	-6910	1570	0.068 to 0.083	6,410	440
G104	Boron doped		NA	NA	NA	NA	0.06	--	-8640	3450	0.084 to 0.091	--	Not Ruptured
G105	Boron doped		0.45	0.52	0.53	0.58	0.04	$6.01 \times 10^6$	-6330	4150	0.068 to 0.082	12,780	900
G106	Boron doped		0.36	0.60	0.55	0.63	0.03	$6.00 \times 10^6$	-7100	4830	0.066 to 0.079	13,290	900
G107	Boron doped		0.40	0.59	0.43	0.57	0.05	--	--	--	0.078 to 0.093	Cracked	
G108	Boron doped		0.19	0.36	0.28	0.60	0.10	--	--	--	0.077 to 0.094	Cracked	
G201	Regenerative microstructure	2	No boron				0.03	$5.26 \times 10^6$	-9580	3080	0.081 to 0.089	Cracked	
G202	Regenerative microstructure		No boron				0.03	$6.50 \times 10^6$	-7890	3360	0.069 to 0.082	9,770	690
G203	Regenerative microstructure		No boron				0.03	$5.13 \times 10^6$	-7020	--	0.080 to 0.087	25,880	2100
G204	Regenerative microstructure		No boron				0.03	$6.46 \times 10^6$	-8140	--	0.067 to 0.081	13,410	900
G205	Regenerative microstructure		No boron				0.03	--	--	--	0.081 to 0.086	15,490	1200
G206	Regenerative microstructure		No boron				0.03	$4.93 \times 10^6$	-6310	--	0.069 to 0.086	13,240	900
G207	Regenerative microstructure		No boron				0.04	--	--	--	0.079 to 0.086	Cracked	
G208	Regenerative microstructure		No boron				0.04	--	--	--	0.064 to 0.084	Cracked	

\* NA: Not available

UNCLASSIFIED

UNCLASSIFIED

TABLE XIV  
DESCRIPTION OF RAYTHEON CO. PYROLYTIC GRAPHITE TUBES

Tube No.	Type	Boron Content (%)				Furnace			Maximum Module Diameter (in.)	Wall Thickness Min-Max (in.)	Pressurization Hoop Stress at Rupture (psi)	Rupture Pressure (psig)
		Top		Bottom		Run No.	Temp. (°F)	Press. (mm Hg)				
		Inside	Outside	Inside	Outside							
R101	17 mil/hr	No boron				1	3523	20	0.05	0.065 to 0.072	6000	390
R102	17 mil/hr	No boron				1	3523	20	0.04	0.064 to 0.070	6400	410
R201	20 mil/hr	No boron				2A	3523	20	0.05	0.052 to 0.063	8840	460
R202	20 mil/hr	No boron				2A	3523	20	0.07	0.057 to 0.066	1050	60
R203	18 mil/hr	No boron				2B	3523	15	0.04	0.052 to 0.056	6150	320
R204	18 Mil/hr	No boron				2C	3523	15	0.04	0.045 to 0.055	5780	260
R205	20 mil/hr	No boron				-	--	--	0.04	0.050 to 0.063	4800	240
R206	20 mil/hr	No boron				-	--	--	0.07	0.056 to 0.066	--	Cracked
R301	15 mil/hr	No boron				3	3523	10	0.03	0.070 to 0.091	8570	600
R302	15 mil/hr	No boron				3	3523	10	0.03	0.081 to 0.091	6660	540
R401	30 mil/hr	No boron				4	3362	15	0.03	0.070 to 0.086	3290	230
R402	30 mil/hr	No boron				4	3362	15	0.06	0.070 to 0.097	5430	380
R501	1.5% boron	1.28	1.04	1.38	1.25	5	3362	20	0.04	0.065 to 0.074	4920	320
R502	1.5% boron	1.75	1.32	1.64	1.36	5	3362	20	0.03	0.068 to 0.077	5590	380
R601	1.5% boron	1.53	0.82	1.03	1.01	6	3362	20	0.03	0.063 to 0.075	--	Cracked
R602	1.5% boron	1.39	0.80	1.62	0.98	6	3362	20	0.02	0.065 to 0.075	--	Cracked
R901	1 to 2% boron	0.94	1.44	1.12	1.16	9	3362	15	0.03	0.057 to 0.064	--	Cracked
R1001	1 to 2% boron	1.63	1.99	1.86	1.57	10	3362	15	0.03	0.046 to 0.062	--	Cracked
R1101	One delamination	No boron				-	--	--	0.03	0.123 to 0.129	11000	1260
R1102	One delamination	No boron				-	--	--	0.03	0.108 to 0.125	8175	1000

UNCLASSIFIED

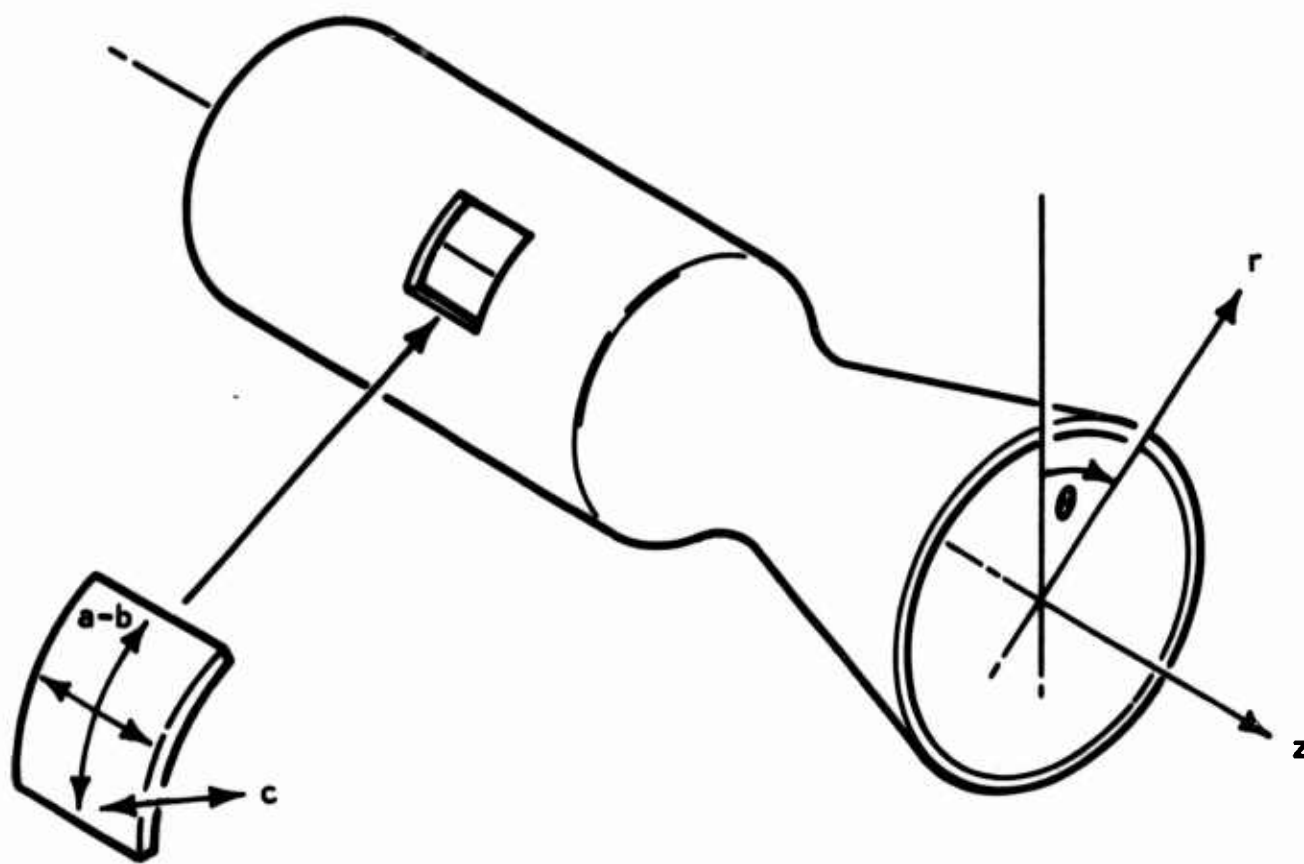


FIGURE 1. Coordinates of Free Standing Pyrolytic Graphite Thrust Chamber



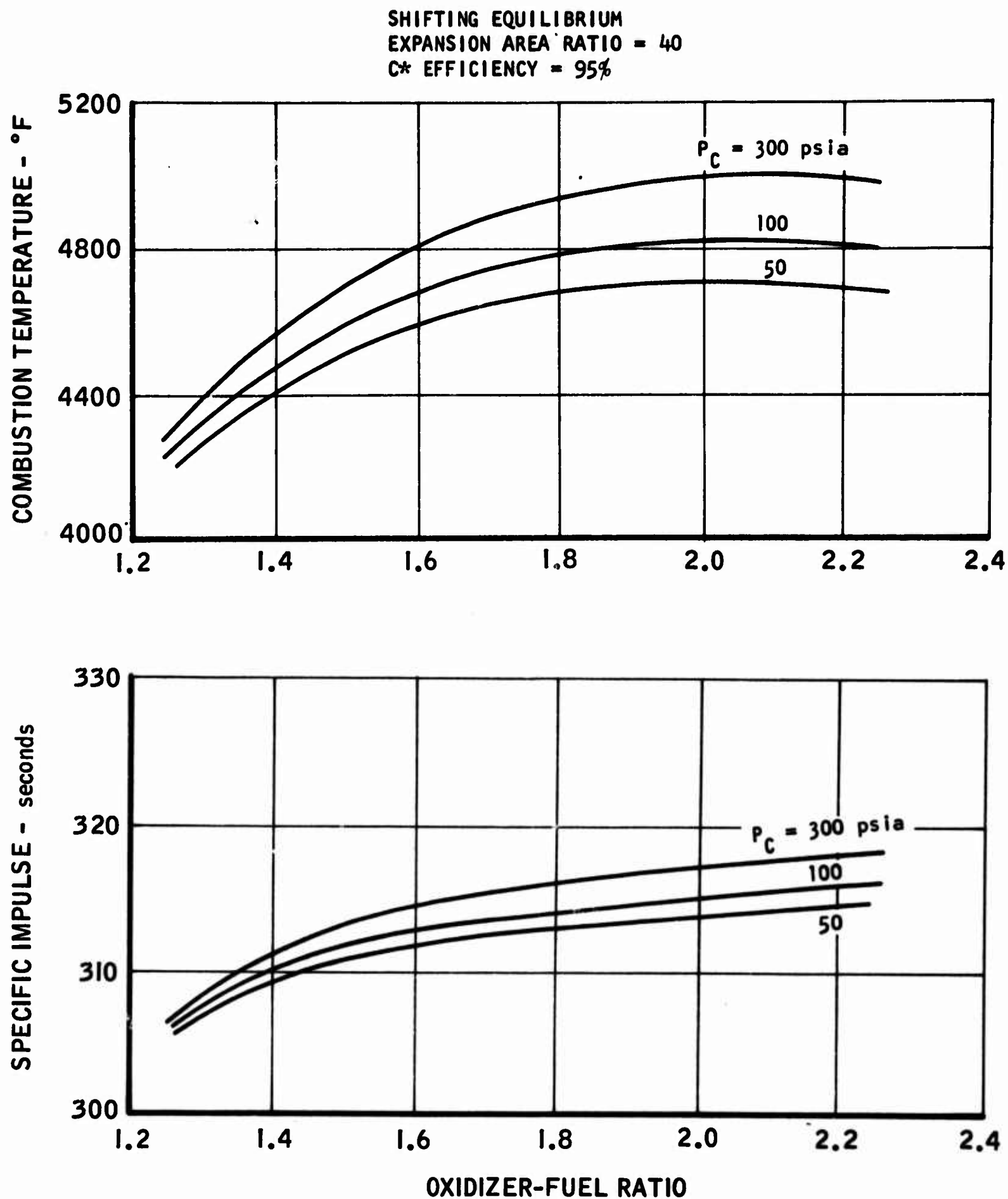
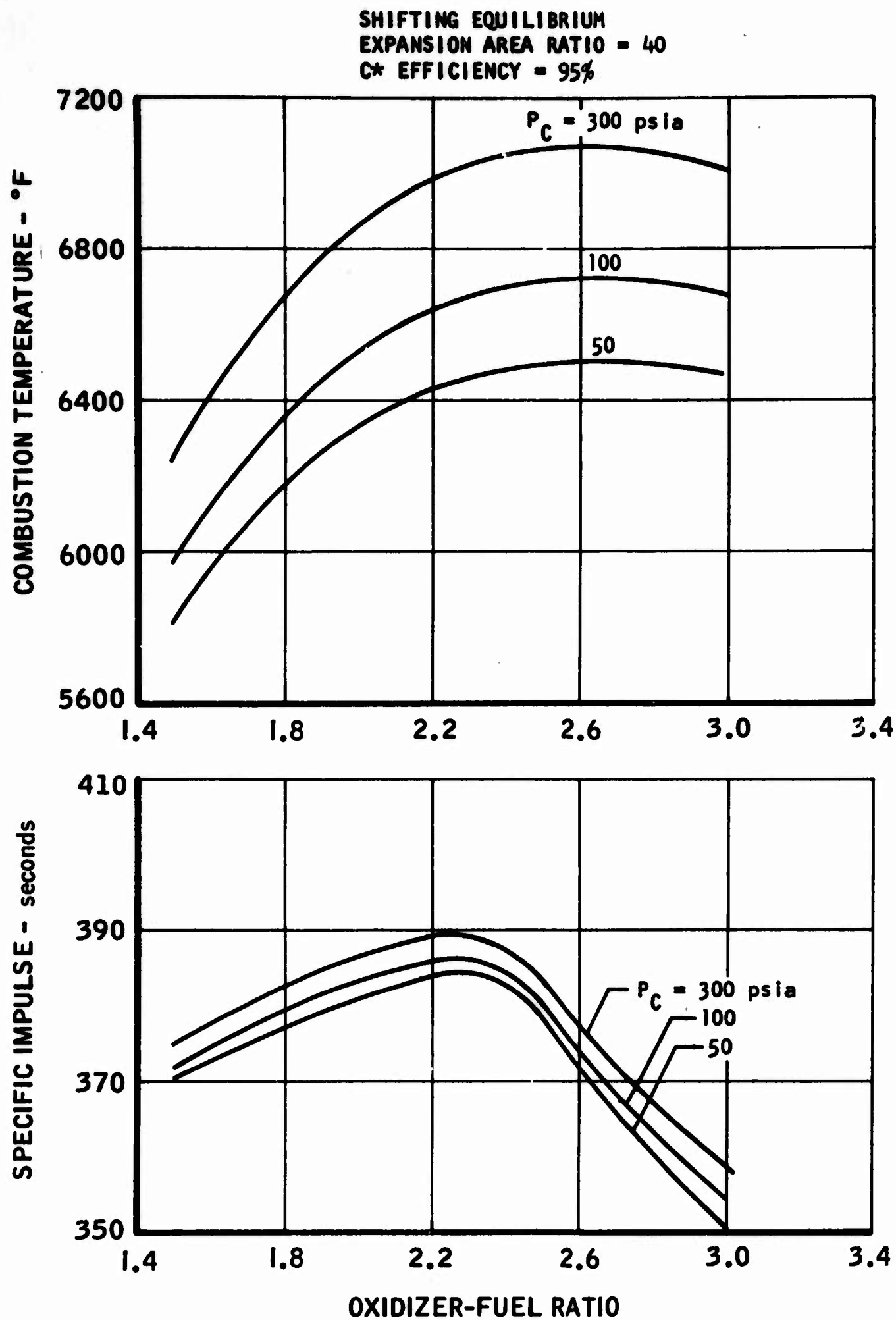
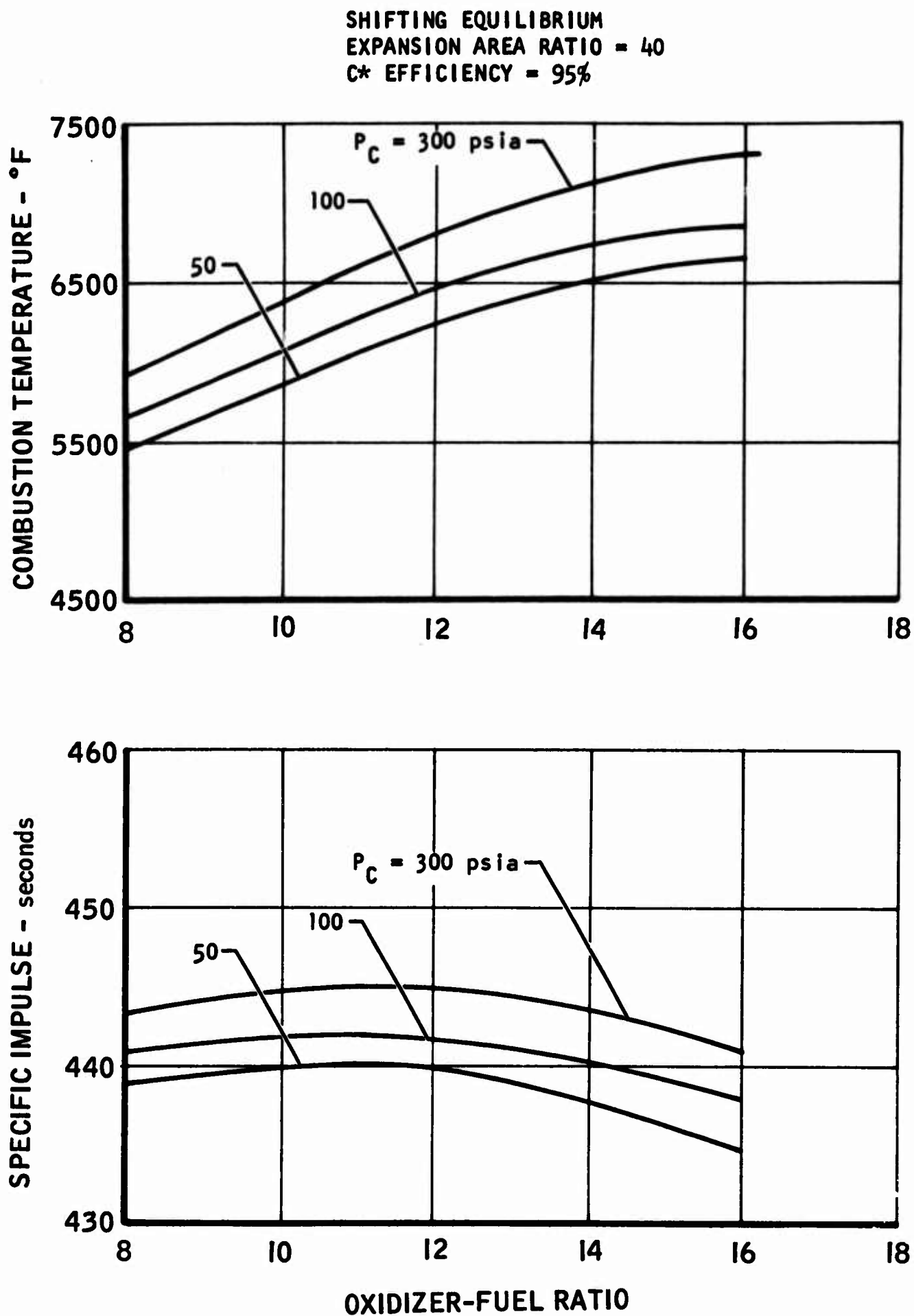


FIGURE 2. Propellant Performance,  $N_2O_4/0.5N_2H_4-0.5$  UDMH

UNCLASSIFIED

FIGURE 3. Propellant Performance,  $F_2/BA1014$ 

UNCLASSIFIED

FIGURE 4. Propellant Performance,  $F_2/H_2$

UNCLASSIFIED

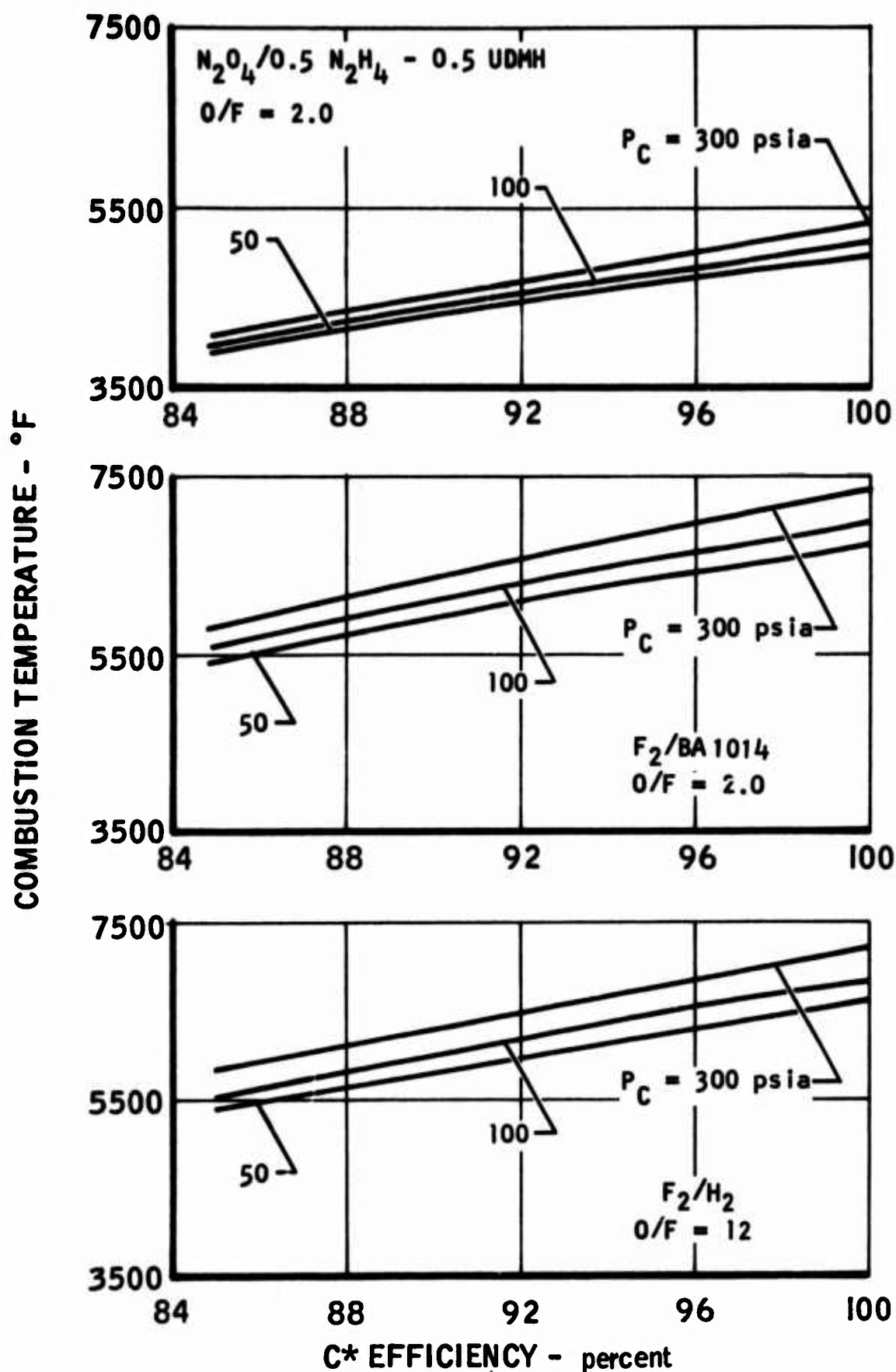


FIGURE 5. Combustion Temperature vs. C\* Efficiency, Shifting Equilibrium

UNCLASSIFIED

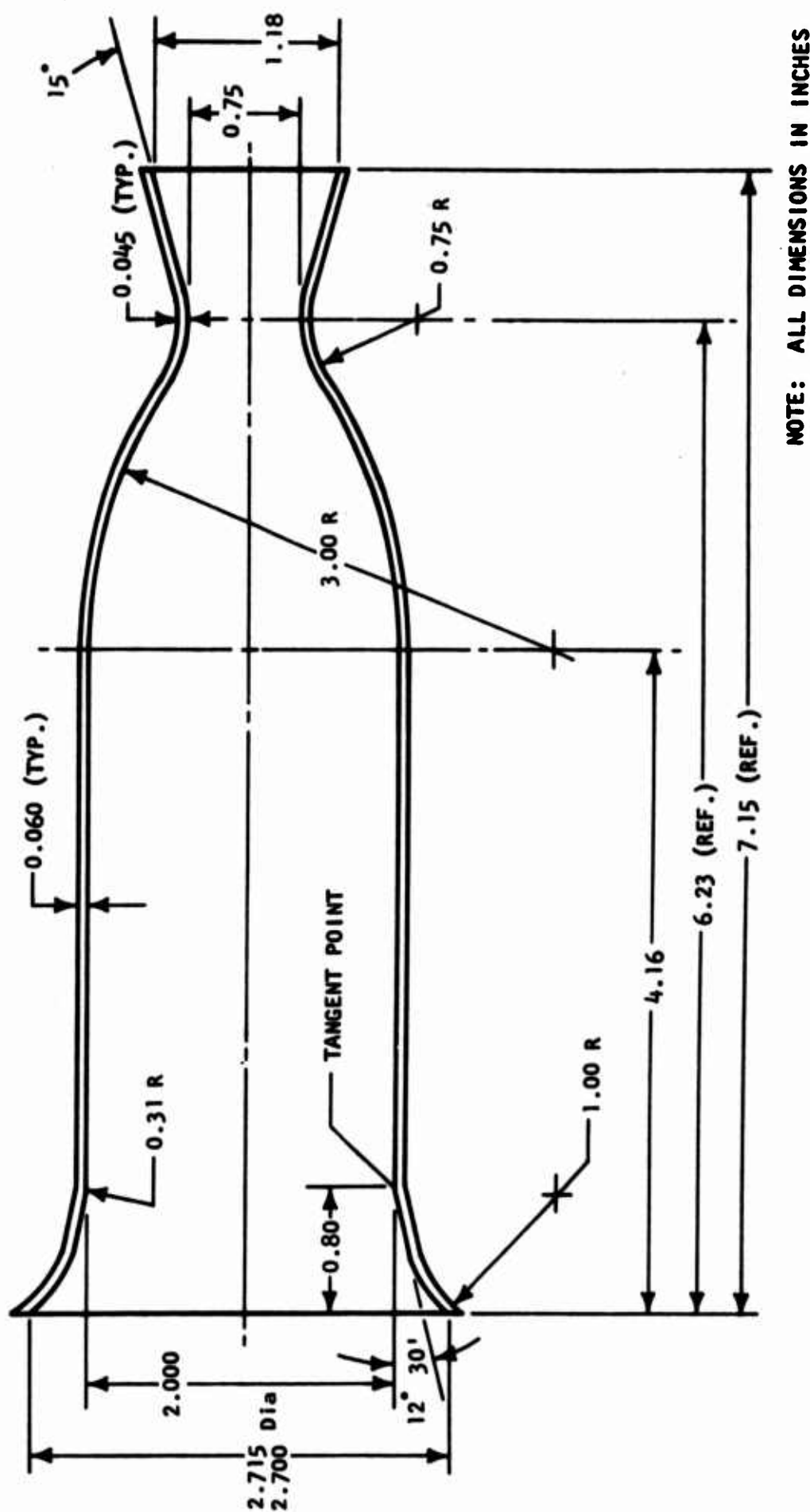


FIGURE 6. 100-pound Thrust Configuration

UNCLASSIFIED

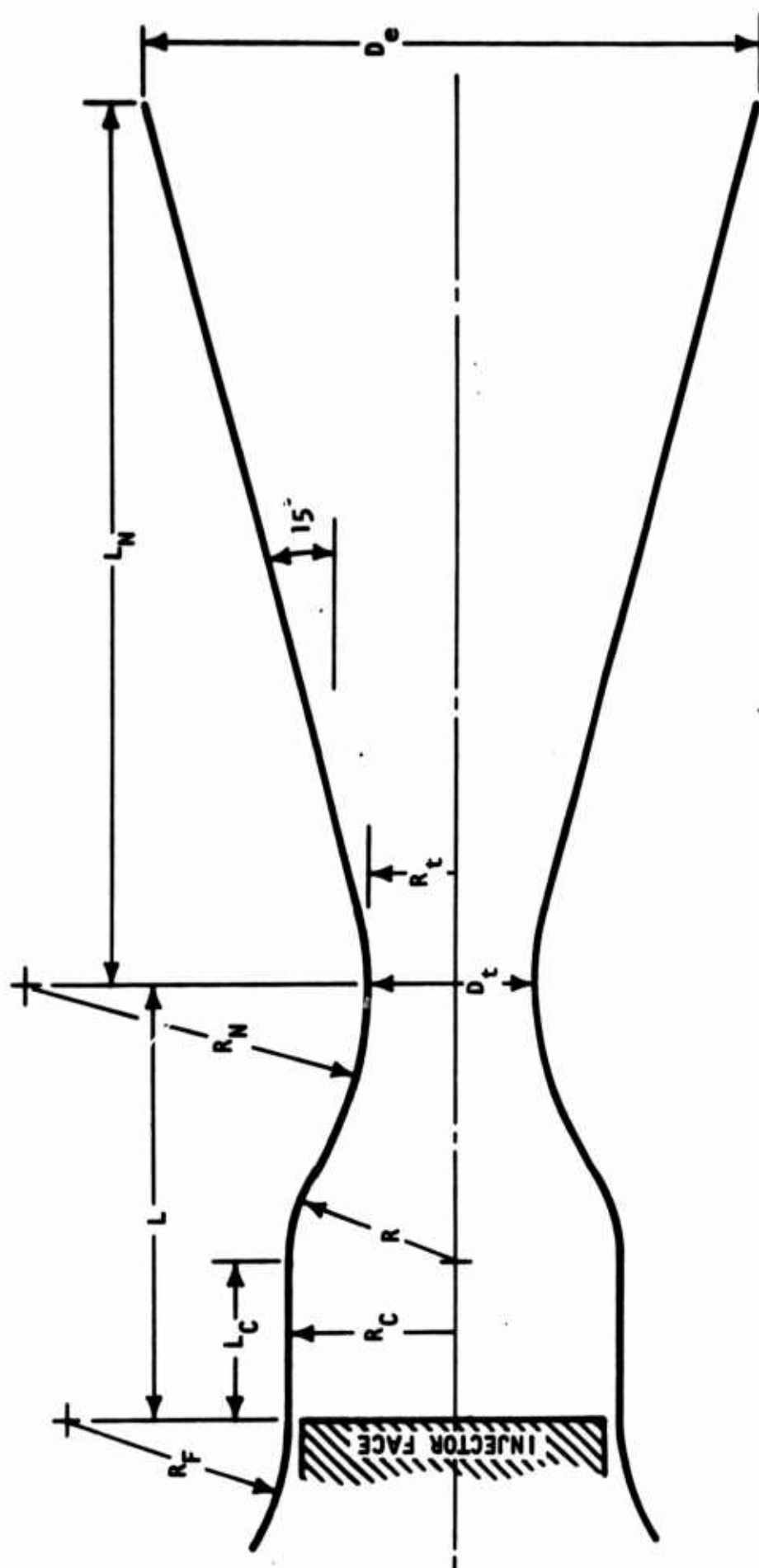


FIGURE 7. Chamber Dimension Nomenclature

UNCLASSIFIED



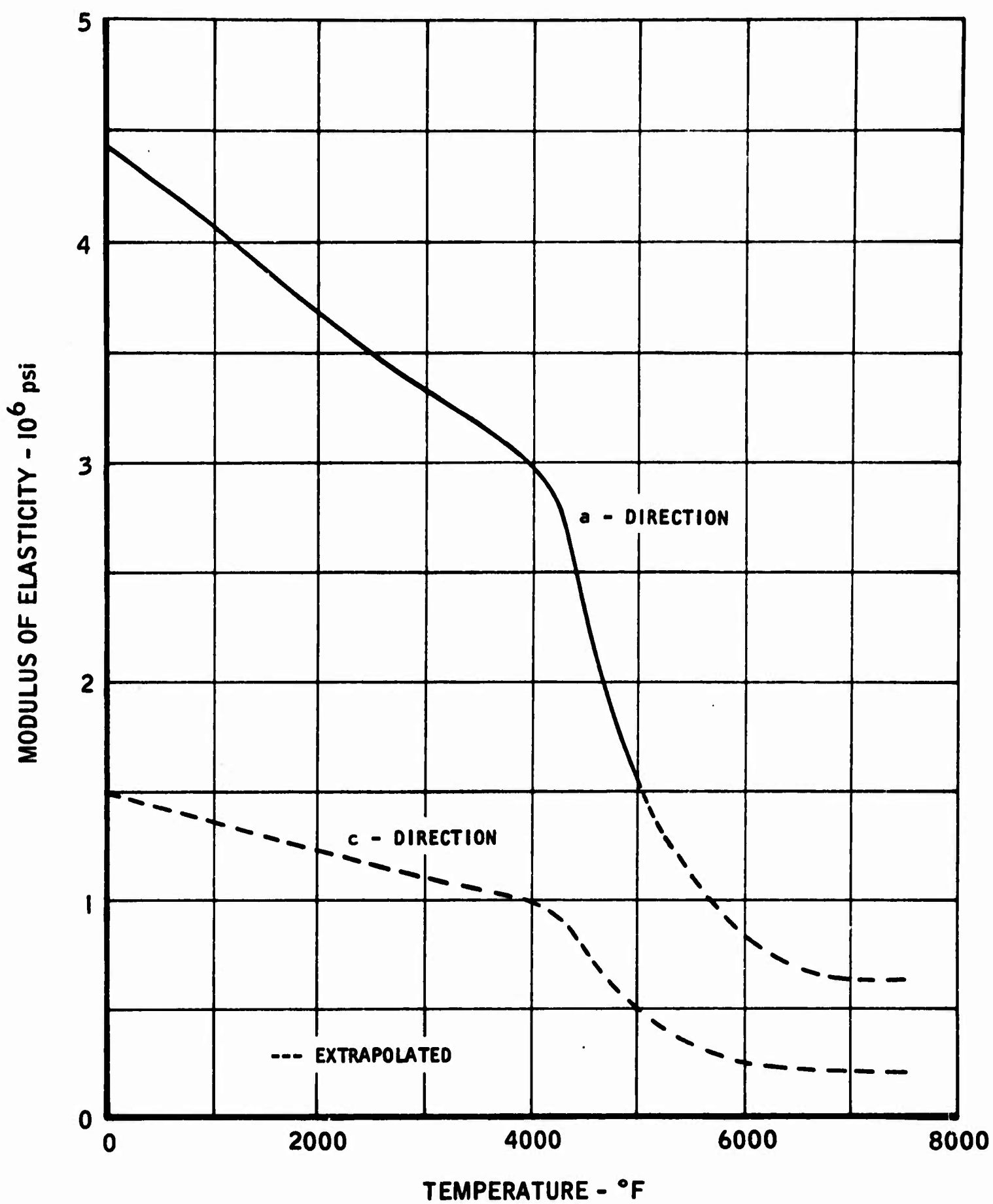


FIGURE 8. Modulus of Elasticity of Pyrolytic Graphite, Analysis Standard

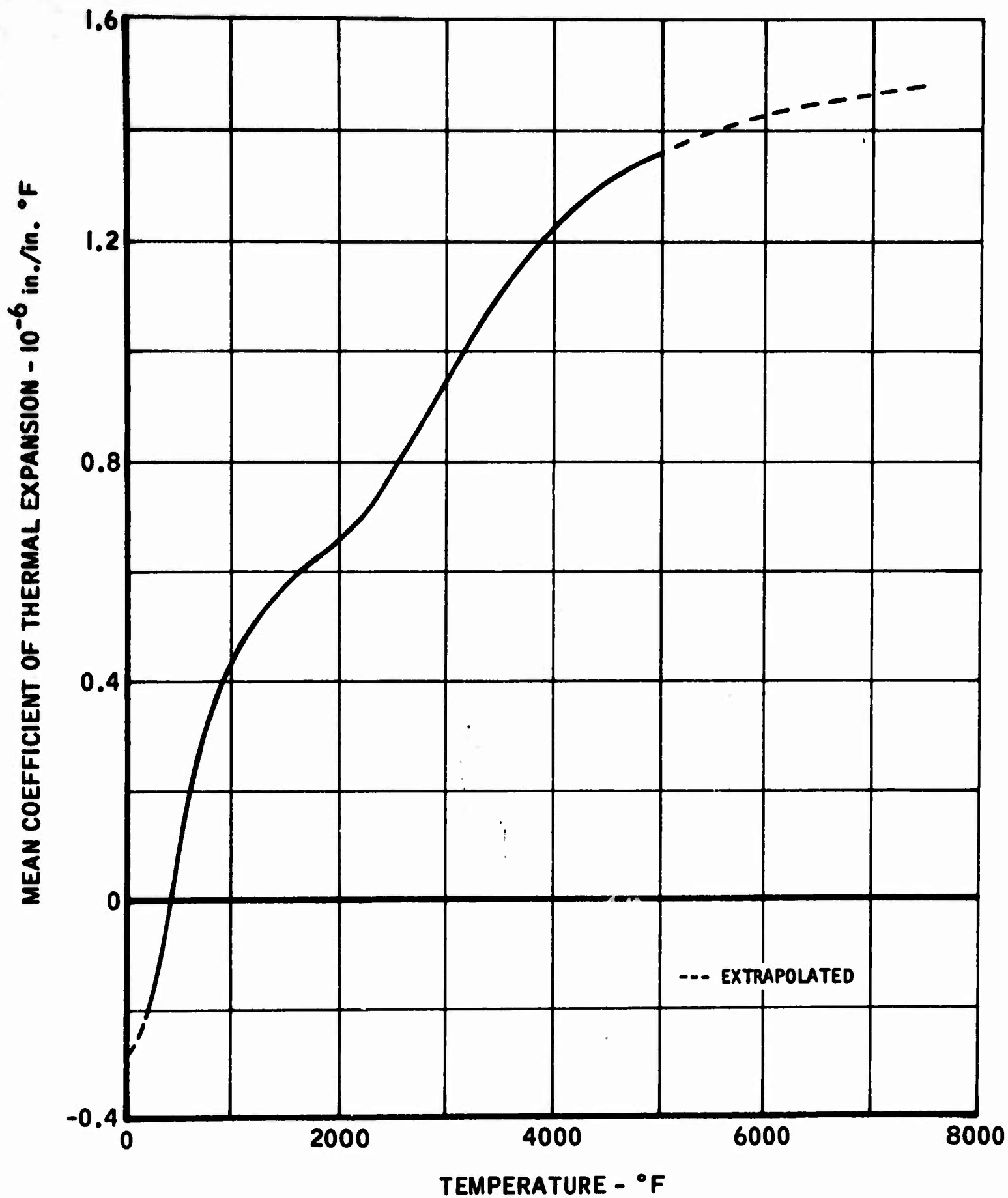


FIGURE 9. Coefficient of Thermal Expansion in the a-Direction for Pyrolytic Graphite, Analysis Standard

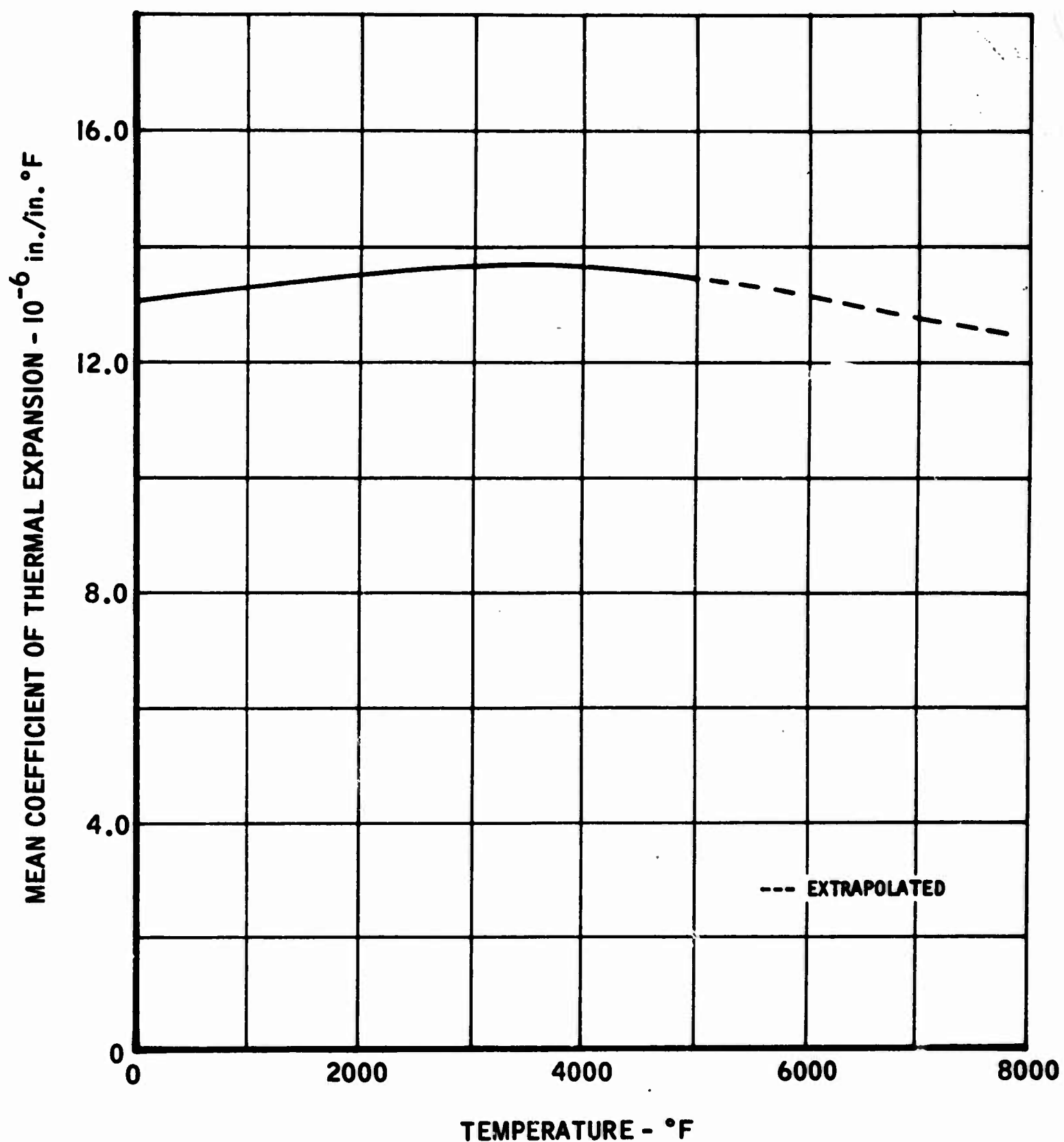


FIGURE 10. Coefficient of Thermal Expansion in the c-Direction for Pyrolytic Graphite, Analysis Standard

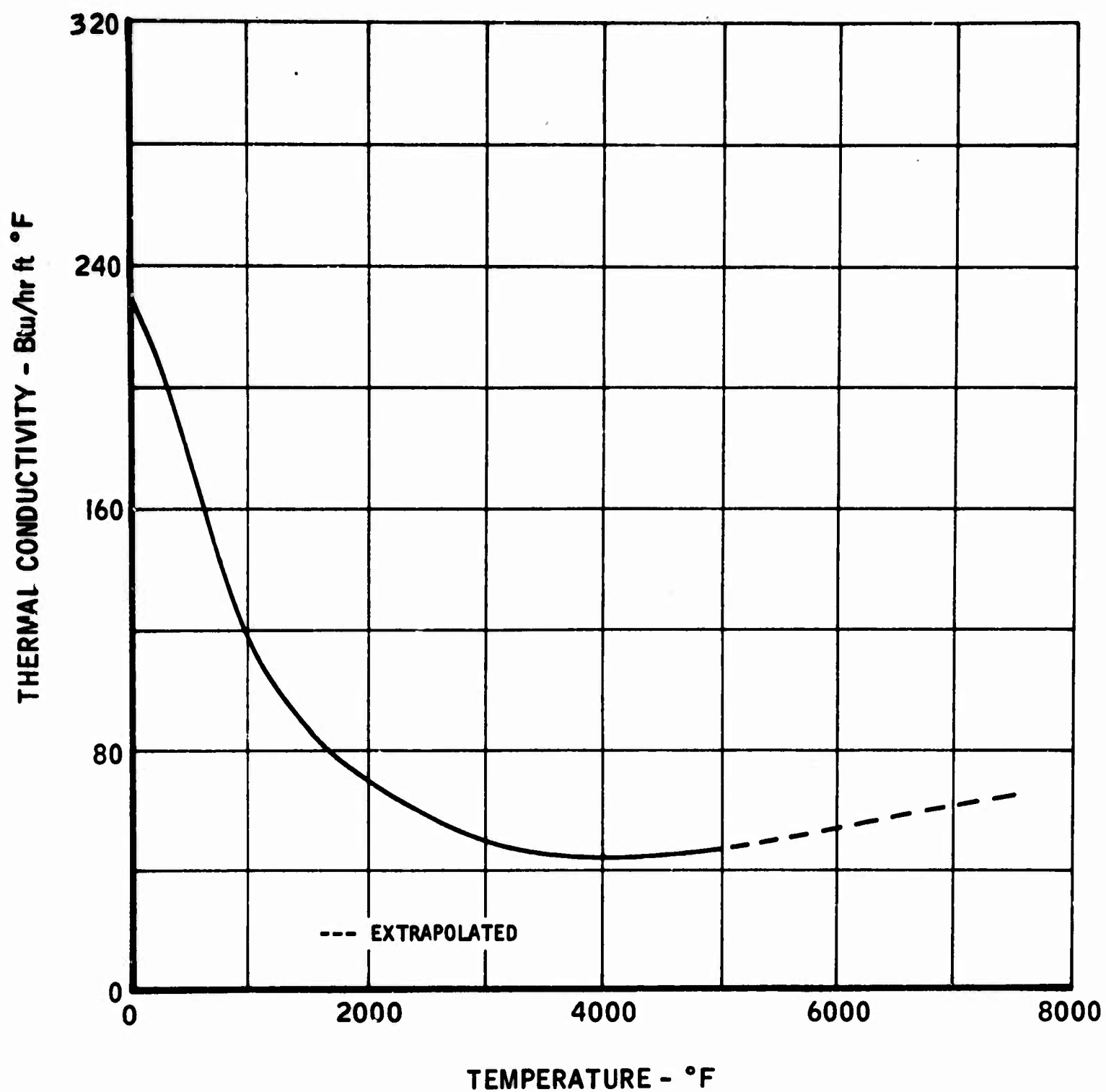


FIGURE 11. Thermal Conductivity in the a-Direction for Pyrolytic Graphite, Analysis Standard

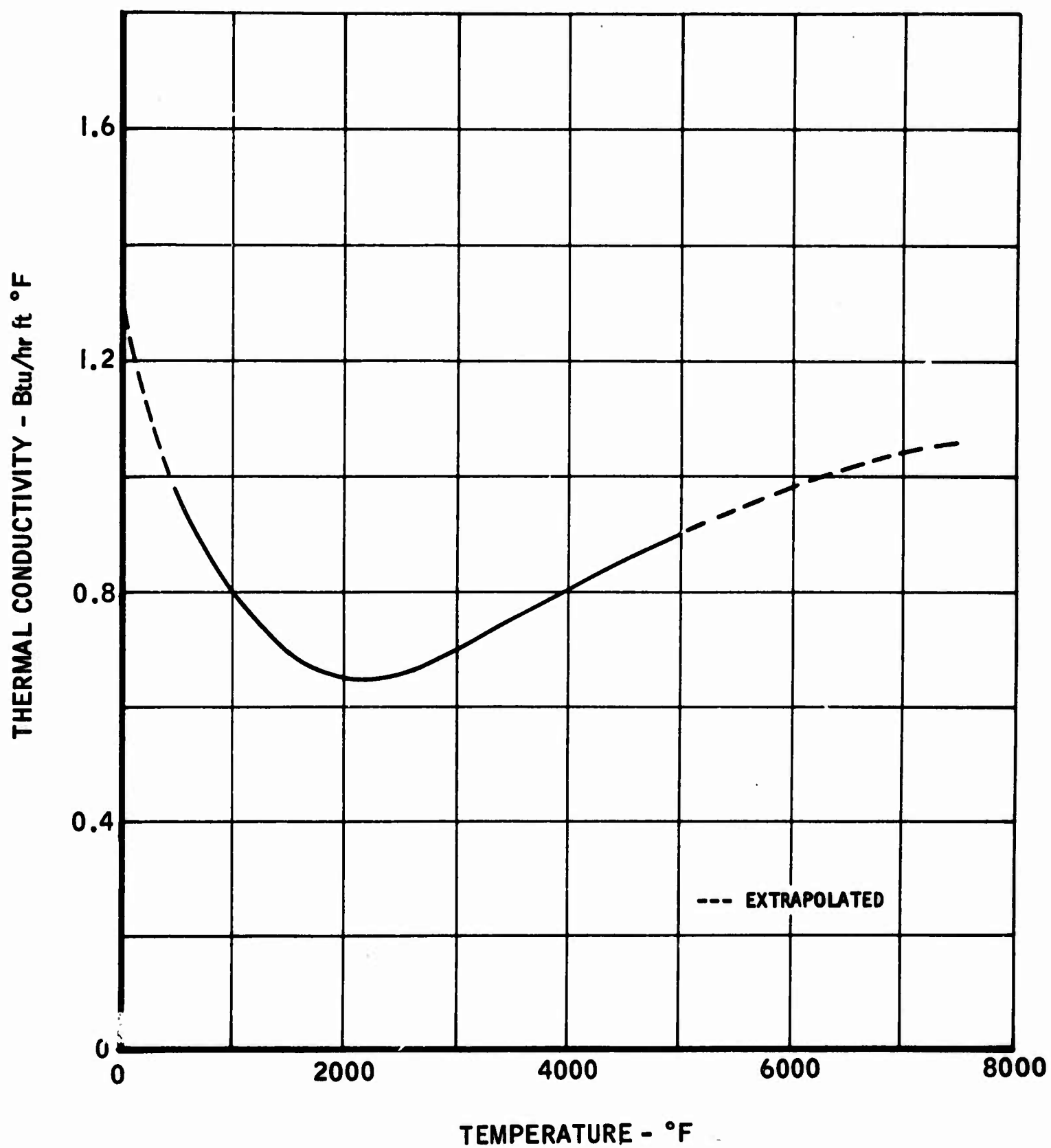


FIGURE 12. Thermal Conductivity in the c-Direction for Pyrolytic Graphite, Analysis Standard

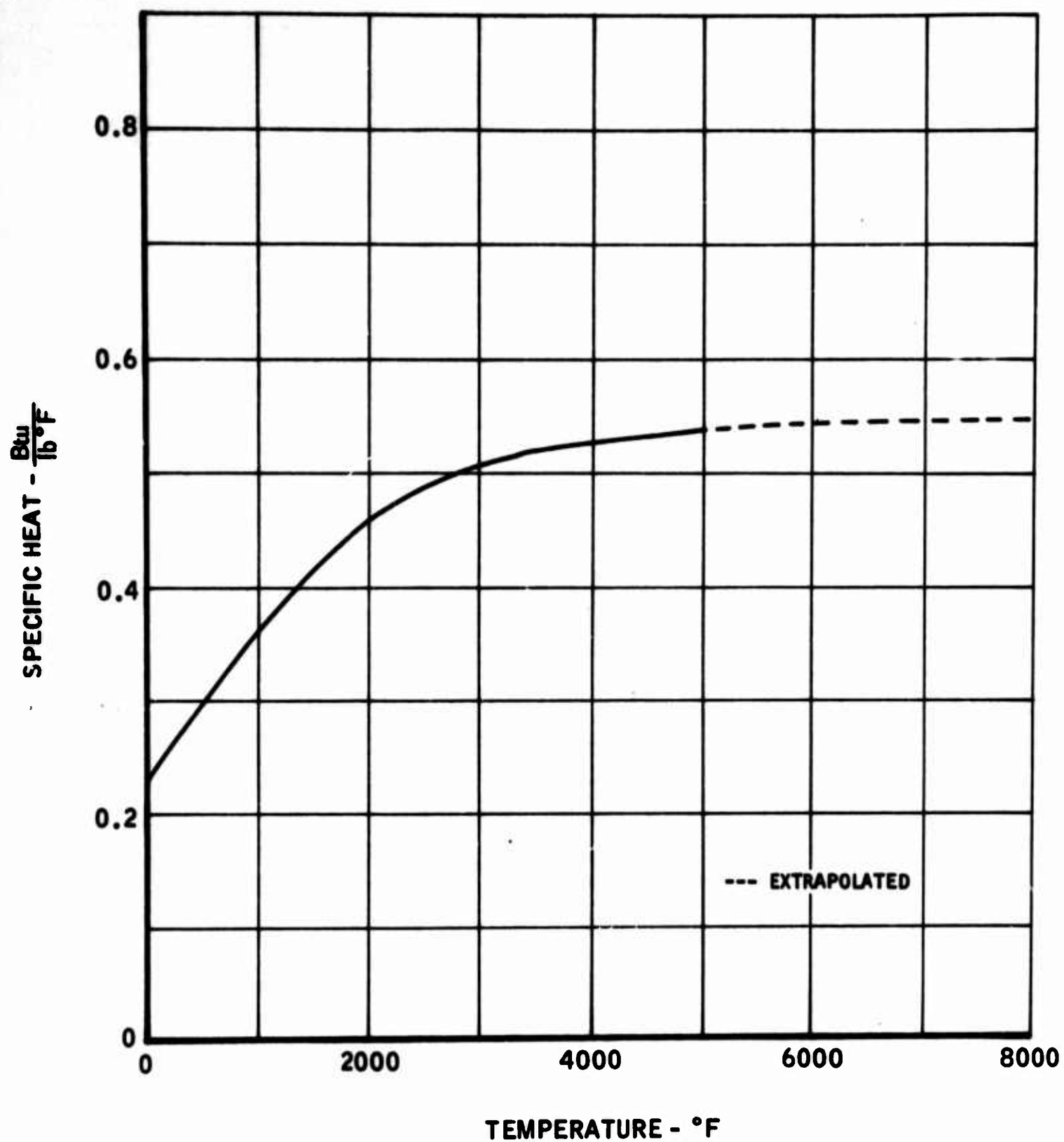


FIGURE 13. Specific Heat for Pyrolytic Graphite, Analysis Standard



UNCLASSIFIED

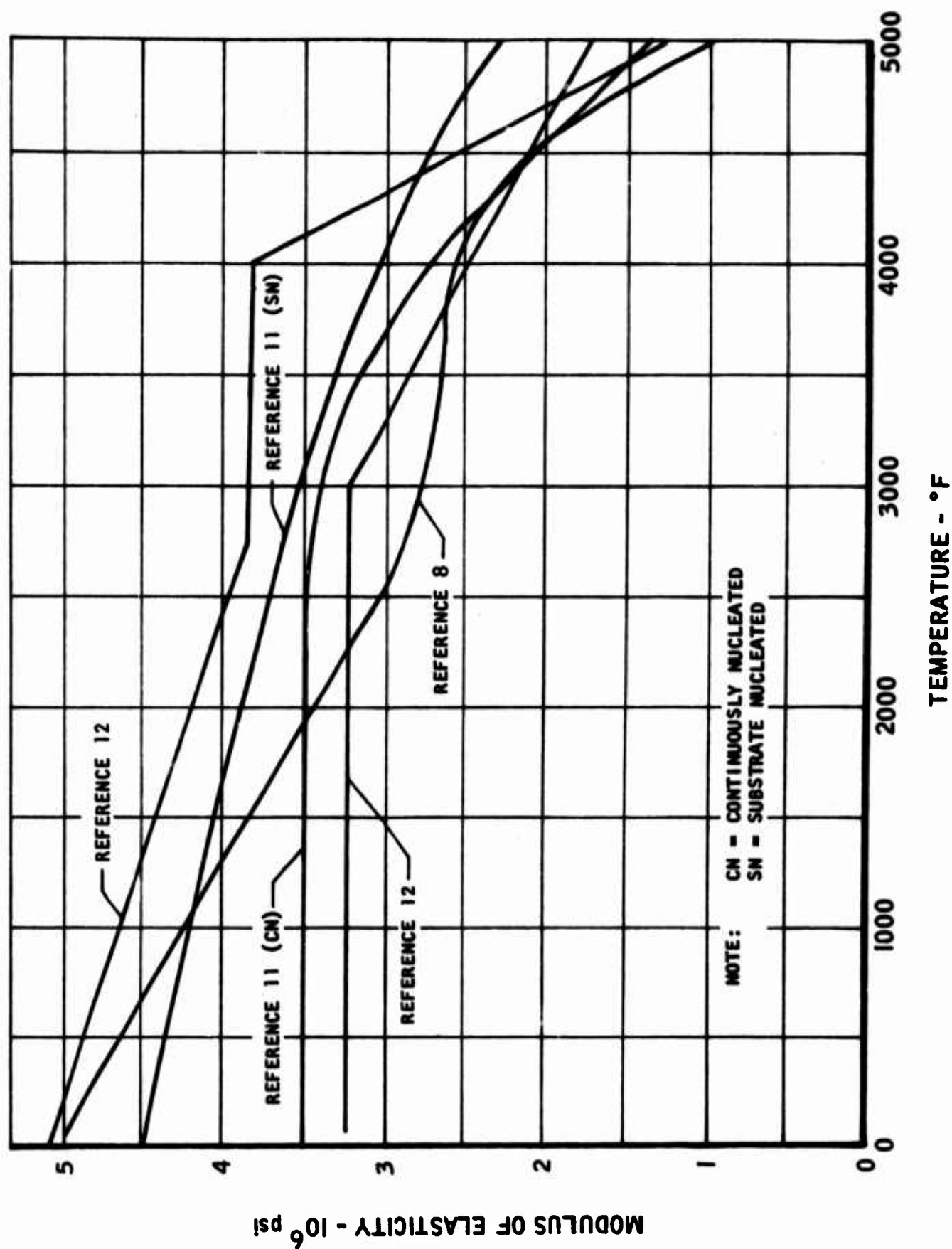


FIGURE 14. Modulus of Elasticity in the a-Direction for Pyrolytic Graphite

UNCLASSIFIED

UNCLASSIFIED

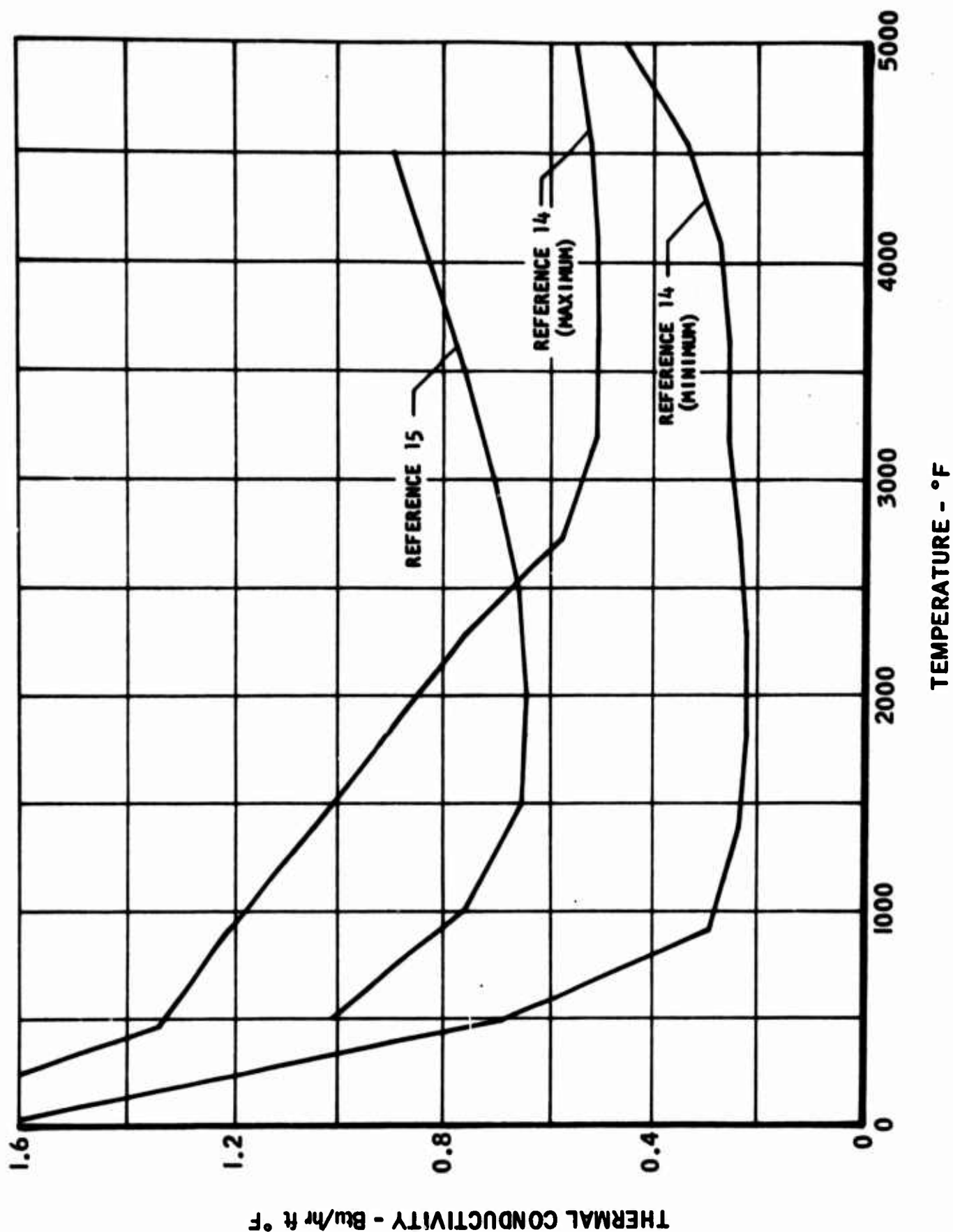


FIGURE 15. Thermal Conductivity in the c-Direction for Pyrolytic Graphite

UNCLASSIFIED

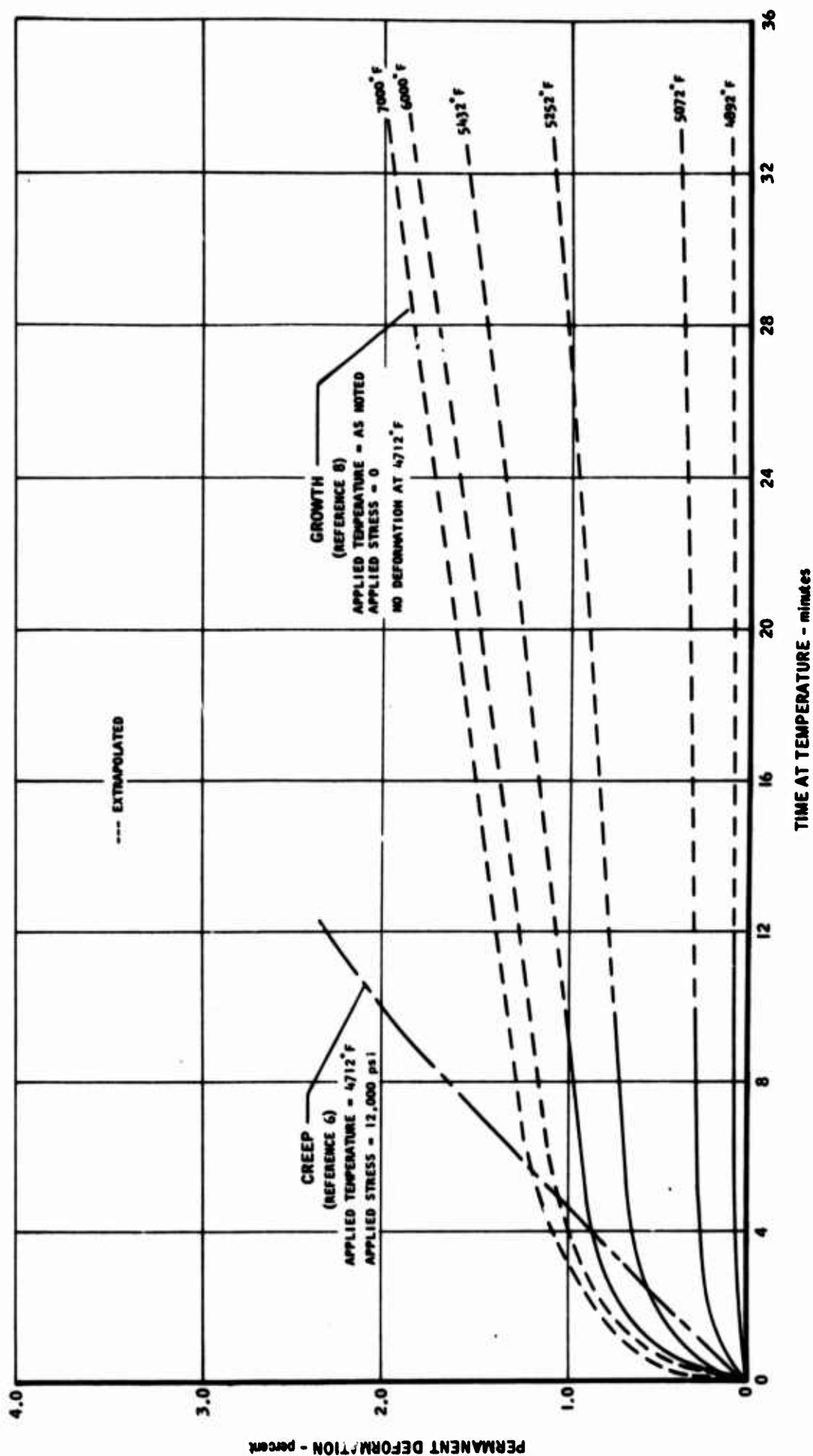


FIGURE 16. Growth and Creep in the a-Direction for Pyrolytic Graphite, Analysis Standard

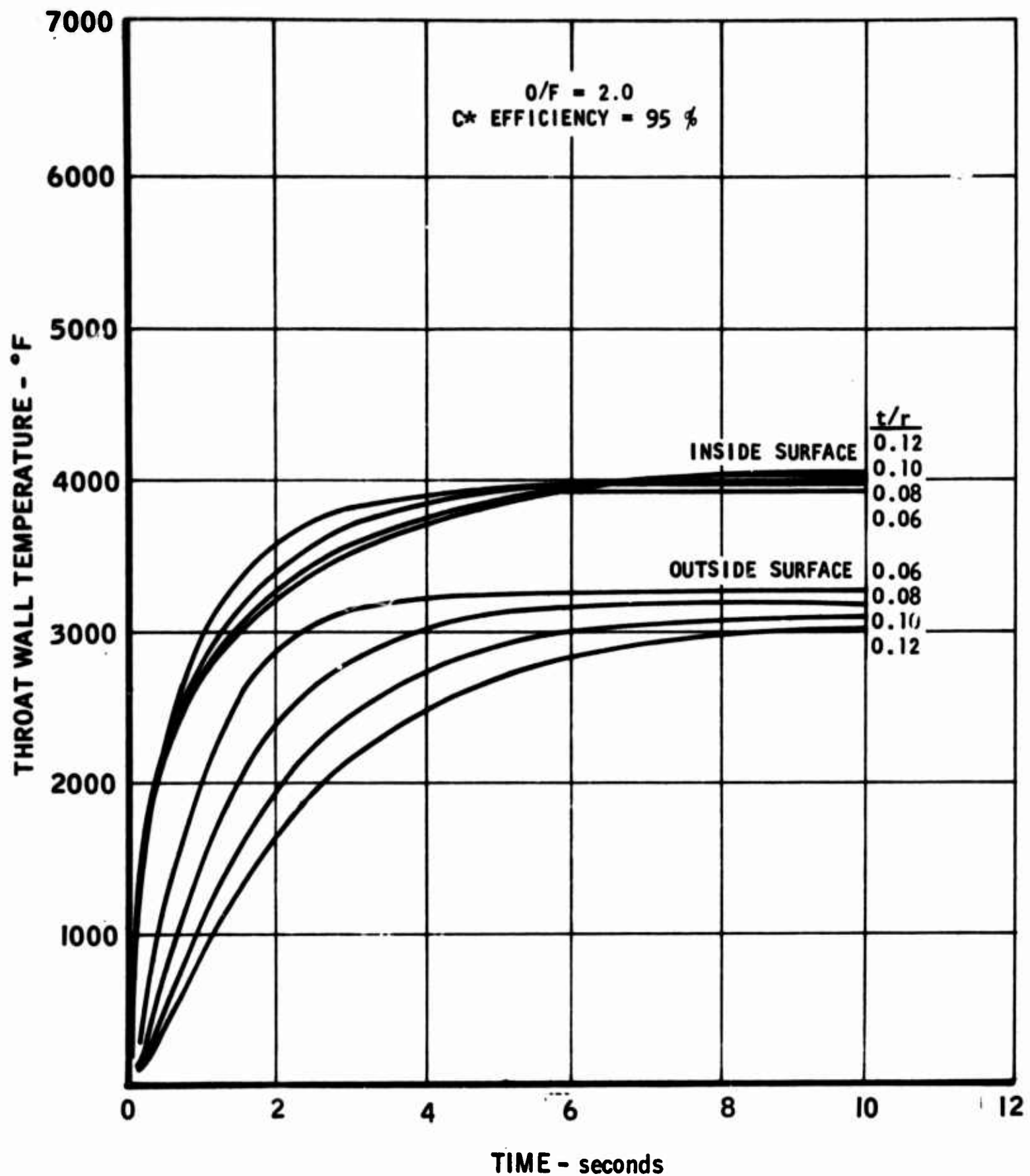


FIGURE 17. Throat Wall Temperature vs. Time, 100-lb Thrust Configuration,  $N_2O_4/0.5 N_2H_4-0.5 UDMH$ ,  $P_c = 50$  psia

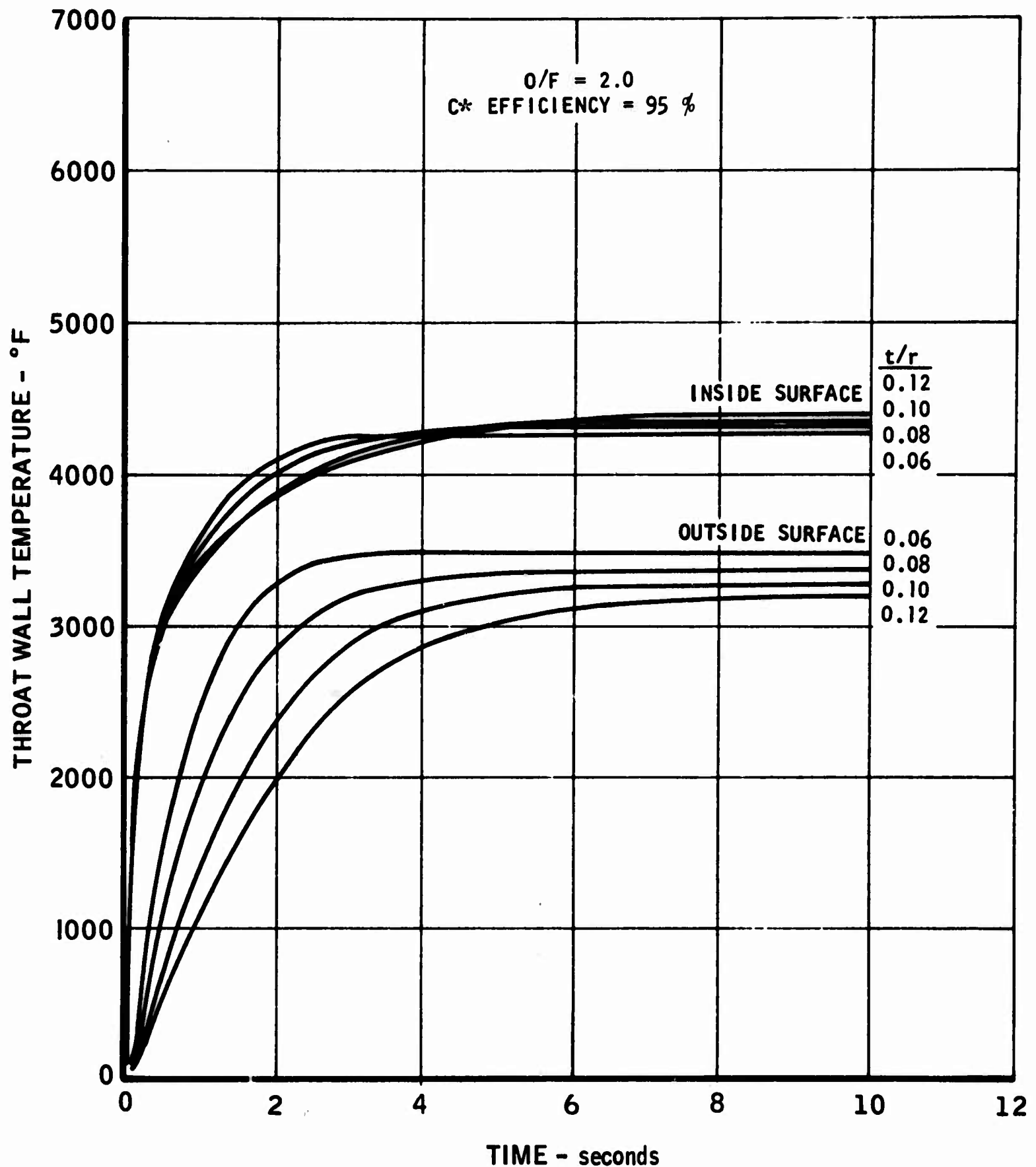


FIGURE 18. Throat Wall Temperature vs. Time, 100-lb Thrust Configuration,  $N_2O_4/0.5 N_2H_4-0.5 UDMH$ ,  $P_c = 100$  psia

UNCLASSIFIED

AFRPL-TR-66-95

Report 6106

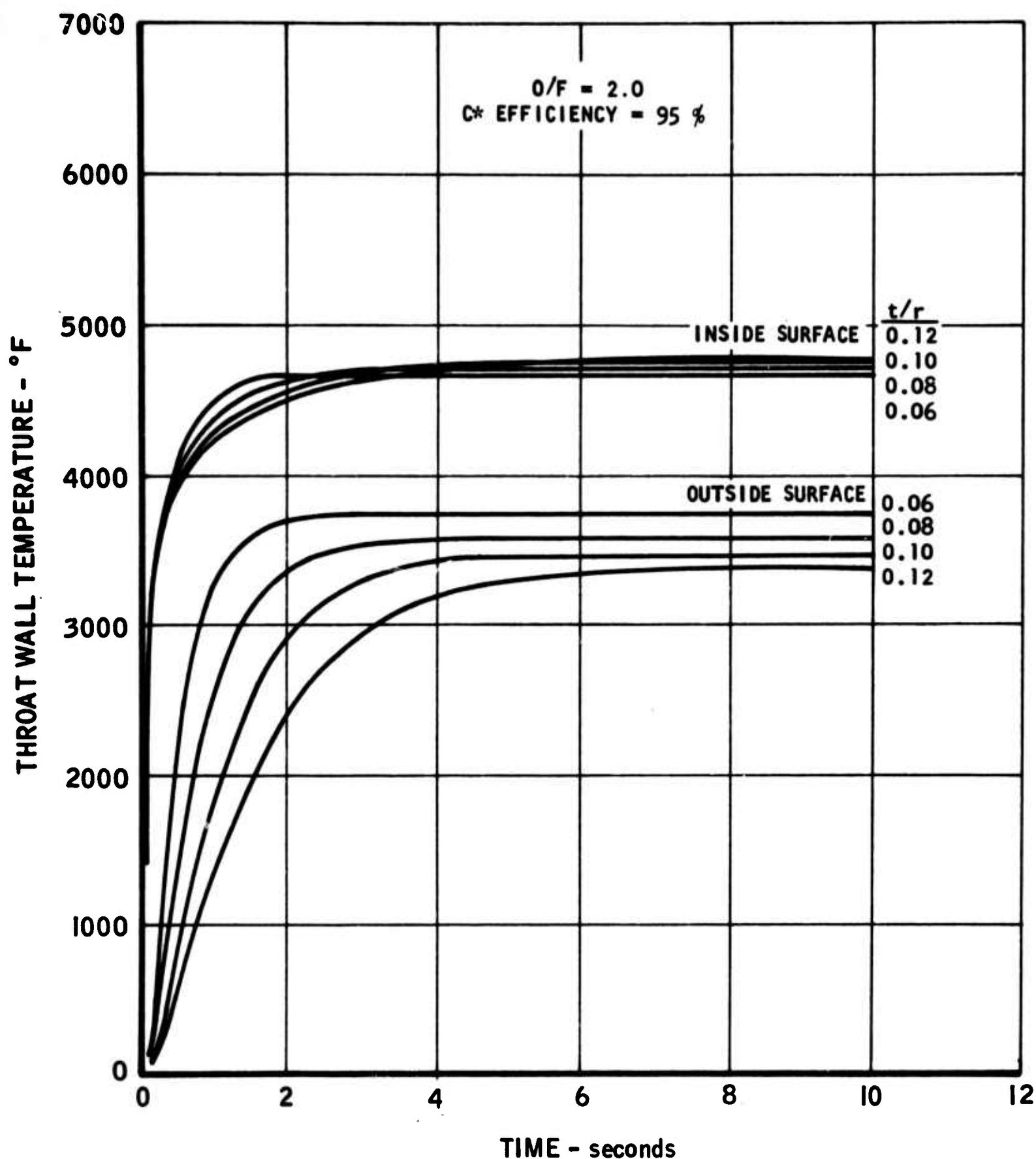


FIGURE 19. Throat Wall Temperature vs. Time, 100-lb Thrust Configuration,  $N_2O_4/0.5 N_2H_4-0.5 UDMH$ ,  $P_c = 300$  psia

5016-127

UNCLASSIFIED



UNCLASSIFIED

AFRPL-TR-66-95

Report 6106

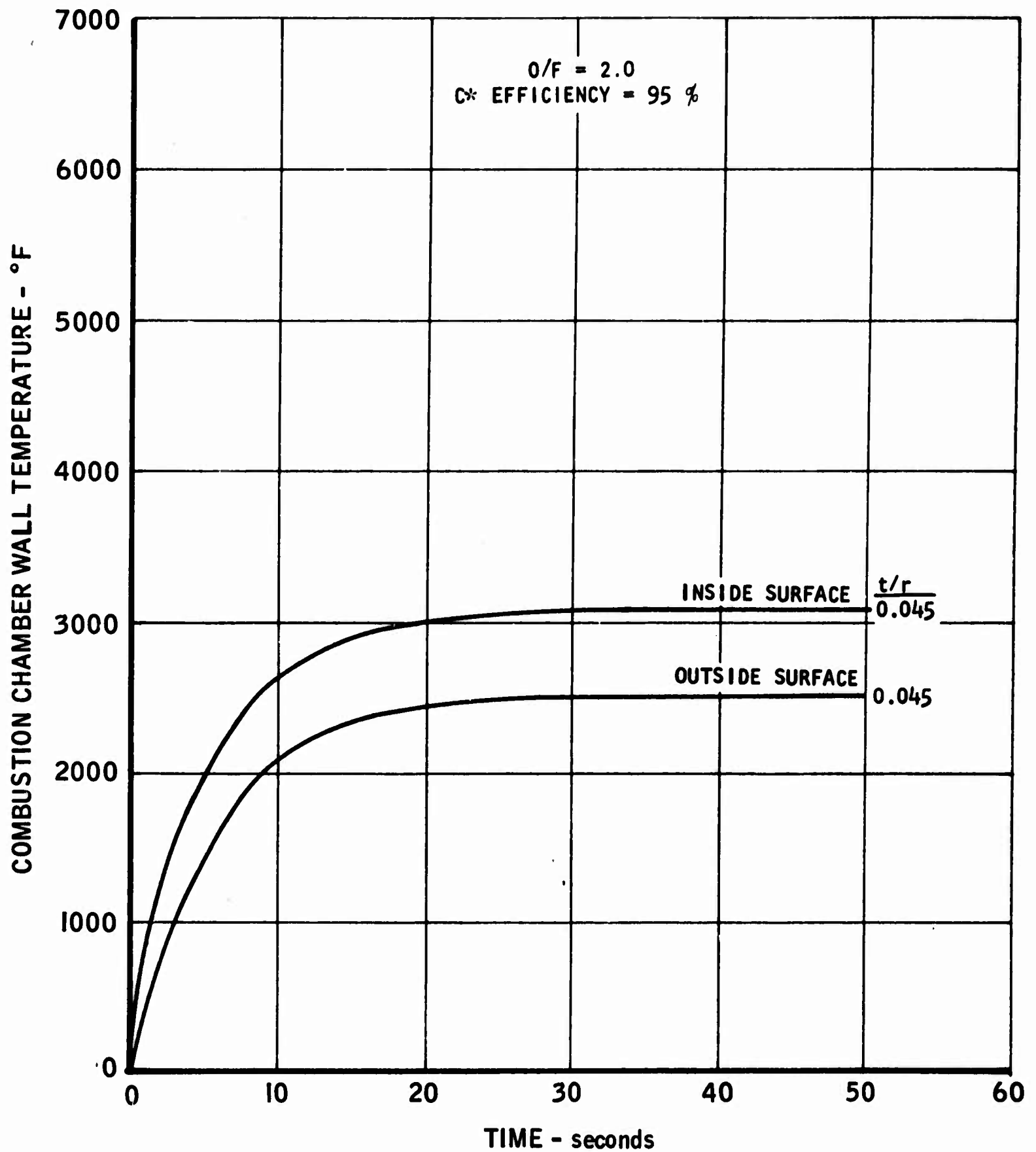


FIGURE 20. Combustion Chamber Wall Temperature vs. Time, 100-lb Thrust Configuration,  $N_2O_4/0.5 N_2H_4 - 0.5 UDMH$ ,  $P_c = 50$  psia

5016-128

UNCLASSIFIED

UNCLASSIFIED

AFRPL-TR-66-95

Report 6106

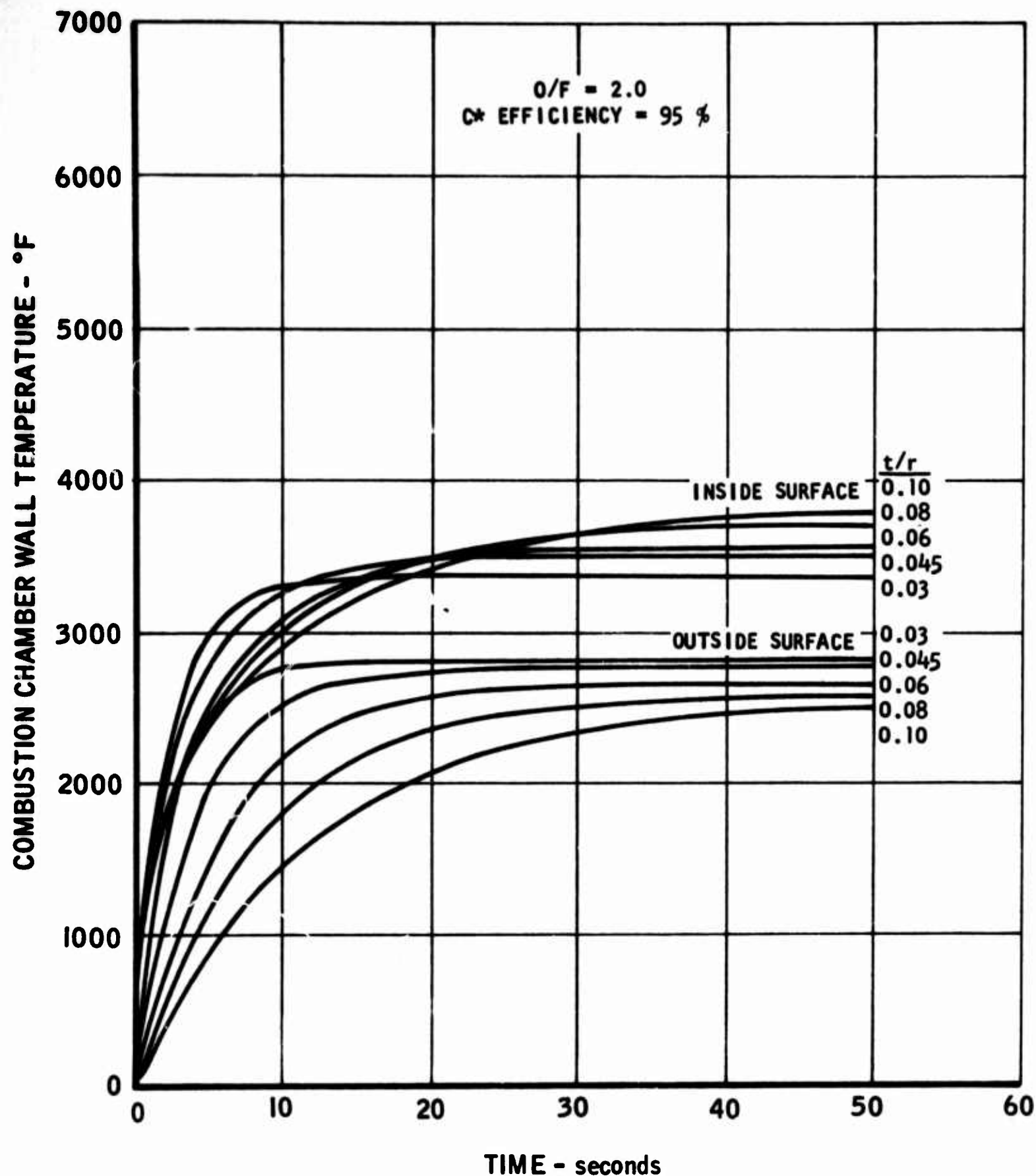


FIGURE 21. Combustion Chamber Wall Temperature vs. Time, 100-lb Thrust Configuration,  $N_2O_4/0.5 N_2H_4-0.5 UDMH$ ,  $P_c = 100$  psia

5016-129

UNCLASSIFIED

# UNCLASSIFIED

AFRPL-TR-66-95

Report 6106

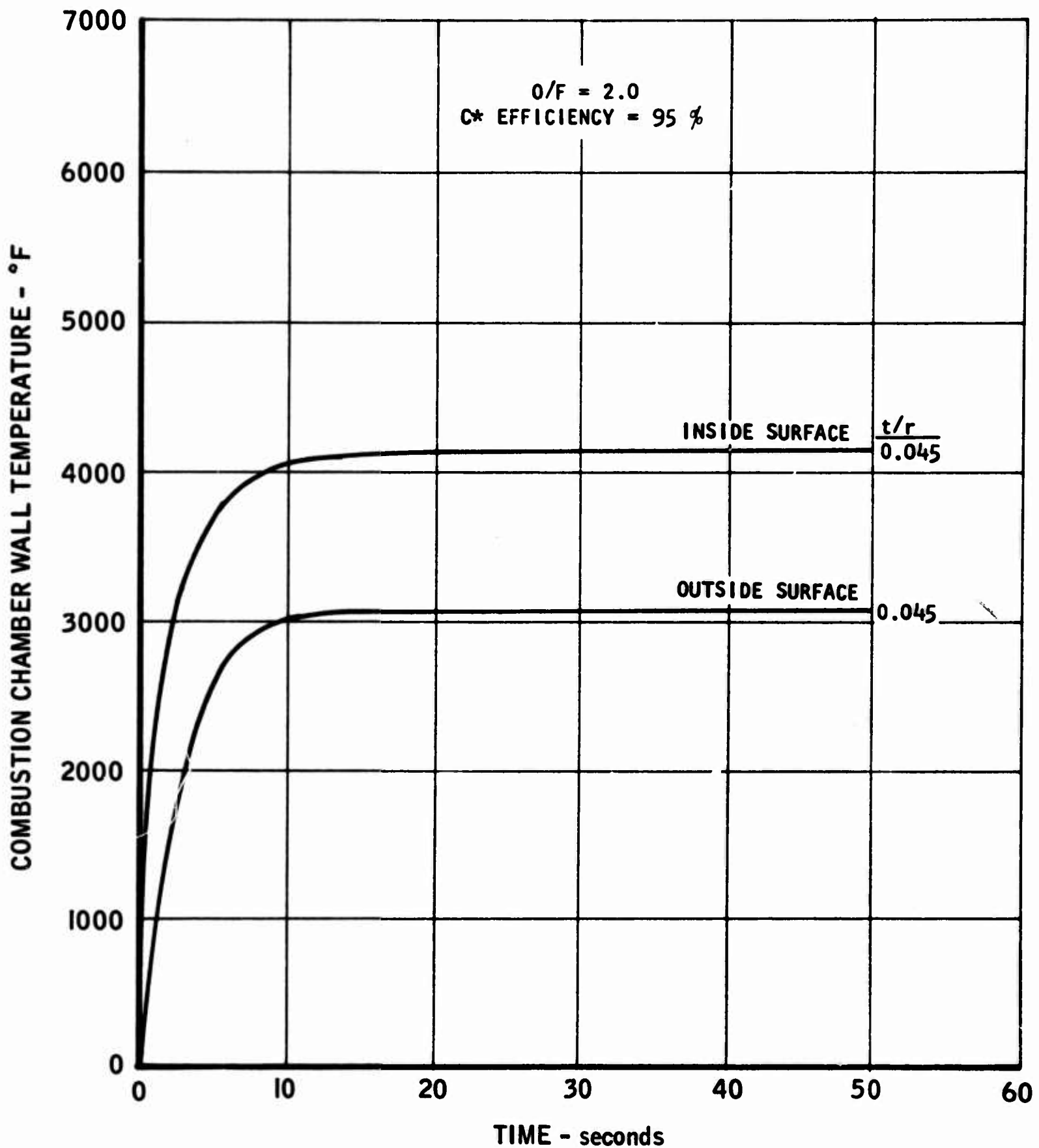


FIGURE 22. Combustion Chamber Wall Temperature vs. Time, 100-lb Thrust Configuration,  $N_2O_4/0.5 N_2H_4-0.5 UDMH$ ,  $P_c = 300$  psia

5016-130

UNCLASSIFIED

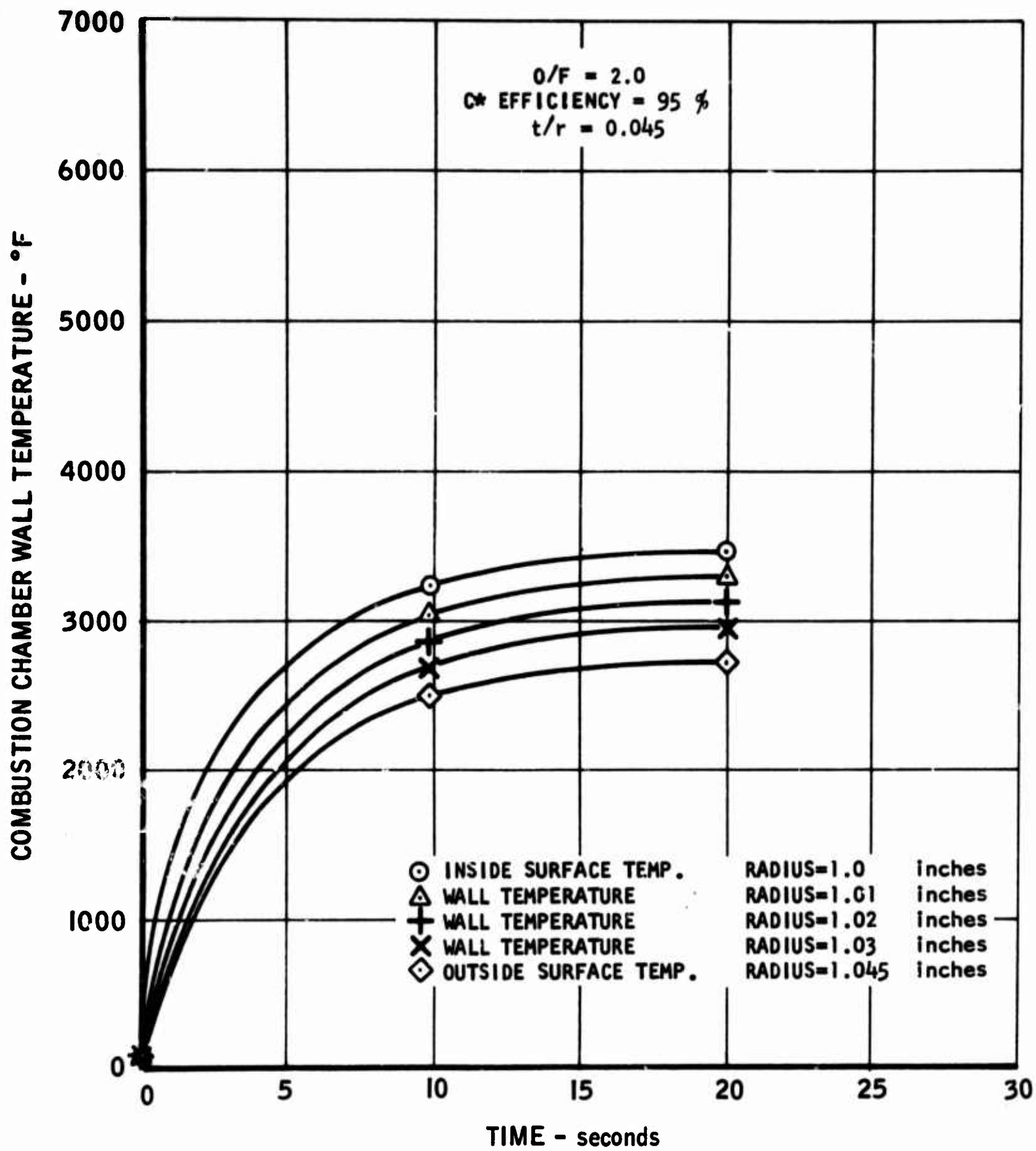


FIGURE 23. Combustion Chamber Wall Temperature Distribution, 100-lb Thrust Configuration,  $N_2O_4/0.5 N_2H_4-0.5 UDMH$ ,  $P_c = 100$  psia

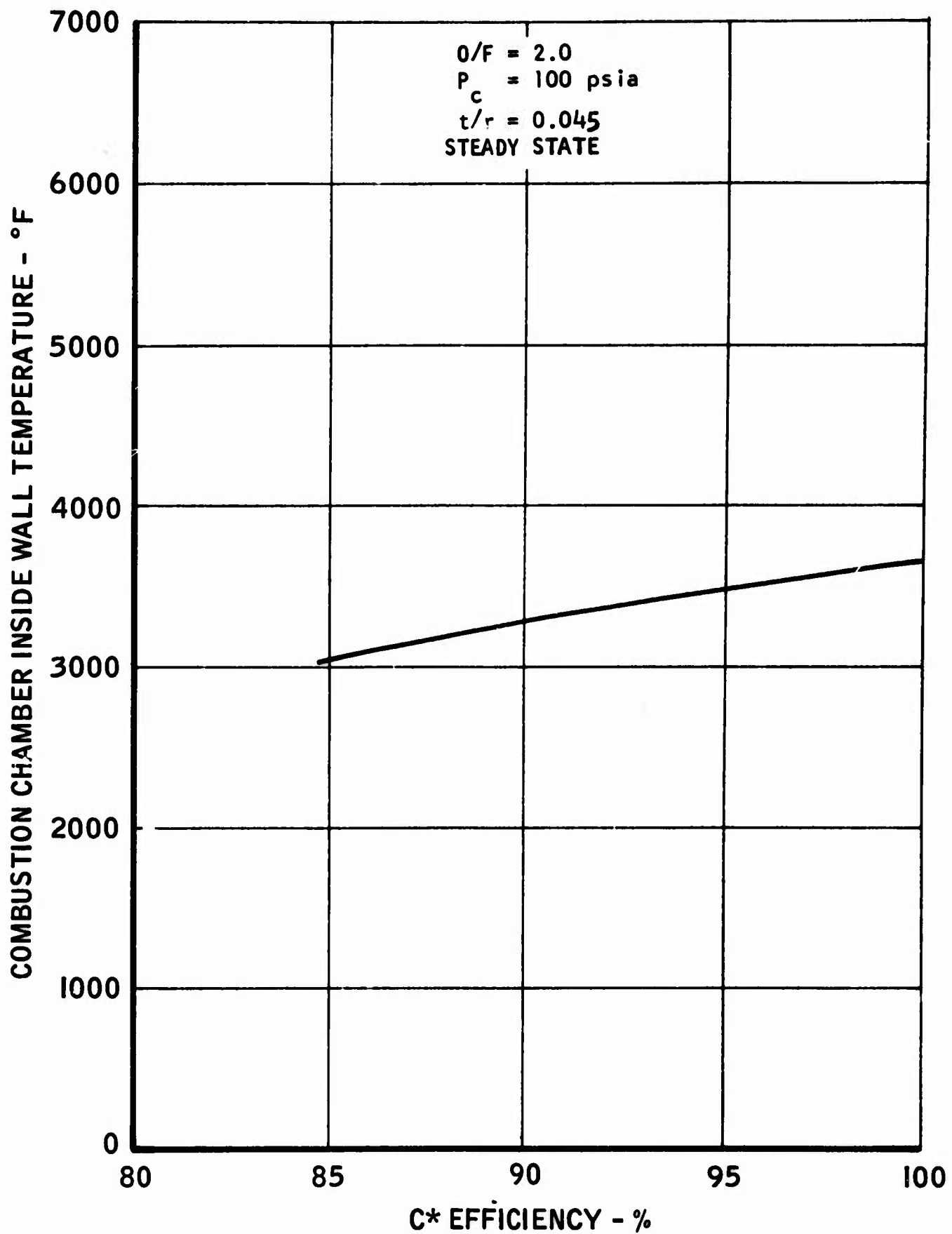


FIGURE 24. Combustion Chamber Inside Wall Temperature vs. C\* Efficiency, 100-lb Thrust Configuration,  $N_2O_4/0.5 N_2H_4-0.5$  UDMH

UNCLASSIFIED

AFRPL-TR-66-95

Report 6106

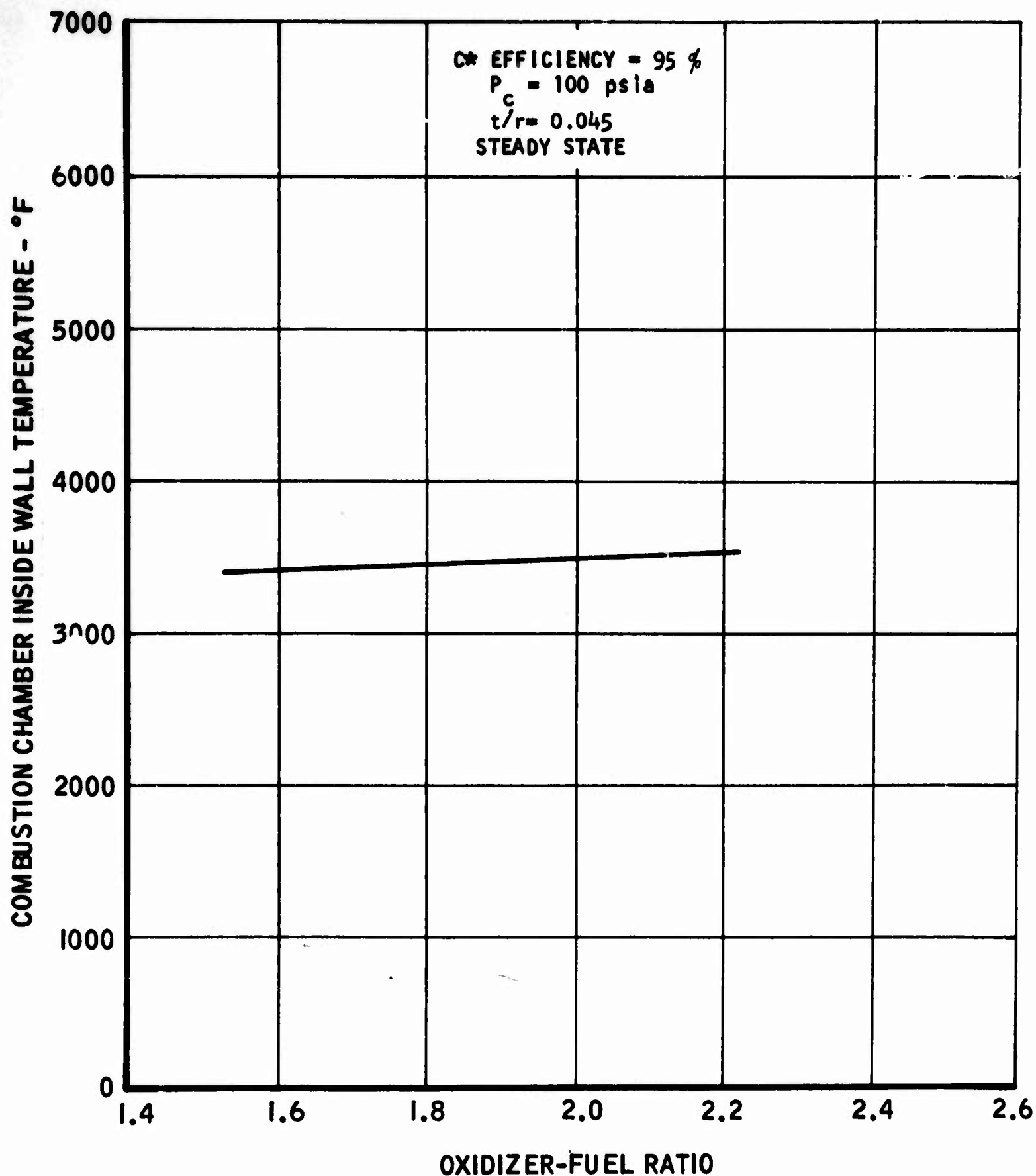


FIGURE 25. Combustion Chamber Inside Wall Temperature vs. Oxidizer-Fuel Ratio, 100-lb Thrust Configuration,  $N_2O_4/0.5 N_2H_4-0.5$  UDMH

5016-133

UNCLASSIFIED

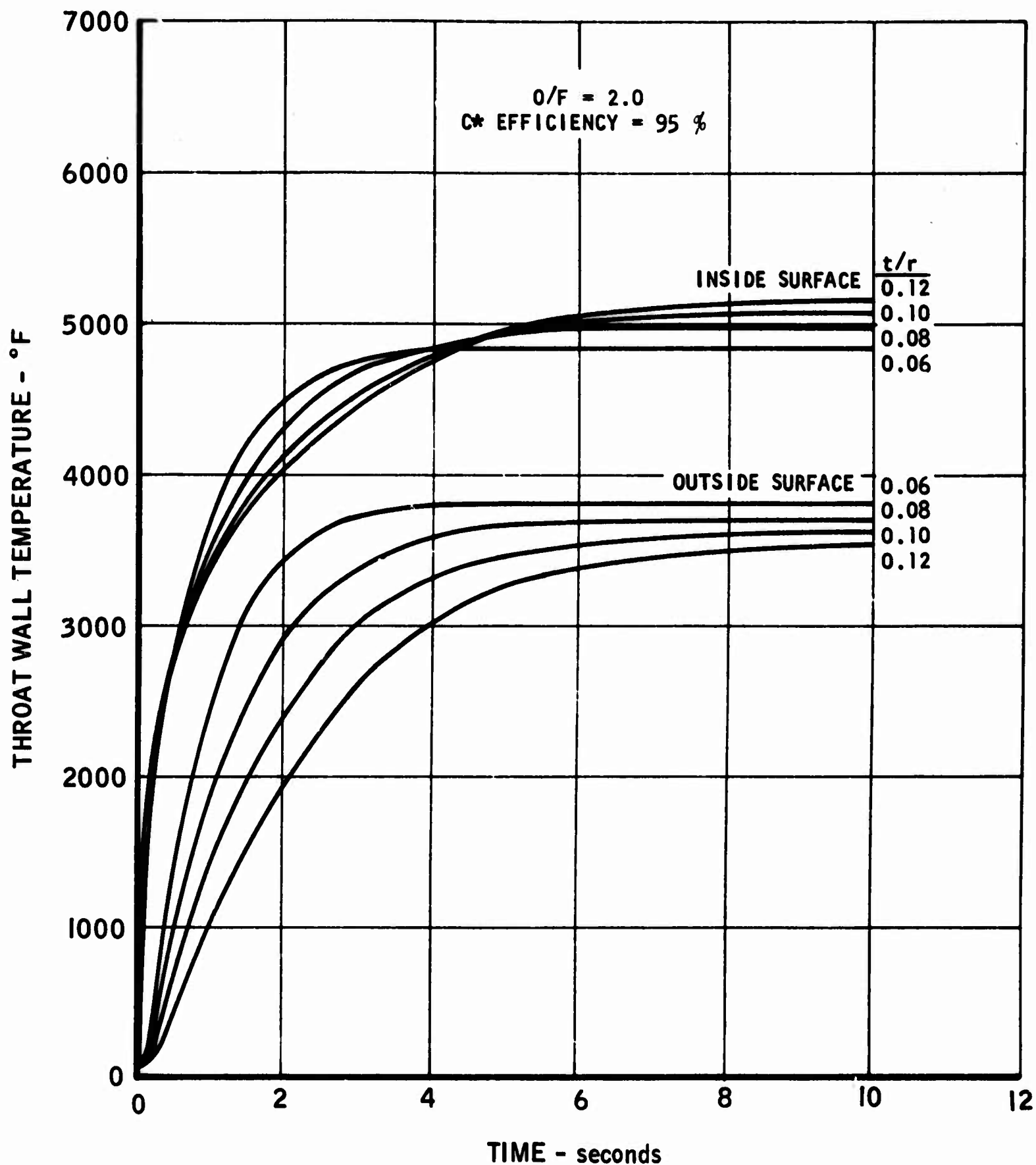


FIGURE 26. Throat Wall Temperature vs. Time, 100-lb Thrust Configuration,  
 $F_2/BA1014$ ,  $P_c = 50$  psia



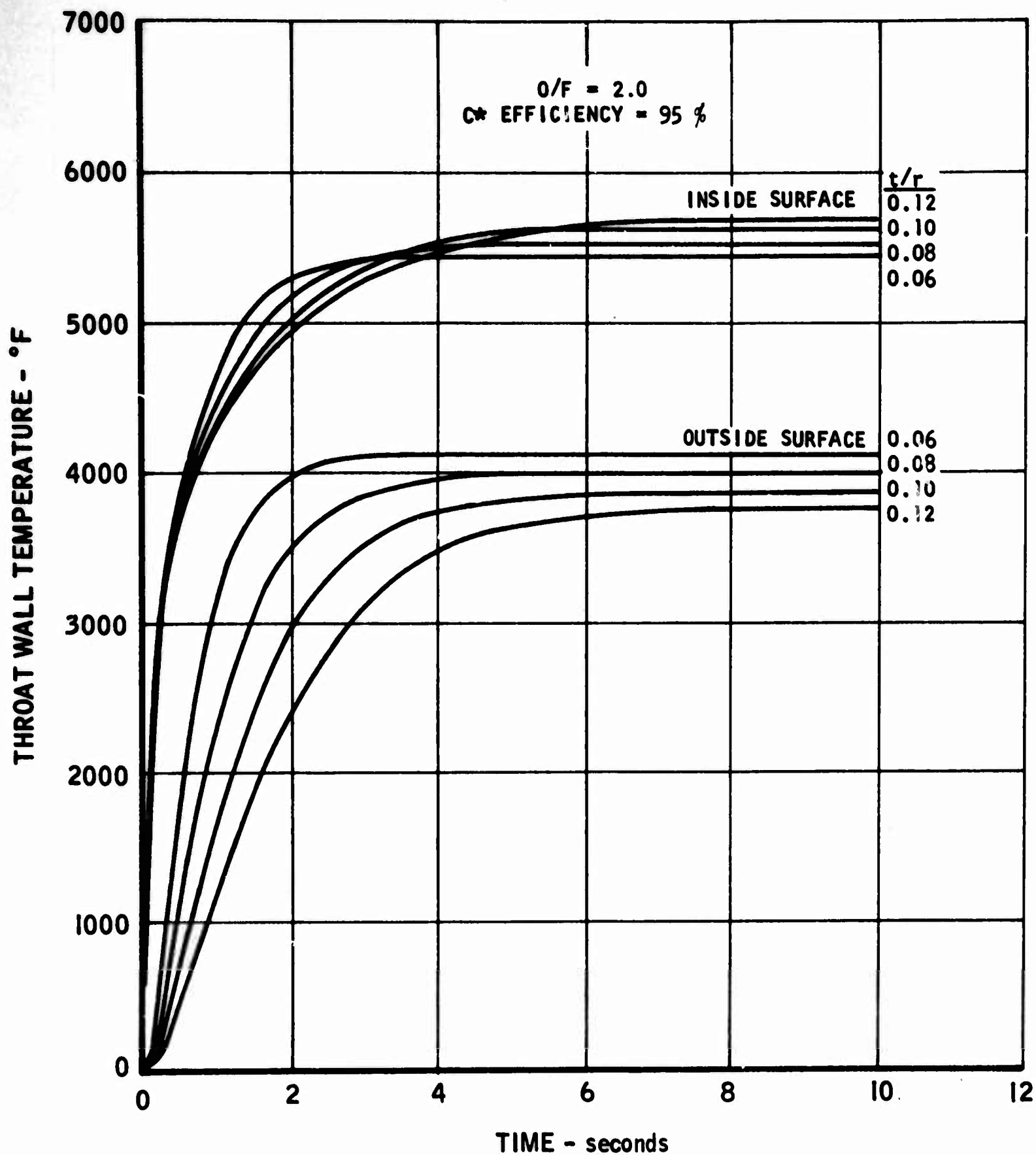


FIGURE 27. Throat Wall Temperature vs. Time, 100-lb Thrust Configuration,  
 $F_2/BA1014$ ,  $P_c = 100$  psia

UNCLASSIFIED

AFRPL-TR-66-95

Report 6106

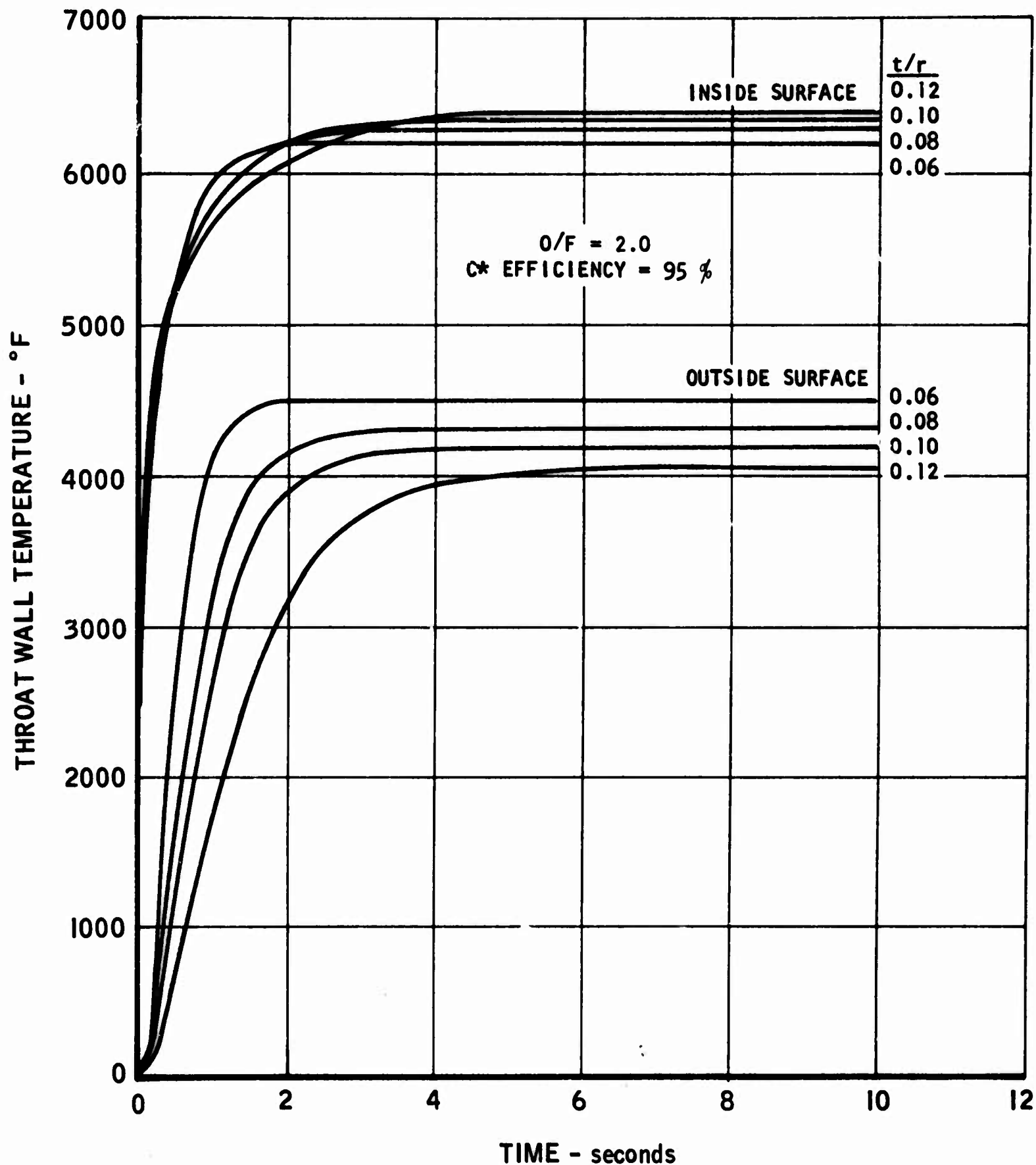


FIGURE 28. Throat Wall Temperature vs. Time, 100-lb Thrust Configuration,  $F_2/BA1014$ ,  $P_c = 300$  psia

5016-136

UNCLASSIFIED

UNCLASSIFIED

AFRPL-TR-66-95

Report 6106

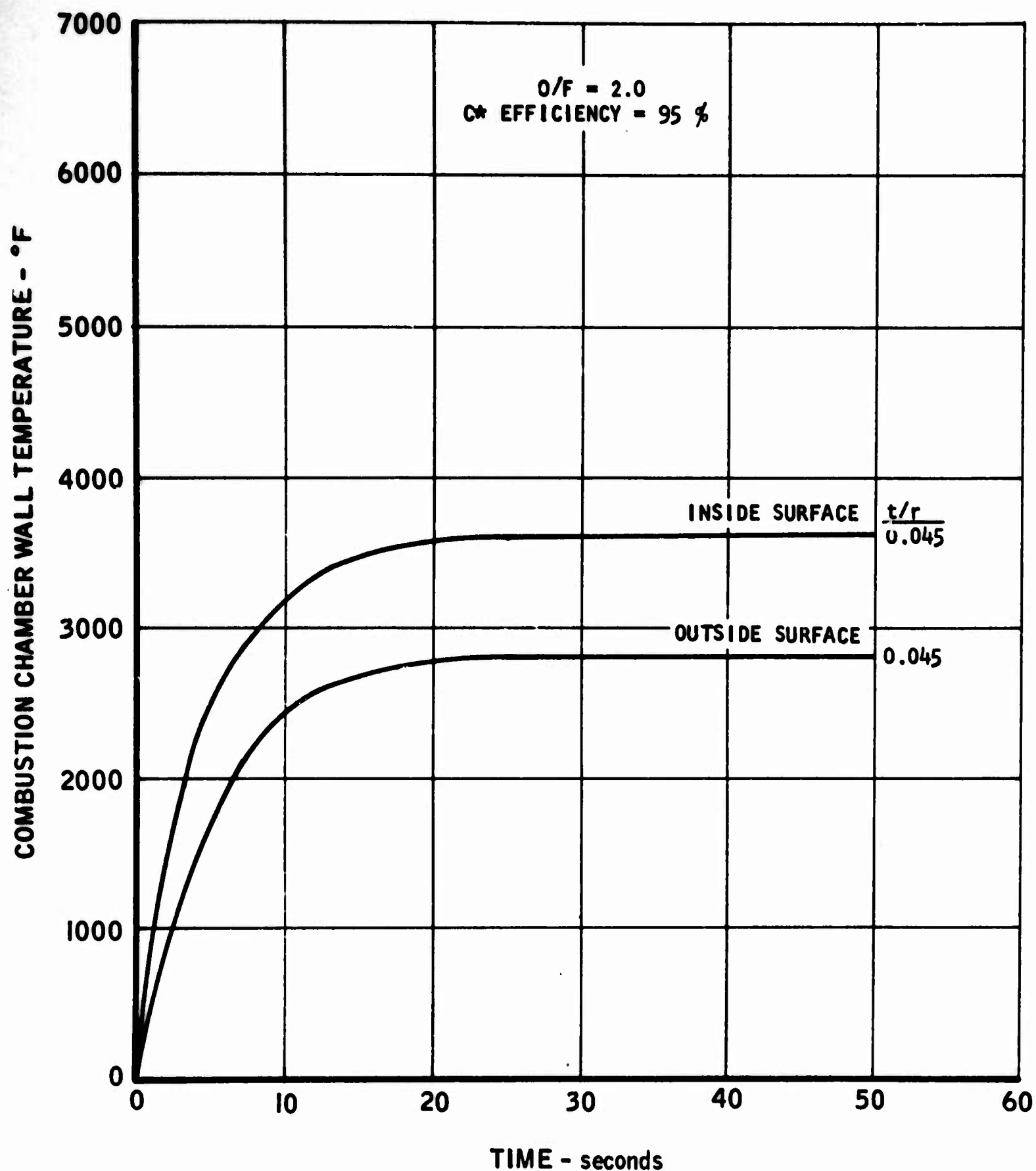


FIGURE 29. Combustion Chamber Wall Temperature vs. Time, 100-lb Thrust Configuration,  $F_2/BA1014$ ,  $P_c = 50$  psia

5016-137

UNCLASSIFIED

# UNCLASSIFIED

AFRPL-TR-66-95

Report 6106

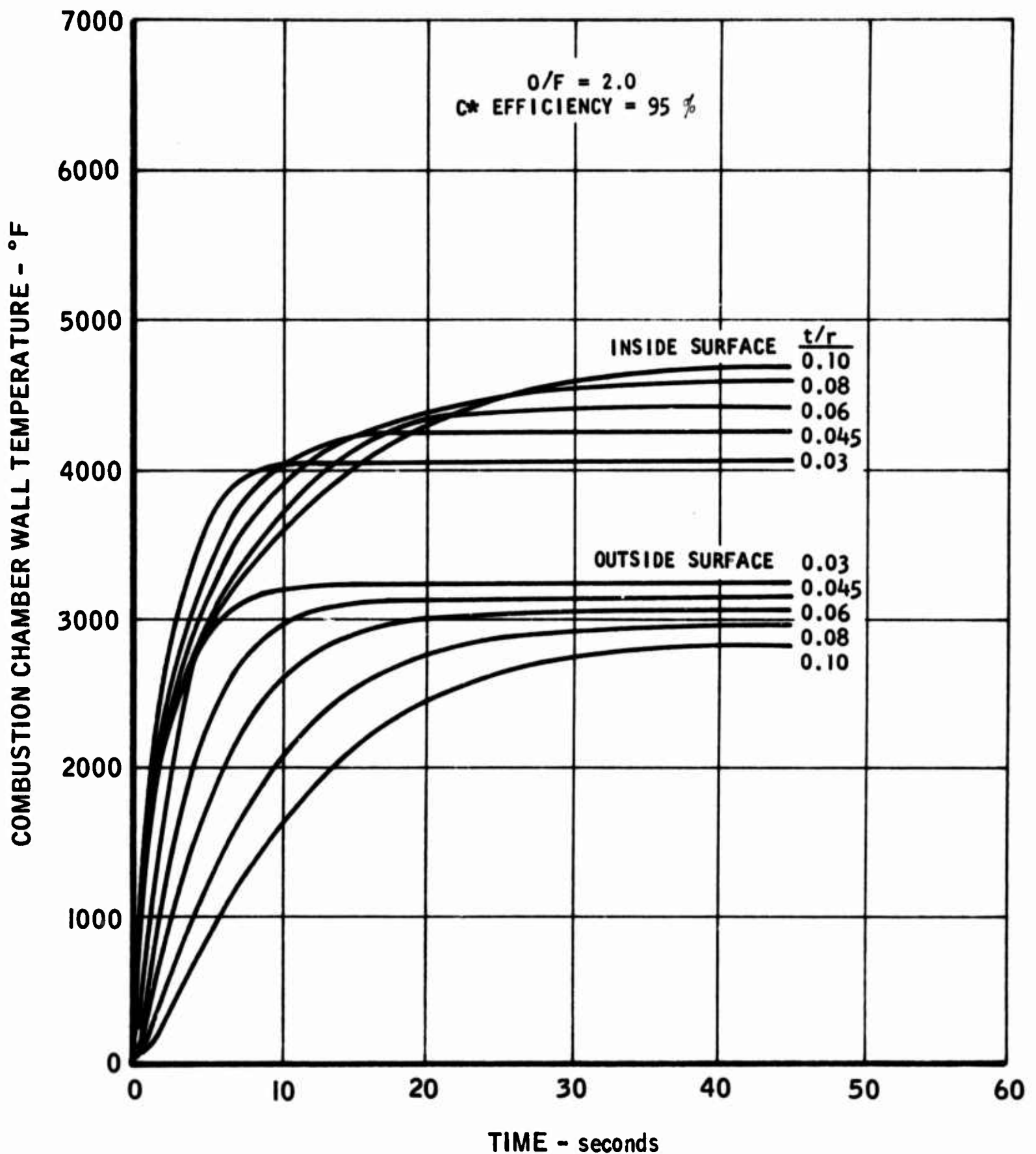


FIGURE 30. Combustion Chamber Wall Temperature vs. Time, 100-lb Thrust Configuration,  $F_2/BA1014$ ,  $P_c = 100$  psia

5016-138

UNCLASSIFIED

# UNCLASSIFIED

AFRPL-TR-66-95

Report 6106

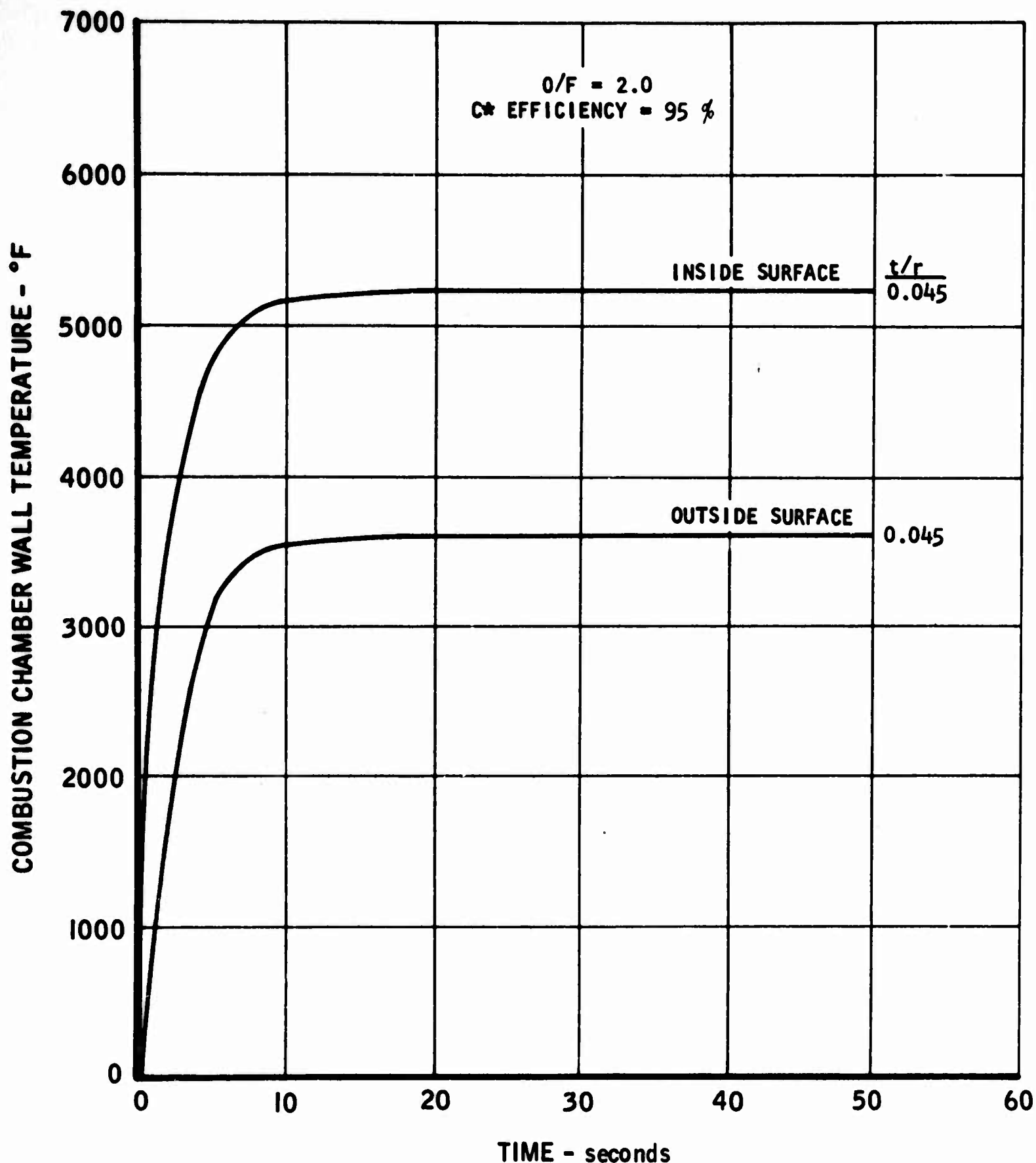


FIGURE 31. Combustion Chamber Wall Temperature vs. Time, 100-lb Thrust Configuration,  $F_2/BA1014$ ,  $P_c = 300$  psia

5016-139

UNCLASSIFIED

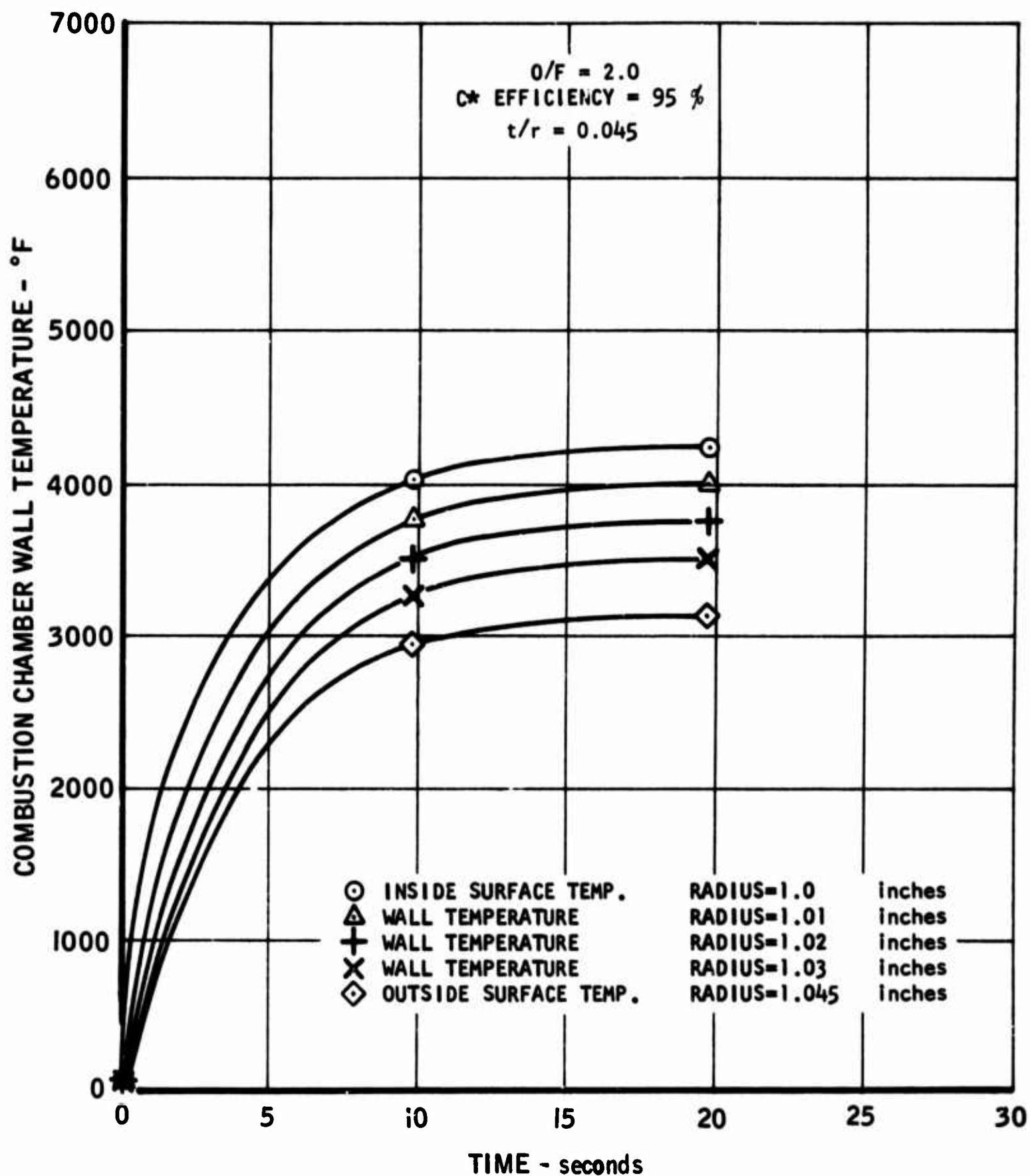


FIGURE 32. Combustion Chamber Wall Temperature Distribution, 100-lb Thrust Configuration,  $F_2/BA1014$ ,  $P_c = 100$  psia

UNCLASSIFIED

AFRPL-TR-66-95

Report 6106

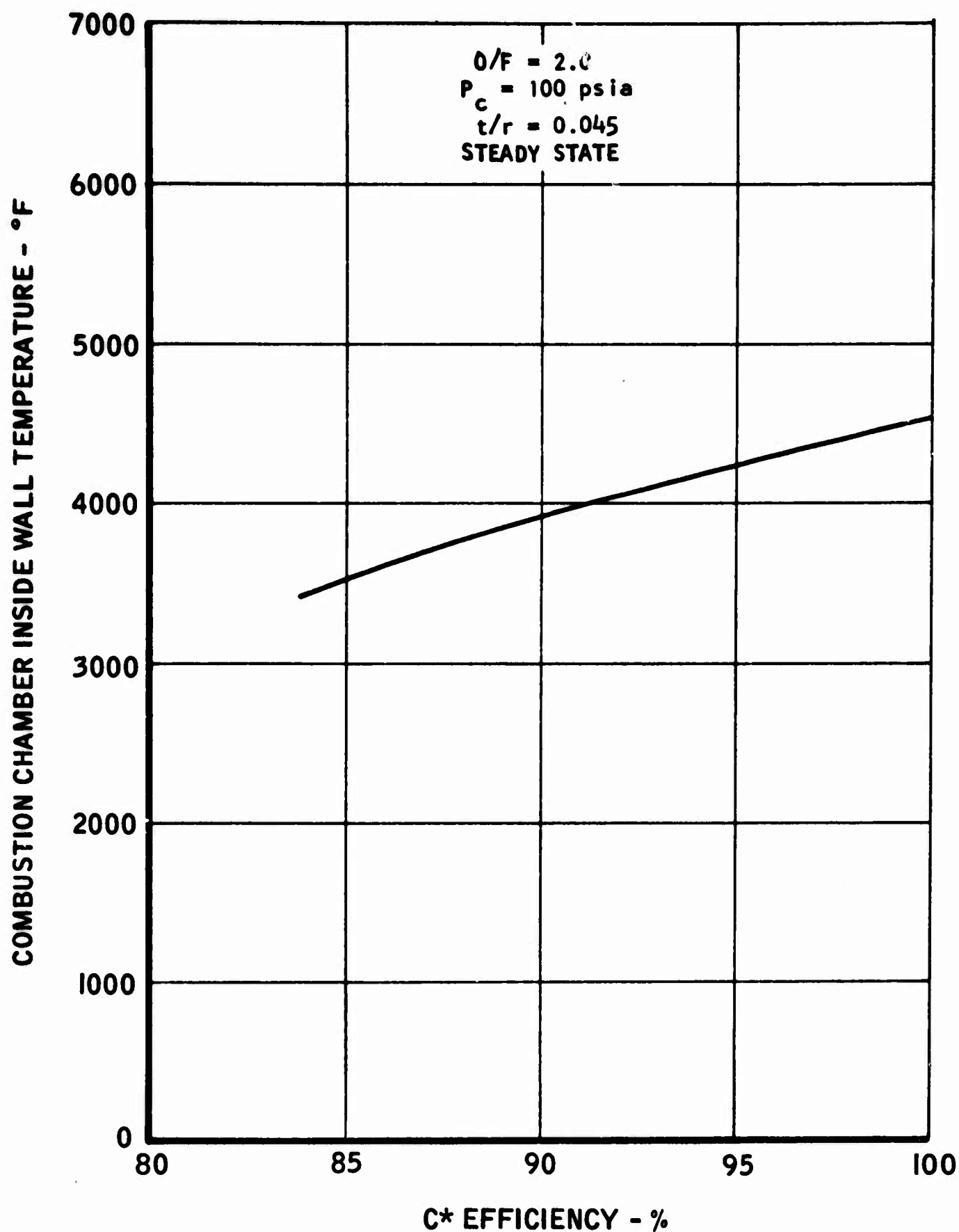


FIGURE 33. Combustion Chamber Inside Wall Temperature vs. C\* Efficiency, 100-lb Thrust Configuration,  $F_2/BA1014$

5016-141

UNCLASSIFIED



UNCLASSIFIED

AFRPL-TR-66-95

Report 6106

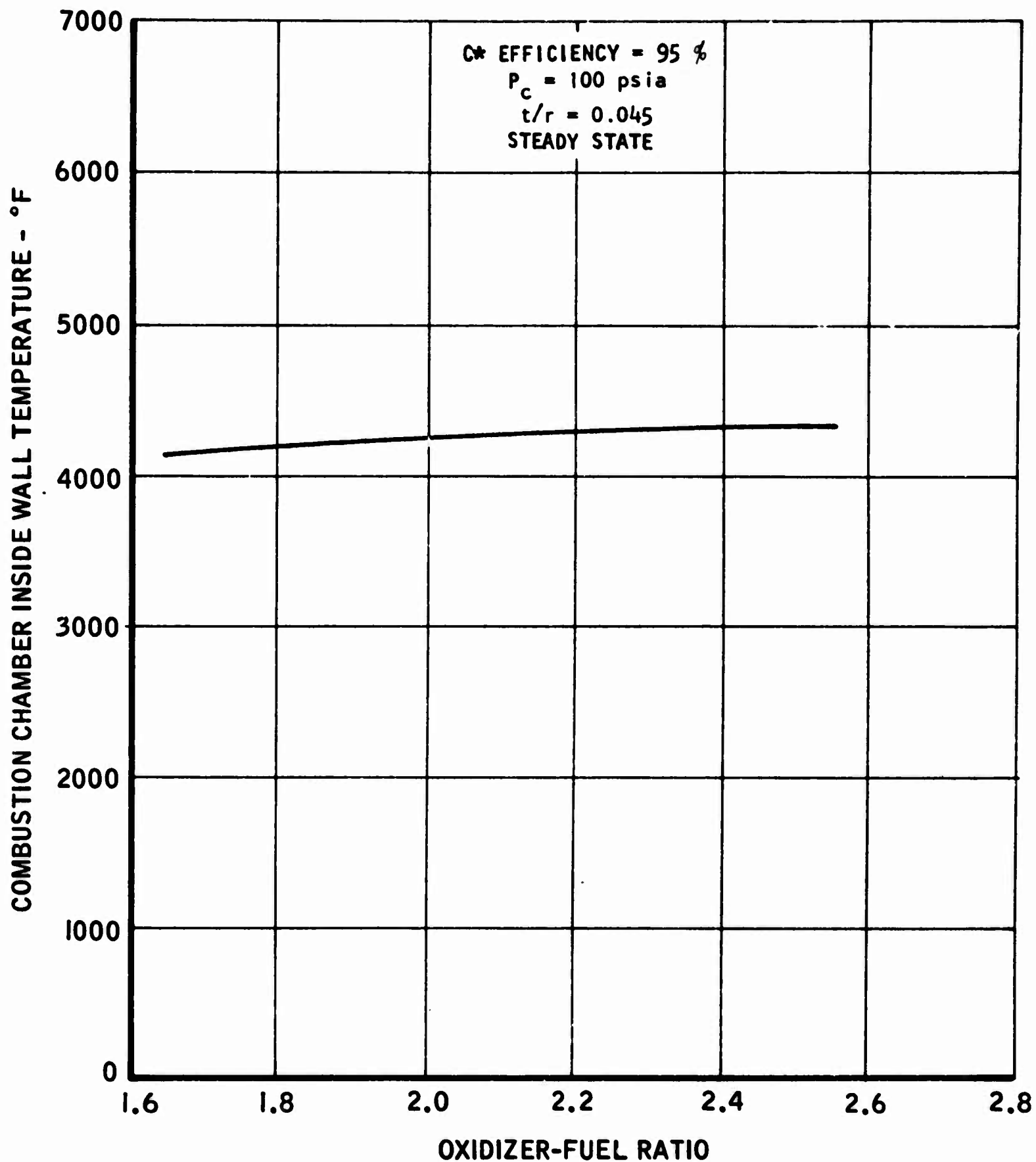


FIGURE 34. Combustion Chamber Inside Wall Temperature vs. Oxidizer-Fuel Ratio, 100-lb Thrust Configuration,  $F_2/BA1014$

5016-142

UNCLASSIFIED

# UNCLASSIFIED

AFRPL-TR-66-95

Report 6106

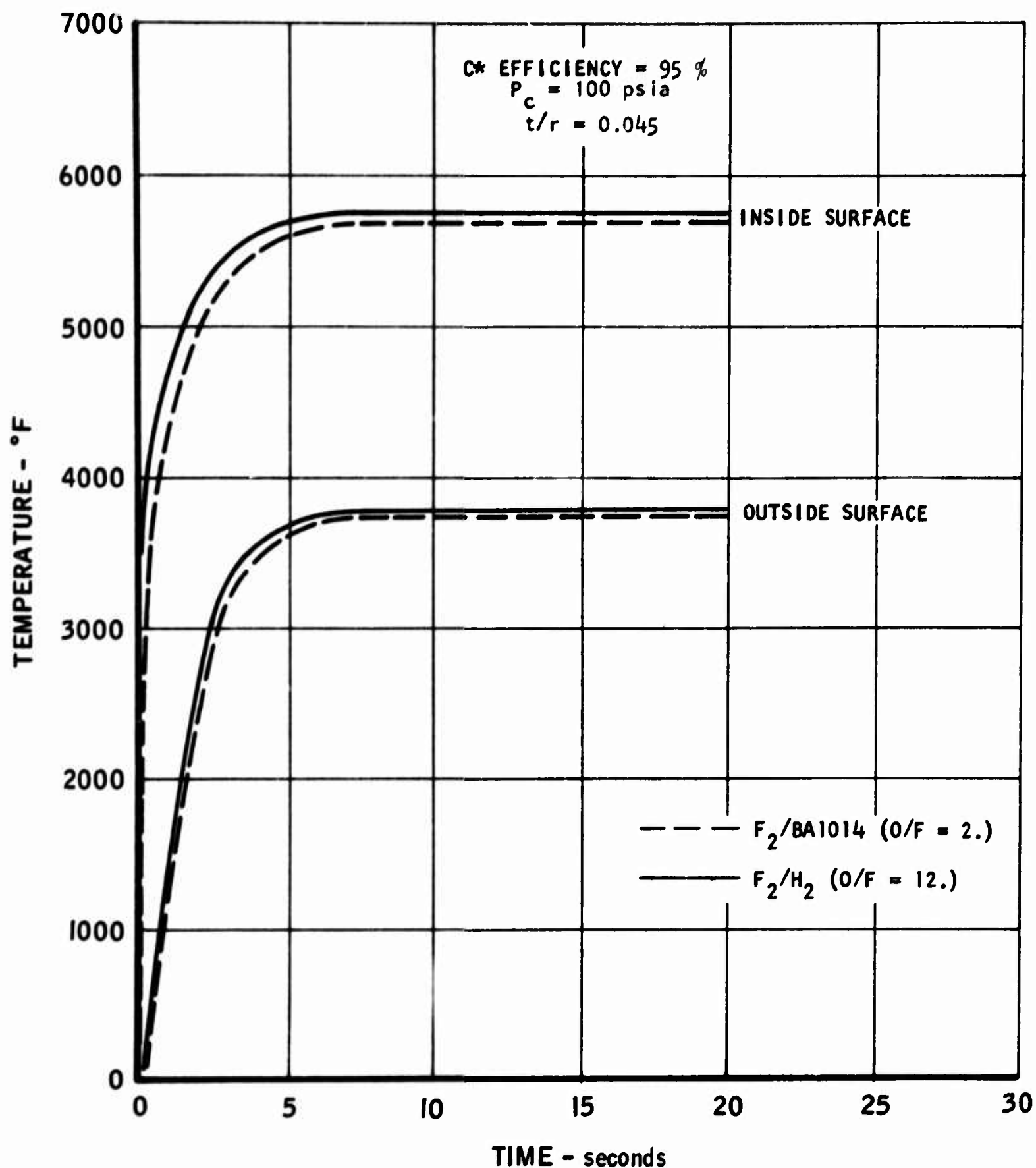


FIGURE 35. Throat Wall Temperature Comparison, 100-lb Thrust Configuration,  $F_2/BA1014$  and  $F_2/H_2$

5016-143

UNCLASSIFIED

# UNCLASSIFIED

AFRPL-TR-66-95

Report 6106

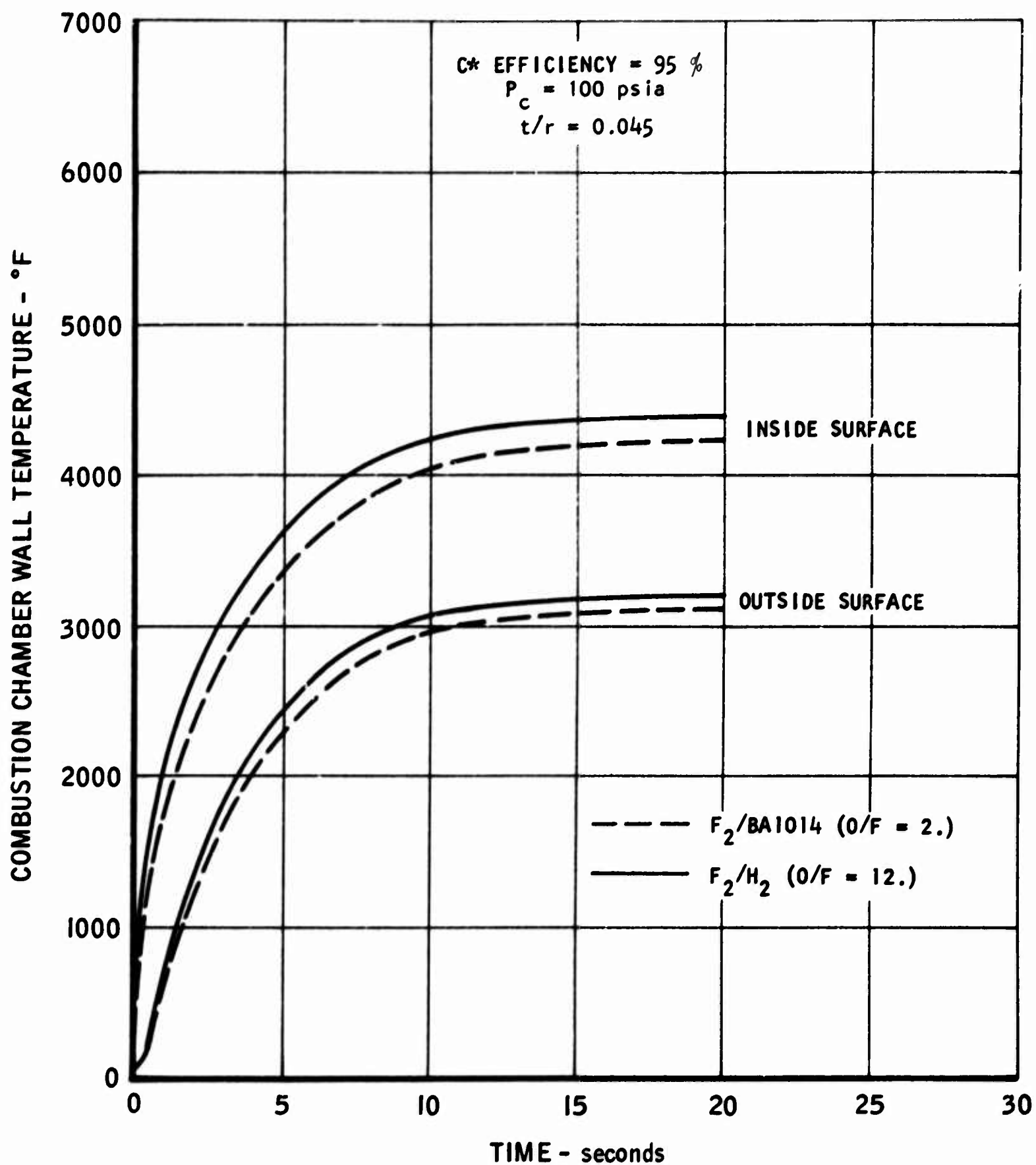


FIGURE 36. Combustion Chamber Wall Temperature Comparison, 100-lb Thrust Configuration,  $F_2/BA1014$  and  $F_2/H_2$

5016-144

UNCLASSIFIED

UNCLASSIFIED

AFRPL-TR-66-95

Report 6106

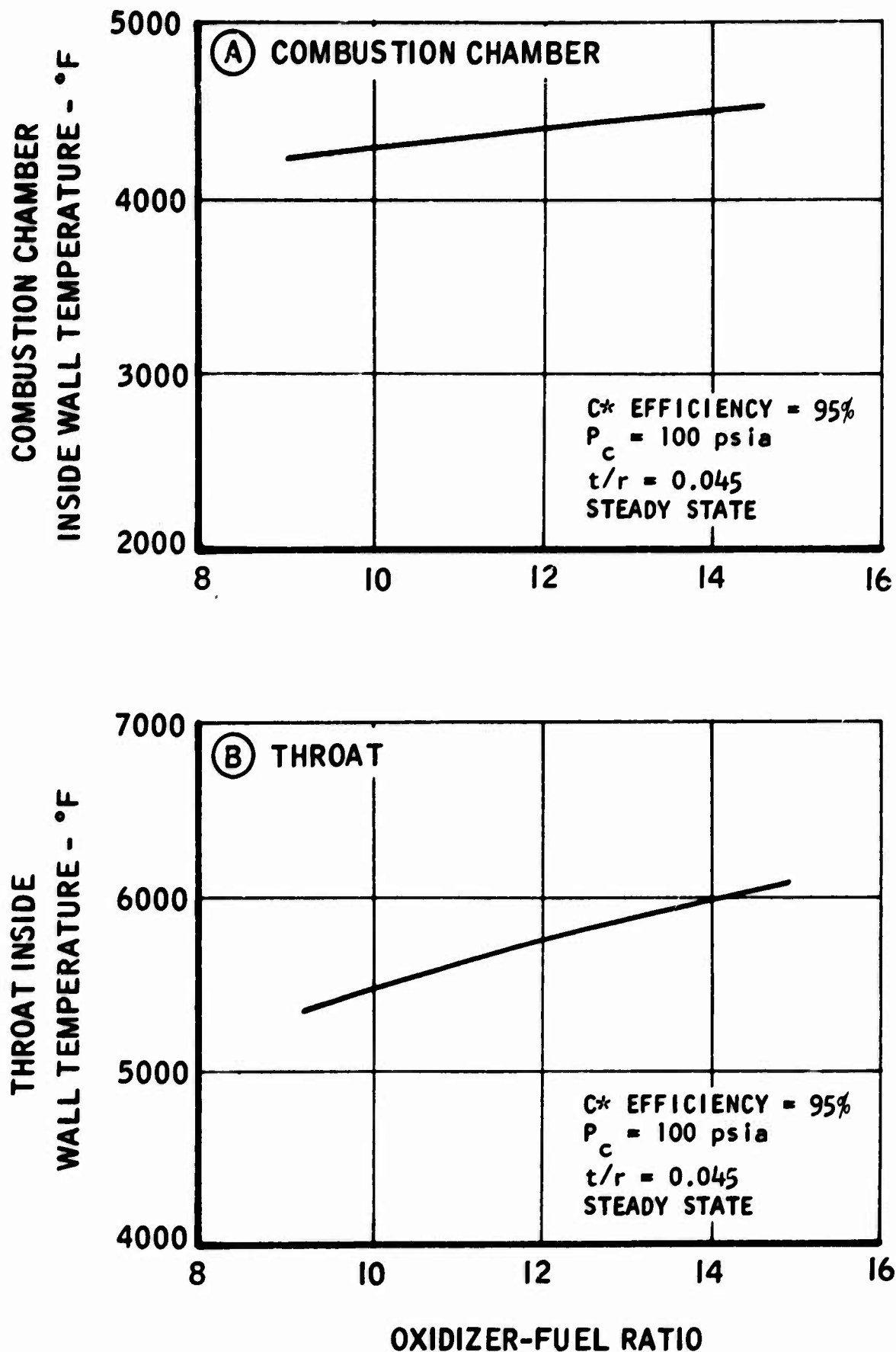


FIGURE 37. Combustion Chamber and Throat Inside Wall Temperatures vs. Oxidizer-Fuel Ratio, 100-lb Thrust Configuration,  $F_2/H_2$

5016-145

UNCLASSIFIED

# UNCLASSIFIED

AFRPL-TR-66-95

Report 6106

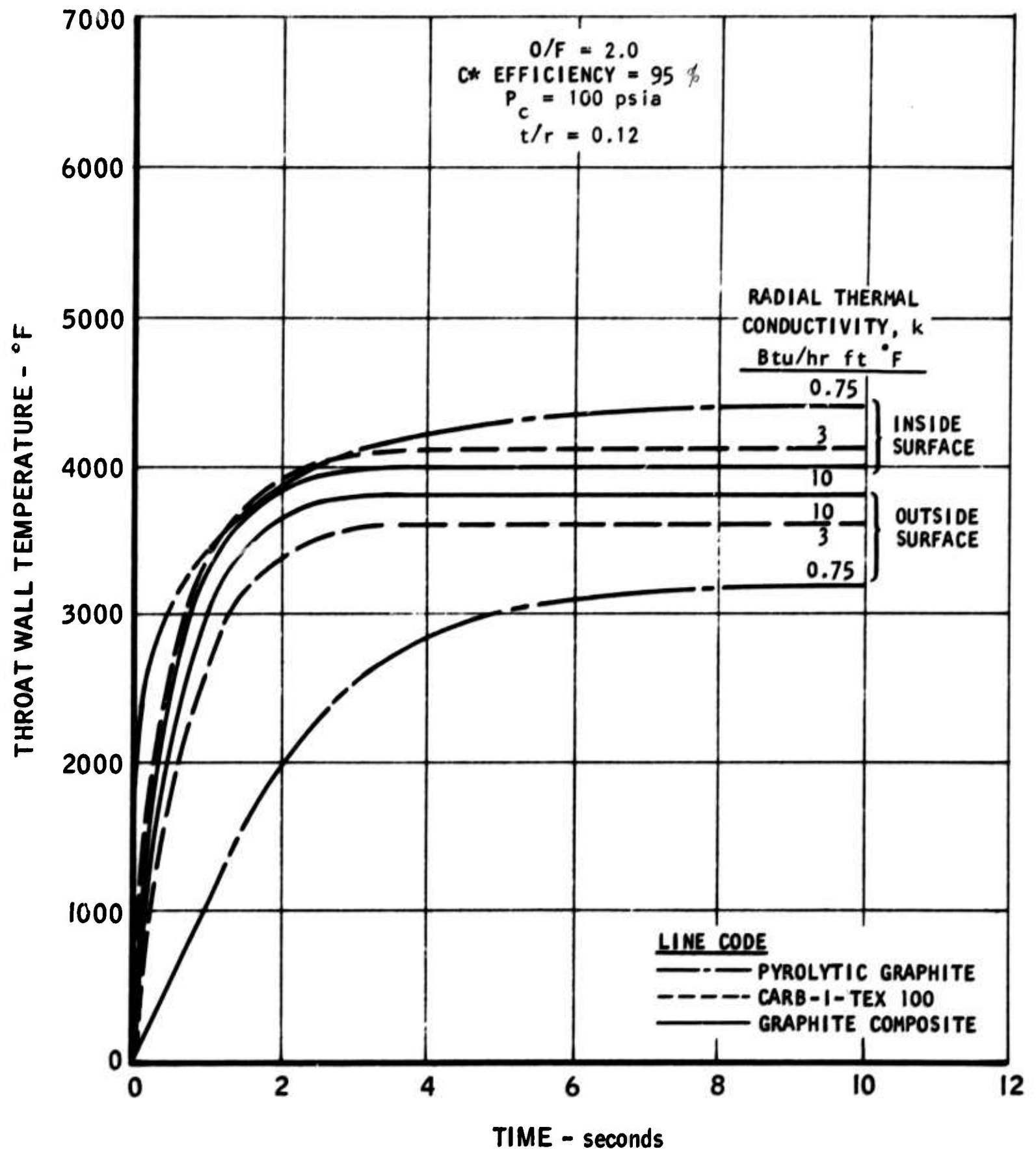


FIGURE 38. Variation of Radial Thermal Conductivity with Throat Wall Temperature and Time, 100-lb Thrust Configuration,  $N_2O_4/0.5 N_2H_4-0.5 \text{ UDMH}$

5016-42

# UNCLASSIFIED

# UNCLASSIFIED

AFRPL-TR-66-95

Report 6106

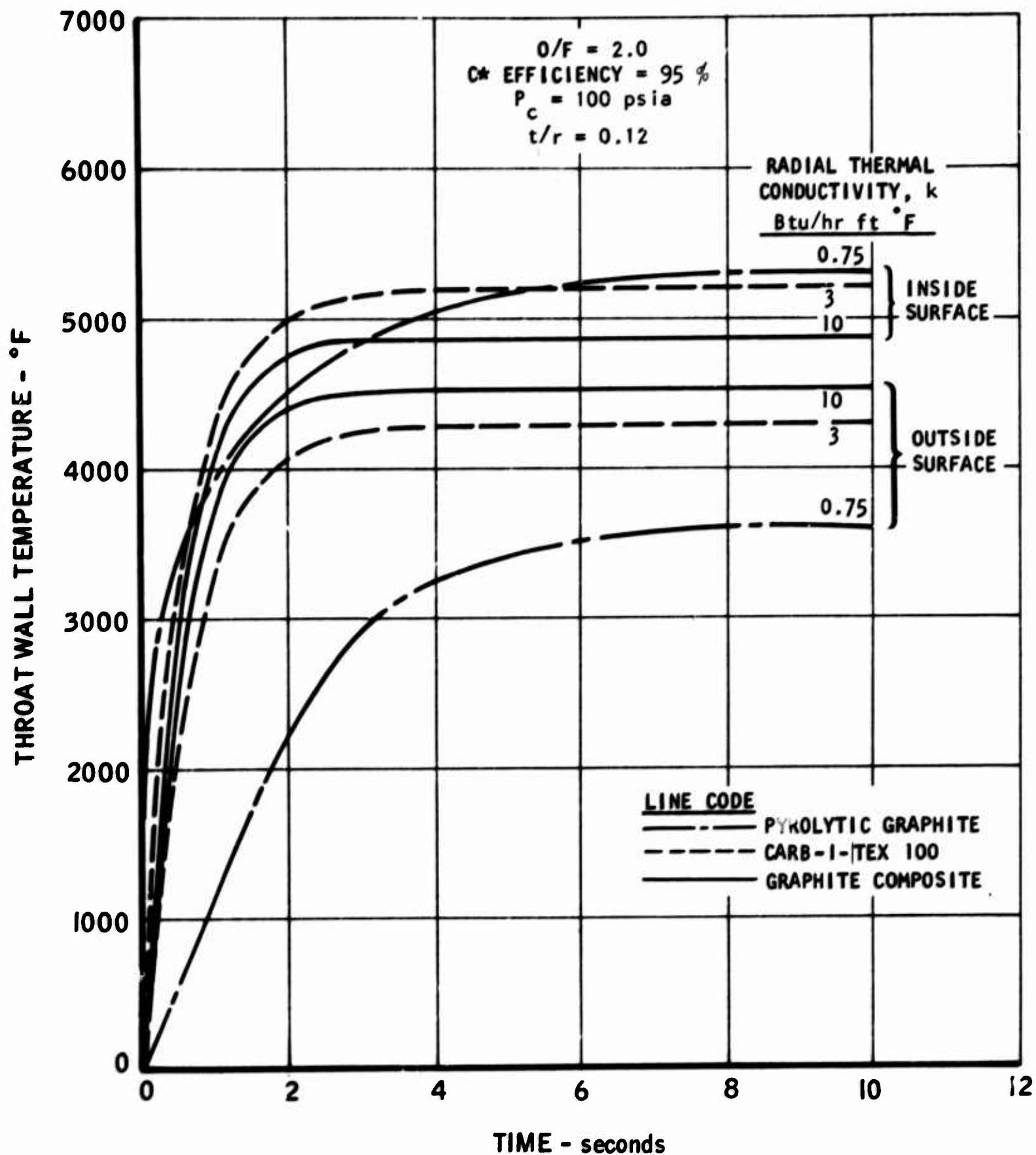


FIGURE 39. Variation of Radial Thermal Conductivity with Throat Wall Temperature and Time, 100-lb Thrust Configuration,  $F_2/BA1014$

5016-43

UNCLASSIFIED

# UNCLASSIFIED

AFRPL-TR-66-95

Report 6106

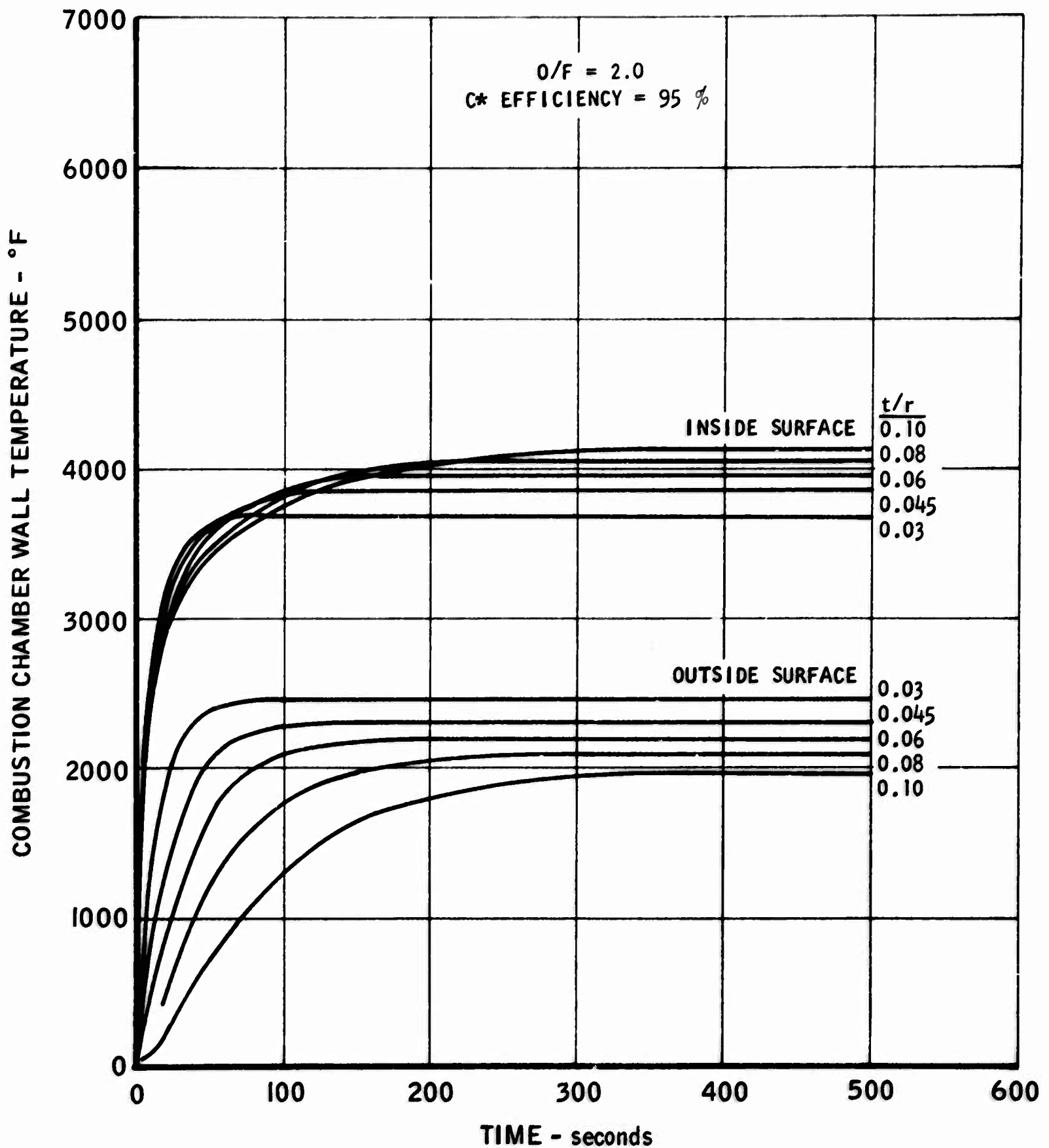


FIGURE 40. Combustion Chamber Wall Temperature vs. Time, 1000-lb Thrust Configuration,  $N_2O_4/0.5 N_2H_4-0.5 UDMH$ ,  $P_c = 50$  psia

5016-114

UNCLASSIFIED



UNCLASSIFIED

AFRPL-TR-66-95

Report 6106

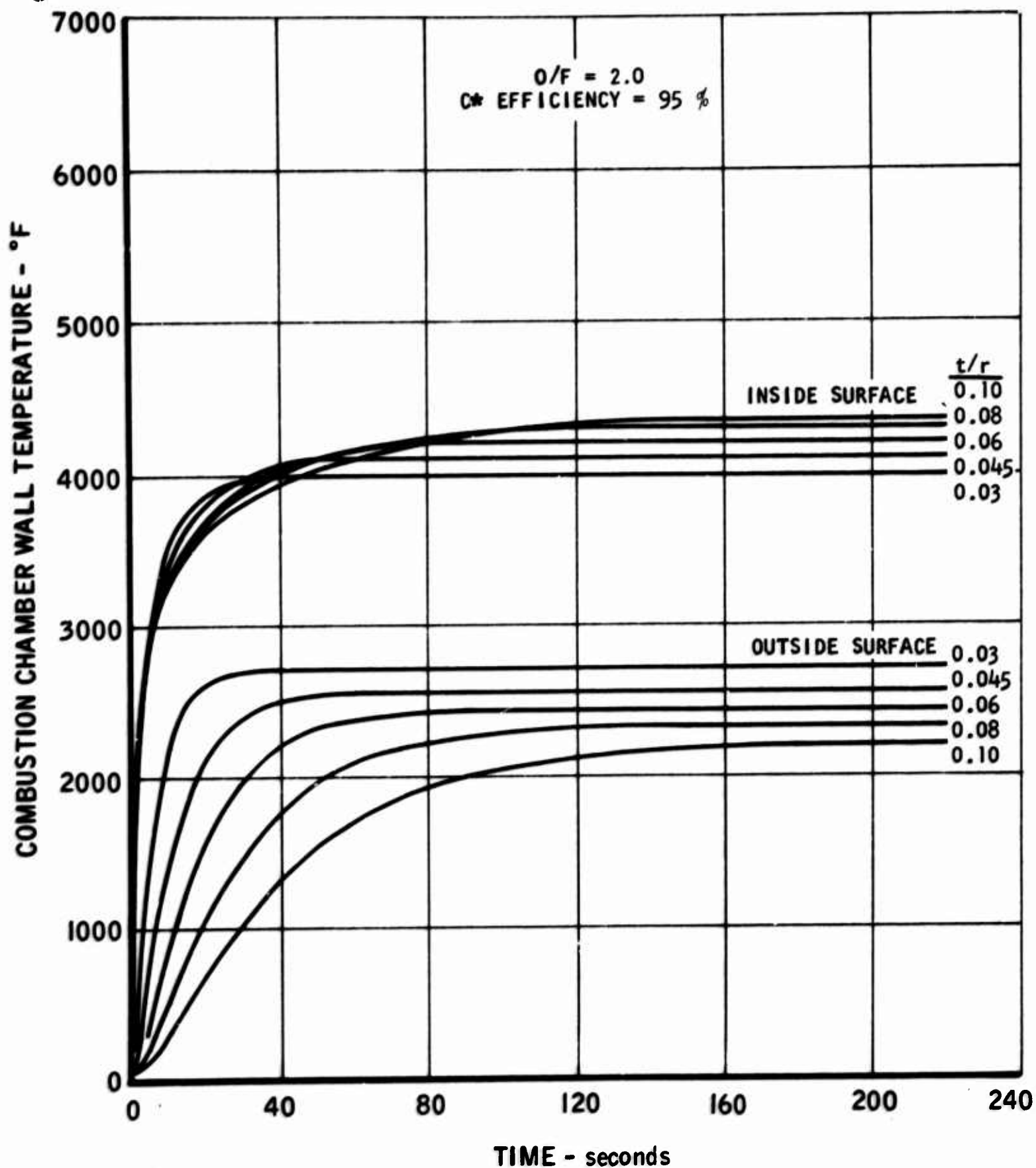


FIGURE 41. Combustion Chamber Wall Temperature vs. Time, 1000-lb Thrust Configuration,  $N_2O_4/0.5 N_2H_4-0.5 UDMH$ ,  $P_c = 100 \text{ psia}$

5016-113

UNCLASSIFIED

UNCLASSIFIED

AFRPL-TR-66-95

Report 6106

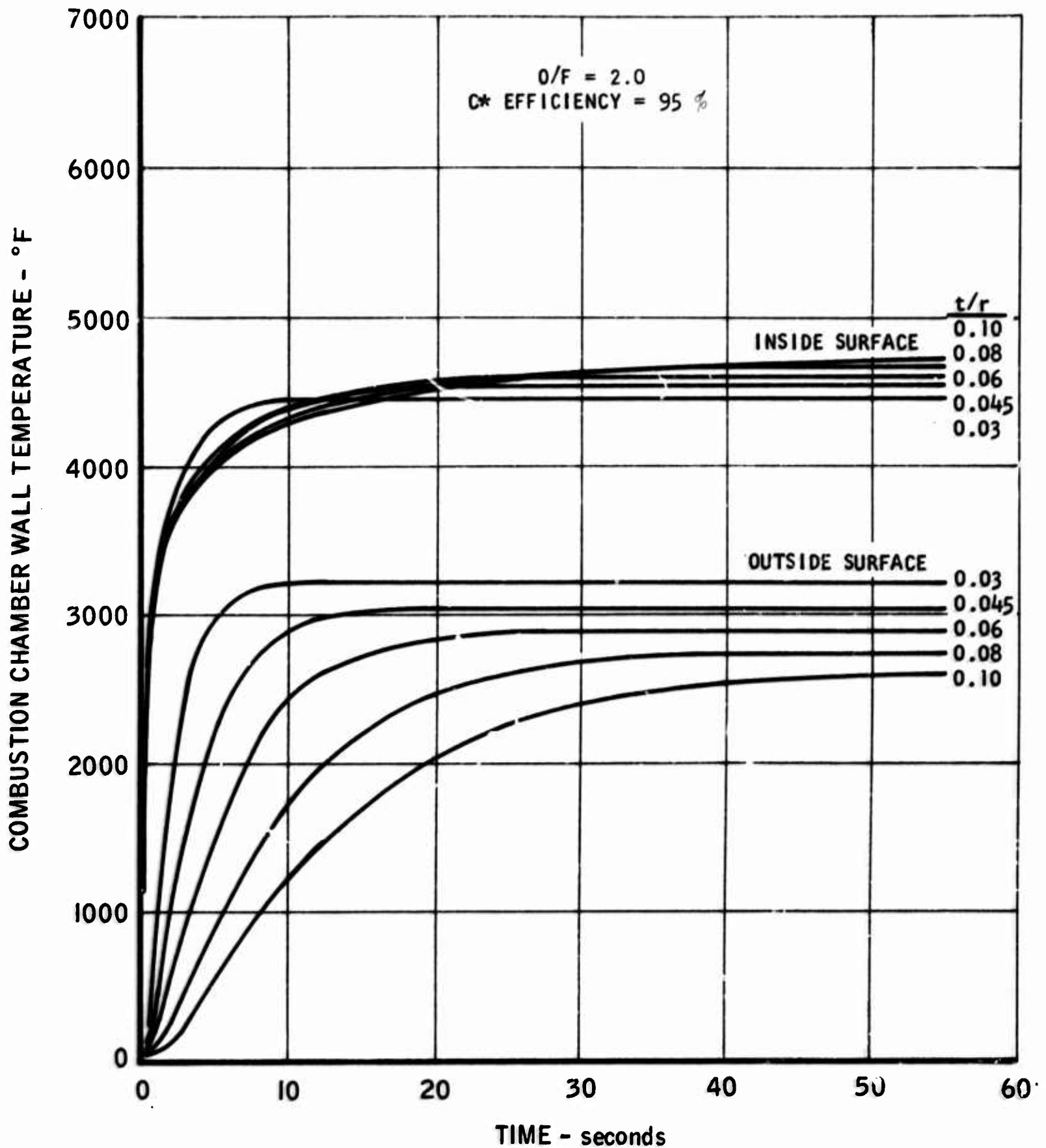


FIGURE 42. Combustion Chamber Wall Temperature vs. Time, 1000-lb Thrust Configuration,  $N_2O_4/0.5 N_2H_4-0.5 UDMH$ ,  $P_c = 300$  psia

5016-112

UNCLASSIFIED

UNCLASSIFIED

AFRPL-TR-66-95

Report 6106

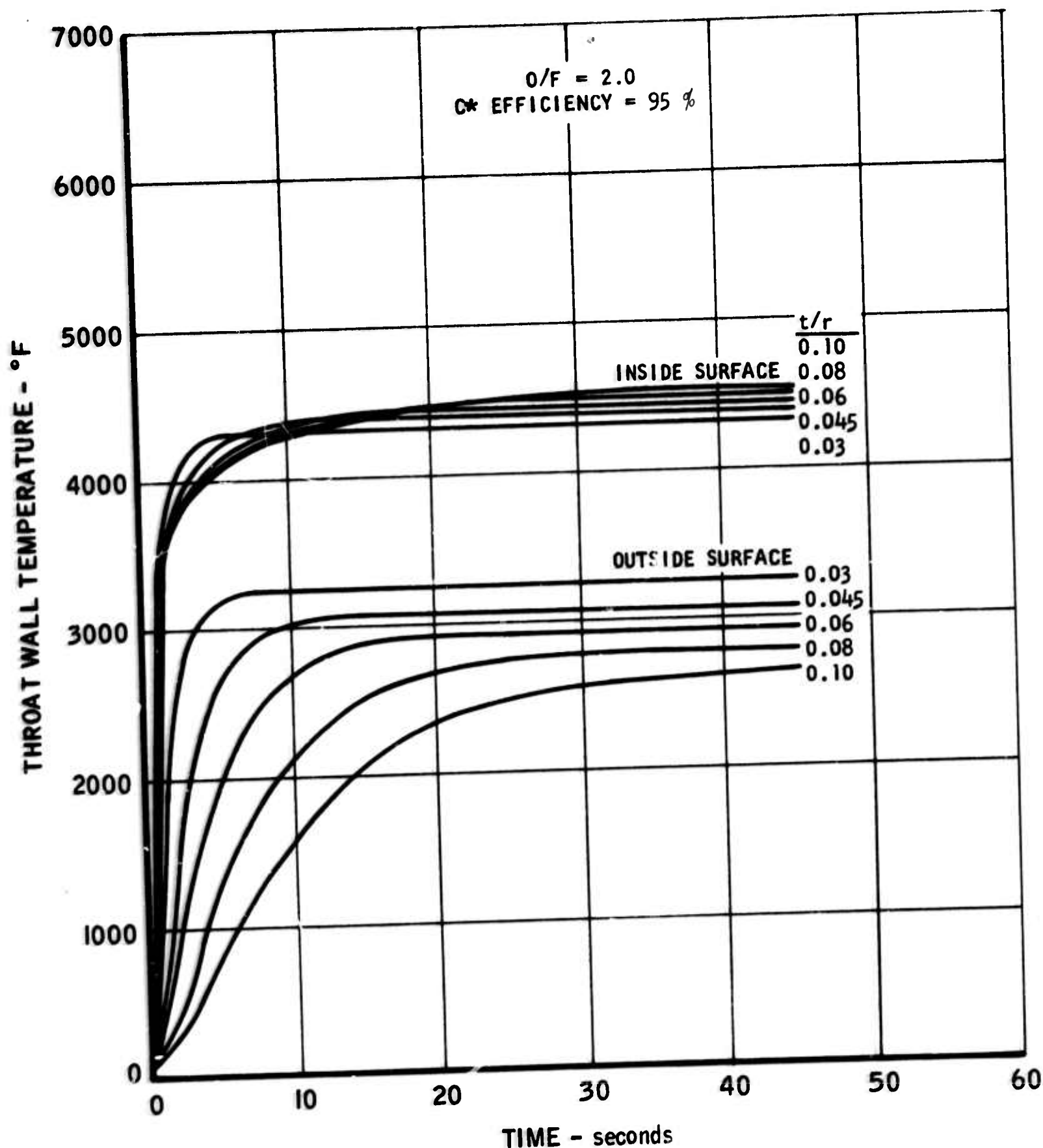


FIGURE 43. Throat Wall Temperature vs. Time, 1000-lb Thrust Configuration,  $N_2O_4/0.5 N_2H_4-0.5 UDMH$ ,  $P_c = 100 \text{ psia}$

5016-146

UNCLASSIFIED

UNCLASSIFIED

AFRPL-TR-66-95

Report 6106

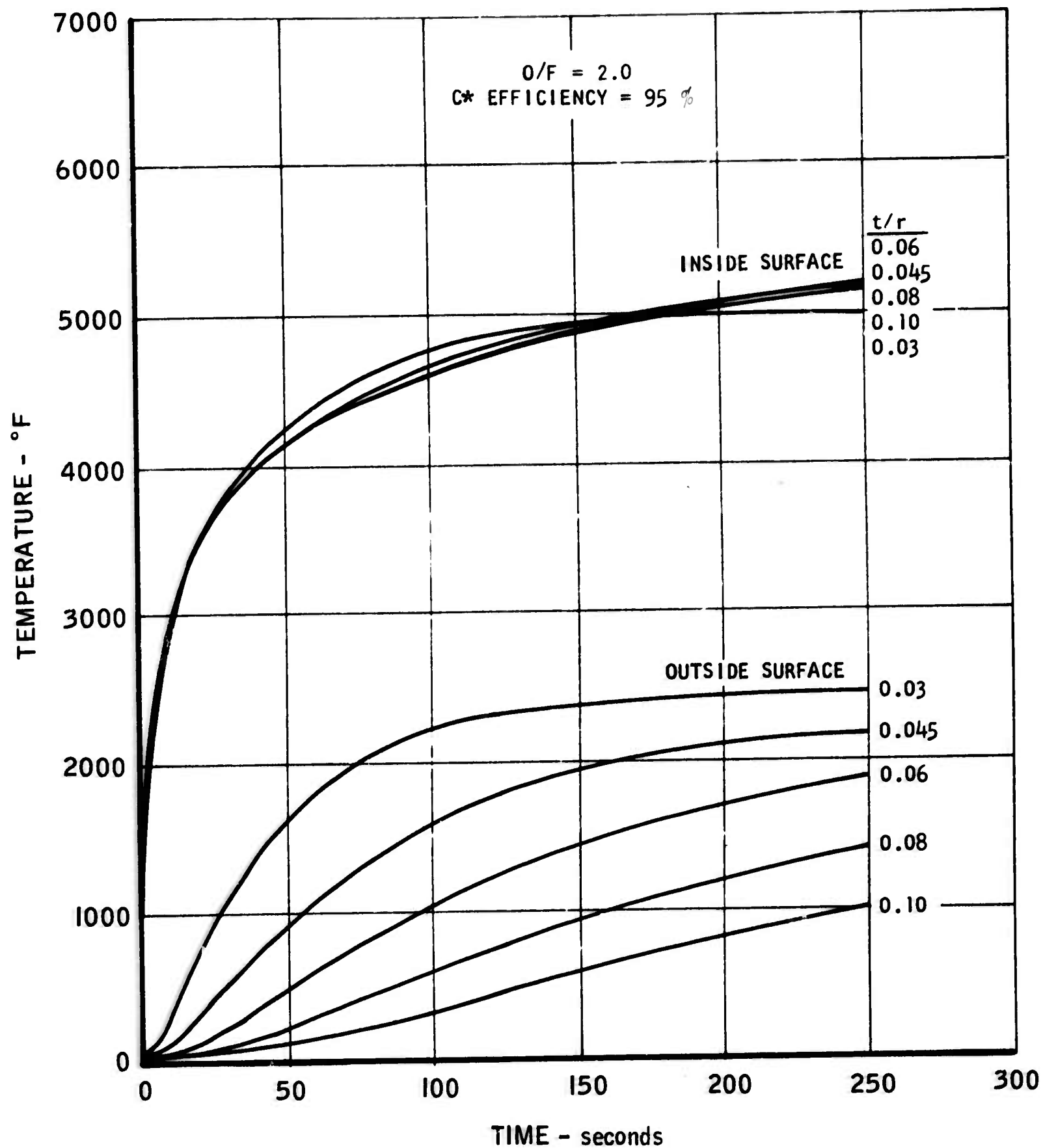


FIGURE 44. Combustion Chamber Wall Temperature vs. Time, 5000-lb Thrust Configuration,  $F_2/BA1014$ ,  $P_c = 50$  psia

5016-147

UNCLASSIFIED

UNCLASSIFIED

AFRPL-TR-66-95

Report 6106

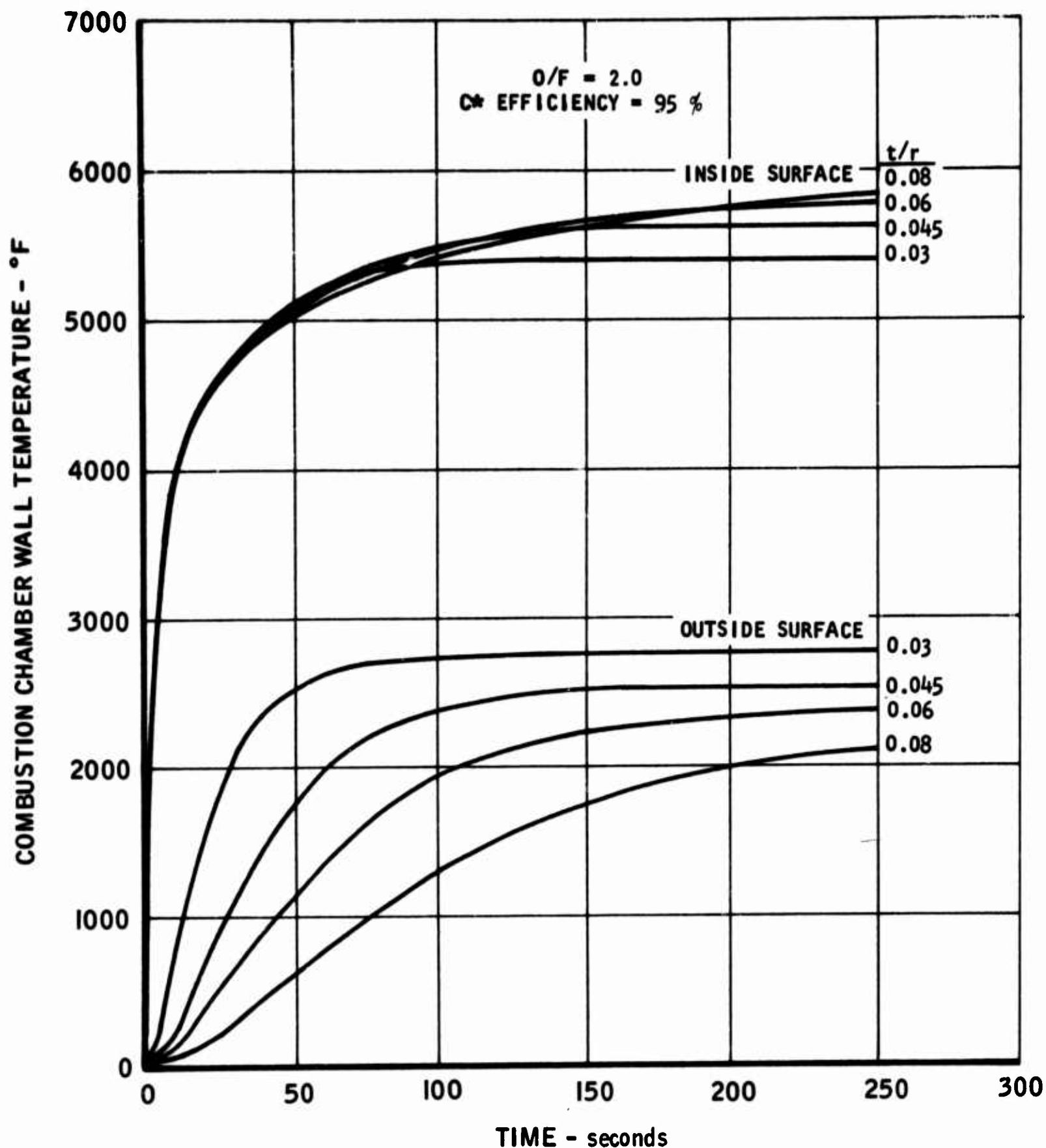


FIGURE 45. Combustion Chamber Wall Temperature vs. Time, 5000-lb Thrust Configuration,  $F_2/BA1014$ ,  $P_c = 100$  psia

5016-148

UNCLASSIFIED

UNCLASSIFIED

AFRPL-TR-66-95

Report 6106

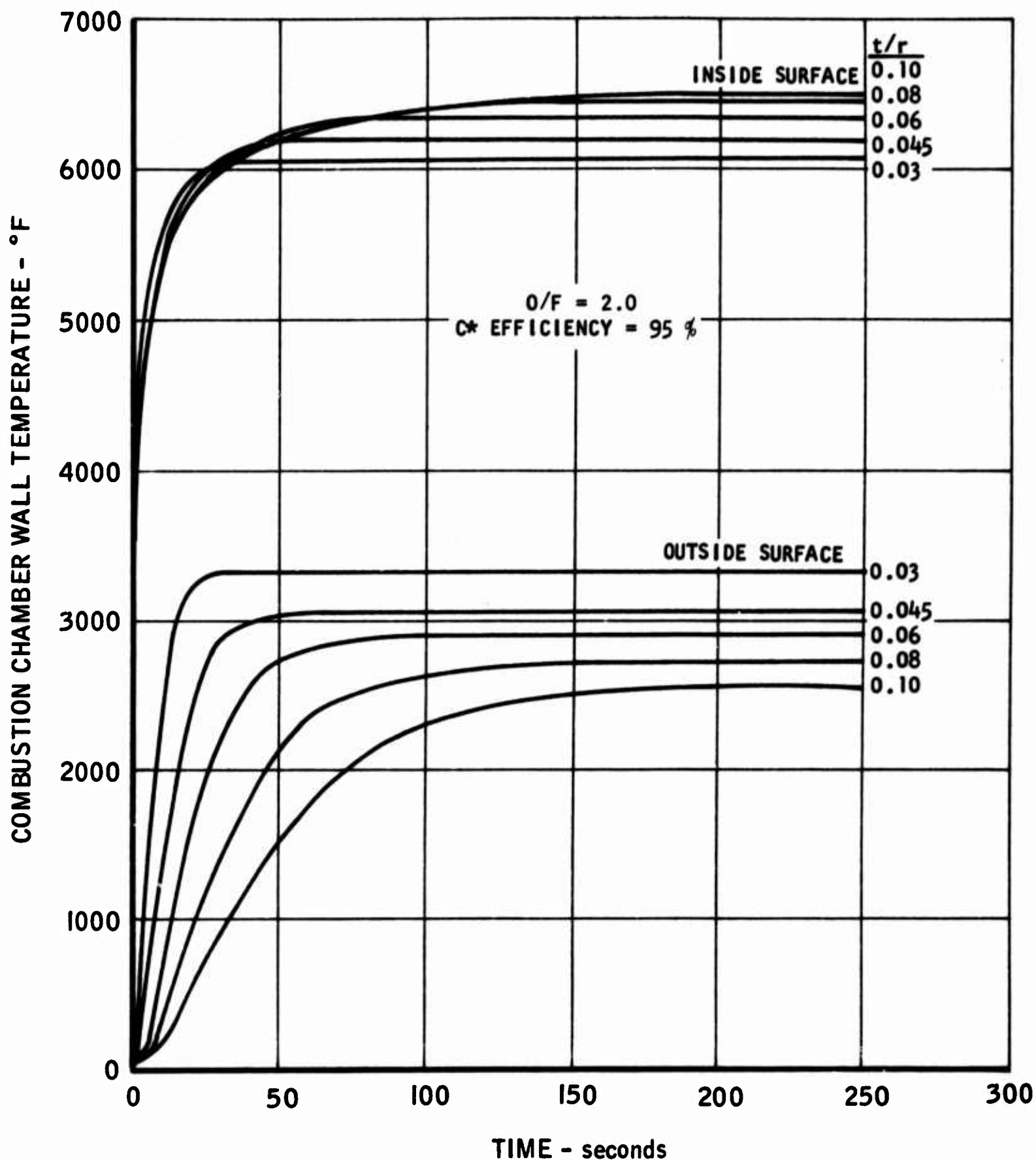


FIGURE 46. Combustion Chamber Wall Temperature vs. Time, 5000-lb Thrust Configuration,  $F_2/BA1014$ ,  $P_c = 300$  psia

5016-149

UNCLASSIFIED



UNCLASSIFIED

AFRPL-TR-66-95

Report 6106

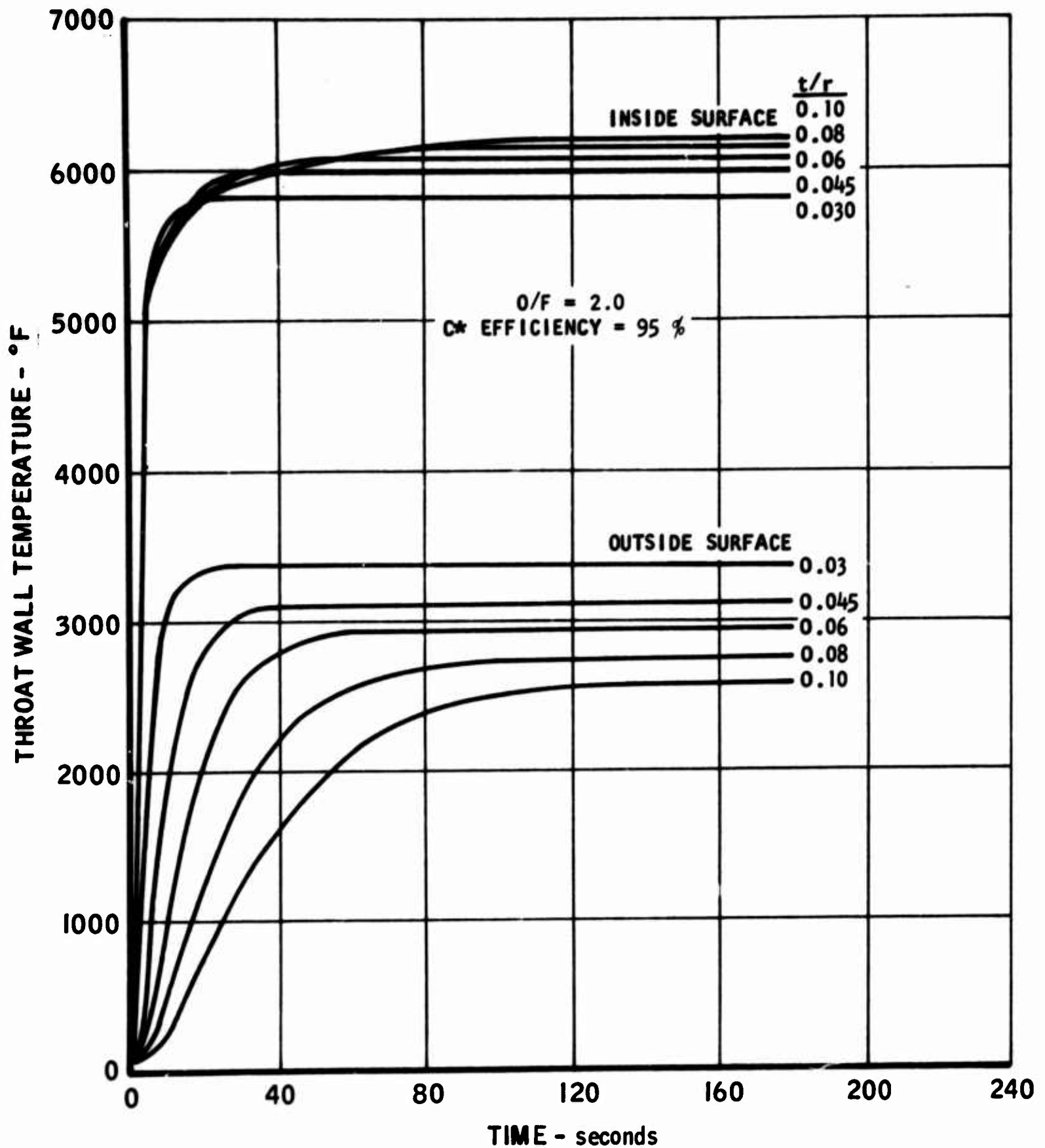


FIGURE 47. Throat Wall Temperature vs. Time, 5000-lb Thrust Configuration,  $F_2/BA1014$ ,  $P_c = 100$  psia

5016-150

UNCLASSIFIED

-122-



UNCLASSIFIED

AFRPL-TR-66-95

Report 6106

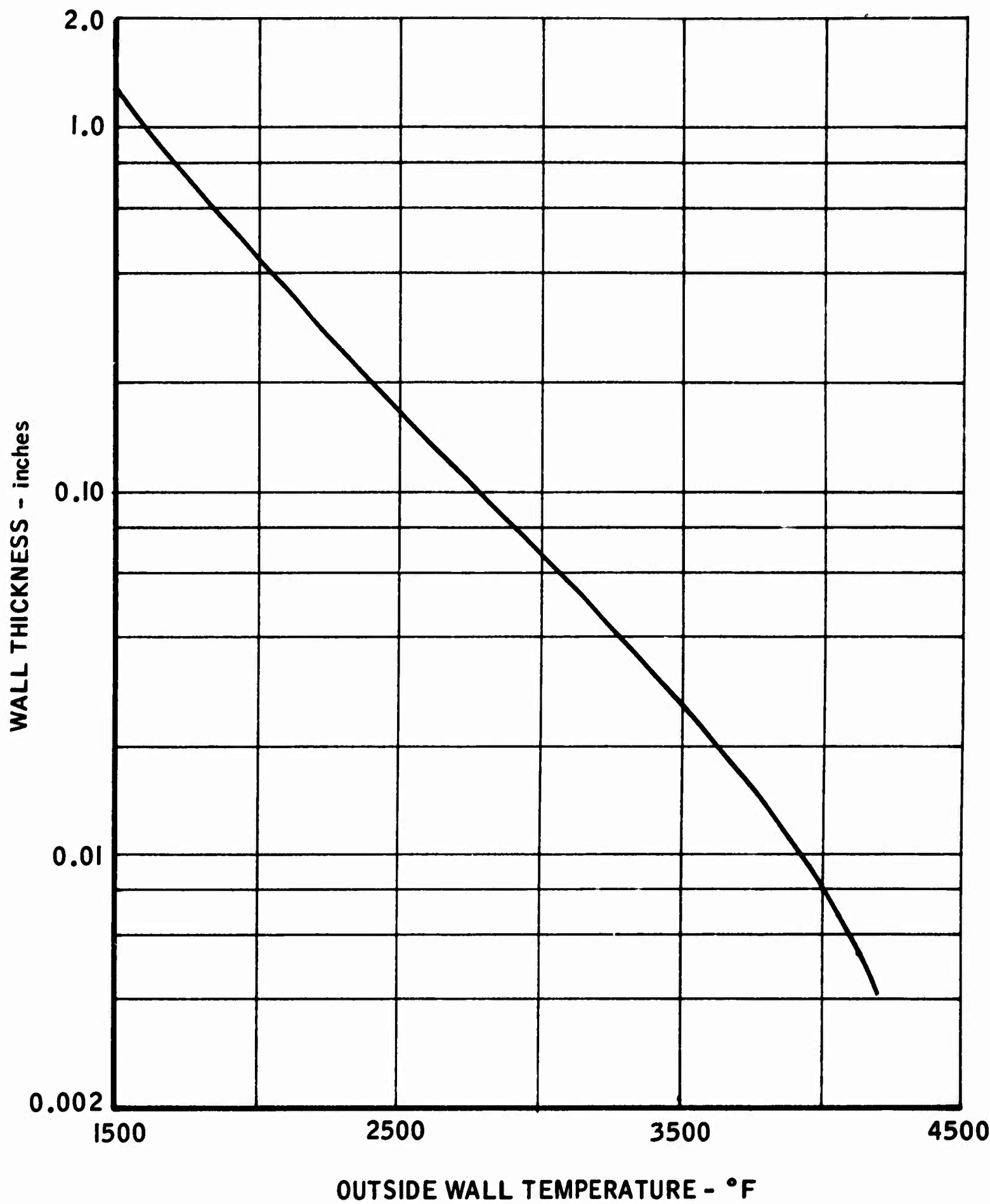


FIGURE 48. Outside Wall Temperature vs. Wall Thickness, Controlled Wall Temperature Chamber, Inside Wall Temperature = 4500°F

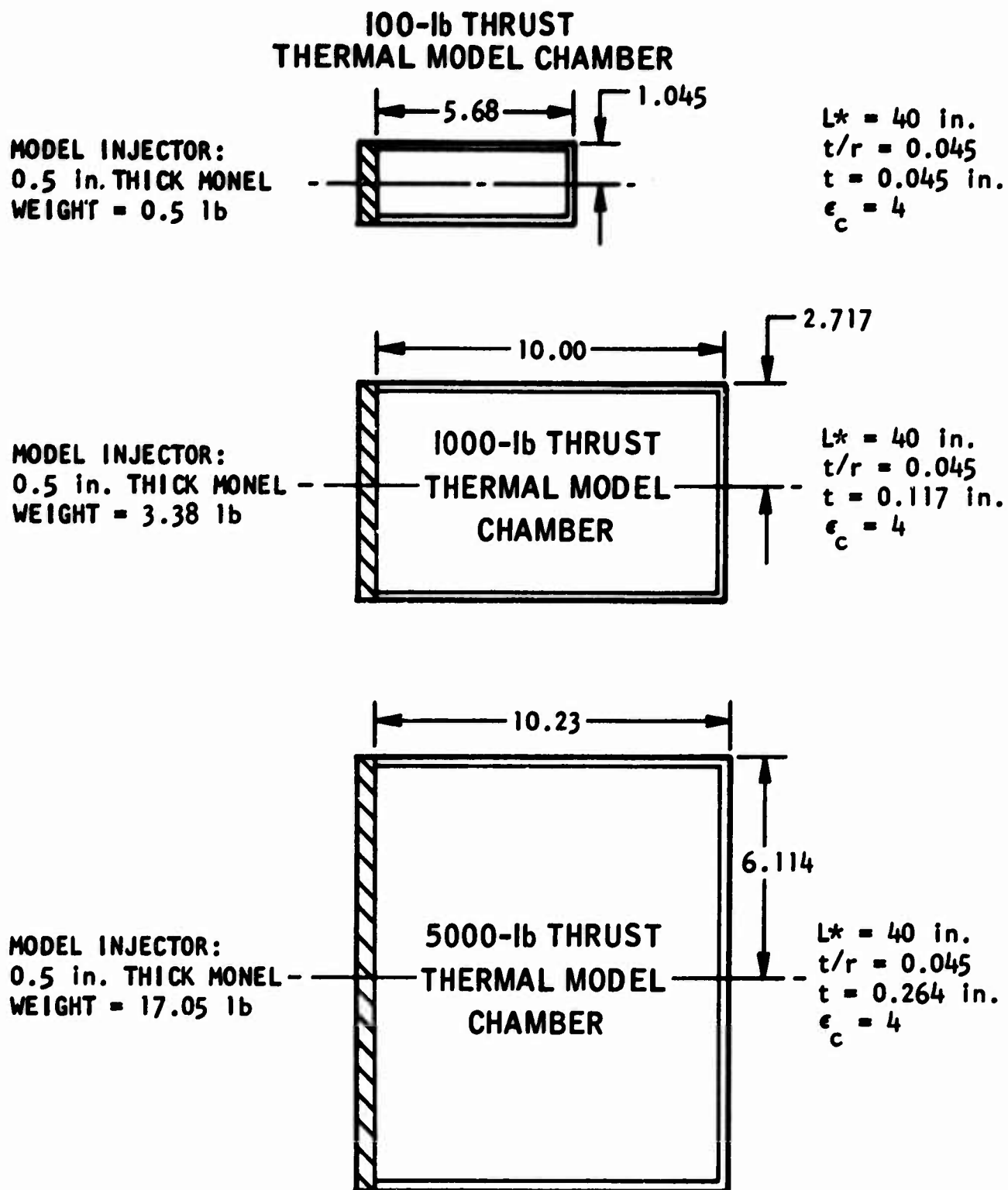
5016-44

UNCLASSIFIED  
-123-

UNCLASSIFIED

AFRPL-TR-66-95

Report 6106



NOTE: ALL DIMENSIONS IN INCHES

FIGURE 49. Dimensions of Thermal Model Chambers Used for Preliminary Heat Soak Back Analysis

5016-151

UNCLASSIFIED

UNCLASSIFIED

AFRPL-TR-66-95

Report 6106

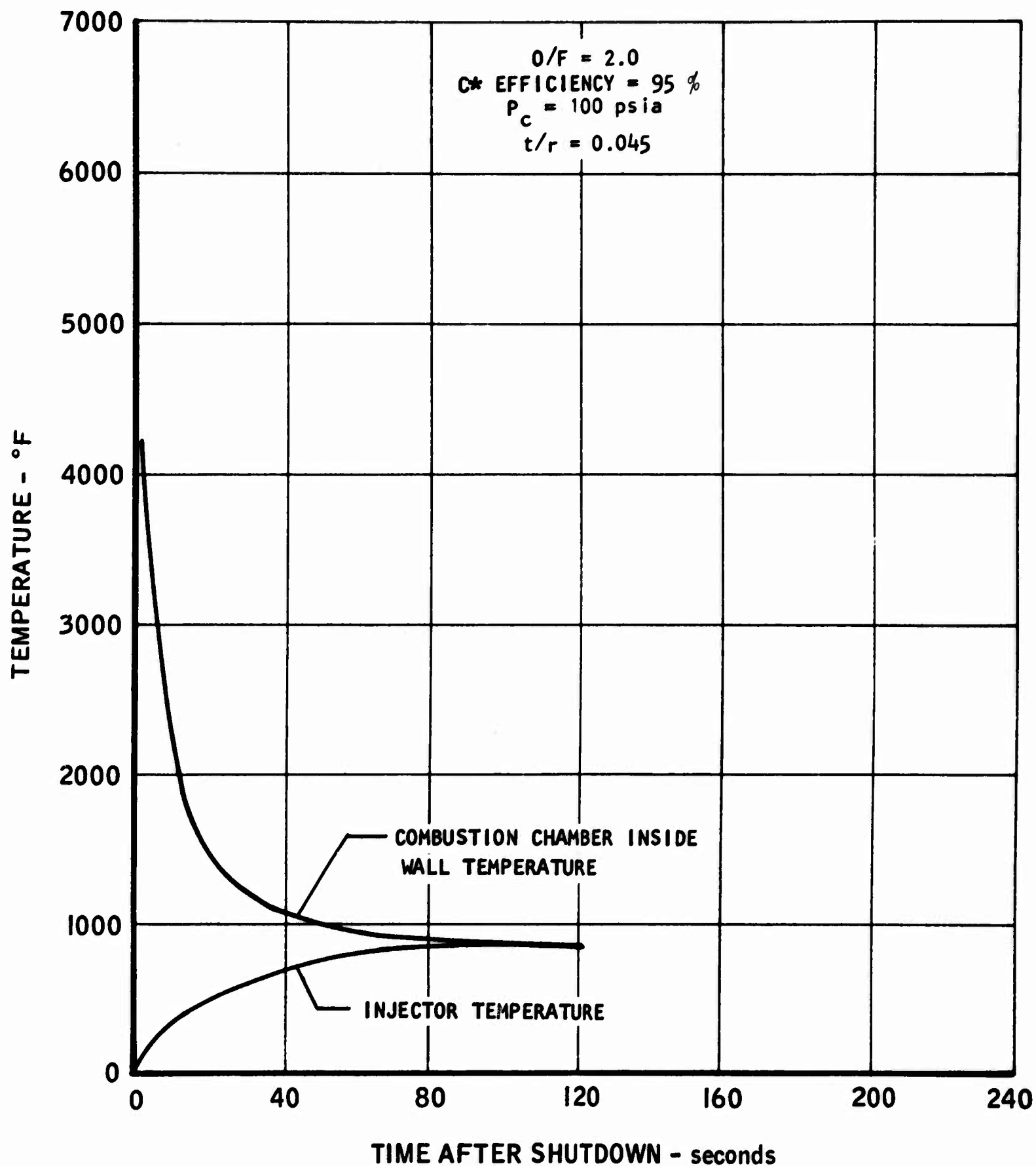


FIGURE 50. Injector Soak Back Temperature, 100-lb Thrust Thermal Model Chamber, No Thermal Resistance Between Chamber and Injector,  $F_2/BA1014$

5016-152

UNCLASSIFIED

UNCLASSIFIED

AFRPL-TR-66-95

Report 6106

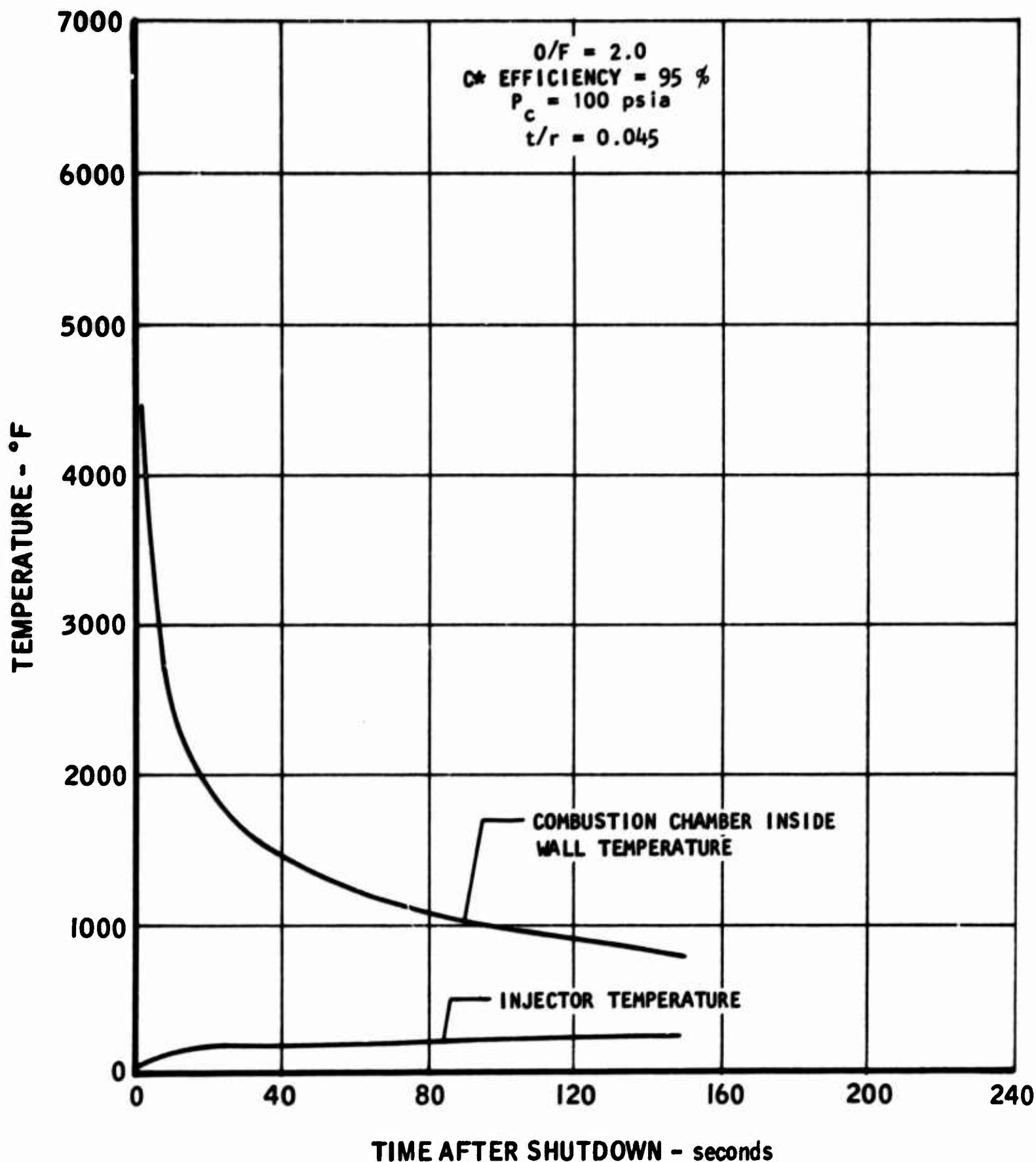


FIGURE 51. Injector Soak Back Temperature, 100-lb Thrust Thermal Model Chamber, Infinite Thermal Resistance Between Chamber and Injector, F<sub>2</sub>/BA1014

5016-153

UNCLASSIFIED

# UNCLASSIFIED

AFRPL-TR-66-95

Report 6106

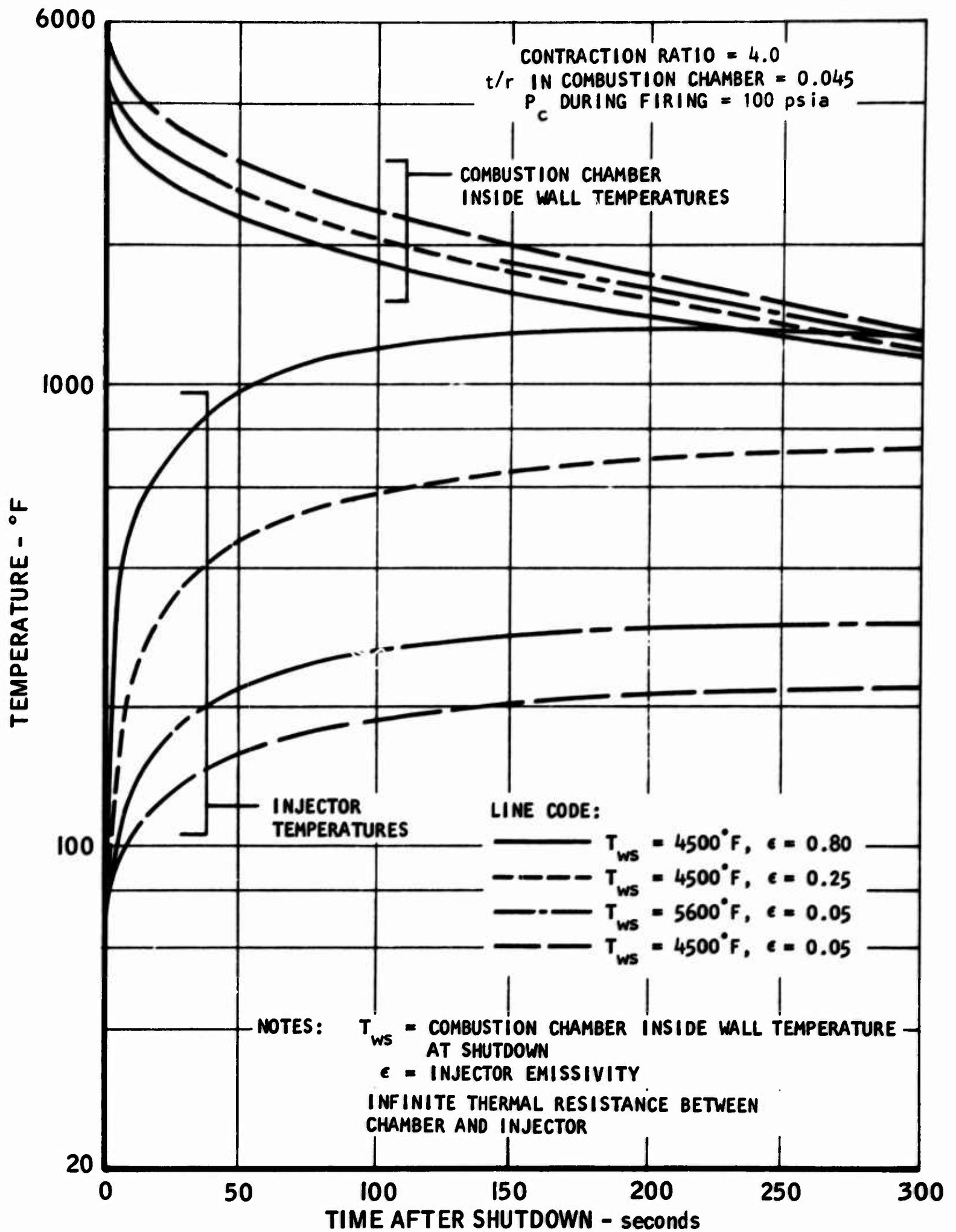


FIGURE 52. Injector Soak Back Temperature vs. Injector Emissivity, 5000-lb Thrust Configuration

5016-154

# UNCLASSIFIED

UNCLASSIFIED

AFRPL-TR-66-95

Report 6106

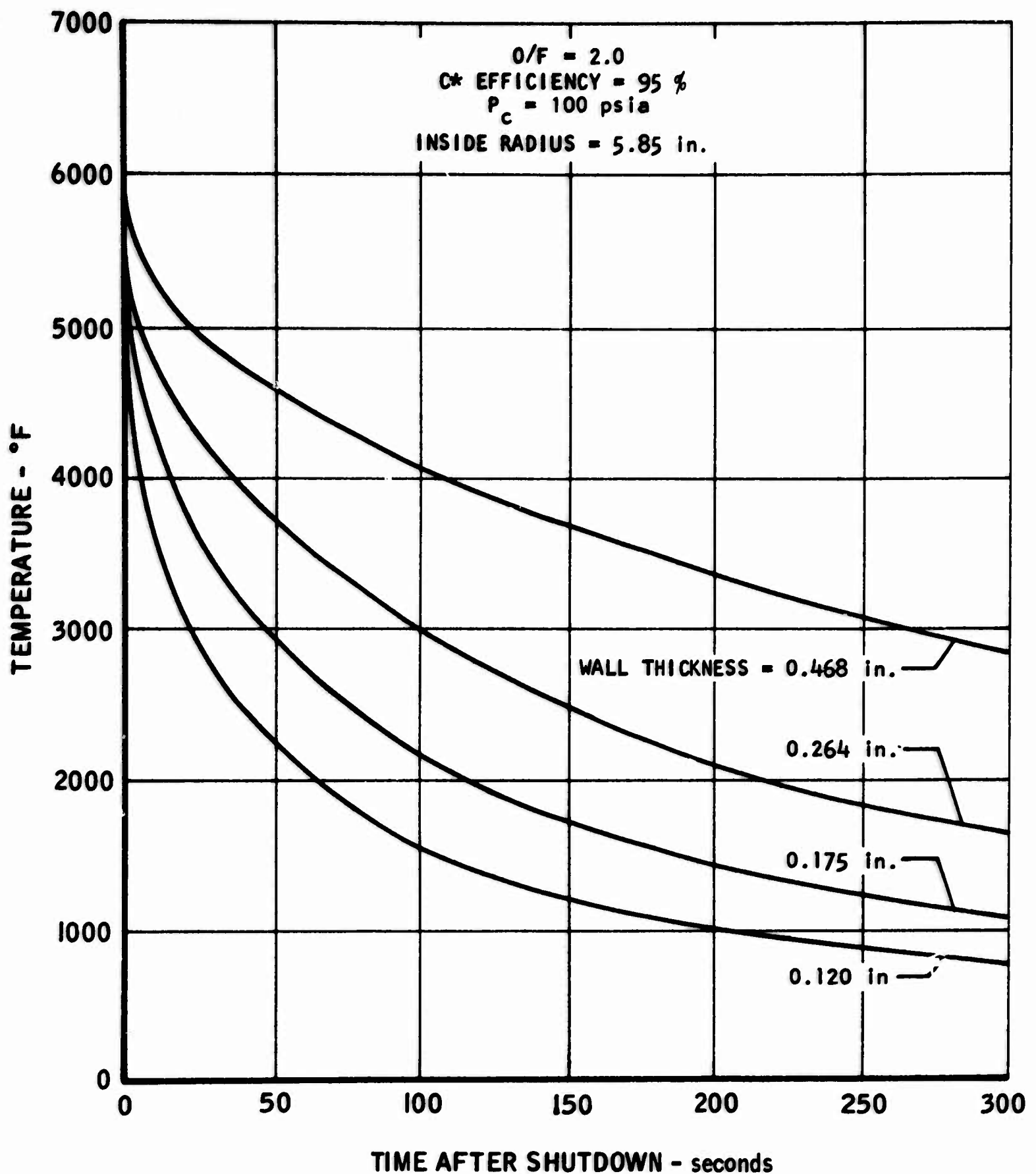


FIGURE 53. Combustion Chamber Inside Wall Cooldown vs. Time After Shutdown, 5000-lb Thrust Configuration,  $F_2/BA1014$

5016-48

UNCLASSIFIED



UNCLASSIFIED

AFRPL-TR-66-95

Report 6106

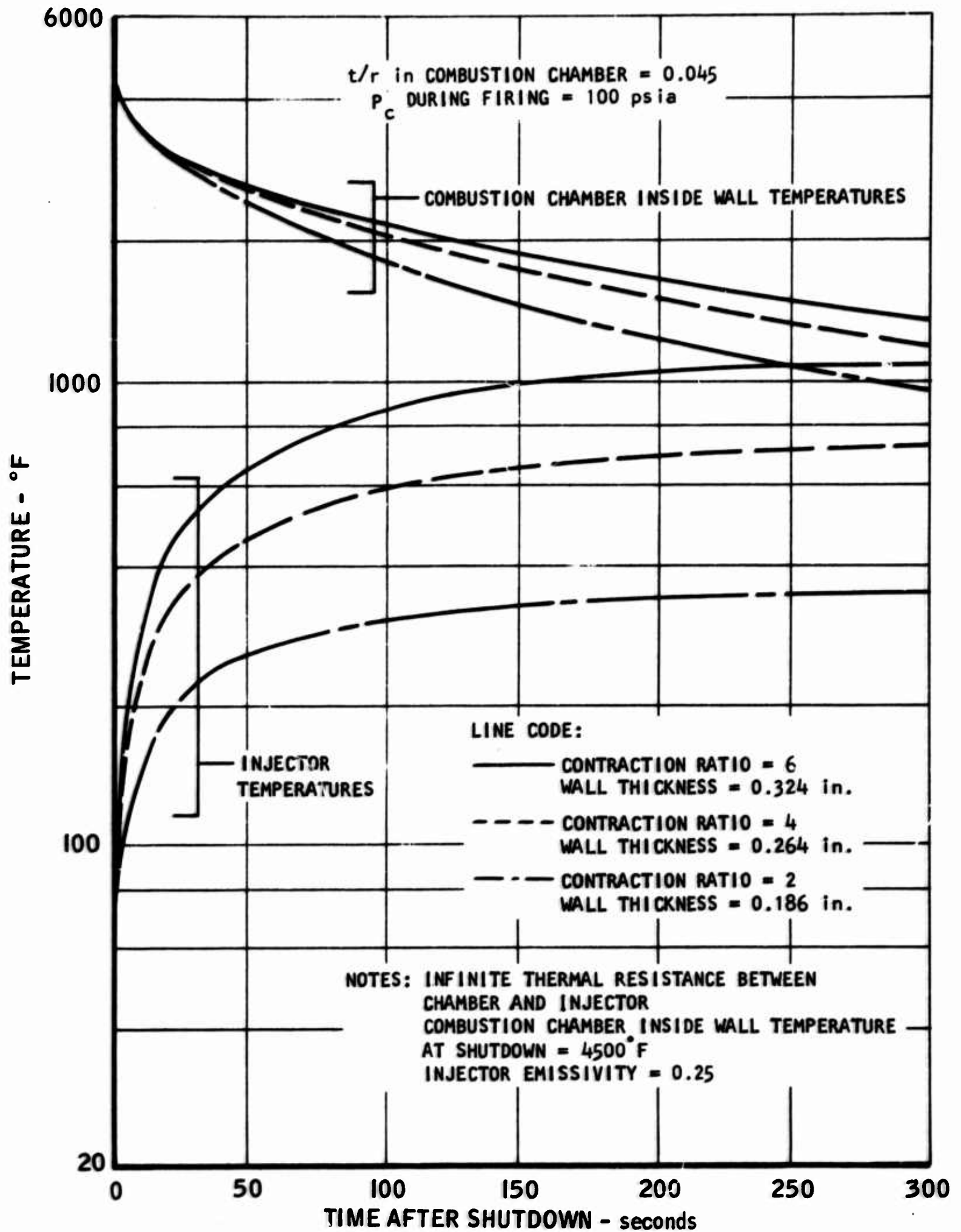


FIGURE 54. Injector Soak Back Temperature vs. Contraction Ratio, 5000-lb Thrust Configuration

5016-155

UNCLASSIFIED



UNCLASSIFIED

AFRPL-TR-66-95

Report 6106

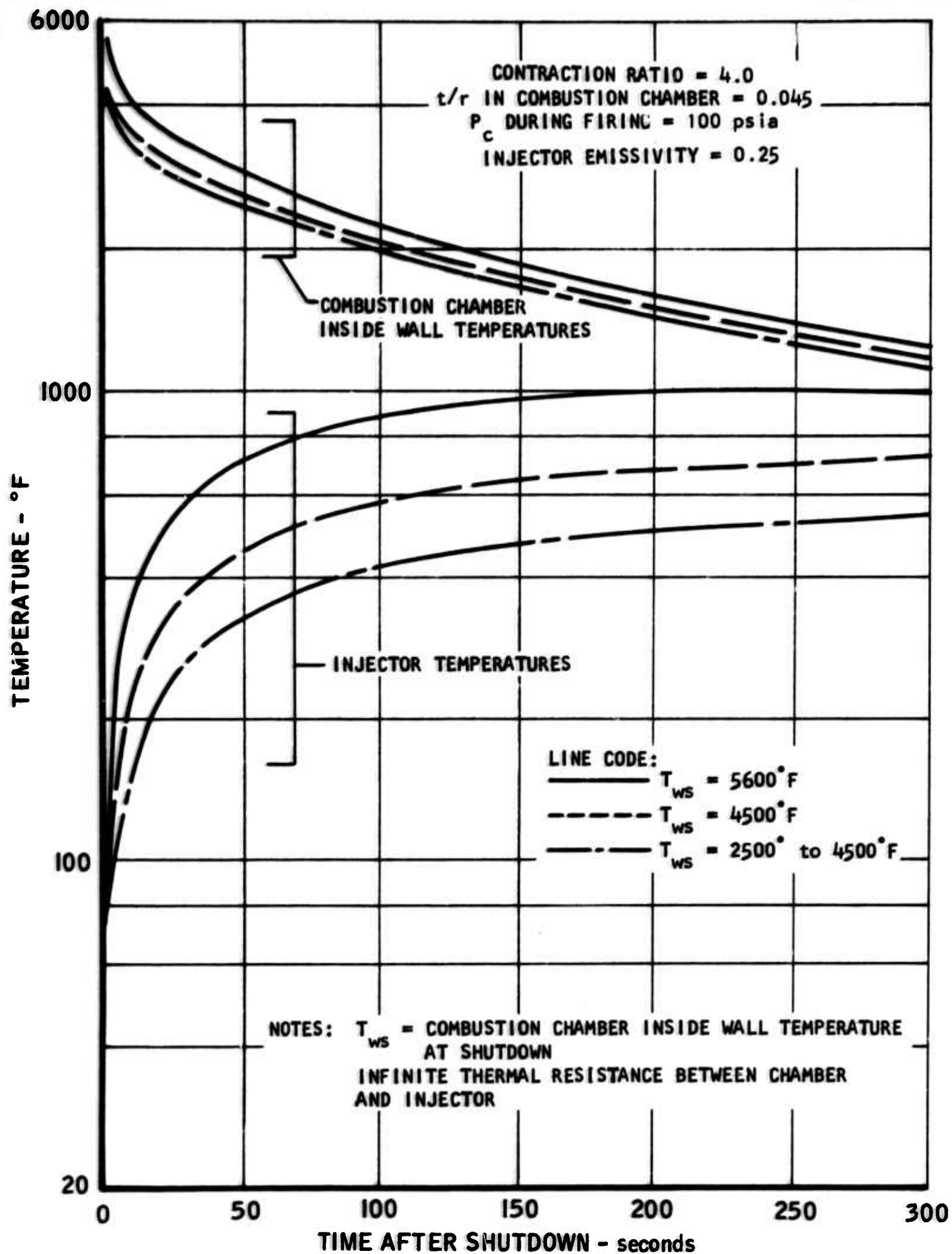


FIGURE 55. Injector Soak Back Temperature vs. Combustion Chamber Inside Wall Temperature at Shutdown, 5000-lb Thrust Configuration

5016-156

UNCLASSIFIED

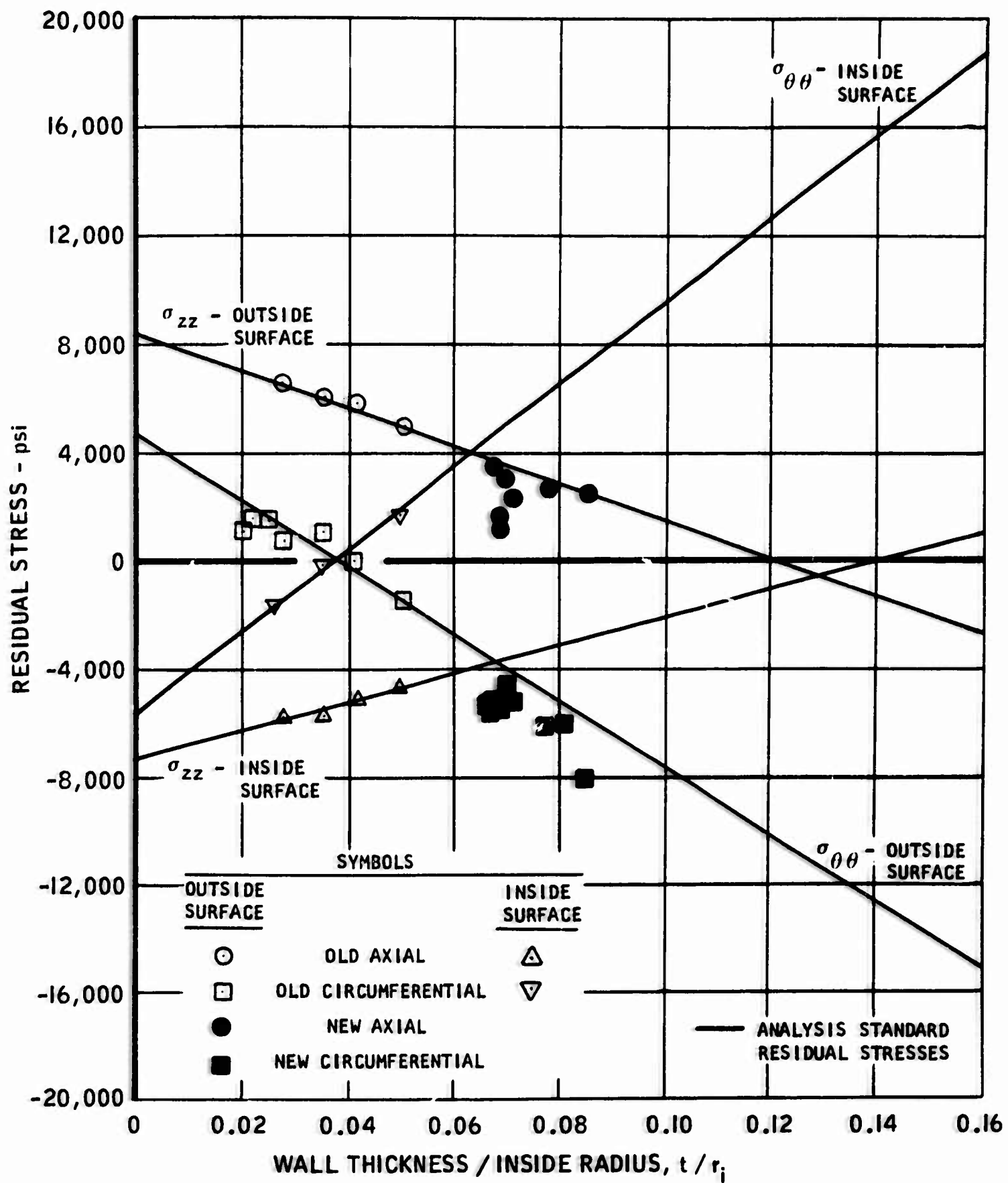


FIGURE 56. Residual Stresses on the Surfaces of As-deposited PG Cylinders and Cones

UNCLASSIFIED

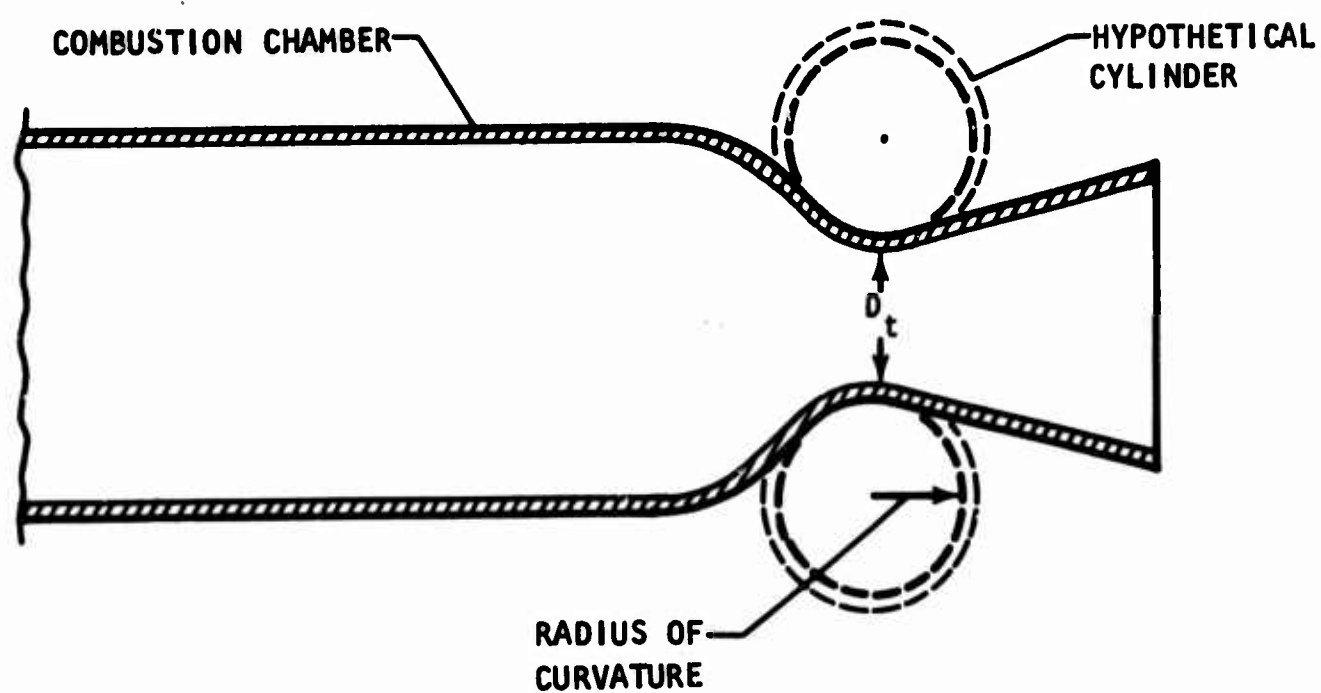


FIGURE 57. Model for Axial Stress Analysis at Throat

UNCLASSIFIED

UNCLASSIFIED

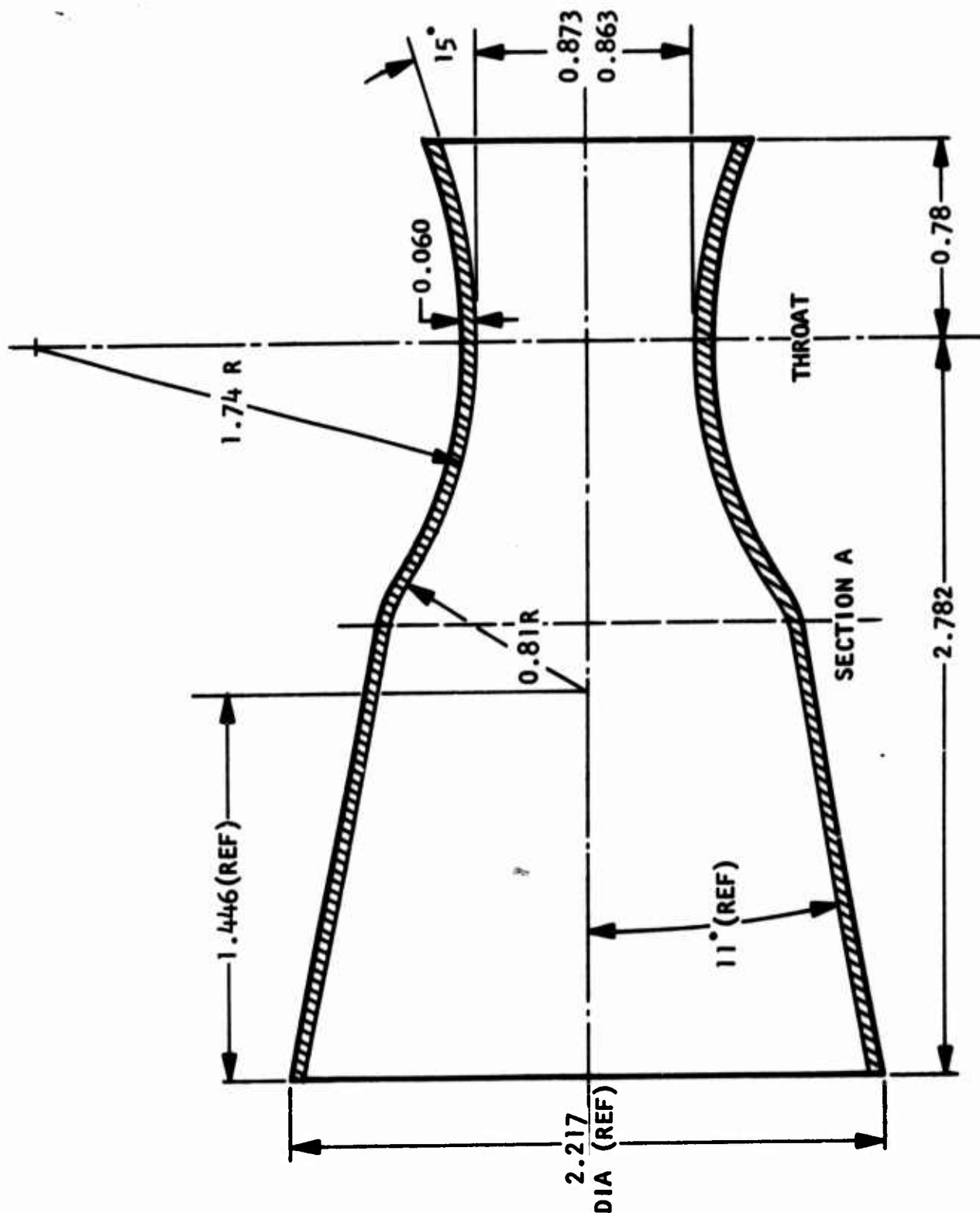


FIGURE 58. PG Thrust Chamber Configuration Used for Residual Stress Measurements

UNCLASSIFIED

UNCLASSIFIED

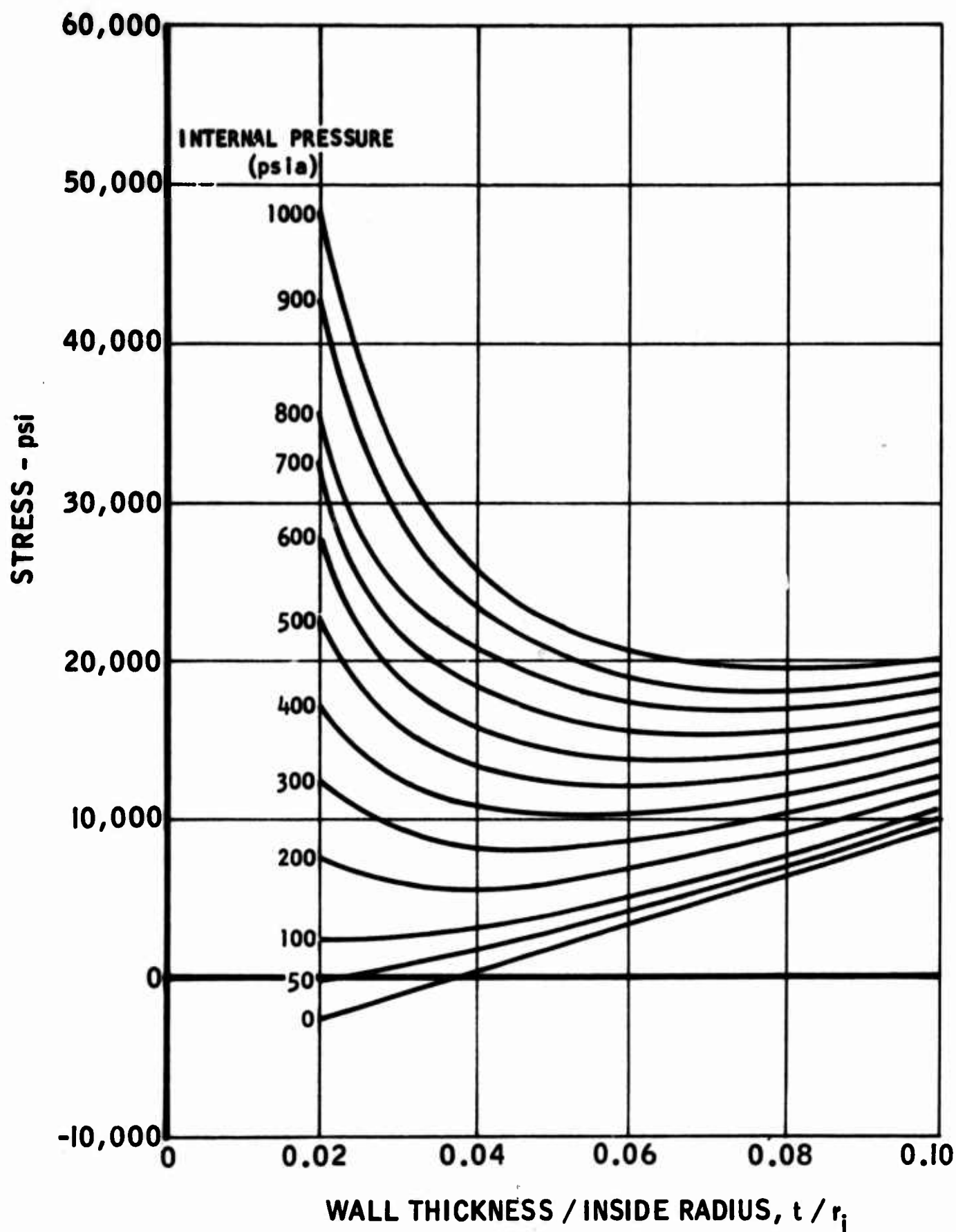


FIGURE 59. Circumferential Proof Stress on Inside Surface of Combustion Chamber for As-deposited Material

UNCLASSIFIED

UNCLASSIFIED

AFRPL-TR-66-95

Report 6106

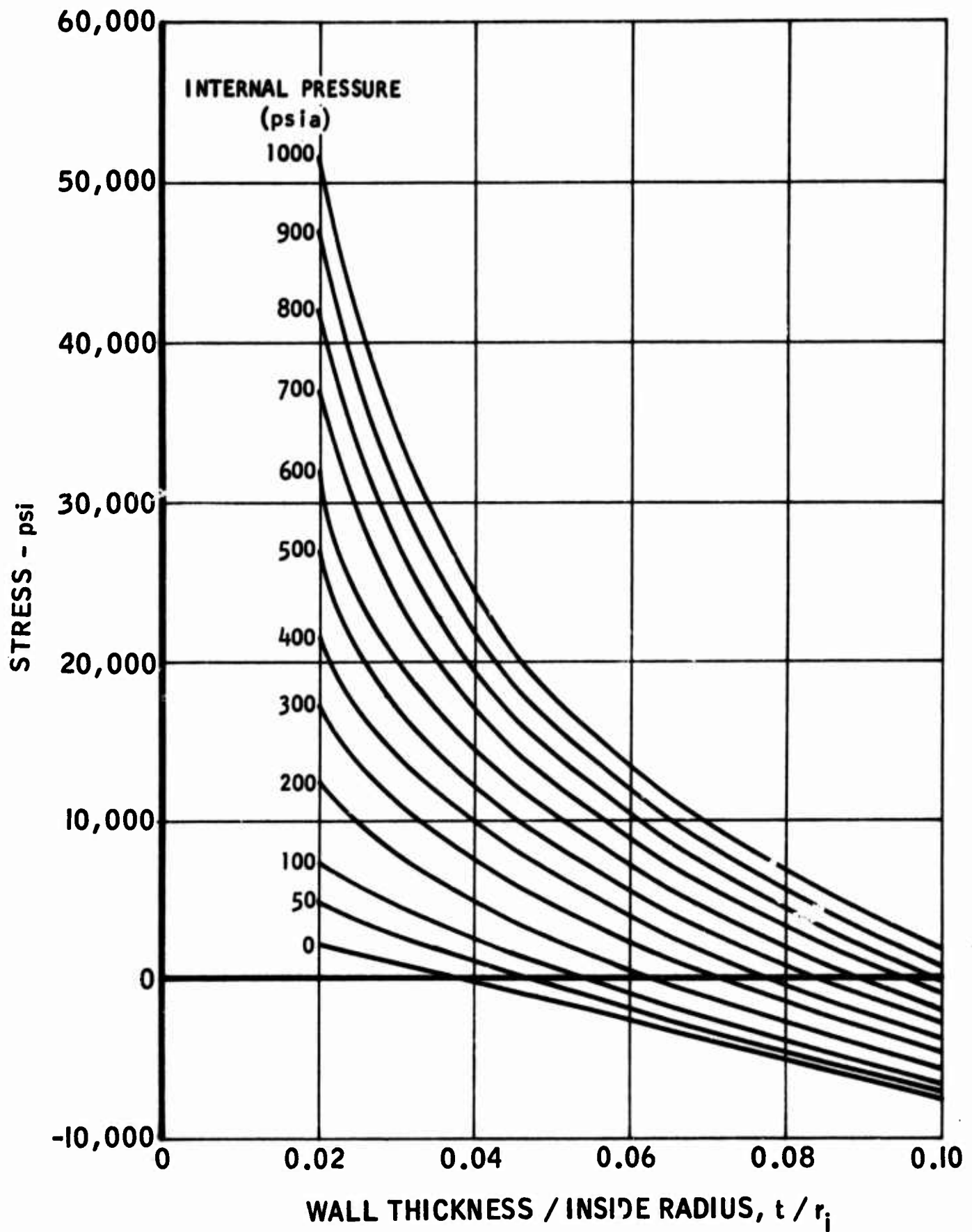


FIGURE 60. Circumferential Proof Stress on Outside Surface of Combustion Chamber for As-deposited Material

5016-20

UNCLASSIFIED



UNCLASSIFIED

AFRPL-TR-66-95

Report 6106

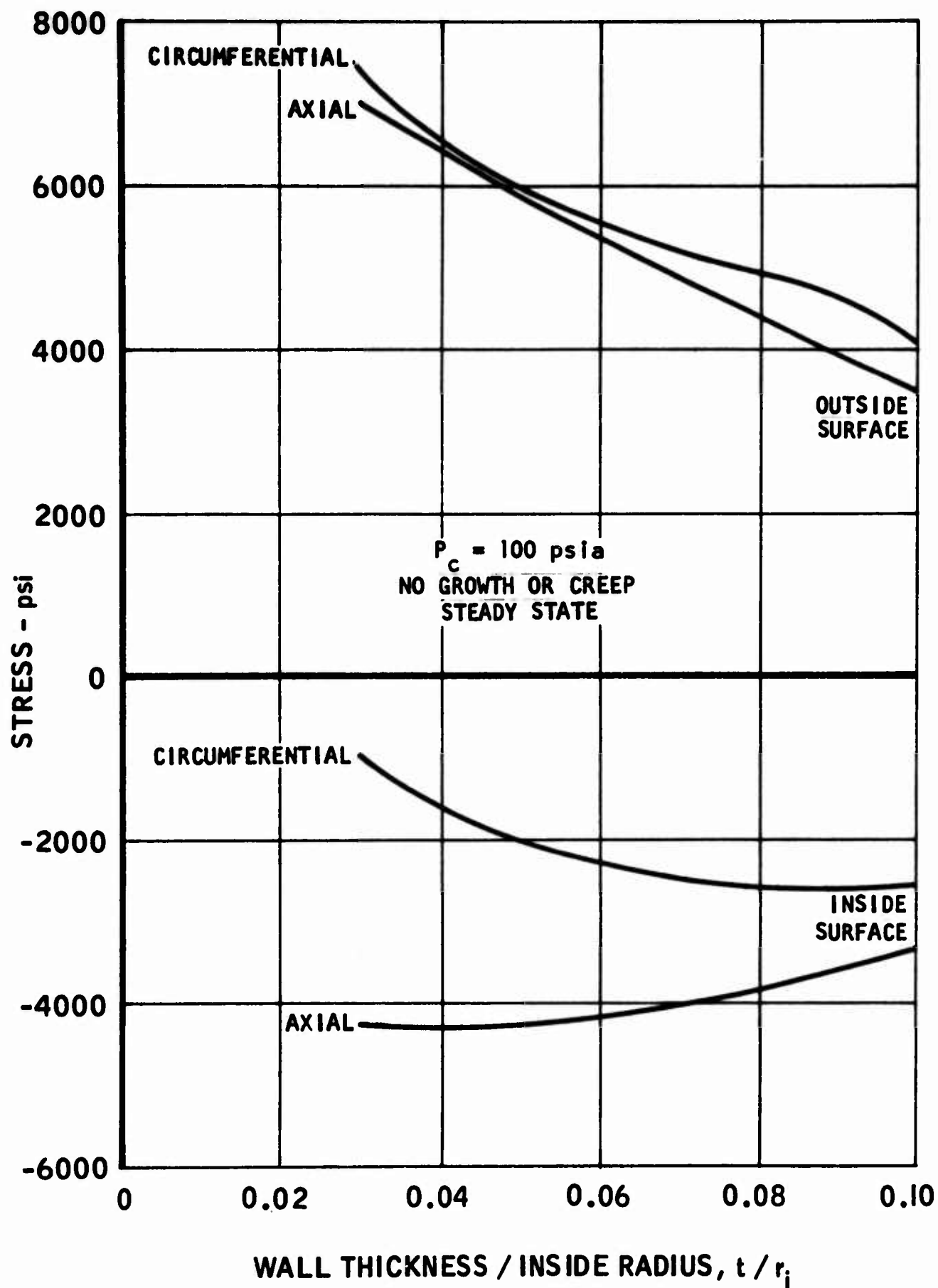


FIGURE 61. Chamber Operating Stresses vs.  $t/r$ , 100-lb Thrust Configuration,  
 $N_2O_4/0.5 N_2H_4 - 0.5$  UDMH

5016-167

UNCLASSIFIED



UNCLASSIFIED

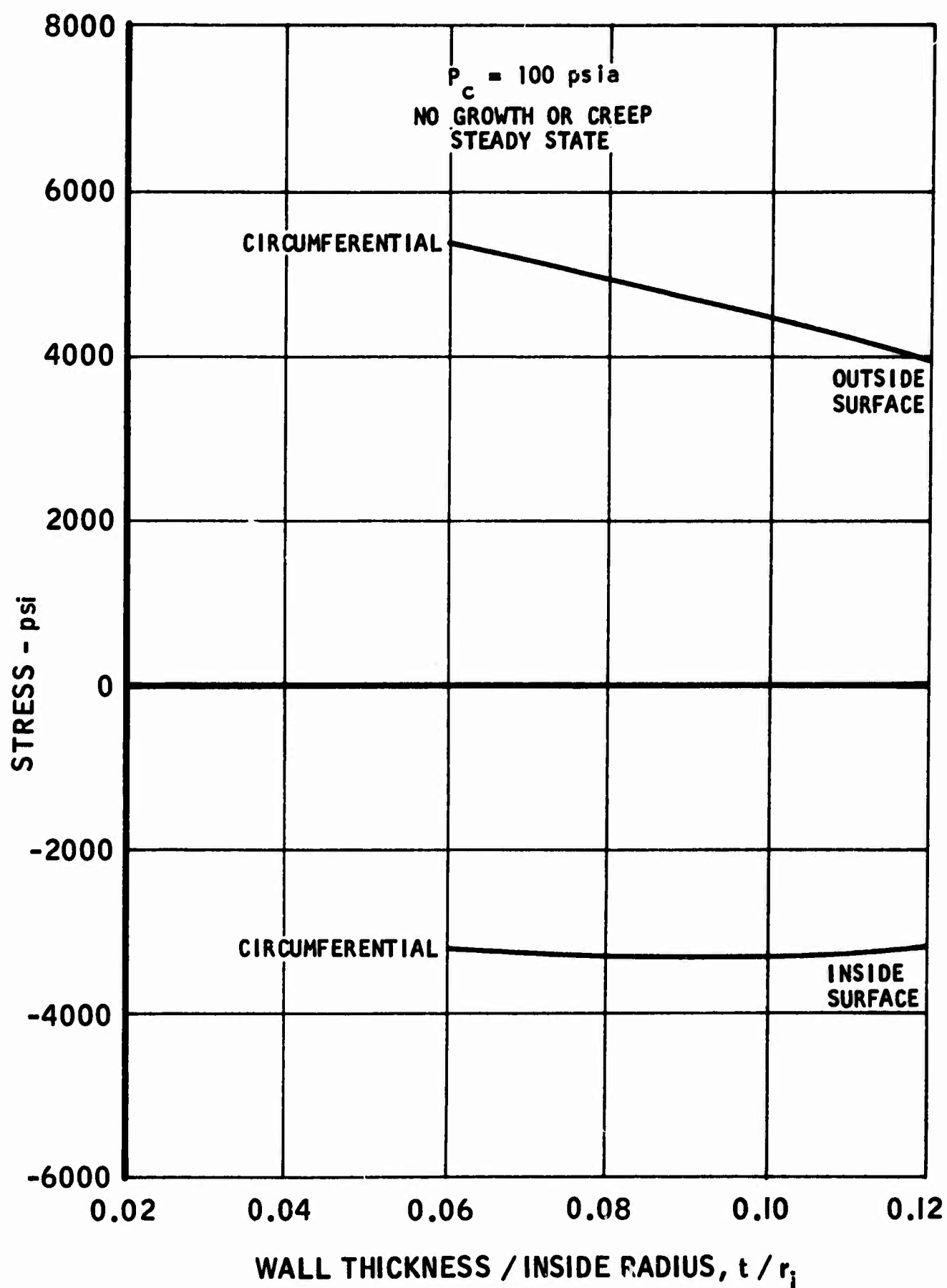


FIGURE 62. Throat Operating Stresses vs.  $t/r$ , 100-lb Thrust Configuration,  
 $N_2O_4/0.5 N_2H_4 - 0.5$  UDMH

UNCLASSIFIED

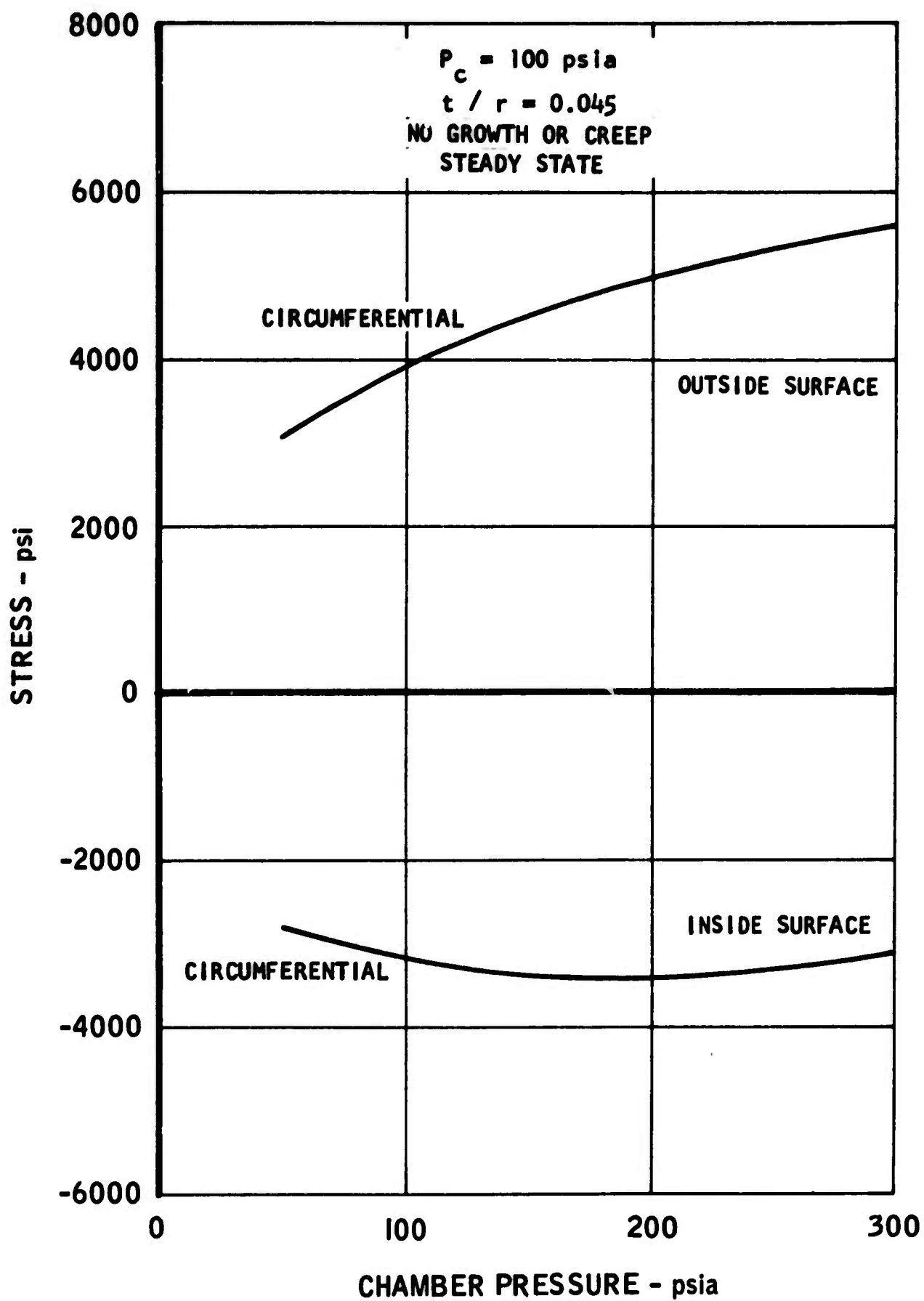


FIGURE 63. Throat Operating Stresses vs. Chamber Pressure, 100-lb Thrust Configuration,  $N_2O_4/0.5 N_2H_4 - 0.5$  UDMH

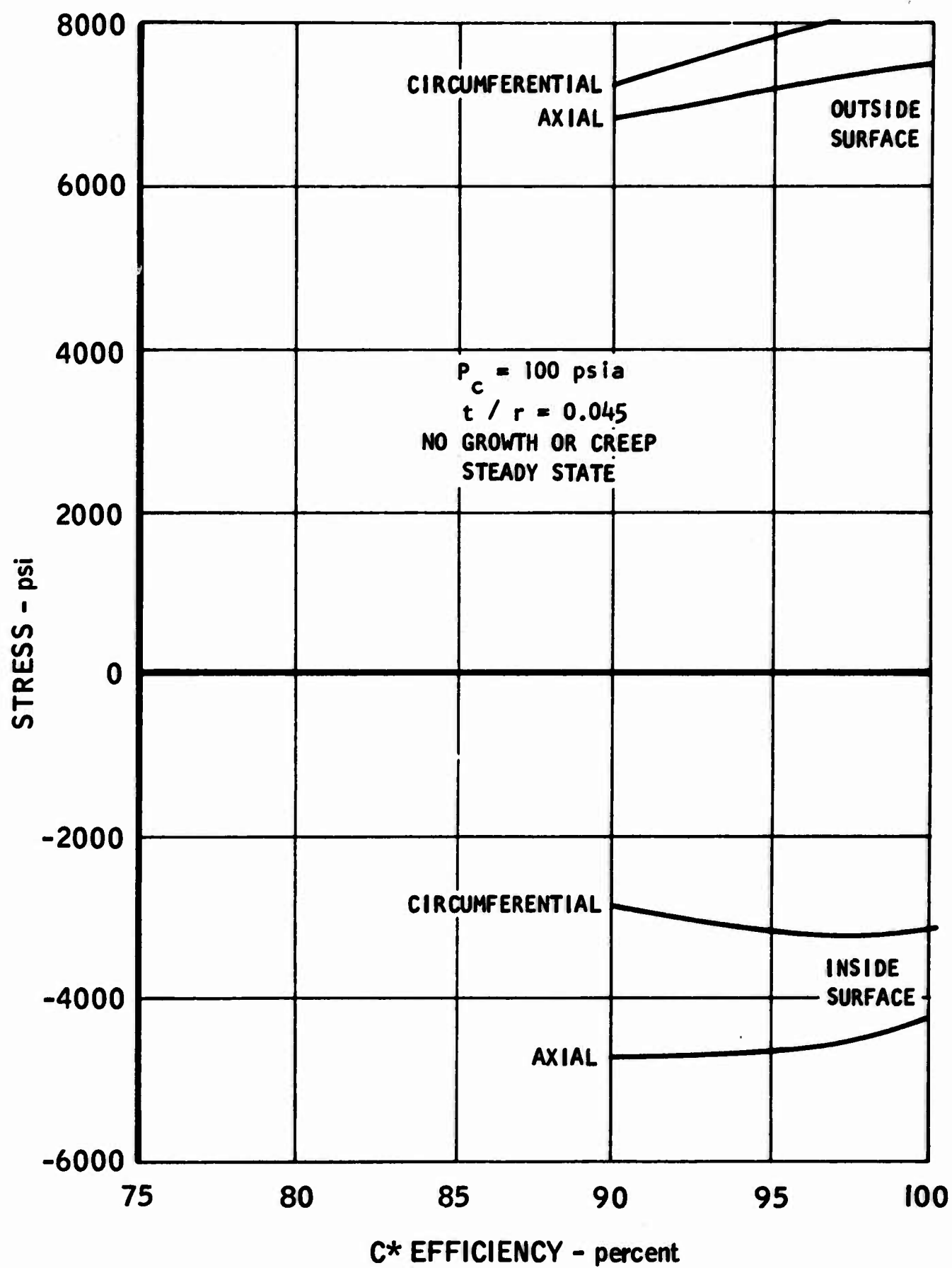


FIGURE 64. Chamber Operating Stresses vs. C\* Efficiency,  
100-lb Thrust Configuration,  $F_2/BA1014$

UNCLASSIFIED

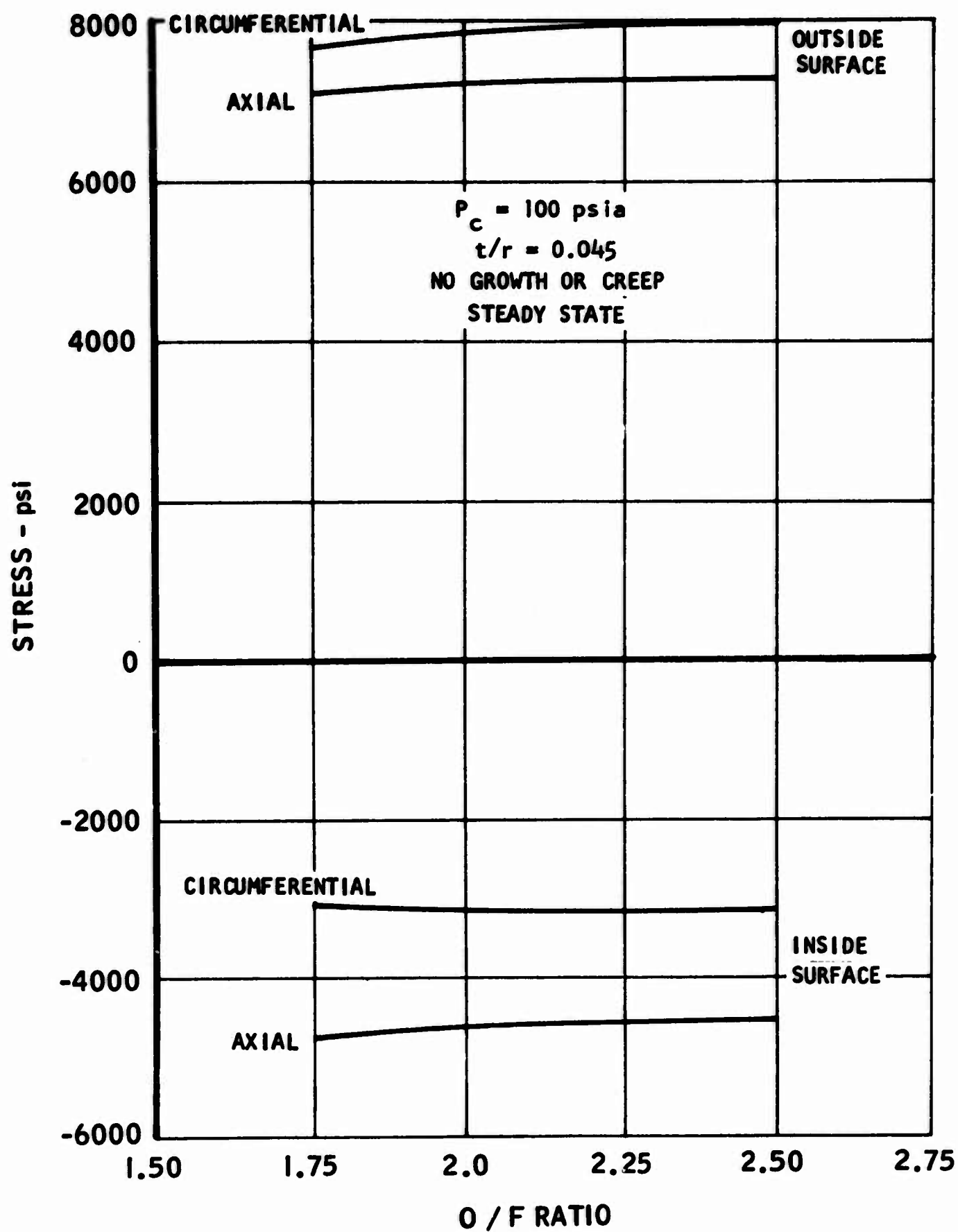


FIGURE 65. Chamber Operating Stresses vs. Oxidizer-Fuel Ratio, 100-lb Thrust Configuration,  $F_2/BA1014$

UNCLASSIFIED

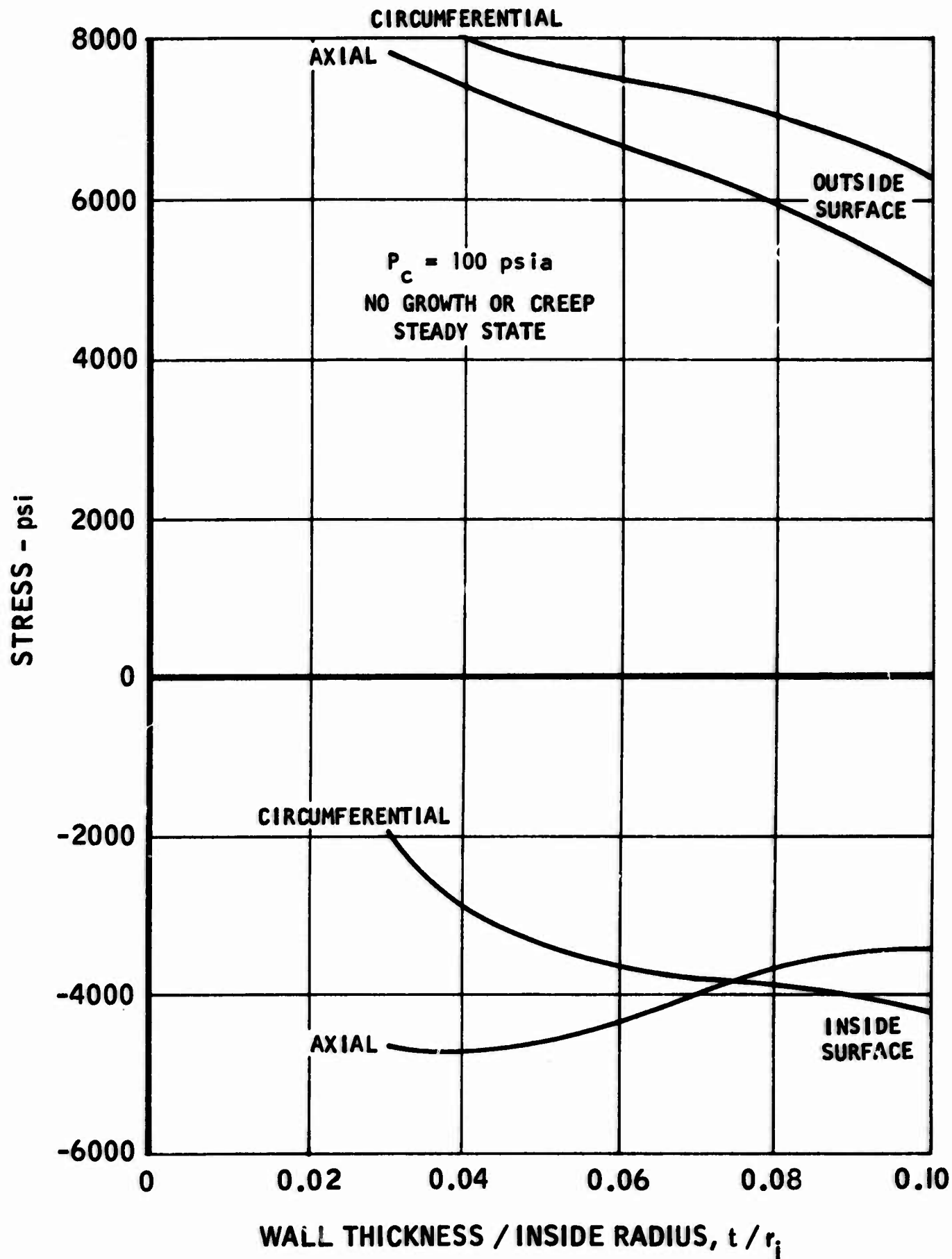


FIGURE 66. Chamber Operating Stresses vs.  $t/r$ ,  
100-lb Thrust Configuration,  $F_2/BA1014$

UNCLASSIFIED

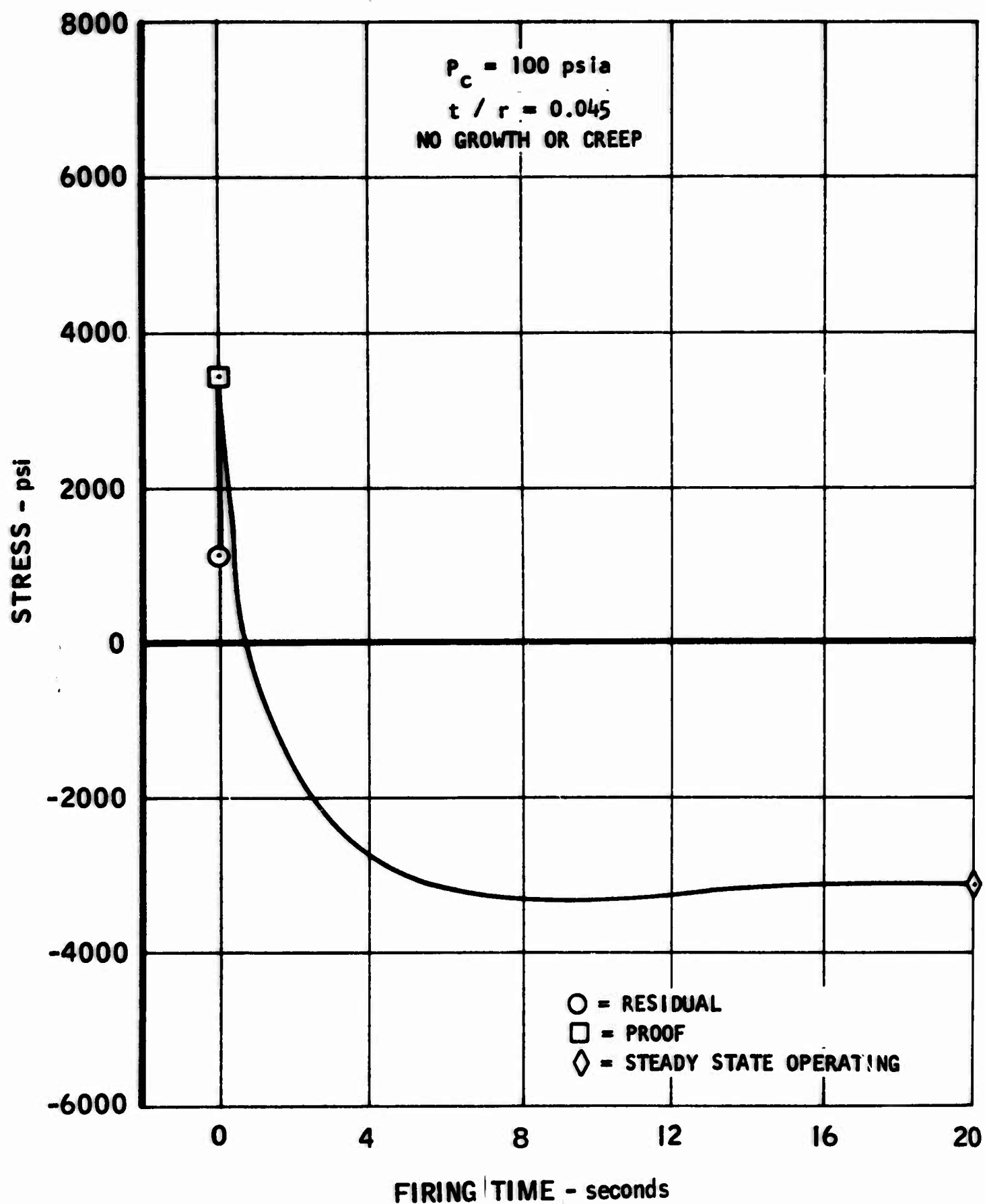


FIGURE 67. Chamber Transient Stresses, Circumferential Stress on Inside Surface vs. Time, 100-lb Thrust Configuration,  $F_2/BA1014$

UNCLASSIFIED

UNCLASSIFIED

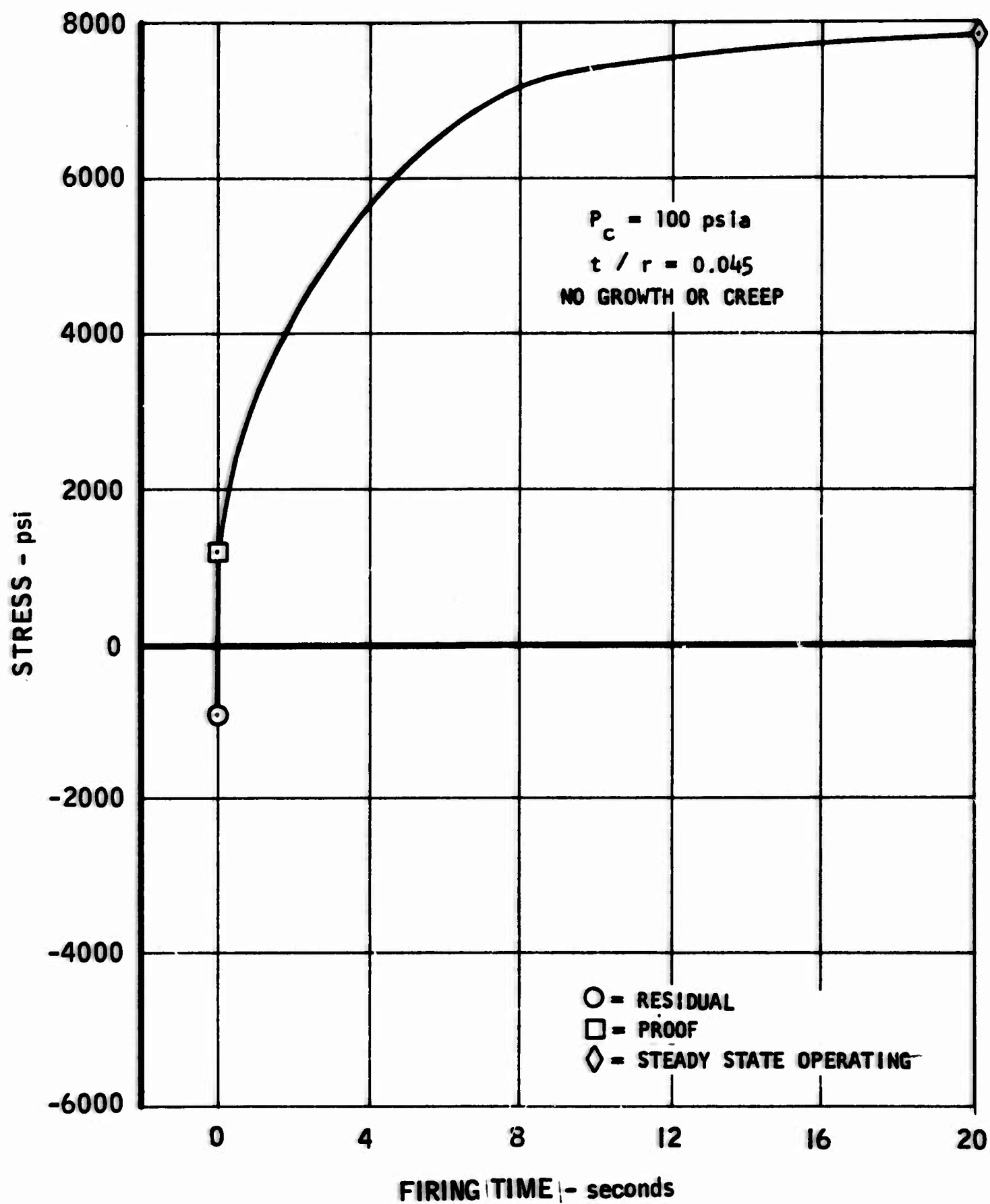


FIGURE 68. Chamber Transient Stresses, Circumferential Stress on Outside Surface vs. Time, 100-lb Thrust Configuration, F<sub>2</sub>/BA1014

UNCLASSIFIED



UNCLASSIFIED

AFRPL-TR-66-95

Report 6106

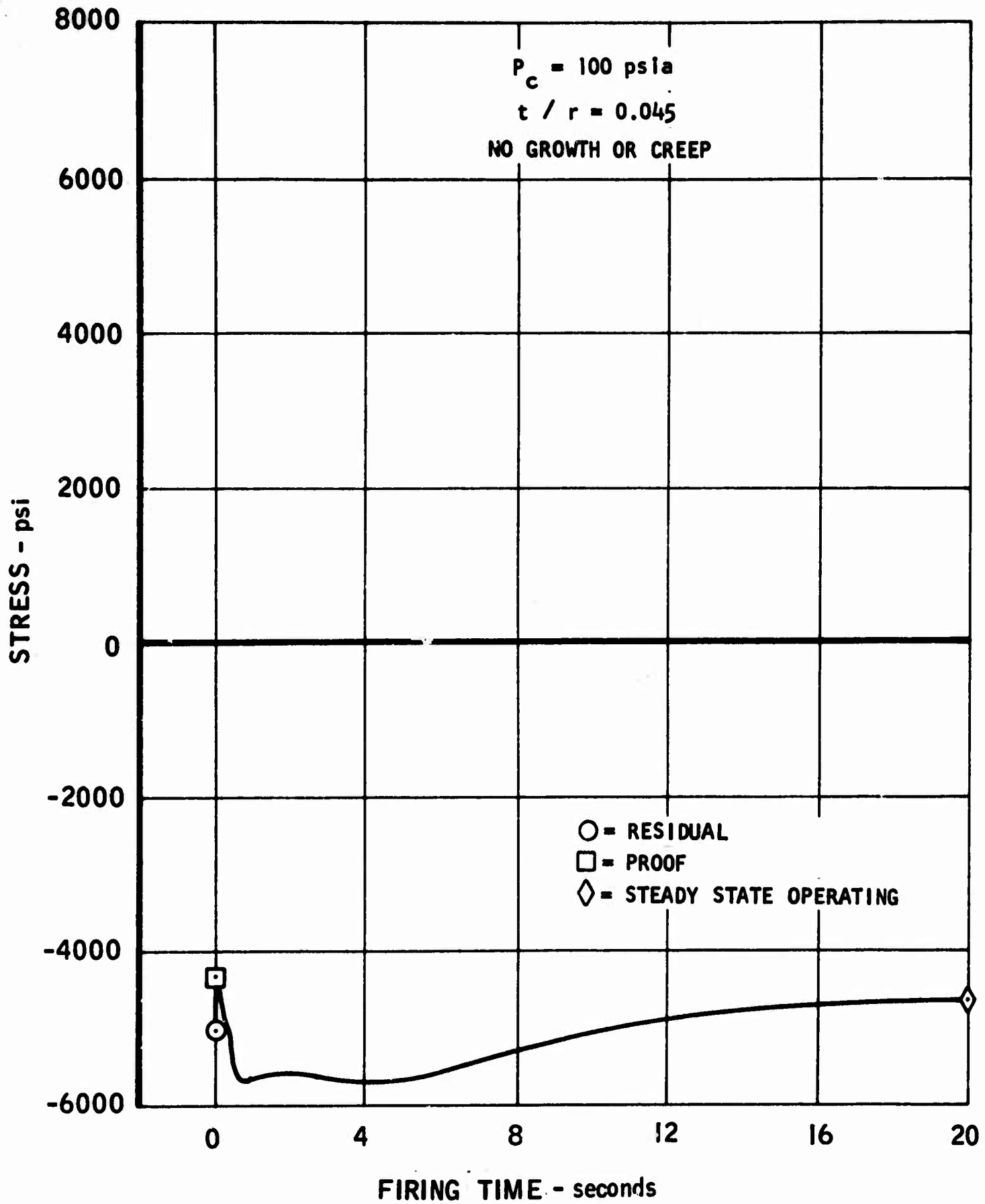


FIGURE 69. Chamber Transient Stresses, Axial Stress on Inside Surface vs. Time, 100-lb Thrust Configuration,  $F_2/BA1014$

5016-17

UNCLASSIFIED

UNCLASSIFIED

AFRPL-TR-66-95

Report 6106

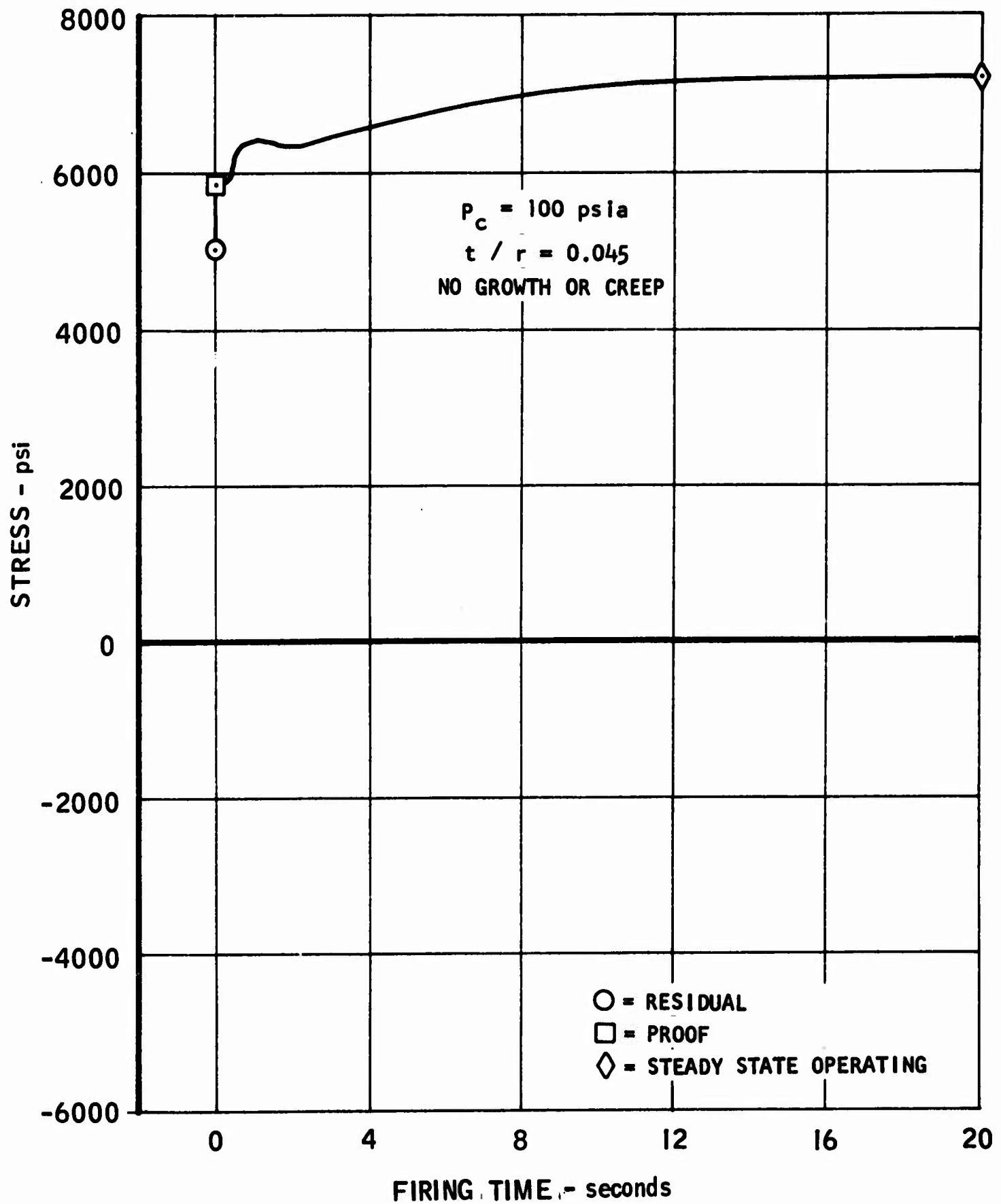


FIGURE 70. Chamber Transient Stresses, Axial Stresses on Outside Surface vs. Time, 100-lb Thrust Configuration,  $F_2/BA1014$

5016-18

UNCLASSIFIED

UNCLASSIFIED

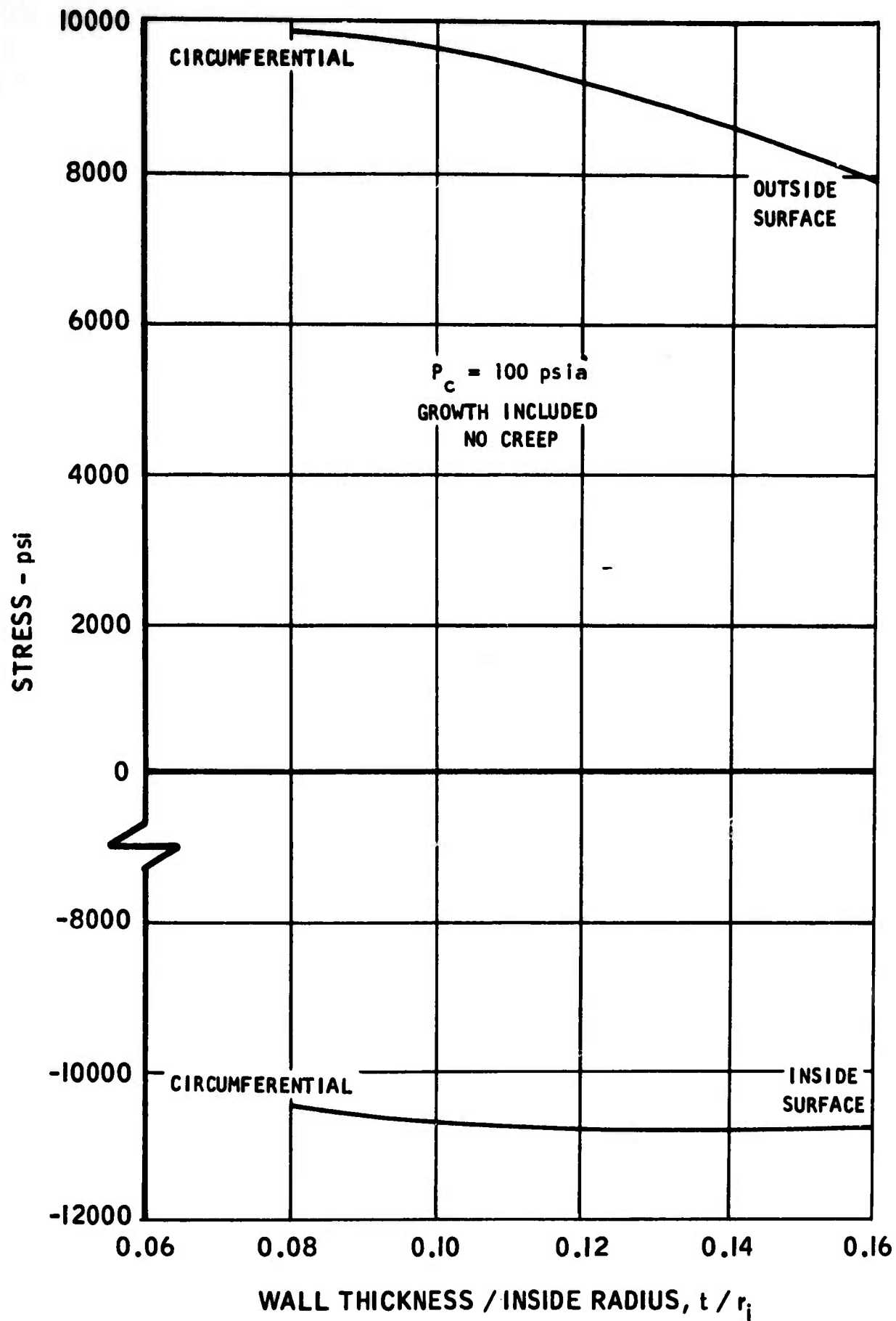


FIGURE 71. Throat Operating Stresses at 600 seconds vs.  $t/r$ ,  
100-lb Thrust Configuration,  $F_2/BA1014$

UNCLASSIFIED

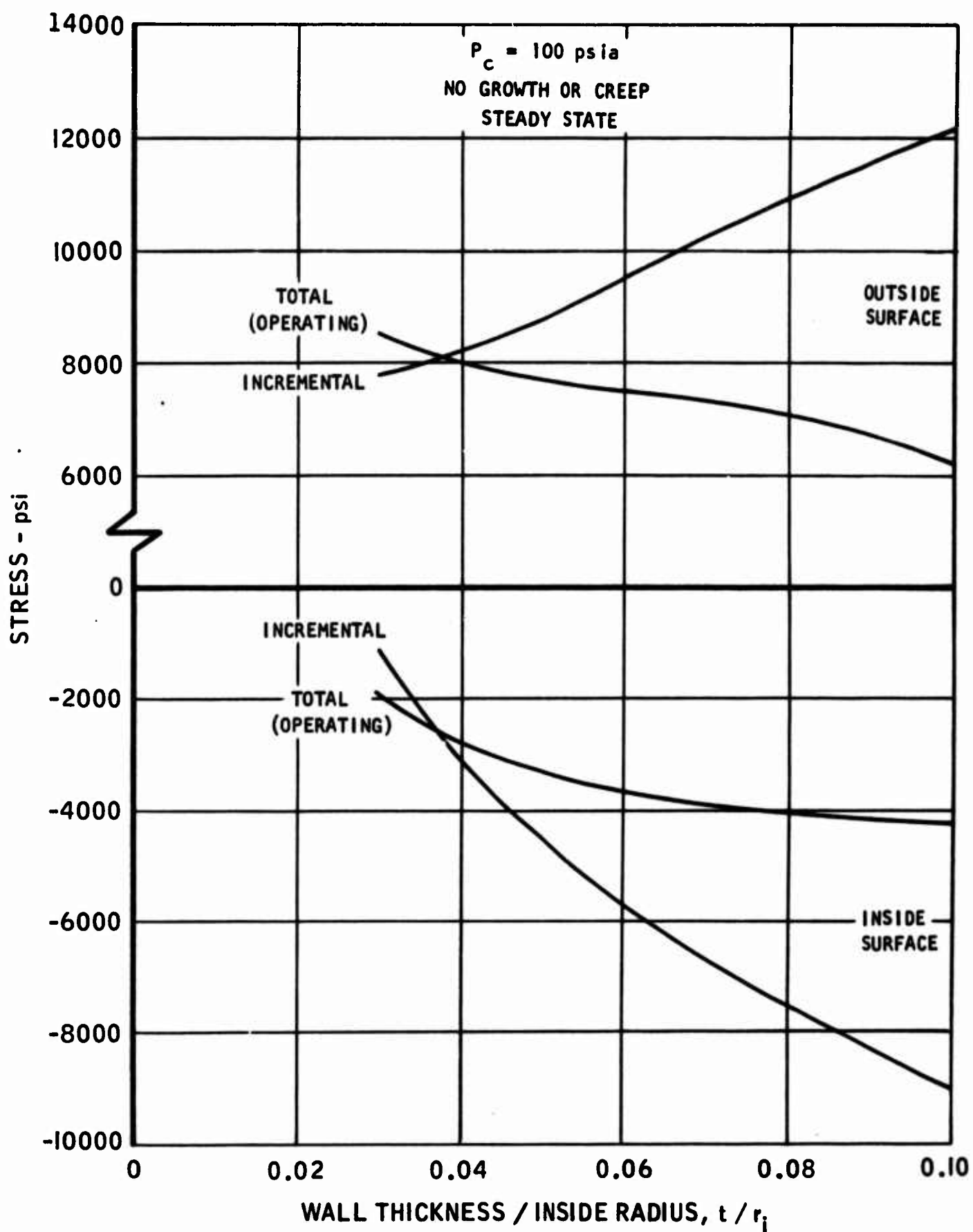


FIGURE 72. Chamber Total and Incremental Circumferential Stresses vs.  $t/r$ , 100-lb Thrust Configuration,  $F_2/BA1014$

UNCLASSIFIED

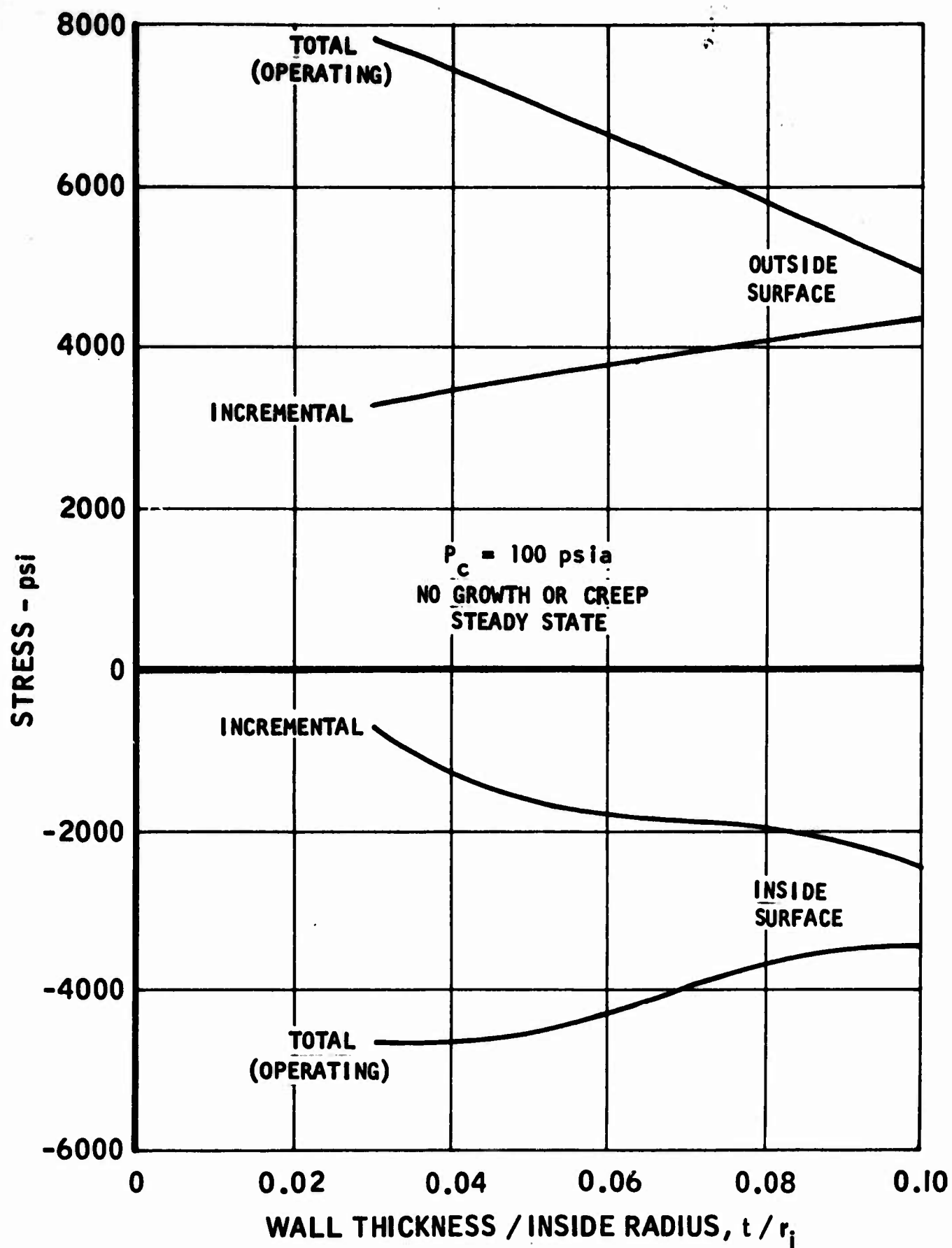


FIGURE 73. Chamber Total and Incremental Axial Stresses vs.  $t/r$ ,  
100-lb Thrust Configuration,  $F_2/BA1014$

UNCLASSIFIED

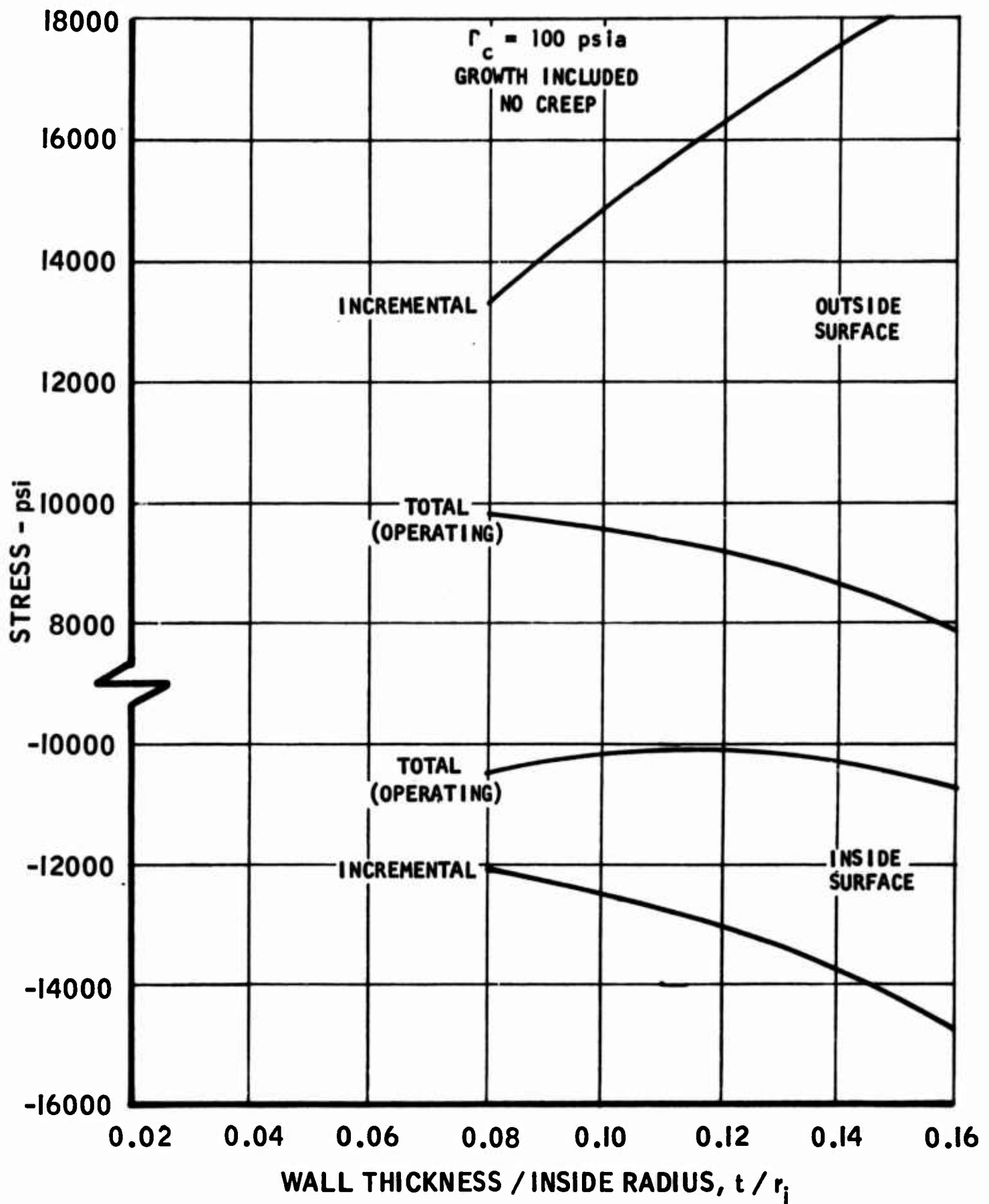


FIGURE 74. Throat Total and Incremental Circumferential Stresses at 600 seconds vs.  $t/r_i$ , 100-lb Thrust Configuration,  $F_2/BA1014$

UNCLASSIFIED

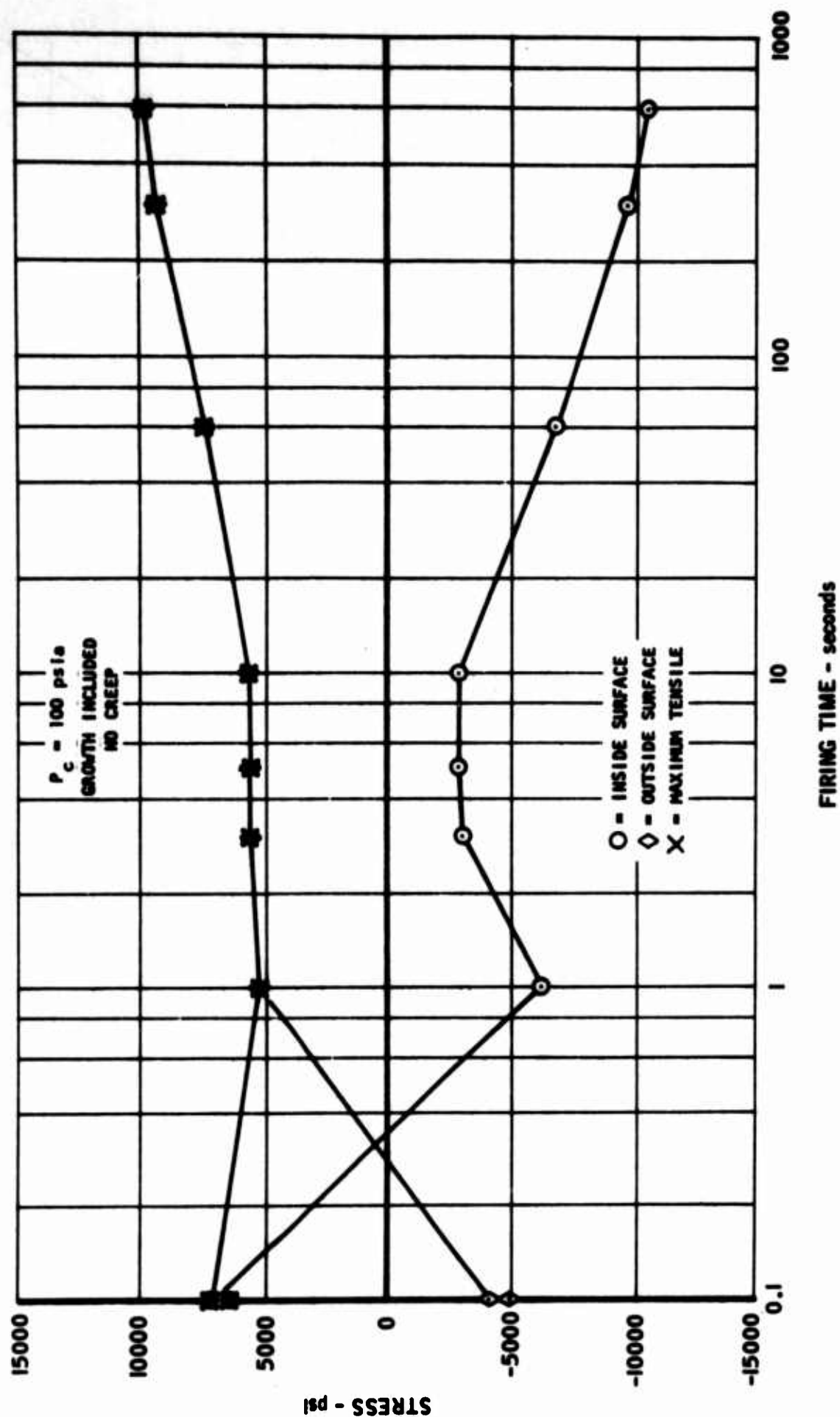


FIGURE 75. Throat Circumferential Operating Stresses vs. Firing Time,  
100-lb Thrust Configuration,  $F_2/BAL014$ ,  $t/r = 0.08$

UNCLASSIFIED



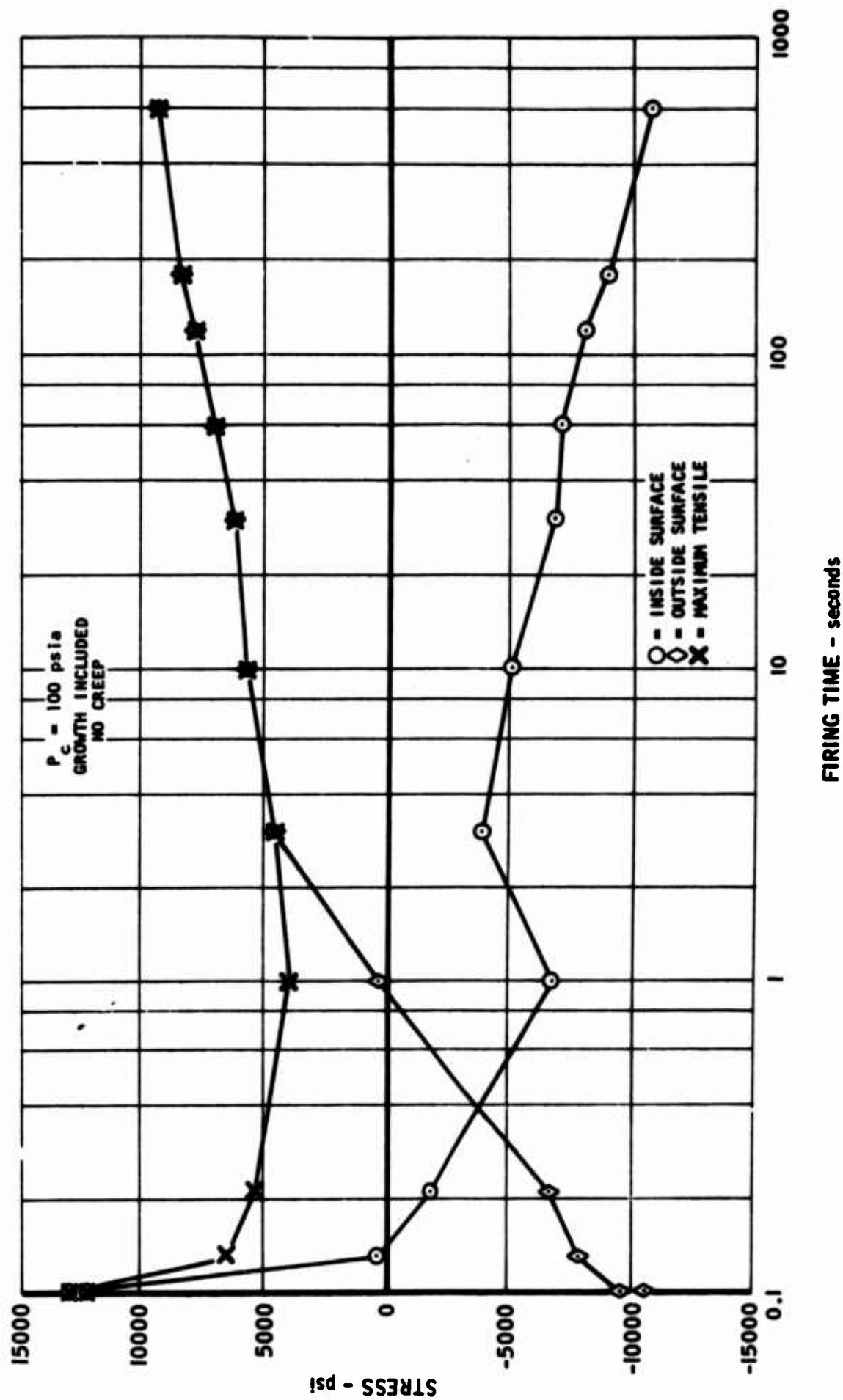


FIGURE 76. Throat Circumferential Operating Stresses vs. Firing Time, 100-lb Thrust Configuration,  $F_2/BA1014$ ,  $t/r = 0.12$

UNCLASSIFIED

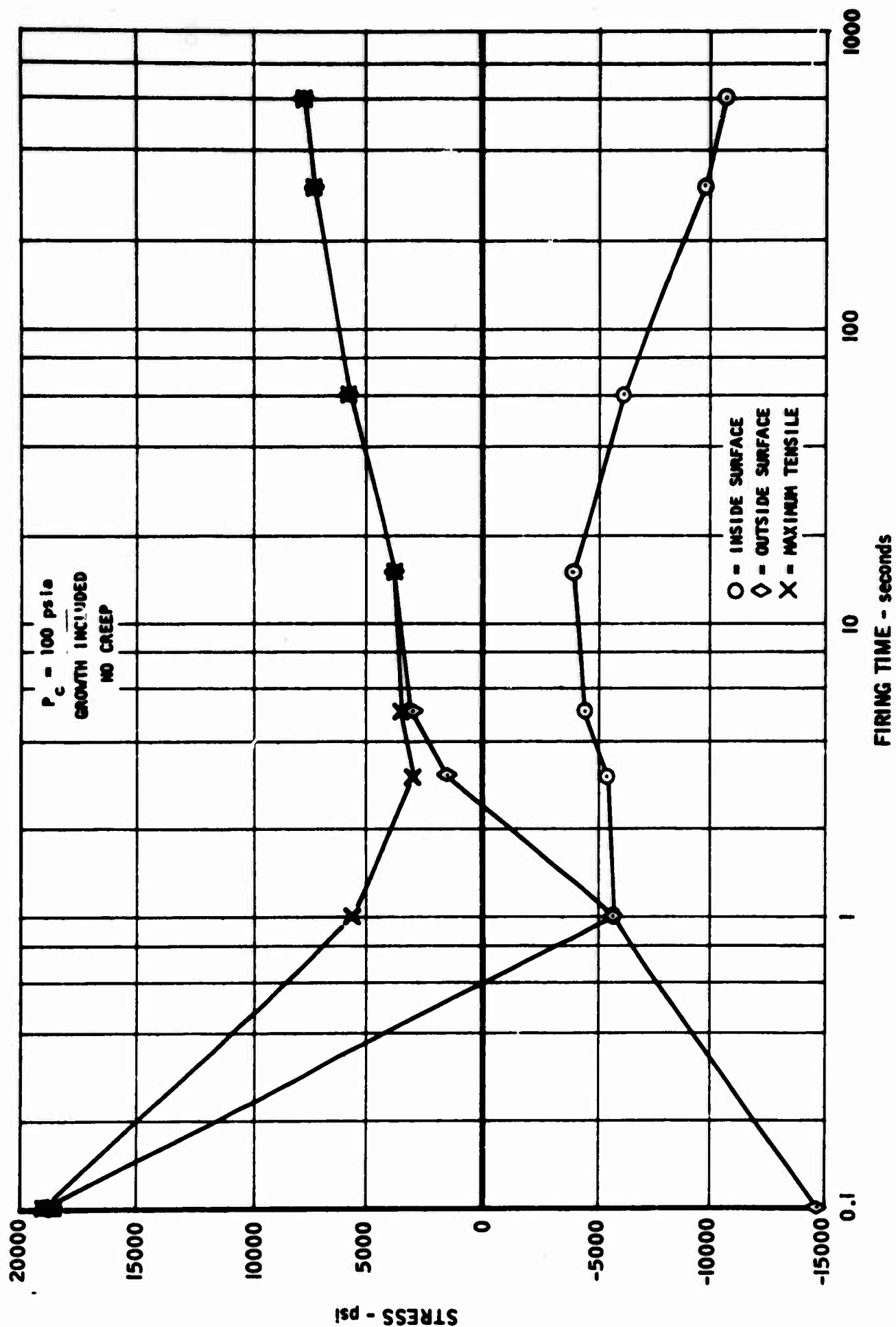


FIGURE 77. Throat Circumferential Operating Stresses vs. Firing Time,  
100-lb Thrust Configuration, F<sub>2</sub>/BAL014, t/r = 0.16

UNCLASSIFIED

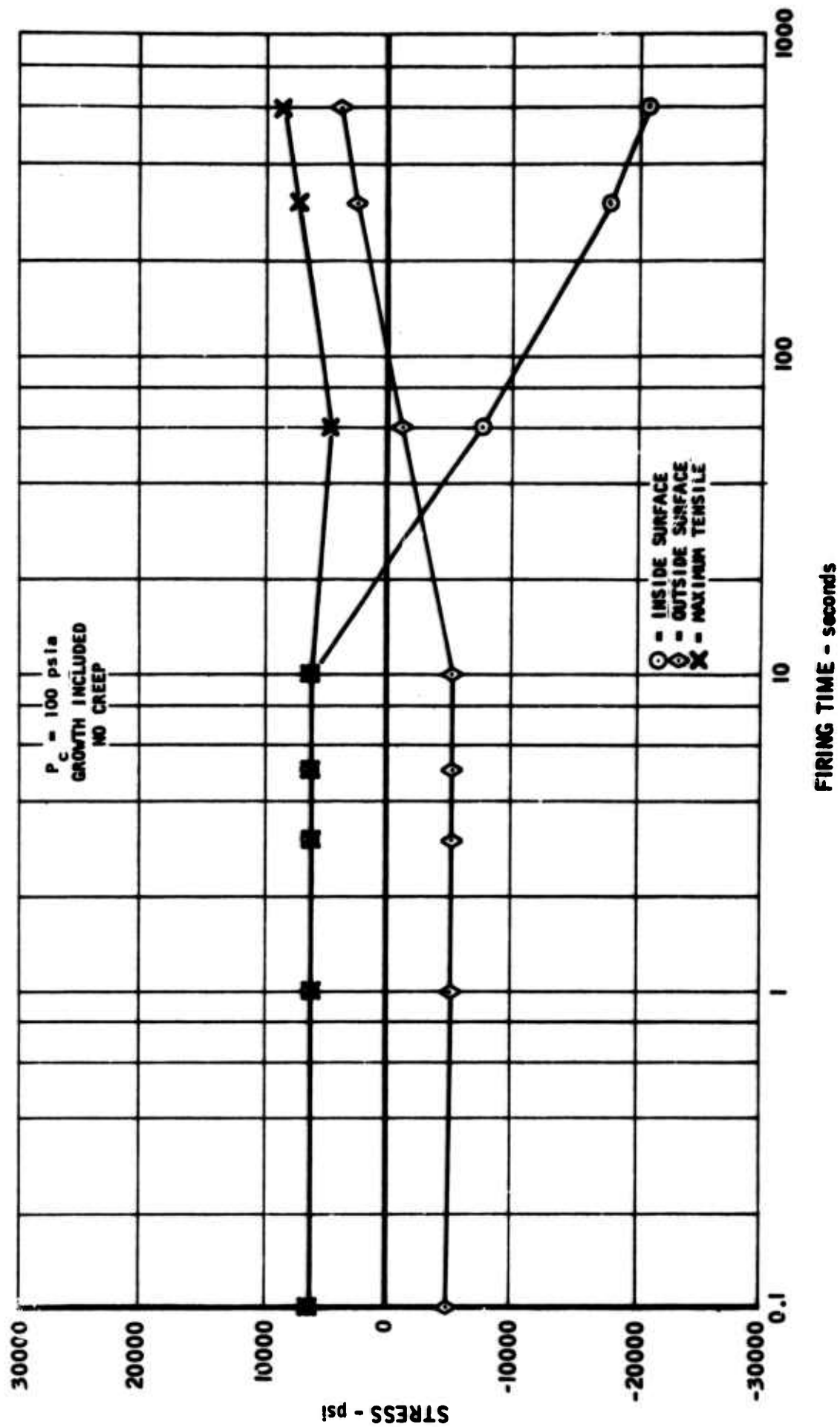


FIGURE 78. Throat Circumferential Posttension Stresses vs. Firing Time, 100-lb Thrust Configuration,  $F_0/BA1014$ ,  $t/r = 0.08$

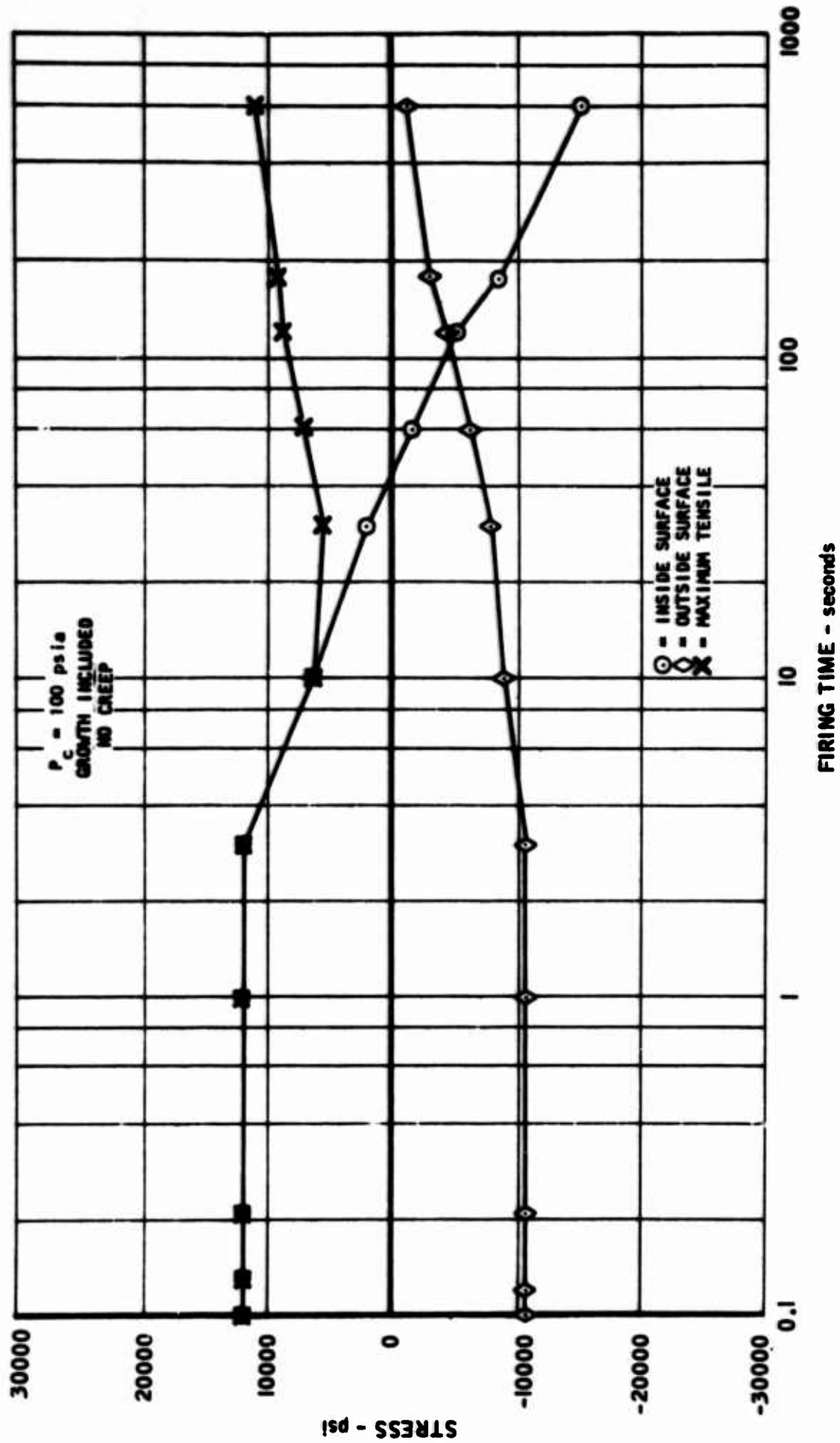


FIGURE 79. Throat Circumferential Postrun Stresses vs. Firing Time,  
100-lb Thrust Configuration,  $F_2/\text{BAL014}$ ,  $t/r = 0.12$

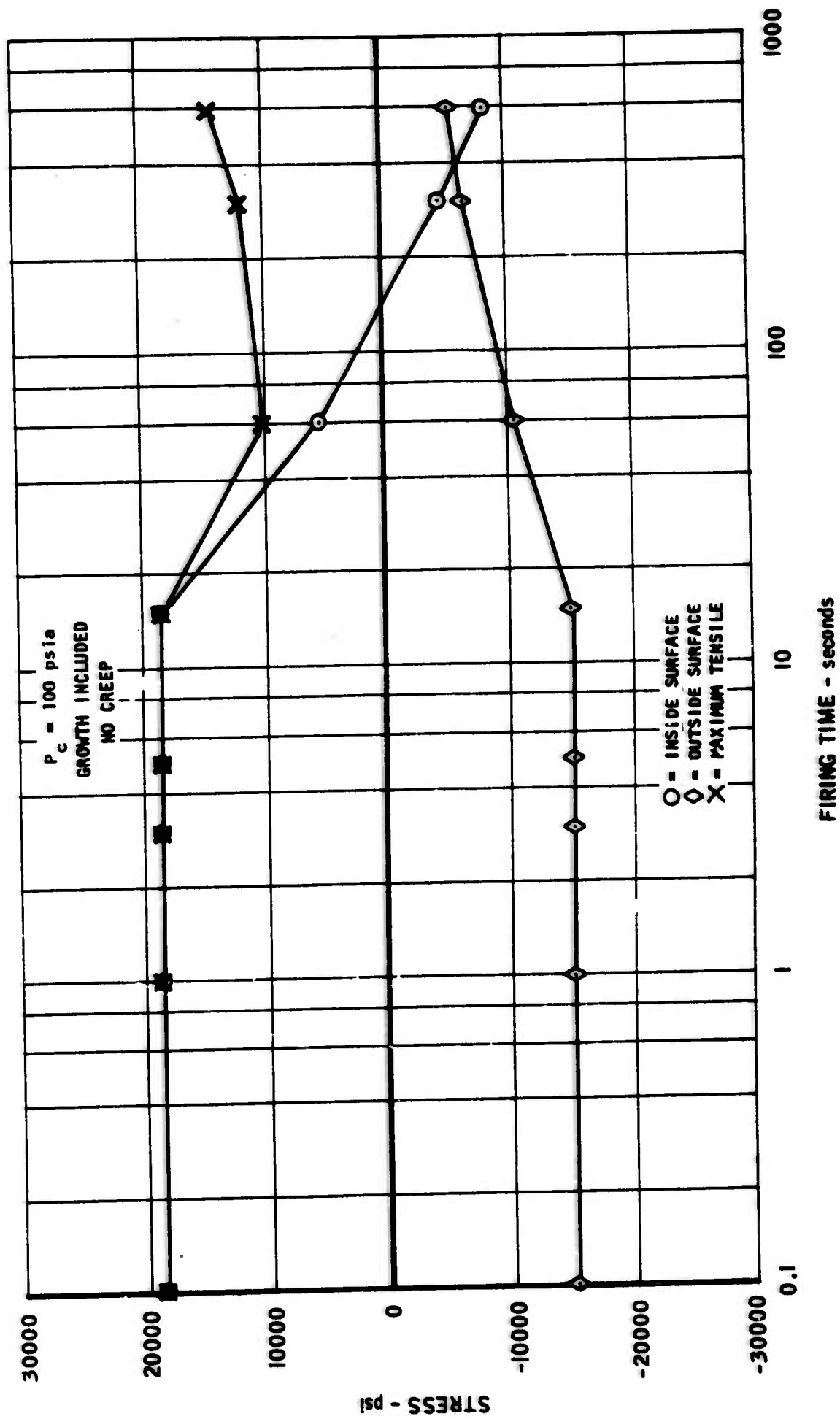


FIGURE 80. Throat Circumferential Postrun Stresses vs. Firing Time,  
100-lb Thrust Configuration,  $F_2/BA101^b$ ,  $t/r = 0.16$

UNCLASSIFIED

AFRPL-TR-66-95

Report 6106

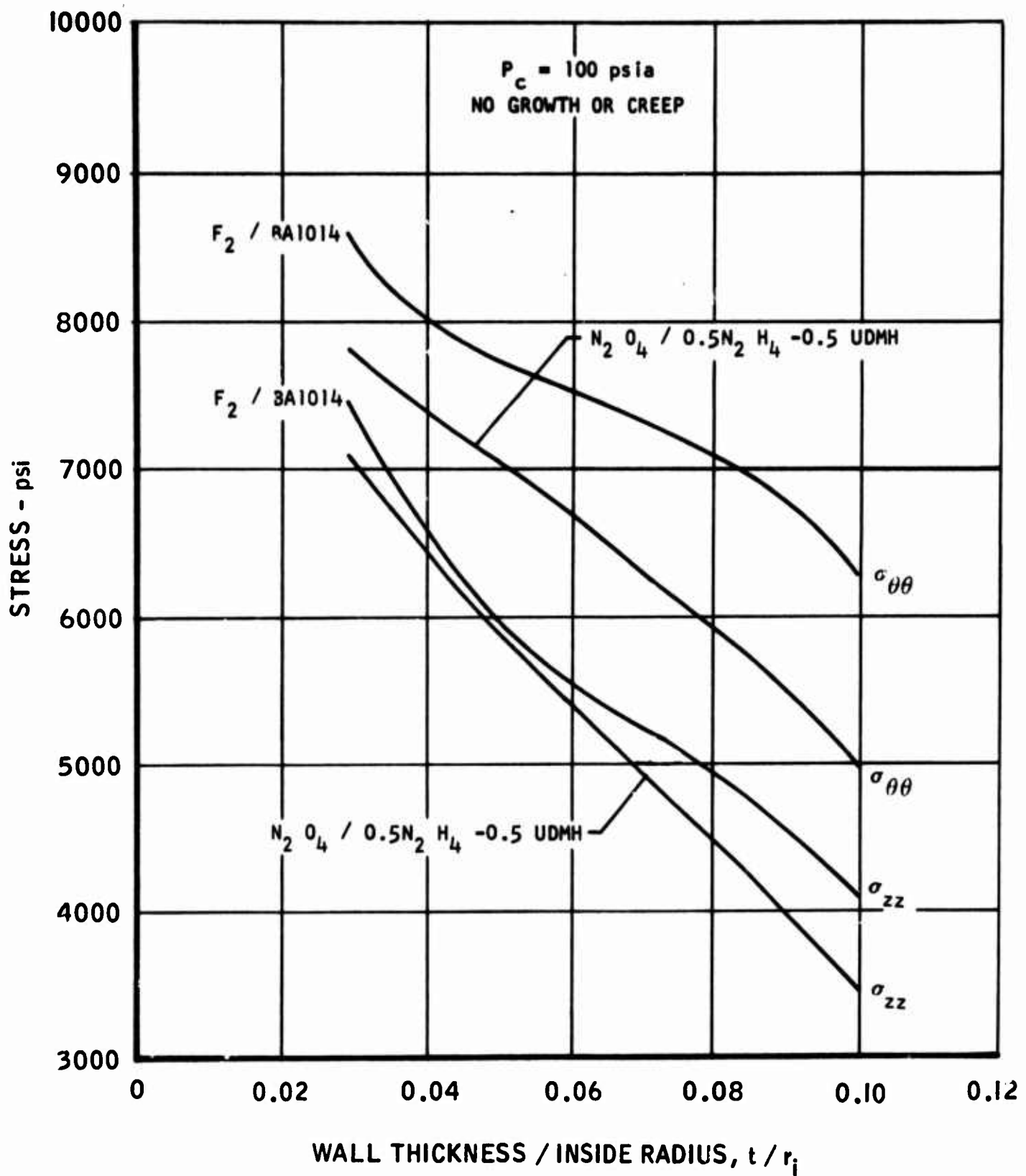


FIGURE 81. Comparison of Propellants, Chamber Operating Stresses on Outside Surface vs.  $t/r$ , 100-lb Thrust Configuration

5016-180

UNCLASSIFIED

UNCLASSIFIED

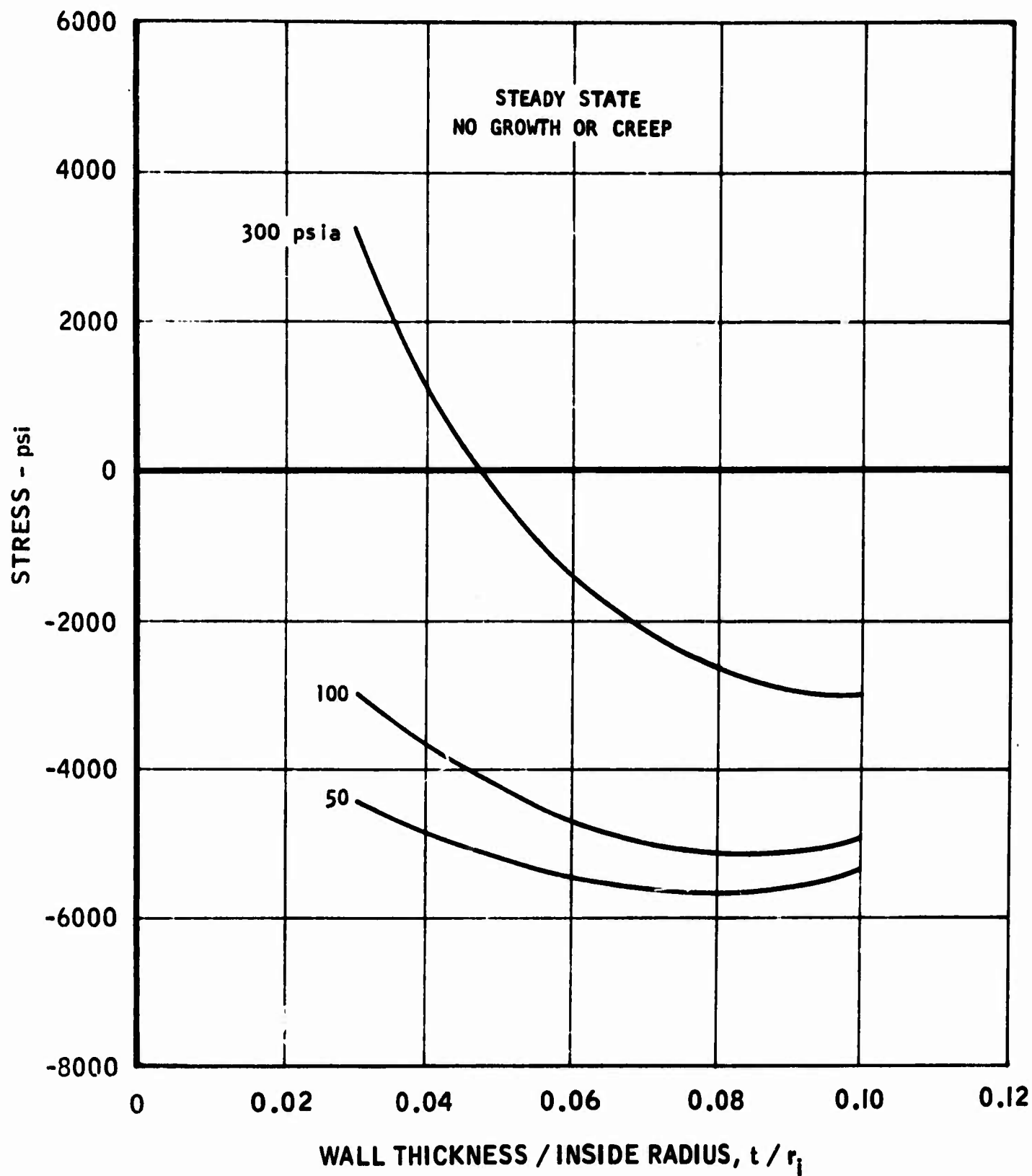


FIGURE 82. Chamber Circumferential Operating Stresses on Inside Surface vs.  $t/r$ , 1000-lb Thrust Configuration,  $N_2O_4/0.5 N_2H_4 - 0.5$  UDMH

UNCLASSIFIED



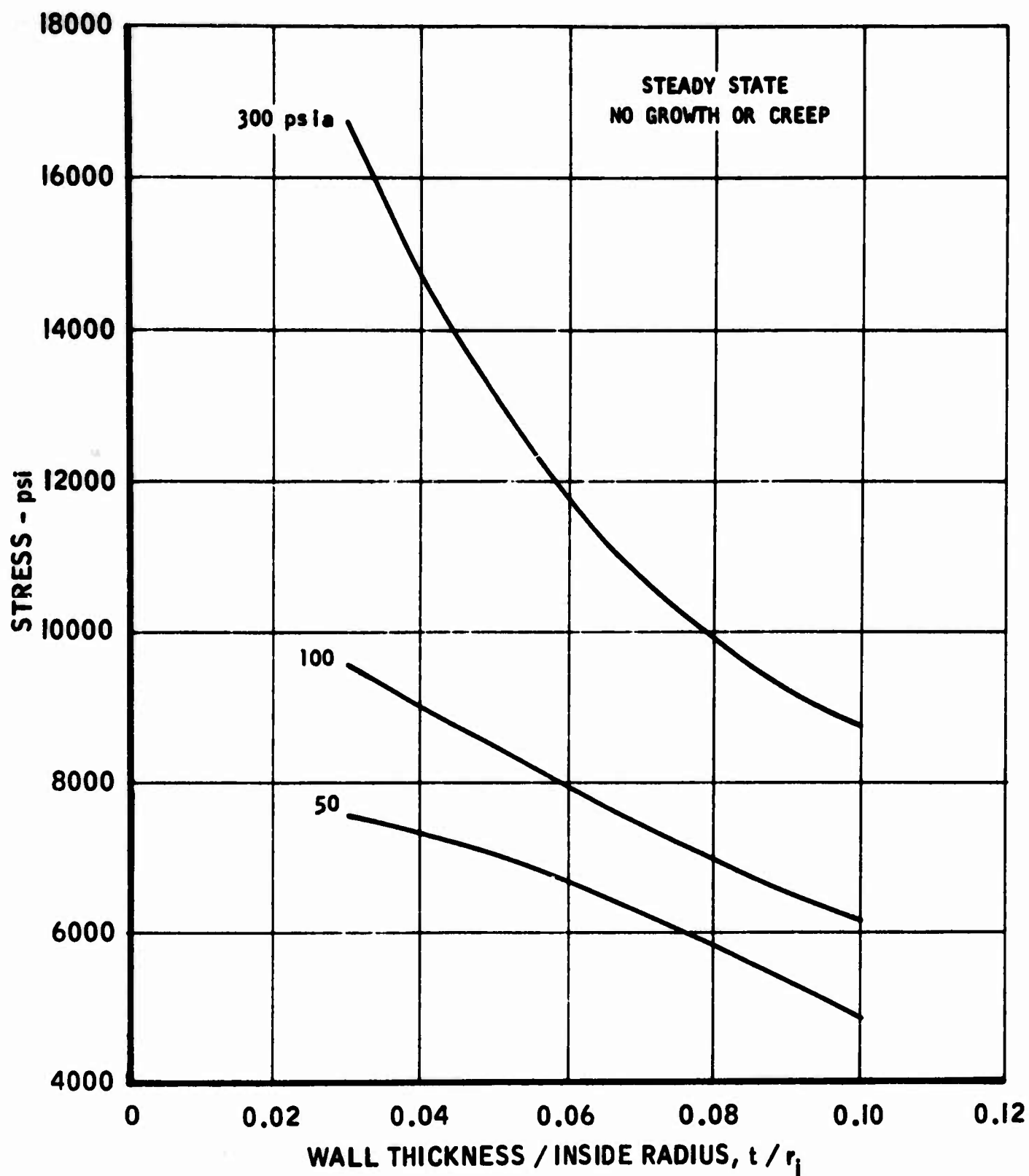


FIGURE 83. Chamber Circumferential Operating Stresses on Outside Surface vs.  $t/r$ , 1000-lb Thrust Configuration,  $N_2O_4/0.5 N_2H_4 - 0.5 UDMH$

UNCLASSIFIED

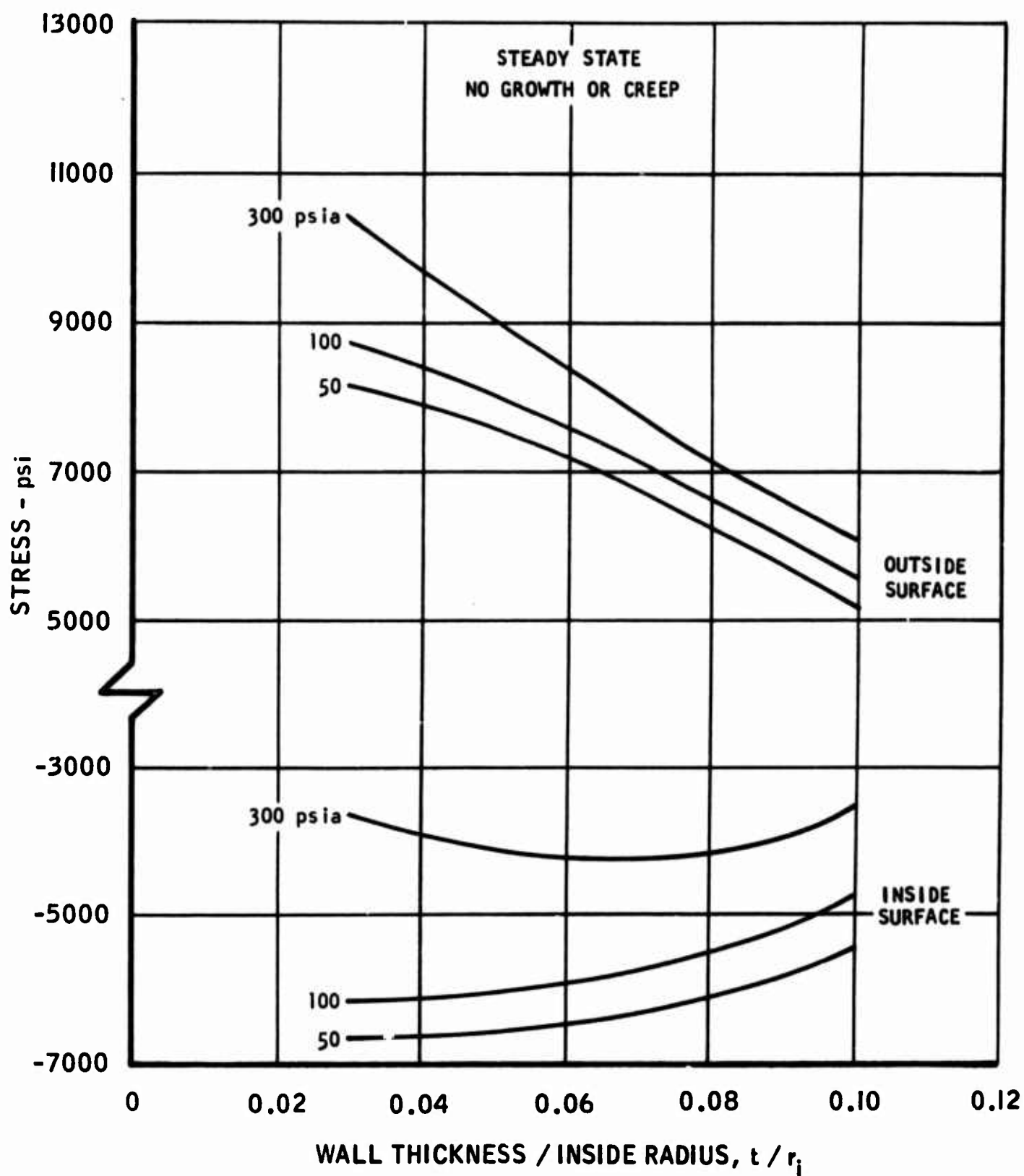


FIGURE 2. Chamber Axial Operating Stresses vs.  $t/r$ , 1000-lb Thrust Configuration,  $N_2O_4/0.5 N_2H_4 - 0.5$  UDME

UNCLASSIFIED

UNCLASSIFIED

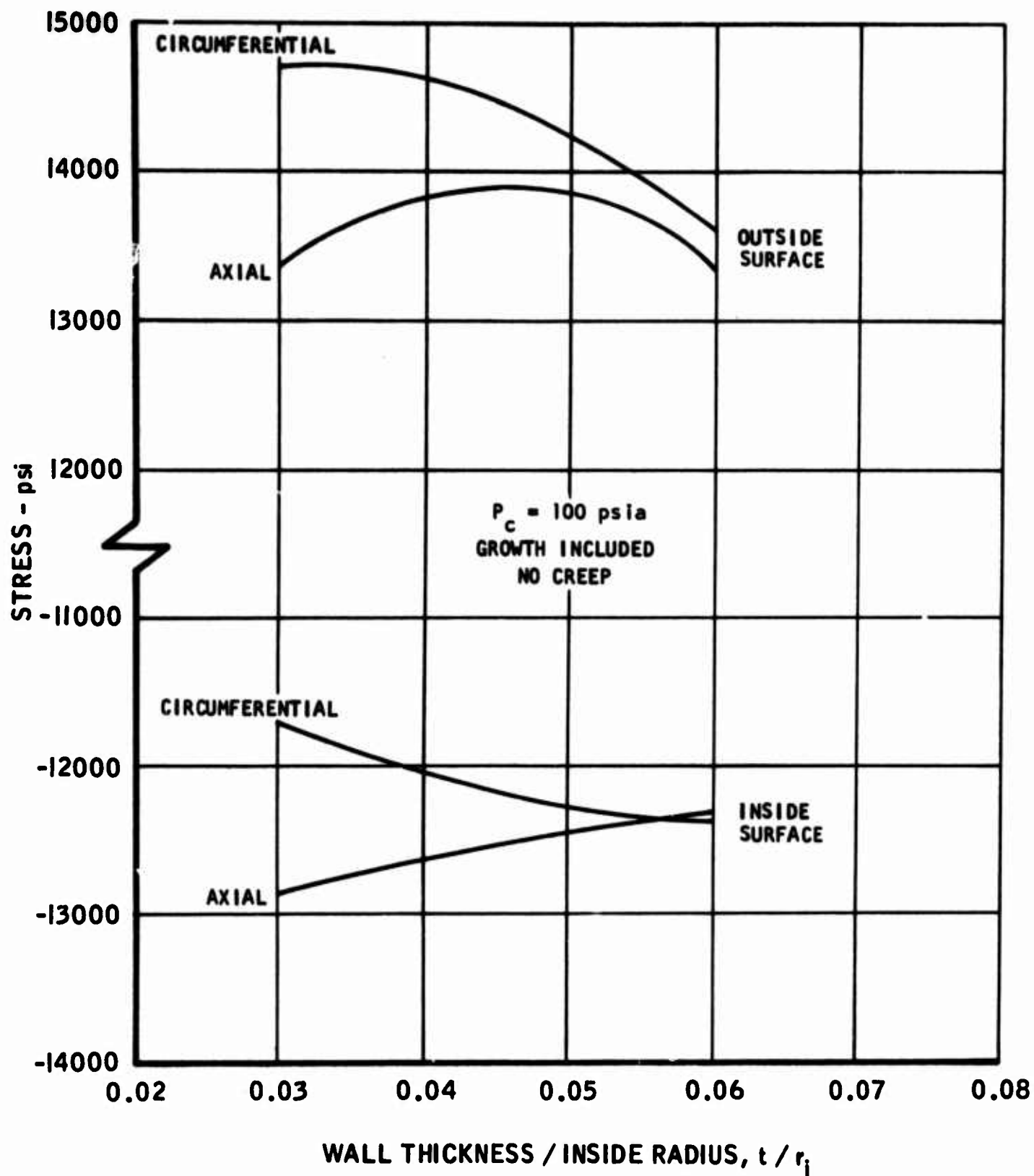


FIGURE 85. Chamber Operating Stresses at 600 seconds vs.  $t/r$ ,  
5000-lb Thrust Configuration,  $F_2/BA1014$

UNCLASSIFIED

UNCLASSIFIED

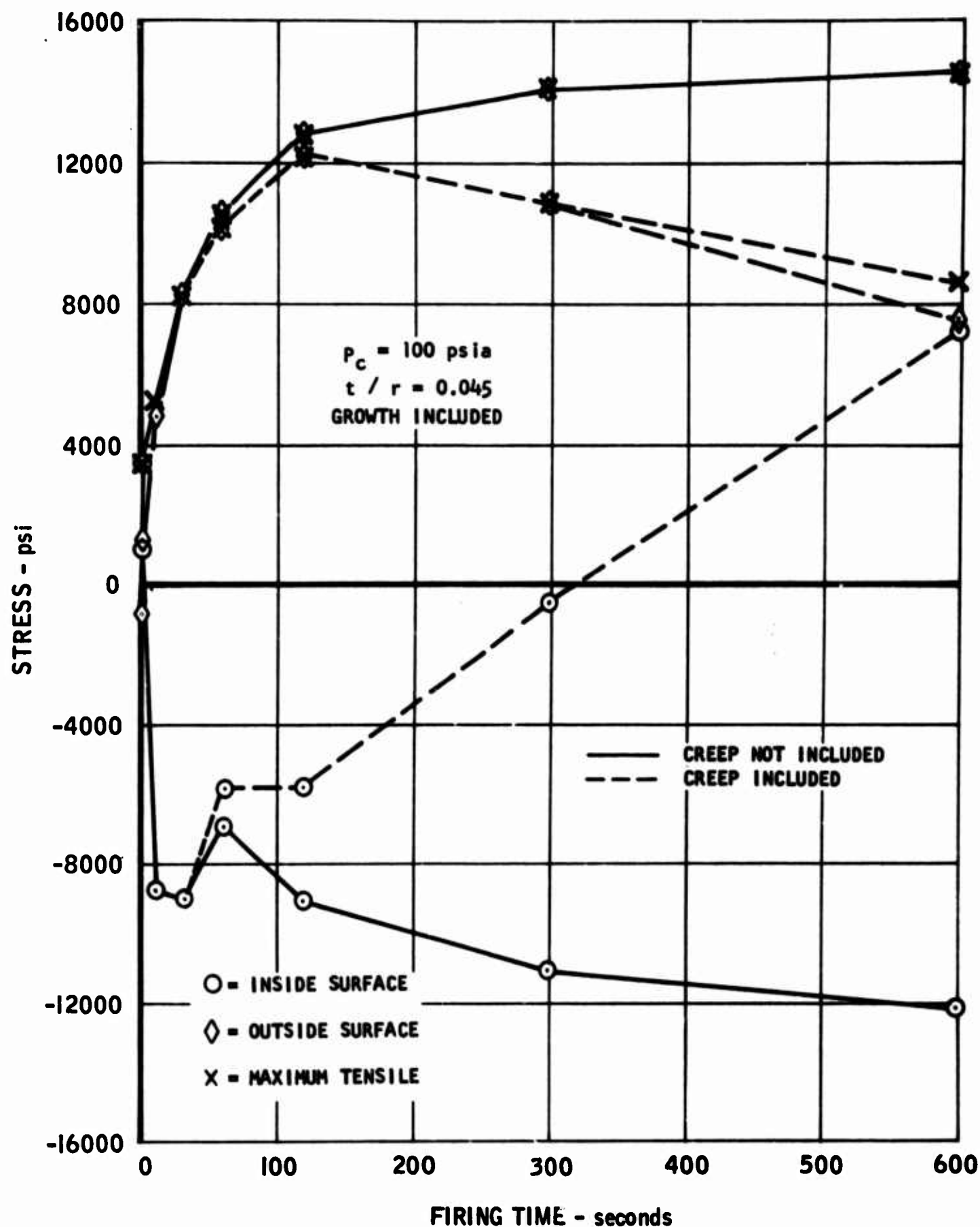


FIGURE 86. Chamber Circumferential Operating Stresses vs. Firing Time,  
5000-lb Thrust Configuration,  $F_2/BA1014$

UNCLASSIFIED

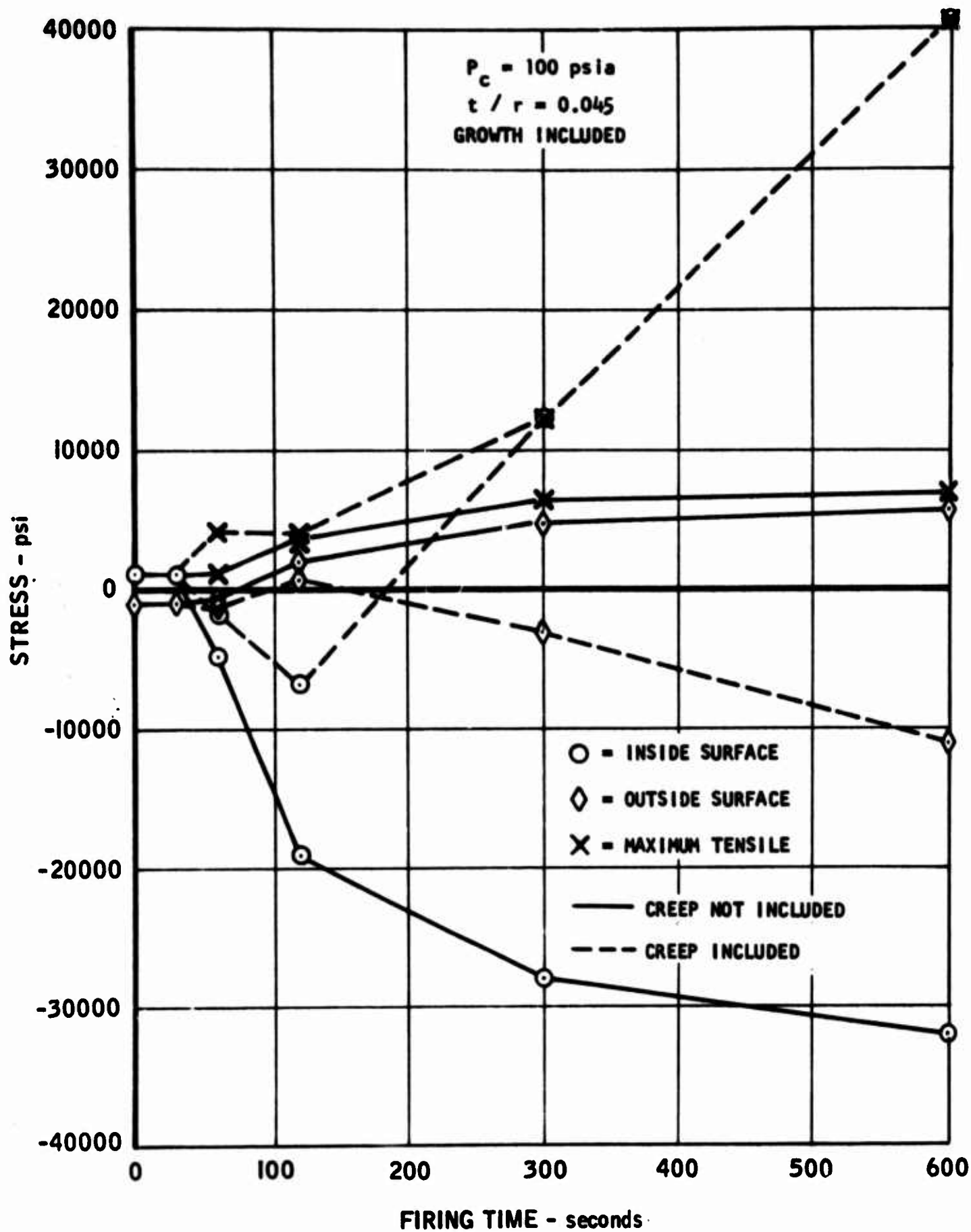


FIGURE 87. Chamber Circumferential Postrun Stresses vs. Firing Time, 5000-lb Thrust Configuration,  $F_2/BA1014$

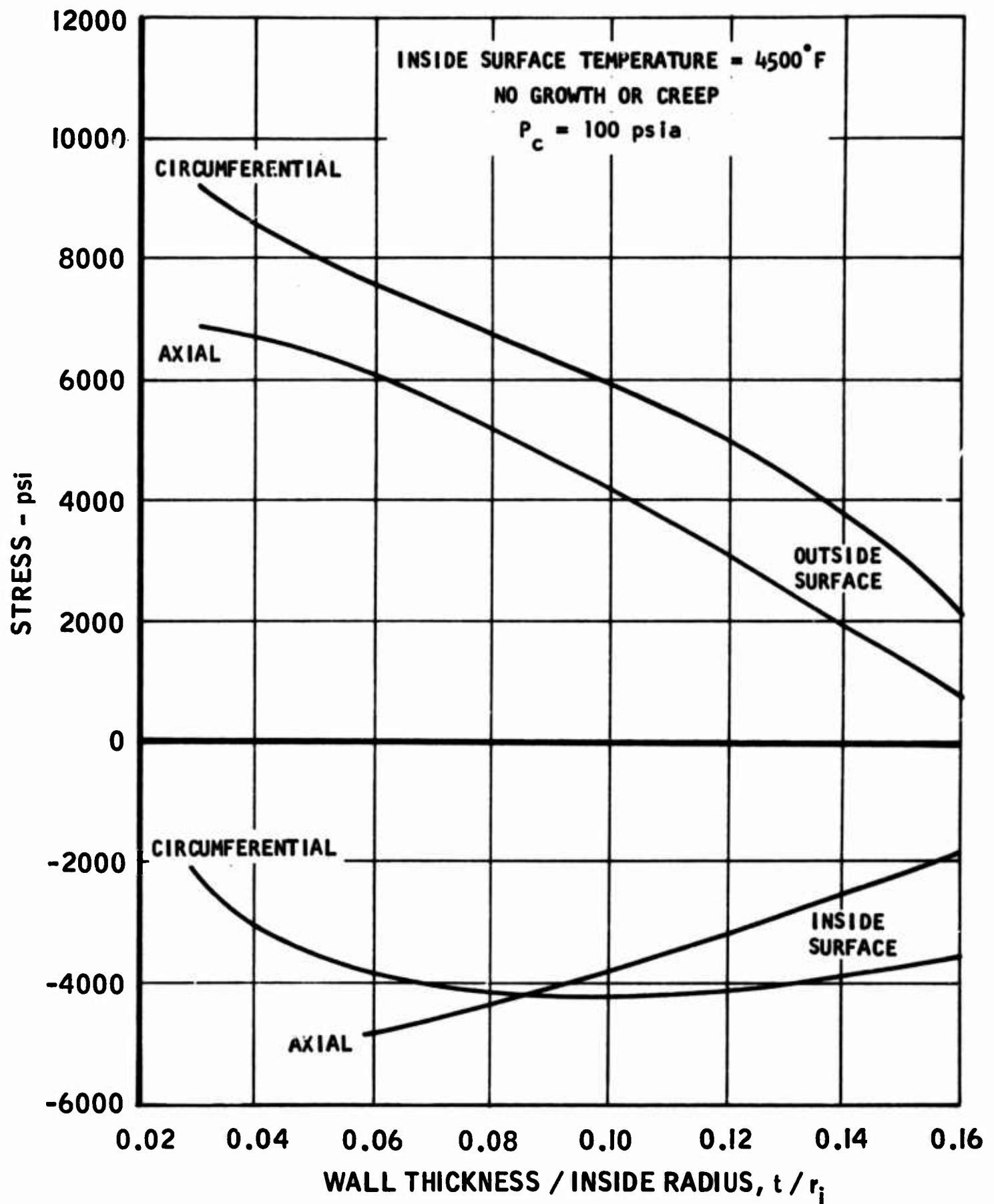


FIGURE 88. Operating Stresses, Controlled Wall Temperature Chamber, vs.  $t/r$ , 100-lb Thrust Configuration

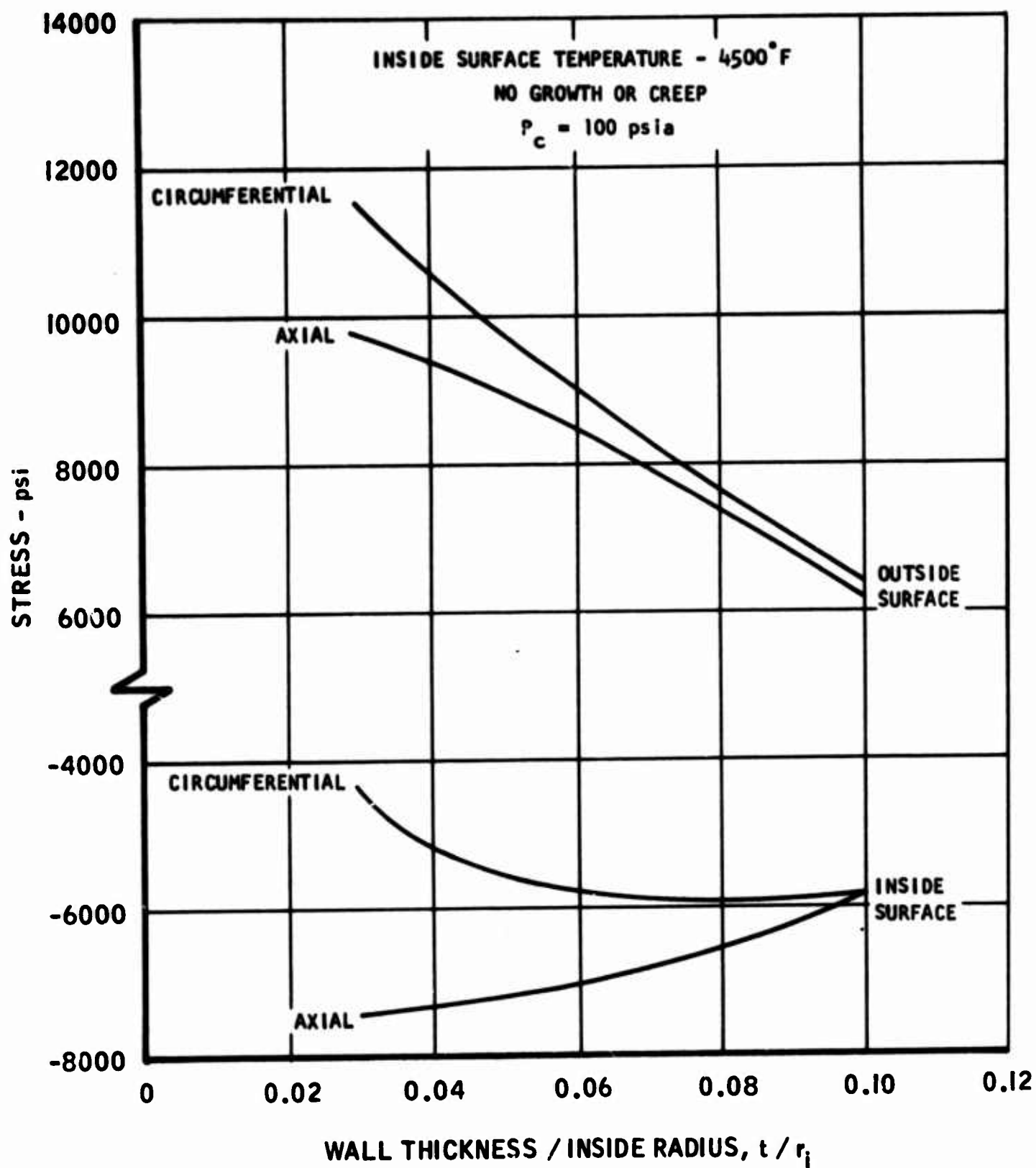


FIGURE 89. Operating Stresses, Controlled Wall Temperature Chamber, vs.  $t/r$ , 5000-lb Thrust Configuration



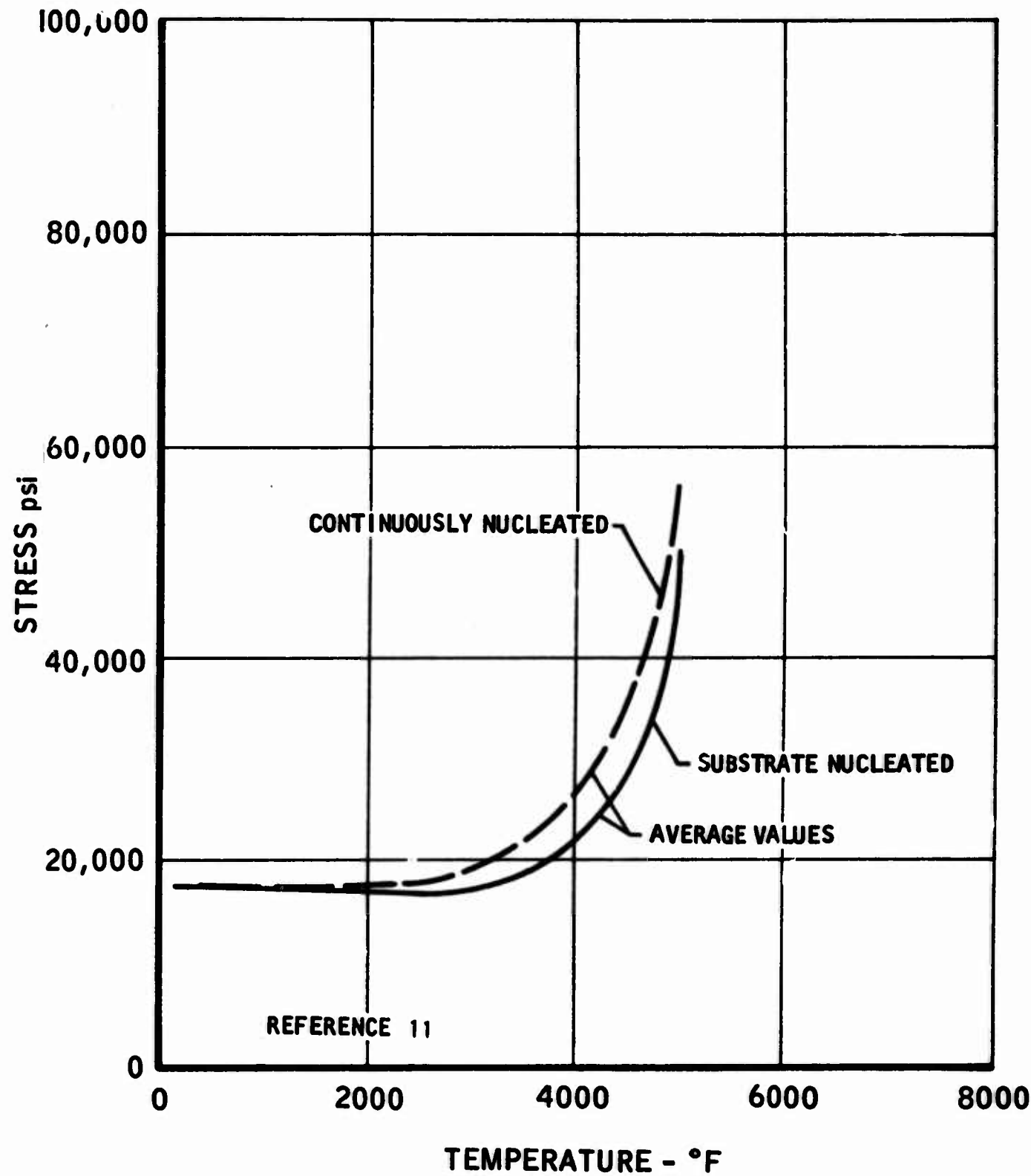


FIGURE 90. Tensile Strength of Pyrolytic Graphite in the a-Direction

UNCLASSIFIED

AFRPL-TR-66-95

Report 6106

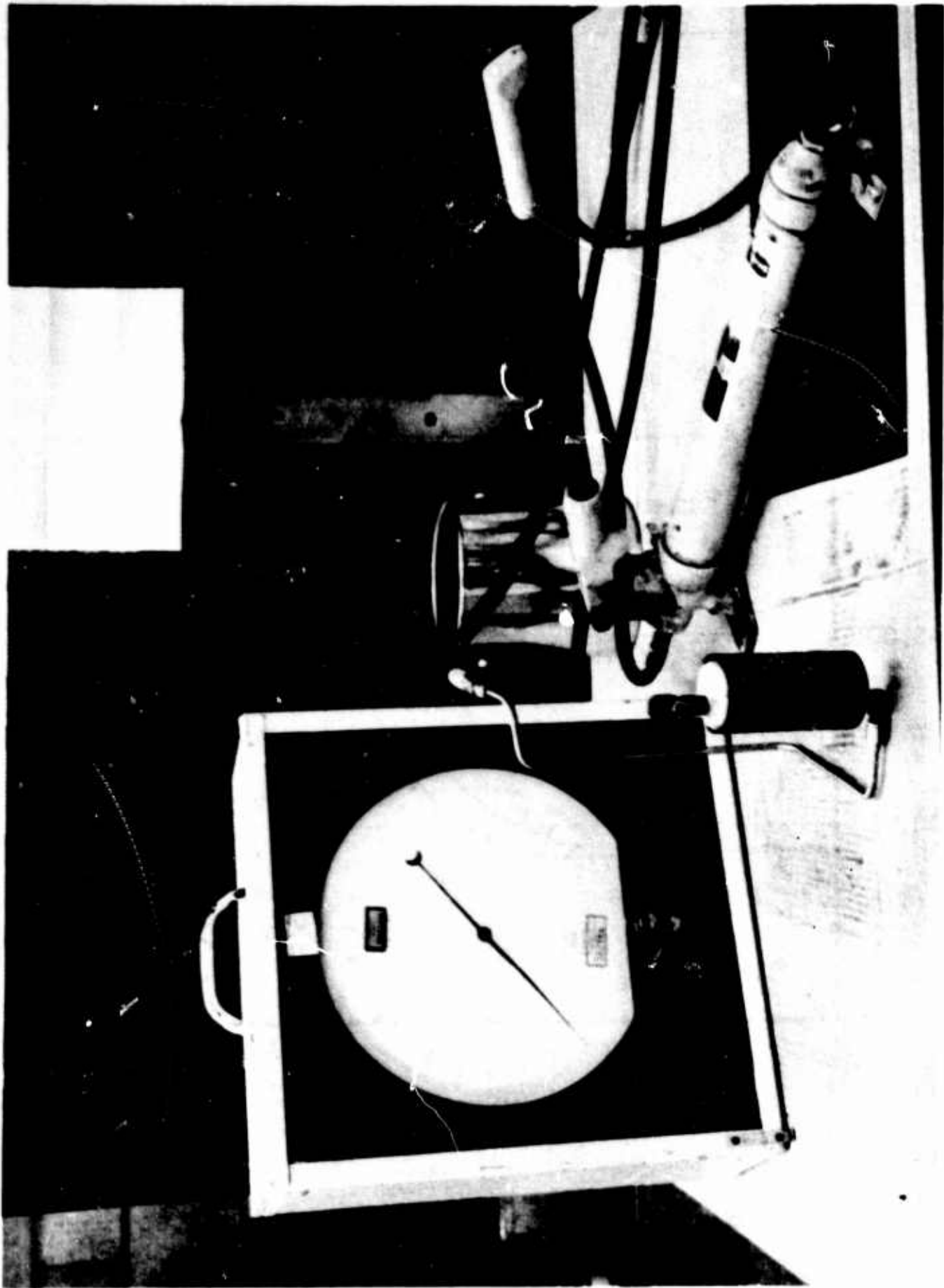


FIGURE 91. Setup for Rupture Test of Pyrolytic Graphite Tubes

T11263-1

UNCLASSIFIED  
-166-

UNCLASSIFIED

AFRPL-TR-66-95

Report 6106



FIGURE 92. Typical Pyrolytic Graphite Tube After Rupture Test Failure

T11263-2

UNCLASSIFIED  
-167-

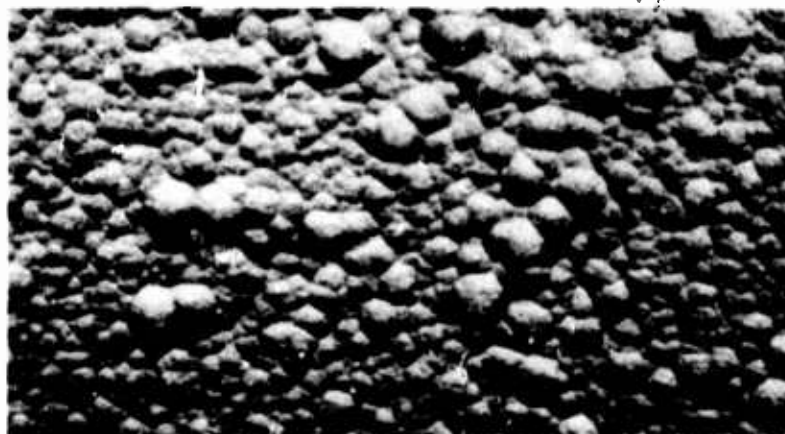
UNCLASSIFIED

AFRPL-TR-66-95

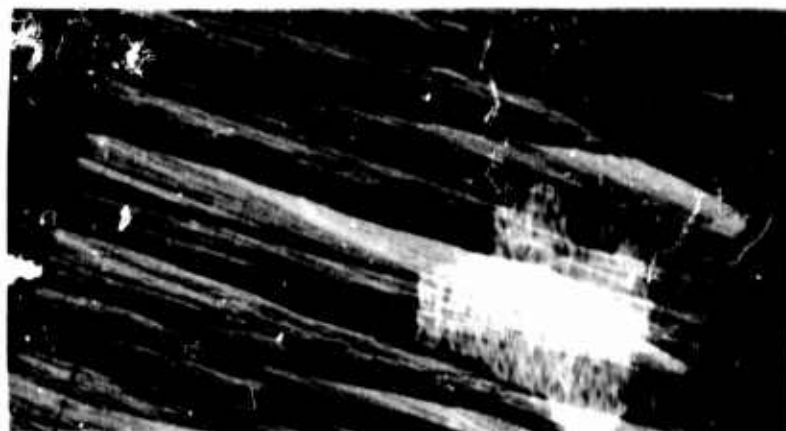
Report 6106



A. OD Surface (10X)



B. ID Surface (10X)



C. Cross Section (50X)

FIGURE 93. Microstructure of PG Tube S-103,  
Rupture Pressure = 370 psig, National CS Graphite Mandrel

UNCLASSIFIED  
-168-

UNCLASSIFIED

AFRPL-TR-66-95

Report 6106



A. OD Surface (10X)



B ID Surface (10X)



C. Cross Section (50X)

FIGURE 94. Microstructure of Tube S-102,  
Rupture Pressure = 380 psig, National ATJ Graphite Mandrel

UNCLASSIFIED

UNCLASSIFIED

AFRPL-TR-66-95

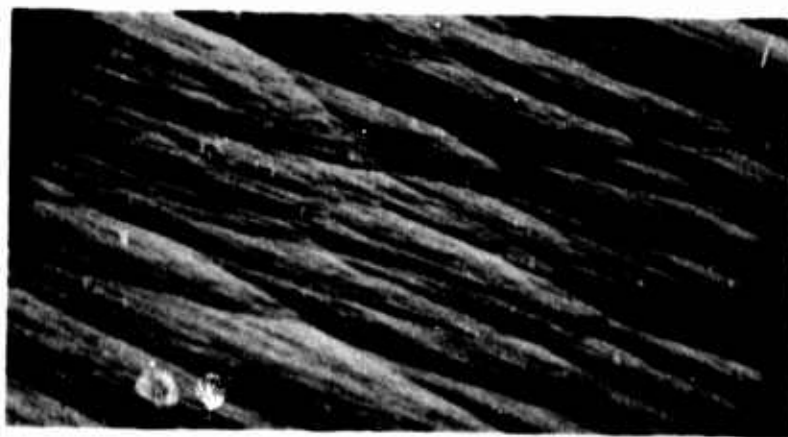
Report 6106



A. OD Surface (10X)



B. ID Surface (10X)



C. Cross Section (50X)

FIGURE 95. Microstructure of PG Tube S-101,  
Rupture Pressure = 680 psig, Speer 34995 Graphite Mandrel

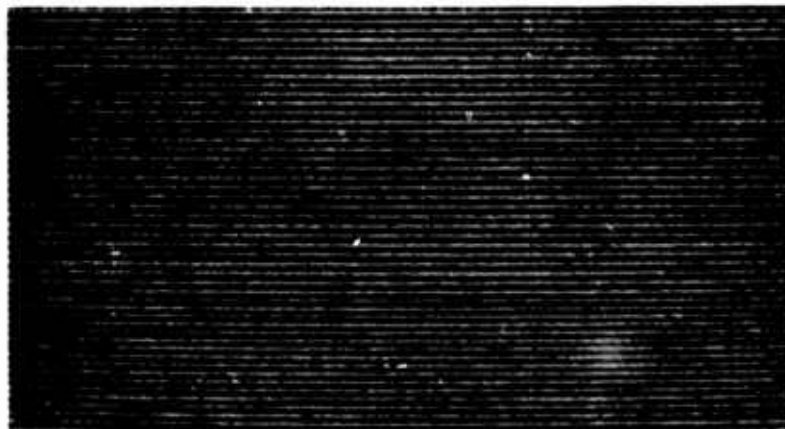
UNCLASSIFIED



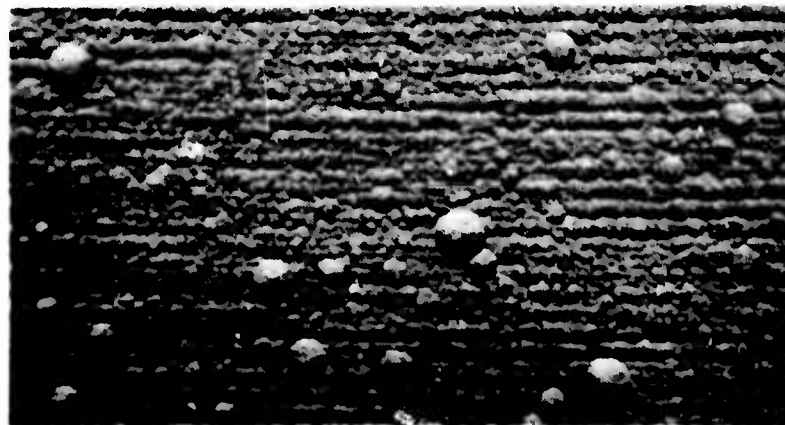
UNCLASSIFIED

AFRPL-TR-66-95

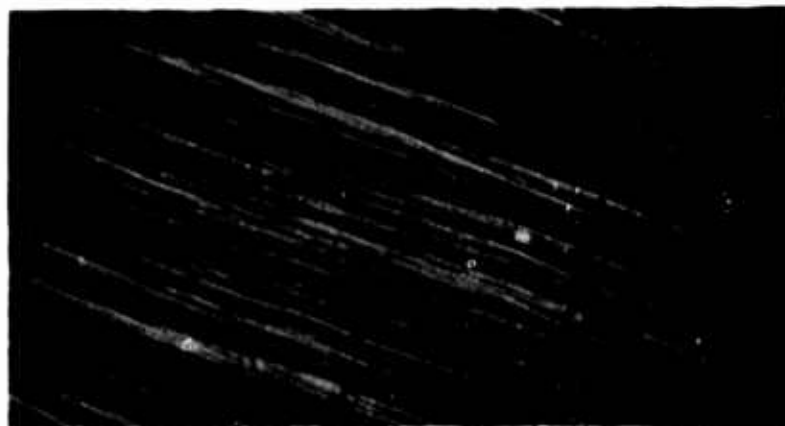
Report 6106



A. OD Surface (10X)



B. ID Surface (10X)



C. Cross Section (50X)

FIGURE 96. Microstructure of PG Tube S-104  
Rupture Pressure = 900 psig, Poco Graphite Mandrel

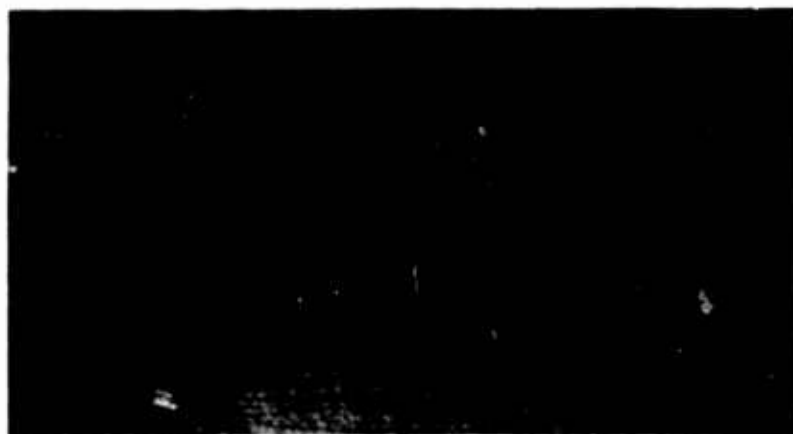
UNCLASSIFIED



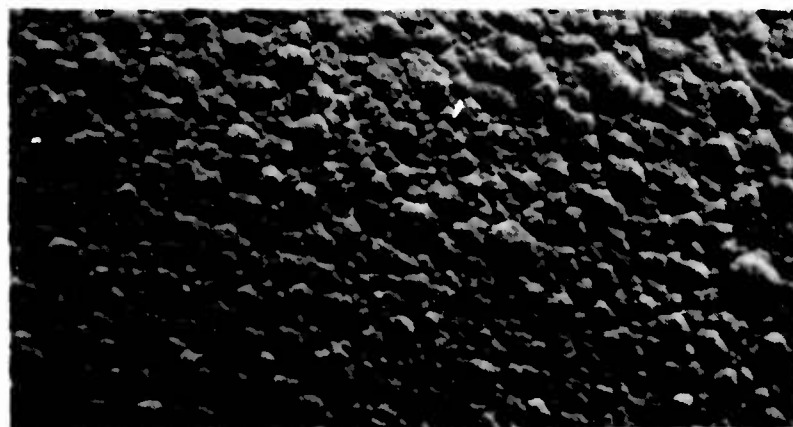
UNCLASSIFIED

AFRPL-TR-66-95

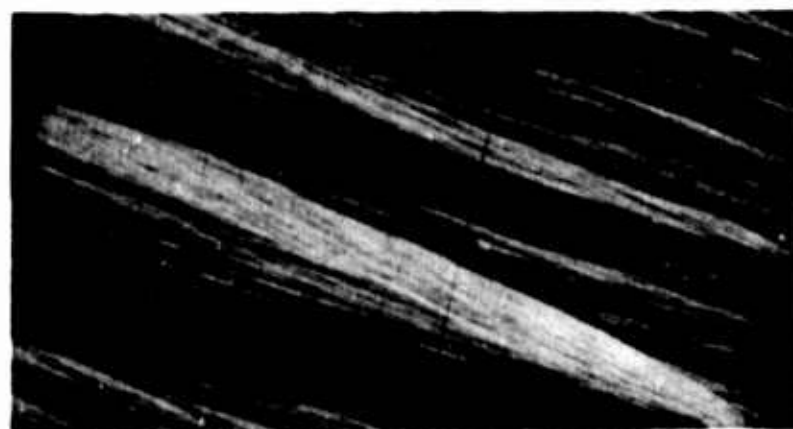
Report 6106



A. OD Surface (10X)



B. ID Surface (10X)



C. Cross Section (50X)

FIGURE 97. Microstructure of PG Tube G102  
Rupture Pressure = 940 psig, Boron-Doped

UNCLASSIFIED  
-172-

UNCLASSIFIED

AFRPL-TR-66-95

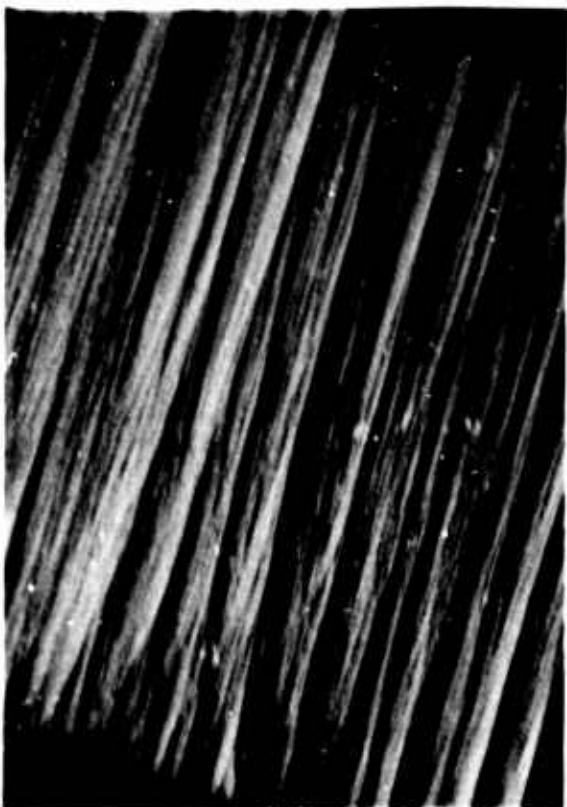
Report 6106



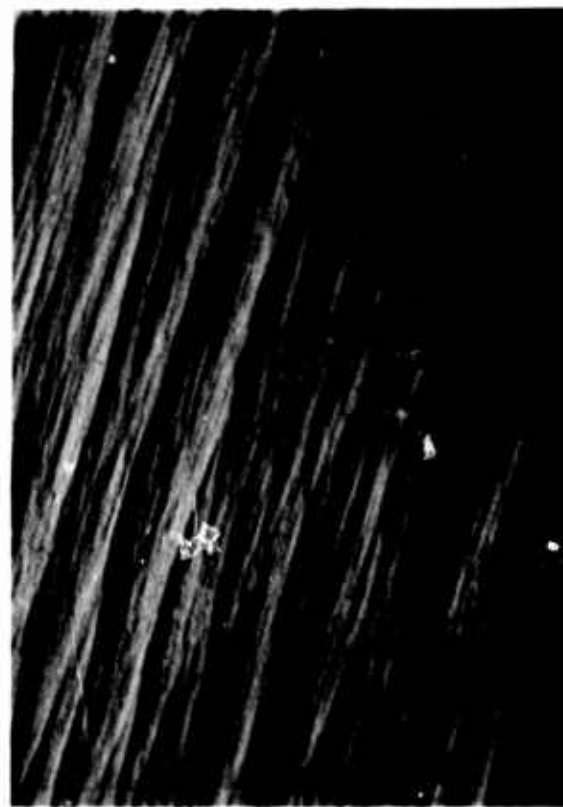
A. OD Surface (10X)



B. ID Surface (10X)



C. Top Cross Section (50X)



D. Bottom Cross Section (50X)

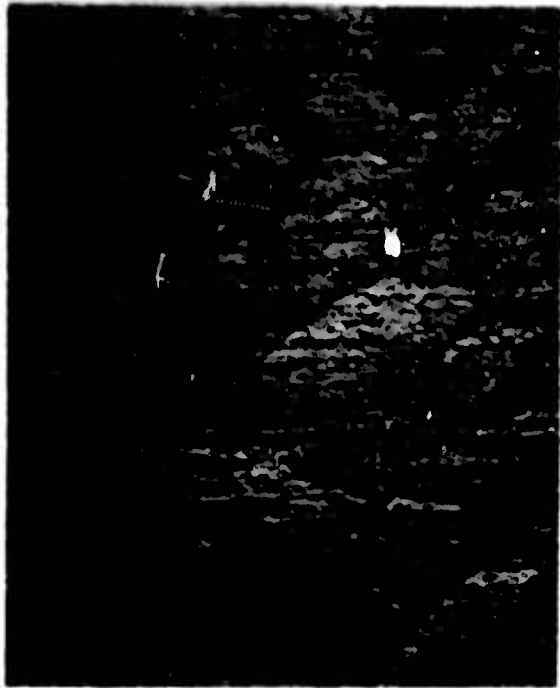
FIGURE 98. Microstructure of PG Tube G202, Rupture Pressure = 690 psia, Regenerative Microstructure, ATJ Graphite Mandrel

UNCLASSIFIED

UNCLASSIFIED

AFRPL-TR-66-95

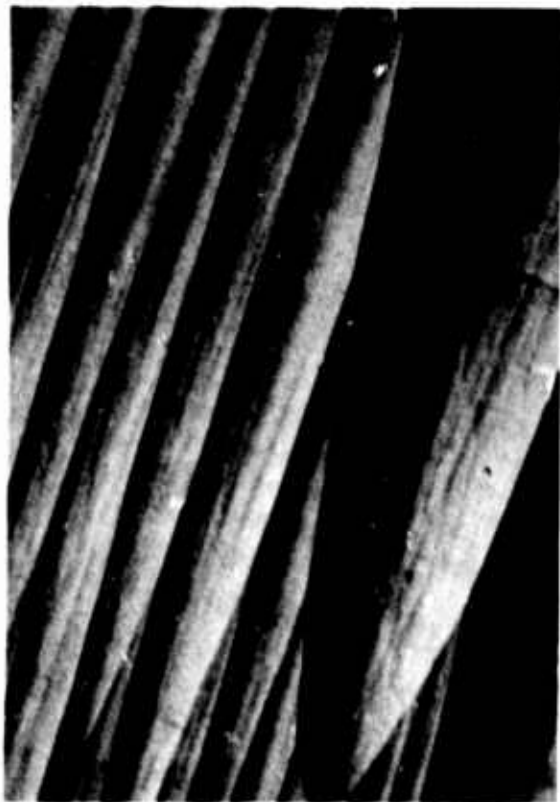
Report 6106



A. OD Surface (10X)



B. ID Surface (10X)



C. Top Cross Section (50X)



D. Bottom Cross Section (50X)

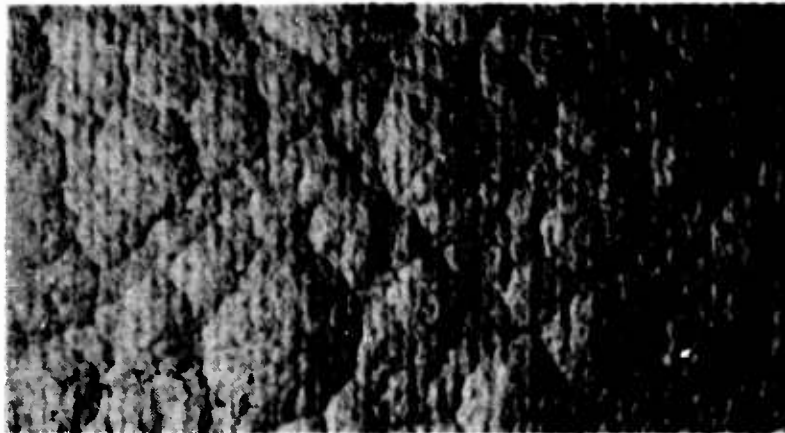
FIGURE 99. Microstructure of PG Tube G203, Rupture Pressure = 2100 psia, Regenerative Microstructure, ATJ Graphite Mandrel

UNCLASSIFIED

UNCLASSIFIED

AFRPL-TR-66-95

Report 6106



A. OD Surface (10X)



B. Cross Section (11X)

FIGURE 100. Microstructure of PG Tube P401,  
Rupture Pressure = 100 psig, ATJ Graphite Mandrel

UNCLASSIFIED

UNCLASSIFIED

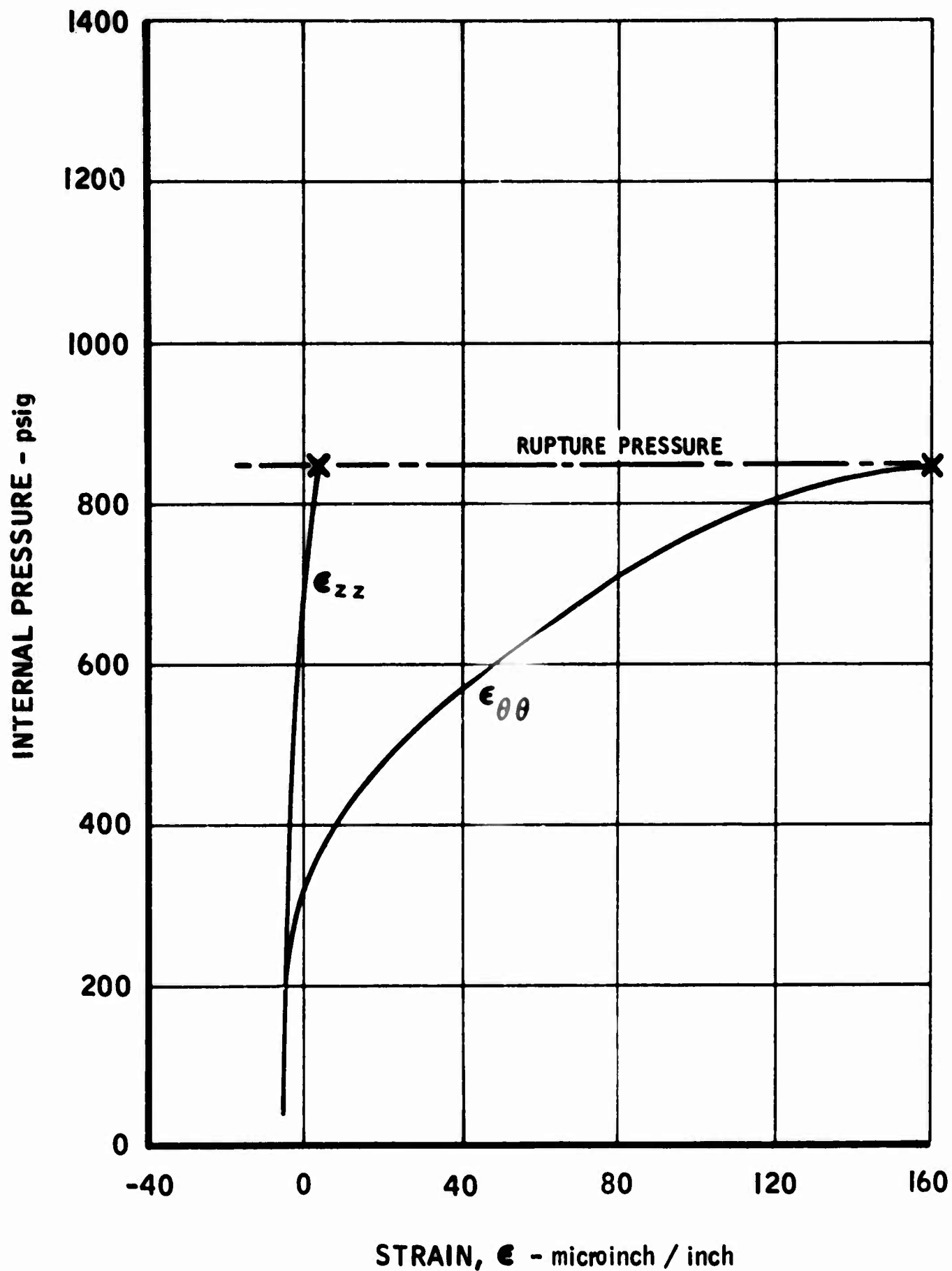


FIGURE 101. Strain on Outside Surface (from Strain Gages) vs. Internal Pressure, Tube H101 (Controlled Delaminations)

UNCLASSIFIED

UNCLASSIFIED

AFRPL-TR-66-95

Report 6106

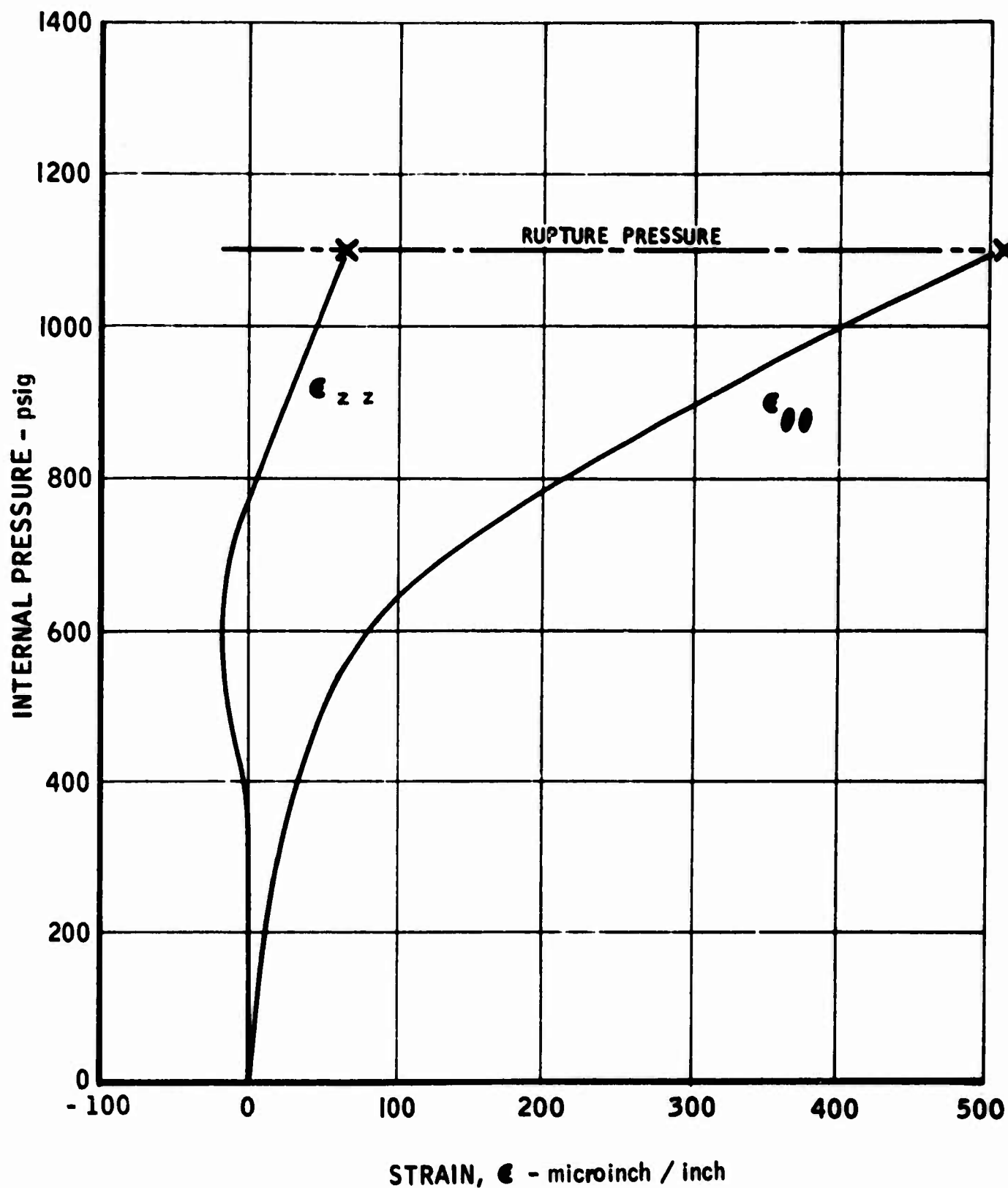


FIGURE 102. Strain on Outside Surface (from Strain Gages) vs. Internal Pressure, Tube H102 (Controlled Delaminations)

5016-37

UNCLASSIFIED

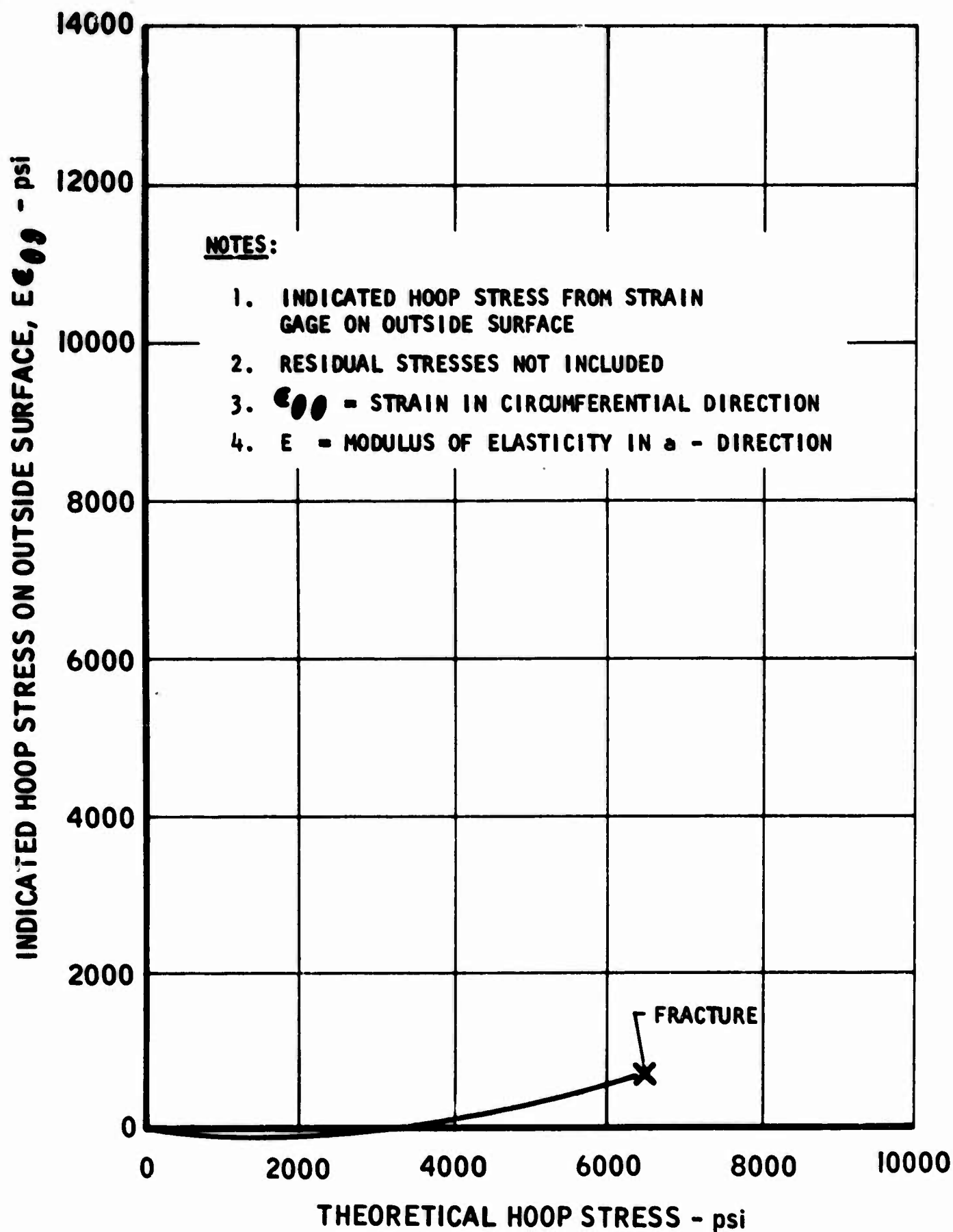


FIGURE 103. Indicated Hoop Stress on Outside Surface vs. Theoretical Hoop Stress, Tube H101 (Controlled Delaminations)



UNCLASSIFIED

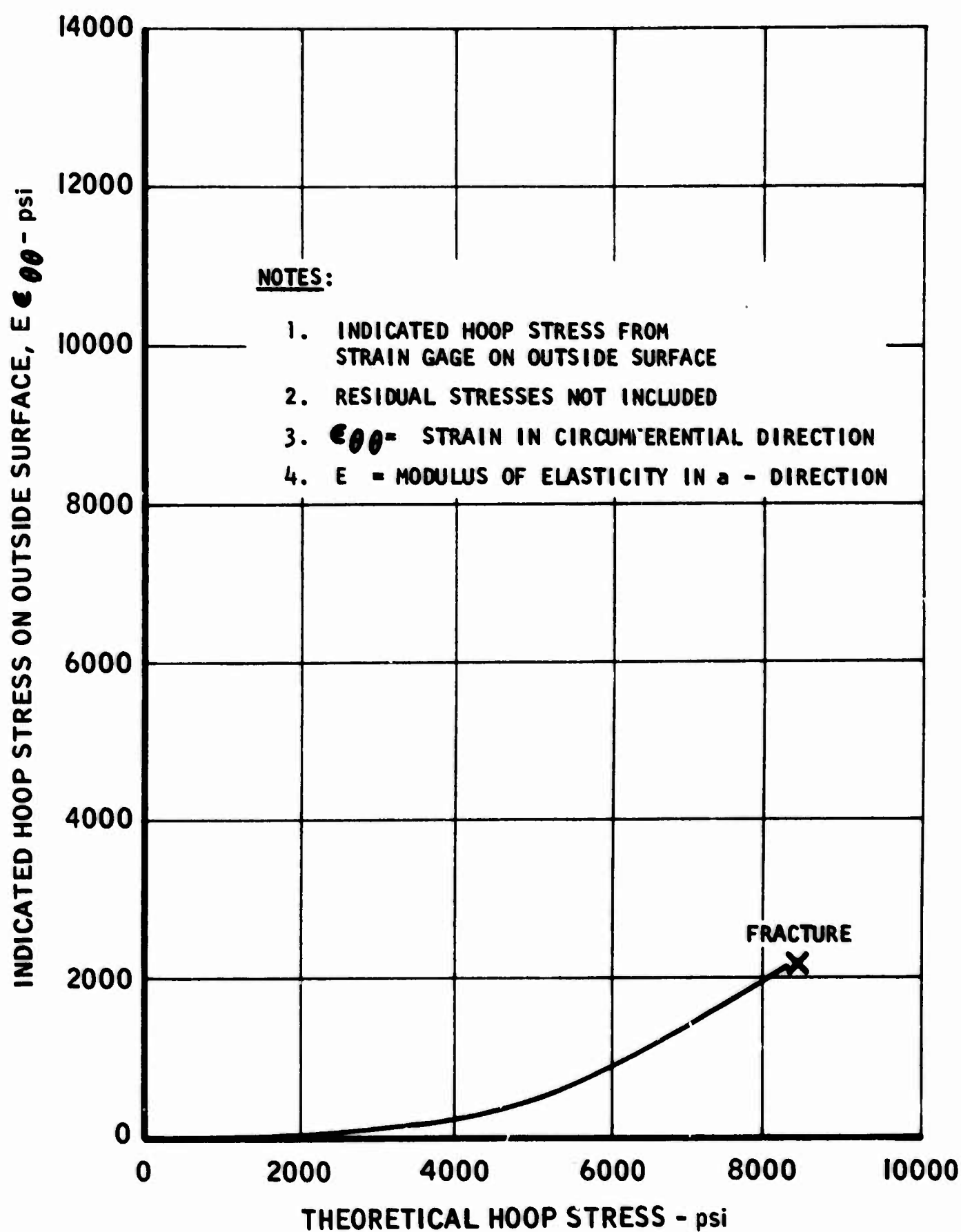


FIGURE 104. Indicated Hoop Stress on Outside Surface vs. Theoretical Hoop Stress, Tube H102 (Controlled Delaminations)

UNCLASSIFIED

UNCLASSIFIED

AFRPL-TR-66-95

Report 6106

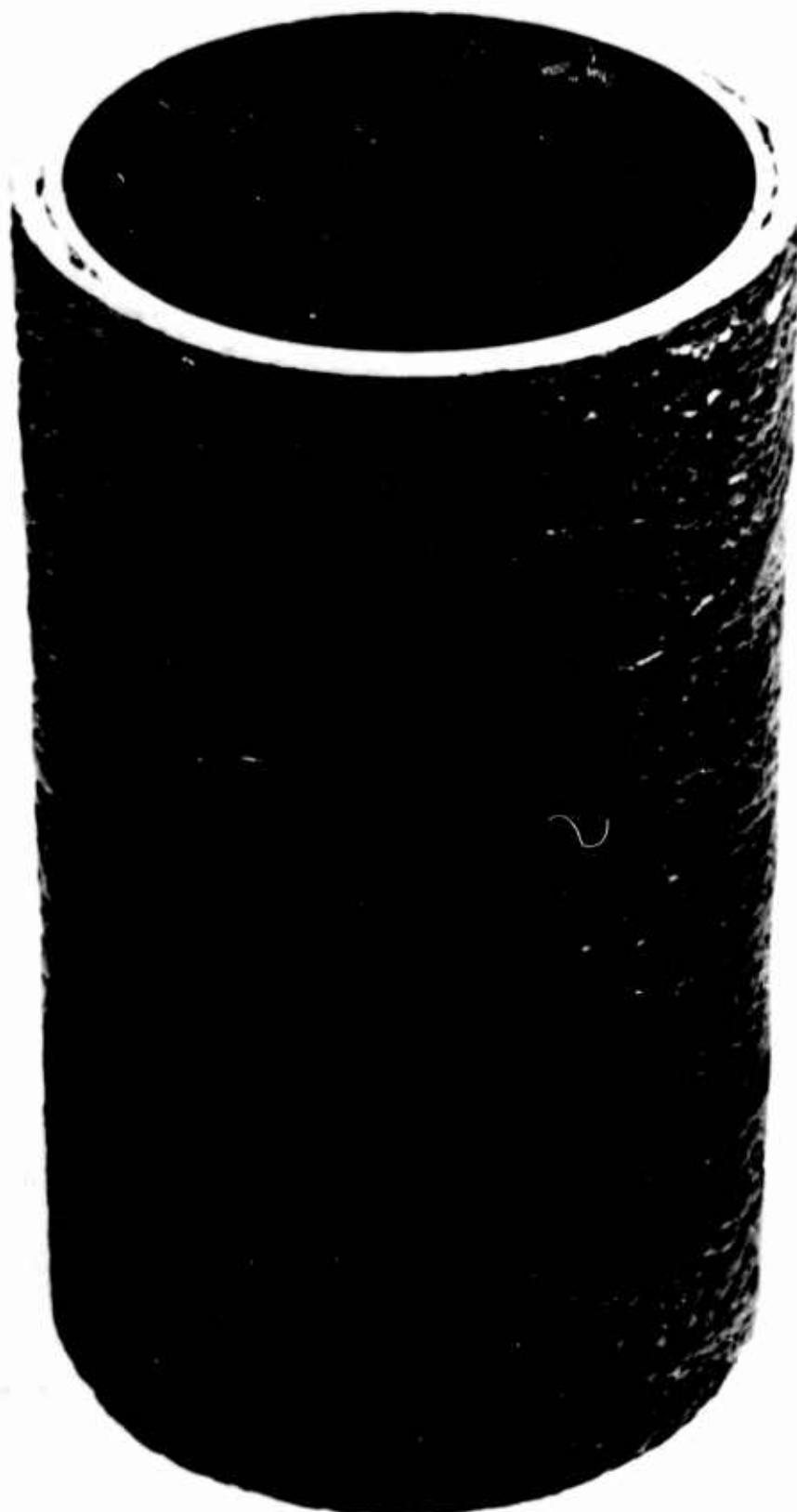


FIGURE 105. HTM Fiber Reinforced Pyrolytic Graphite Tube

7022-1

UNCLASSIFIED

UNCLASSIFIED

AFRPL-TR-66-95

Report 6106



A. OD Surface (10X)



B. Cross Section (11X)

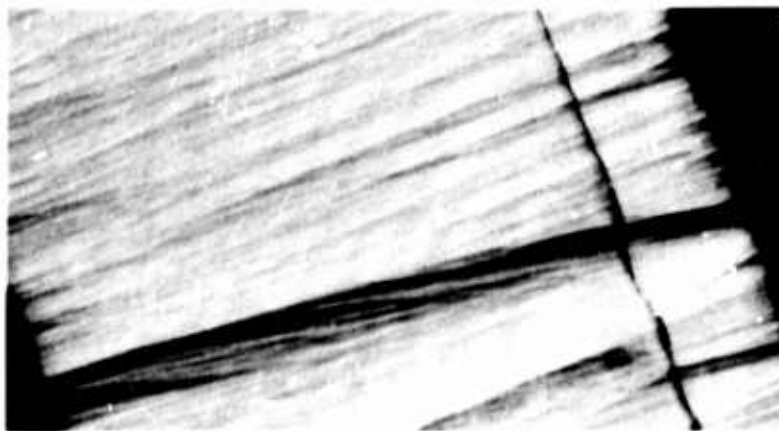
FIGURE 106. Microstructure of PG Tube H202,  
Rupture Pressure = 600 psig

UNCLASSIFIED

UNCLASSIFIED

AFRPL-TR-66-95

Report 6106



A. Tube R1C1



B. Tube R502



C. Tube R1001

FIGURE 107. Microstructures of PG Tubes R101, R502, and R1001 (50X)

UNCLASSIFIED

UNCLASSIFIED

Security Classification

DOCUMENT CONTROL DATA - R&D		
(Security classification of title, body of abstract and indexing annotation must be entered when the overall report is classified)		
1. ORIGINATING ACTIVITY (Corporate author) The Marquardt Corporation Van Nuys, California		2a. REPORT SECURITY CLASSIFICATION UNCLASSIFIED
		2b. GROUP None
3. REPORT TITLE Free Standing Pyrolytic Graphite Thrust Chambers for Space Operation and Attitude Control. Phase I: Analysis and Preliminary Design		
4. DESCRIPTIVE NOTES (Type of report and inclusive dates) Final Report - - Phase I		
5. AUTHOR(S) (Last name, first name, initial) Campbell, J. G. Haas, M. L. Coulbert, C. D.		
6. REPORT DATE June 1966	7a. TOTAL NO. OF PAGES	7b. NO. OF REFS
8a. CONTRACT OR GRANT NO. AF 04(611)-10790	9a. ORIGINATOR'S REPORT NUMBER(S) AFRPL-TR-66-95	
b. PROJECT NO. AFSC 3058		
c. AF Program Element Code: 6.24.05.18.4.	9b. OTHER REPORT NO(S) (Any other numbers that may be assigned this report) TMC Report 6106	
d.		
10. AVAILABILITY/LIMITATION NOTICES This document is subject to special export controls and each transmittal to foreign governments or foreign nationals may be made only with prior approval of AFRPL (RPPR-STINFO), Edwards, California 93523.		
11. SUPPLEMENTARY NOTES		12. SPONSORING MILITARY ACTIVITY Air Force Rocket Propulsion Laboratory Research and Technology Division Air Force Systems Command Edwards Air Force Base, California
13. ABSTRACT Free standing pyrolytic graphite (PG) thrust chambers were evaluated for application to high energy upper stage and attitude control liquid rocket engines. The results of stress analyses, heat transfer analyses, and a vendor product survey and evaluation are presented. Stress calculations included the effects of PG anisotropy, creep, and growth and showed the feasibility of fabricating and firing free standing PG thrust chambers up to 5000 pounds thrust. Chamber pressures up to 300 psia appear feasible. Growth and creep at high operating temperatures may be critical. Heat transfer studies investigated transient and steady state temperature distributions. High inside surface temperatures encountered with fluorine propellants create heat soak back problems in the injector. Five vendors supplied 78 free standing thin wall PG tubes 2 in. ID and 4 in. long which were evaluated by burst testing. Parameters included mandrel material, mandrel surface finish, nucleated microstructure, controlled delaminations, boron alloying, and fiber reinforcement. The critical effect of nodule size on maximum tube strength was confirmed. Boron alloy tubes were strongest. A burst pressure of 1000 psig appears to be a reasonable target for currently available PG.		

DD FORM 1473 0101-807-6800

UNCLASSIFIED

Security Classification

UNCLASSIFIED

## Security Classification

14. KEY WORDS	LINK A		LINK B		LINK C	
	ROLE	WT	ROLE	WT	ROLE	WT
THRUST CHAMBERS						
PYROLYTIC GRAPHITE						
SPACE OPERATION						
ATTITUDE CONTROL						

## INSTRUCTIONS

1. **ORIGINATING ACTIVITY:** Enter the name and address of the contractor, subcontractor, grantee, Department of Defense activity or other organization (*corporate author*) issuing the report.

2a. **REPORT SECURITY CLASSIFICATION:** Enter the overall security classification of the report. Indicate whether "Restricted Data" is included. Marking is to be in accordance with appropriate security regulations.

2b. **GROUP:** Automatic downgrading is specified in DoD Directive 5200.10 and Armed Forces Industrial Manual. Enter the group number. Also, when applicable, show that optional markings have been used for Group 3 and Group 4 as authorized.

3. **REPORT TITLE:** Enter the complete report title in all capital letters. Titles in all cases should be unclassified. If a meaningful title cannot be selected without classification, show title classification in all capitals in parenthesis immediately following the title.

4. **DESCRIPTIVE NOTES:** If appropriate, enter the type of report, e.g., interim, progress, summary, annual, or final. Give the inclusive dates when a specific reporting period is covered.

5. **AUTHOR(S):** Enter the name(s) of author(s) as shown on or in the report. Enter last name, first name, middle initial. If military, show rank and branch of service. The name of the principal author is an absolute minimum requirement.

6. **REPORT DATE:** Enter the date of the report as day, month, year; or month, year. If more than one date appears on the report, use date of publication.

7a. **TOTAL NUMBER OF PAGES:** The total page count should follow normal pagination procedures, i.e., enter the number of pages containing information.

7b. **NUMBER OF REFERENCES:** Enter the total number of references cited in the report.

8a. **CONTRACT OR GRANT NUMBER:** If appropriate, enter the applicable number of the contract or grant under which the report was written.

8b, 8c, & 8d. **PROJECT NUMBER:** Enter the appropriate military department identification, such as project number, subproject number, system numbers, task number, etc.

9a. **ORIGINATOR'S REPORT NUMBER(S):** Enter the official report number by which the document will be identified and controlled by the originating activity. This number must be unique to this report.

9b. **OTHER REPORT NUMBER(S):** If the report has been assigned any other report numbers (*either by the originator or by the sponsor*), also enter this number(s).

10. **AVAILABILITY/LIMITATION NOTICES:** Enter any limitations on further dissemination of the report, other than those

imposed by security classification, using standard statements such as:

- (1) "Qualified requesters may obtain copies of this report from DDC."
- (2) "Foreign announcement and dissemination of this report by DDC is not authorized."
- (3) "U. S. Government agencies may obtain copies of this report directly from DDC. Other qualified DDC users shall request through \_\_\_\_\_."
- (4) "U. S. military agencies may obtain copies of this report directly from DDC. Other qualified users shall request through \_\_\_\_\_."
- (5) "All distribution of this report is controlled. Qualified DDC users shall request through \_\_\_\_\_."

If the report has been furnished to the Office of Technical Services, Department of Commerce, for sale to the public, indicate this fact and enter the price, if known.

11. **SUPPLEMENTARY NOTES:** Use for additional explanatory notes.

12. **SPONSORING MILITARY ACTIVITY:** Enter the name of the departmental project office or laboratory sponsoring (*paying for*) the research and development. Include address.

13. **ABSTRACT:** Enter an abstract giving a brief and factual summary of the document indicative of the report, even though it may also appear elsewhere in the body of the technical report. If additional space is required, a continuation sheet shall be attached.

It is highly desirable that the abstract of classified reports be unclassified. Each paragraph of the abstract shall end with an indication of the military security classification of the information in the paragraph, represented as (TS), (S), (C), or (U).

There is no limitation on the length of the abstract. However, the suggested length is from 150 to 225 words.

14. **KEY WORDS:** Key words are technically meaningful terms or short phrases that characterize a report and may be used as index entries for cataloging the report. Key words must be selected so that no security classification is required. Identifiers, such as equipment model designation, trade name, military project code name, geographic location, may be used as key words but will be followed by an indication of technical context. The assignment of links, roles, and weights is optional.

UNCLASSIFIED

Security Classification